

Mechanics of Bone-substituting Meta-biomaterials

Ahmadi, Mohammad

DOI

[10.4233/uuid:aa2fdb6-34a3-43e7-b8fa-8ae9b1777506](https://doi.org/10.4233/uuid:aa2fdb6-34a3-43e7-b8fa-8ae9b1777506)

Publication date

2018

Document Version

Final published version

Citation (APA)

Ahmadi, M. (2018). *Mechanics of Bone-substituting Meta-biomaterials*. [Dissertation (TU Delft), Delft University of Technology]. <https://doi.org/10.4233/uuid:aa2fdb6-34a3-43e7-b8fa-8ae9b1777506>

Important note

To cite this publication, please use the final published version (if applicable).
Please check the document version above.

Copyright

Other than for strictly personal use, it is not permitted to download, forward or distribute the text or part of it, without the consent of the author(s) and/or copyright holder(s), unless the work is under an open content license such as Creative Commons.

Takedown policy

Please contact us and provide details if you believe this document breaches copyrights.
We will remove access to the work immediately and investigate your claim.

Mechanics of Bone-Substituting Meta- Biomaterials

Mechanics of Bone-Substituting Meta- Biomaterials

Dissertation

for the purpose of obtaining the degree of doctor

at Delft University of Technology

by the authority of the Rector Magnificus, Prof. Ir. T.H.J.J. van der Hagen

chair of the Board for Doctorates

to be defended publicly on

Tuesday 5 June at 12:30 o'clock

by

Seyed Mohammad AHMADI

Master of Science in Medical Engineering and Sport Engineering,

Amirkabir University of Technology, Tehran, Iran,

Born in Tehran, Iran.

This dissertation has been approved by the promotor.

Composition of the doctoral committee:

Rector Magnificus,	chairperson
Prof. dr. A. A. Zadpoor	Delft University of Technology, promotor
Prof. dr. ir. H. Weinans	University Medical Center Utrecht, promotor

Independent members:

Prof. dr. ir. L. Geris	University of Liege, Belgium
Prof. dr. ir. P. Breedveld	Delft University of Technology
Prof. dr. ir. J. Herder	Delft University of Technology
Prof. dr. ir. J. Sietsma	Delft University of Technology

Other member:

Dr. S. Amin Yavari	University Medical Center Utrecht
--------------------	-----------------------------------

This research was carried out in the Department of Biomechanical Engineering of Delft University of Technology.

Keywords: Additive manufacturing, mechanical characterization, fatigue behaviour, porous biomaterial, titanium, CoCr, Ti6Al4V

Printed by: Gildeprint – www.gildeprint.nl

Copyright©: 2018 by S. M. Ahmadi

An electronic copy of this dissertation is available at <http://repository.tudelft.nl/>.

تقديم به بنفشه

Contents

Contents.....	vii
List of Figures	xi
List of Tables	xv
Chapter 1 Introduction	1
1.1 Introduction	1
1.2 Central theme of this thesis.....	5
1.3 Thesis outline	5
1.4 References	8
Chapter 2 Mechanical behavior of regular open-cell porous biomaterials made of diamond lattice unit cells	11
2.1 Abstract.....	12
2.2 Introduction	13
2.3 Materials and methods.....	14
2.3.1 Analytical model.....	14
2.3.2 Finite element model.....	23
2.3.3 Experiments	24
2.4 Results.....	26
2.5 Discussion.....	28
2.6 Conclusion.....	31
2.7 References	31
Chapter 3 Revival of pure titanium for dynamically loaded porous implants using additive manufacturing.....	38
3.1 Abstract.....	39
3.2 Introduction	39
3.3 Materials and Methods.....	42
3.3.1 Materials and manufacturing.....	42
3.3.2 Morphological analysis	43

3.3.3	Mechanical testing.....	44
3.4	Results.....	46
3.4.1	Morphological properties	46
3.4.2	Mechanical properties	46
3.5	Discussion.....	49
3.6	Conclusion.....	52
3.7	Acknowledgements.....	53
3.8	References	53
Chapter 4	Additively manufactured open-cell porous biomaterials made from six different space-filling unit cells: the mechanical and morphological properties.....	60
4.1	Abstract.....	61
4.2	Introduction	62
4.3	Materials and methods.....	63
4.3.1	Materials and manufacturing.....	63
4.3.2	Morphological characterization.....	66
4.3.3	Mechanical testing.....	67
4.4	Results.....	68
4.5	Discussion.....	84
4.5.1	Comparison between the Different Types of Unit Cells	84
4.5.2	Ratio of Plateau Stress to Yield Stress.....	86
4.5.3	Energy Absorption.....	87
4.5.4	Anisotropy.....	87
4.5.5	Applications in the Design of Implants and Tissue Engineering Scaffolds.....	88
4.5.6	Future research.....	89
4.6	Conclusion.....	90
4.7	Author contribution	90
4.8	Conflicts of interest.....	91
4.9	References	91
Chapter 5	Relationship between unit cell type and porosity and the fatigue behavior of selective laser melted meta-biomaterials.....	100
5.1	Abstract.....	101
5.2	Introduction	102
5.3	Materials and methods.....	103
5.3.1	Manufacturing techniques.....	103
5.3.2	Morphological characterization.....	105

5.3.3	Static mechanical testing	106
5.3.4	Fatigue mechanical testing	107
5.4	Results.....	107
5.5	Discussion.....	112
5.6	Conclusion.....	117
5.7	References	117
Chapter 6	Effects of laser processing parameters on the mechanical properties, topology, and microstructure of additively manufactured porous metallic biomaterials: a vector-based approach	124
6.1	Abstract.....	125
6.2	Introduction	125
6.3	Materials and methods.....	127
6.3.1	Materials and manufacturing.....	127
6.3.2	Static mechanical testing	130
6.3.3	Characterization.....	130
6.4	Results.....	132
6.5	Discussion.....	139
6.6	Conclusion.....	141
6.7	References	142
Chapter 7	Isolated and Modulated effects of topological design and material type on the mechanical properties of additively manufactured porous biomaterials	147
7.1	Abstract.....	148
7.2	Introduction	148
7.3	Materials and method	150
7.3.1	Materials and manufacturing.....	150
7.3.2	Topological characterization.....	154
7.3.3	Microstructural analysis.....	155
7.3.4	Static mechanical testing	156
7.3.5	Analytical relationship.....	157
7.4	Results.....	158
7.5	Discussion.....	168
7.5.1	Mechanistic aspects.....	169
7.5.2	Difference between various mechanical properties.....	172
7.6	Conclusion.....	176
7.7	References	177
Chapter 8	Fatigue performance of additively manufactured meta-biomaterials: the effects of topology and material type.....	181

8.1	Abstract.....	182
8.2	Introduction	182
8.3	Materials and methods.....	184
8.3.1	Materials and manufacturing.....	184
8.3.2	Topological characterization.....	186
8.3.3	Microstructural characterization	187
8.3.4	Mechanical testing.....	188
8.3.5	Statistical analysis	189
8.4	Results.....	189
8.5	Discussion.....	196
8.5.1	Topological/material modulation	196
8.5.2	The effects of surface roughness and grain morphology	197
8.5.3	The effects of the mechanical behavior of the bulk material.....	199
8.5.4	HCF/LCF differences.....	200
8.6	Conclusion.....	204
8.7	References	205
Chapter 9	Conclusions	209
9.1	Overview and conclusions	209
9.2	Recommendations for future research.....	213
9.3	Summary	215
9.4	Samenvatting	217
9.5	Author Curriculum Vitae	219
9.5.1	Education	219
9.5.2	Professional experience	219
9.6	List of publications	220
9.7	Acknowledgment	222

List of Figures

Figure 1-1. Biomaterials classification	2
Figure 2-1. The loads, boundary conditions, and one of the unit cells used in the diamond-type cellular structures simulated using three-dimensional finite element models.....	15
Figure 2-2. An arbitrary unit cell under uniaxial compression (a). The free body diagram and deformations of an arbitrary strut in y (b) and x (c) directions.	16
Figure 2-3. The STL file used for manufacturing of the diamond-type cellular structures (a) and a sample of the resulting structures (b).	24
Figure 2-4. Experimentally measured stress–strain curves for solid specimens (a) and two of the cellular structures tested in the current study: one structure with a strut length of 0.65 mm and mean strut diameter of 0.347 mm (b) and one structure with a strut length of 0.65 mm and a mean strut diameter of 0.419 mm (c).....	27
Figure 2-5. Comparison between the elastic modulus (a) Poisson’s ratio (b), and yield stress (c) values obtained using different approaches including analytical, numerical, and experimental approaches (AN-Eu: analytical solution based on the Euler–Bernoulli theory, AN-Tim: analytical solution based on the Timoshenko theory, EXP: experimental results, FE: finite element solution).....	28
Figure 3-1. Additively manufactured porous CP Ti structures: 3D CAD visual representation of the four different structures in isometric (A) and top (B) view and a picture after manufacturing (C).	43
Figure 3-2. Static mechanical properties of open porous SLM processed titanium and tantalum structures: representative compressive stress–strain curve and graphical representation of the calculated values σ_y , σ_{pl} , σ_{130} , e_{ple} for a Ti 120–500 structure in CP Ti (A) and Ti6Al4V ELI (B), both including a picture of a sample after compression testing; and a comparison between the yield strength and plateau stress (C) and stiffness (D) for all three materials versus the actual measured open porosity of each structure	45
Figure 3-3. Dynamic mechanical properties of open porous SLM processed titanium and tantalum structures: S-N curves obtained by compression-compression fatigue testing of all CP Ti samples using absolute (A) and normalized (B) stress values and a power law representing the results of Ti6Al4V ELI and Ta structures from previous studies (B) [17] and [23]; an overview of all fitted power laws for all four porous structures in both titanium materials using absolute stress values, including the structure intersection points marked by ‘X’ (C); an extrapolation of the fitted power laws to 10^6 cycles for all four porous structures in both titanium materials and the actual fatigue limit of the Ta structure versus the actual measured open porosity of each structure (D).....	48
Figure 4-1. Schematic drawings of the unit cells used in the porous structure: (a) Cubic; (b) Diamond; (c) Truncated cube; (d) Truncated cuboctahedron; (e) Rhombic dodecahedron; (f) Rhombicuboctahedron.	64
Figure 4-2. Sample specimens from the porous structures based on different types of unit cells: (a) Cubic; (b) Diamond; (c) Truncated cube; (d) Truncated cuboctahedron; (e) Rhombic dodecahedron; (f) Rhombicuboctahedron.....	66

Figure 4-3. Compressive stress-versus-compressive strain curves for specimens based on the cube unit cell and with different porosities (see Table 2).....	71
Figure 4-4. Stress-strain curves for specimens based on the diamond unit cell and with different porosities (see Table 2).....	72
Figure 4-5. Compressive stress-versus-compressive strain curves for specimens based on the truncated cube unit cell and with different porosities (see Table 2).	73
Figure 4-6. Compressive stress-versus-compressive strain curves for specimens based on the truncated cuboctahedron unit cell and with different porosities (see Table 2).....	74
Figure 4-7. Compressive stress-versus-compressive strain for specimens based on the rhombic dodecahedron unit cell and with different porosities (see Table 2).....	75
Figure 4-8. Compressive stress-versus-compressive strain curves for specimens based on the rhombicuboctahedron unit cell and with different porosities (see Table 2).....	76
Figure 4-9. Summary of the elastic gradient results for porous structures based on different types of unit cell configurations (cubic (C); diamond (D); truncated cube (TC); truncated cuboctahedron (TCO); rhombic dodecahedron (RD); rhombicuboctahedron (RCO)) and different structure relative densities (see Table 2) (Es indicates the elastic gradient of the structure if it was solid).	77
Figure 4-10. Summary of the first maximum stress results for porous structures based on different types of unit cell configurations (cubic (C); diamond (D); truncated cube (TC); truncated cuboctahedron (TCO); rhombic dodecahedron (RD); rhombicuboctahedron (RCO)) and different structure relative densities (see Table 2).....	78
Figure 4-11. Summary of the plateau stress results for porous structures based on different types of unit cell configurations (cubic (C); diamond (D); truncated cube (TC); truncated cuboctahedron (TCO); rhombic dodecahedron (RD); rhombicuboctahedron (RCO)) and different structure relative densities (see Table 2).	79
Figure 4-12. Summary of the yield stress results for porous structures based on different types of unit cell configurations (cubic (C); diamond (D); truncated cube (TC); truncated cuboctahedron (TCO); rhombic dodecahedron (RD); rhombicuboctahedron (RCO)) and different structure relative densities (see Table 2).	80
Figure 4-13. Summary of the energy absorption results for porous structures based on different types of unit cell configurations (cubic (C); diamond (D); truncated cube (TC); truncated cuboctahedron (TCO); rhombic dodecahedron (RD); rhombicuboctahedron (RCO)) and different structure relative densities (see Table 2).....	81
Figure 4-14. Comparison between the mechanical properties measured for different types of porous structures based on the six different unit cells studied here including (a) Elastic gradient; (b) First maximum stress. (c) Plateau stress; (d) Yield stress; (e) Energy absorption. In these figures, the power laws fitted to the experimental data points, and not the experimental data points themselves, are compared with each other.	83
Figure 4-15. (a) The ratio of plateau stress to yield stress as well as (b) the ratio of plateau stress to first maximum stress for different types of unit cells. In these figures, the power laws fitted to the experimental data points, and not the experimental data points themselves, are compared with each other.....	84
Figure 5-1. Schematic drawings of the unit cells used for manufacturing of porous structures studied here (a) as well as some specimens from the different types of porous structures (b).....	104

Figure 5-2. Absolute (a) and normalized (b) S-N curves for the porous structures made from the diamond unit cell.	109
Figure 5-3. Absolute (a) and normalized (b) S-N curves for the porous structures made from the truncated cuboctahedron unit cell.	110
Figure 5-4. Comparison between the normalized S-N curves (fitted power laws) of the porous structures made from diamond, truncated cuboctahedron, and rhombic dodecahedron unit cells.	111
Figure 5-5. Appearance of some sample specimens after partial loss of their stiffness while going through the fatigue protocol.	112
Figure 5-6. SEM pictures of the porous structures made from the cube (a), diamond (b), and truncated cuboctahedron (c) unit cells. Arrows show notches and imperfections in the struts.	114
Figure 6-1. A view of all the specimens manufactured by laser powers in the range of 80 W-128 W and exposure times in the range of 150 μ s-650 μ s.	128
Figure 6-2. Effect of laser power and exposure time on different geometrical and mechanical properties of porous biomaterials: (a) surface roughness, (b) strut diameter, (c) relative density, (d) Vickers hardness, (e) elastic modulus, (f) yield stress, (g) first maximum stress, and (h) plateau stress	134
Figure 6-3 . Comparison of geometrical and mechanical properties curves of different processing parameters between the experimental results, empirical formulas, and analytical prediction: (a) strut diameter, (b) relative density, (c) elastic modulus, (d) yield stress, (e) first maximum stress, and (f) plateau stress.....	136
Figure 6-4. Microscopic images of selected specimens.....	138
Figure 7-1. Side view of the additively manufactured Co-Cr porous structures based on (a) diamond (b) rhombic dodecahedron, and (c) truncated cuboctahedron unit cells	152
Figure 7-2. Stress-strain curves of different bulk materials used for additive manufacturing of porous biomaterials	154
Figure 7-3. Reconstructed CT images of Co-Cr porous structures based on (a) diamond, (b) truncated cuboctahedron, and (c) rhombic dodecahedron unit cells.....	155
Figure 7-4. Microscopic views of the microstructure of additively manufactured (a) pure titanium, (b) Ti-6Al-4V, and (c-d) Co-Cr porous structures with etched cross-sections	159
Figure 7-5. SEM picture of the microstructure of additively manufactured (a) Ti-6Al-4V, (b) Co-Cr porous structures with etched cross-sections	160
Figure 7-6. Comparison of microstructure of additive manufactured solid and porous specimens with different magnifications: (a) Ti-6Al-4V and (b) Co-Cr.	161
Figure 7-7. Stress-strain curves for Co-Cr porous structures based on diamond unit cell with different relative density values: (a) 0.209, (b) 0.267, (c) 0.34, and (d) 0.401.	162
Figure 7-8. Stress-strain curves for Co-Cr porous structures based on rhombic dodecahedron unit cell with different relative density values: (a) 0.299, (b) 0.372, and (c) 0.415.	164
Figure 7-9. Stress-strain curves for Co-Cr porous structures based on truncated octahedron unit cell with different relative density values: (a) 0.236, (b) 0.269, (c) 0.336, and (d) 0.386.	165

Figure 7-10. Comparison of normalized elastic modulus of Ti-6Al-4V, Co-Cr, Tantalum, and CPT porous structures based on (a) diamond, (b) rhombic dodecahedron, and (c) truncated octahedron unit cells.	166
Figure 7-11. Comparison of normalized yield stress of Ti-6Al-4V, Co-Cr, Tantalum, and CPT porous structures based on (a) diamond, (b) rhombic dodecahedron, and (c) truncated octahedron unit cells.	167
Figure 7-12. Comparison of normalized plateau stress of Ti-6Al-4V, Co-Cr, Tantalum, and CPT porous structures based on (a) diamond, (b) rhombic dodecahedron, and (c) truncated octahedron unit cells.	174
Figure 7-13. Comparison of energy absorption of Ti-6Al-4V, Co-Cr, Tantalum, and CPT porous structures based on (a) diamond, (b) rhombic dodecahedron, and (c) truncated octahedron unit cells.	175
Figure 7-14. Different types of irregularities in additively manufactured porous biomaterials: (a) diameter (cross-section area) irregularity and (b) internal pore irregularity in Co-Cr porous structure. It must be noted that the internal pores shown in (b) were very rare in our structures (the percentage of internal pores was less than 0.5%) and this picture was chosen to better demonstrate the internal porosity irregularity.	176
Figure 8-1. Side view of the additively manufactured Co-Cr porous structures based on (a) diamond (b) rhombic dodecahedron, and (c) truncated cuboctahedron unit cells [22]	185
Figure 8-2. Strut surface morphology of selective laser melted (a) Co-Cr (magnification: X30), (b) Co-Cr (magnification: X100), (c) Ti-6Al-4V (magnification: X30), and (d) Ti-6Al-4V (magnification: X100) porous structures based on diamond unit cell	190
Figure 8-3. SEM and optical microscopy images of the microstructure of the struts in selective laser melted (a-b) Co-Cr and (c-d) Ti-6Al-4V porous structure.	191
Figure 8-4. Fatigue fracture morphology of the struts in selective laser melted (a) Co-Cr and (b) Ti-6Al-4V porous structure. Fatigue fracture surfaces are indicated by red arrows.	191
Figure 8-5. Manufacturing defects in the struts of selective laser melted (a) Co-Cr and (b) Ti-6Al-4V porous structures.....	192
Figure 8-6. S-N curves of Co-Cr porous structures based on (a) diamond, (b) rhombic dodecahedron, and (c) truncated cuboctahedron unit cells (σ_c, \max stands for maximum compressive stress, i.e. minimum stress, in each loading cycle)	193
Figure 8-7. Normalized S-N curves of Co-Cr porous structures based on diamond, rhombic dodecahedron, and truncated cuboctahedron unit cells. In equations presented in each graph, y represents the vertical axis parameter (i.e. $\sigma_c, \max/\sigma_x$) and x represents the horizontal parameter (i.e. number of cycles to failure). R2 represents the coefficient of determination for the simple linear regression method used for fitting the curves to the data.....	194
Figure 8-8. Comparison of normalized S-N curves of porous structures made from Co-Cr, Ti-6Al-4V, tantalum, and commercially pure titanium based on (a) diamond, (b) rhombic dodecahedron, and (c) truncated cuboctahedron unit cells.....	195
Figure 8-9. Comparison of normalized S-N curves of Co-Cr porous structures based on different unit cell types	196
Figure 8-10. Morphology of Co-Cr porous structures based on truncated cuboctahedron unit cell with relative densities of 0.236 (TCO-1) and (b) 0.386 (TCO-4).....	199

List of Tables

Table 1-1. Elastic modulus of bone (estimated)	3
Table 1-2. Mechanical properties of several biometals.....	4
Table 2-1. The summary of the mechanical properties of the diamond-type cellular structures with different apparent densities measured using compression tests. Both mean and standard deviation values are presented.....	25
Table 3-1. Literature values of the density and mechanical properties of standard annealed wrought titanium grades [38] and tantalum [39] and [40]: The density, yield strength (YS), the ultimate tensile strength (UTS), Young’s modulus (E) and the elongation (e). Fatigue data are taken from [1].	41
Table 3-2. The geometrical/physical properties of the four different series of porous CP Ti samples tested in the current study	46
Table 3-3. The static mechanical properties of the four different series of porous CP Ti samples tested according to ISO 13314.....	47
Table 3-4. The power laws fitted to the data points of the normalized S-N curves for all four different series of porous CP Ti samples tested. When multiplied by the corresponding value of the yield strength, the power law of the absolute values is obtained. Also the extrapolated values at $N = 10^6$ cycles are listed.	48
Table 4-1. Morphological properties of the porous structures used.....	64
Table 4-2. Summary of the structure relative density results (in %).	69
Table 5-1. The nominal and actual morphological properties of porous structures made from different types of unit cells (Ahmadi et al., 2014b).	105
Table 5-2. Static mechanical properties of porous structures made from different types of unit cells (Ahmadi et al., 2014b).	108
Table 6-1. The laser power and scanning time values used for manufacturing different porous structures studied here.....	129
Table 6-2. The specimens chosen for micro-structural observation	132
Table 7-1. Topological design and morphological properties of the porous structures having different unit cell types and sizes	151
Table 7-2. Mechanical properties of the bulk materials.....	153
Table 8-1. Topological design and morphological properties of the porous structures having different unit cell types and sizes [22]	186
Table 8-2. Vickers hardness values obtained from the hardness tests	193

Chapter 1 Introduction

1.1 Introduction

Global life expectancy is ever increasing thanks to technological advances. The global life expectancy in 1970 was 56.4 for men and 61.2 for women. These numbers increased to 67.5 for men and 73.3 for women in 2010 [1]. The life expectancies of developed countries are even higher (more than 80) [2]. Despite these developments, a large percentage of humans die due to the failure of their organs. There are various factors which cause body organ failure including trauma, acute illness, drugs, and so forth. Thanks to recent achievements in medical science, it is possible to overcome many of those failures either by curing them or by substituting the damaged organs with medical devices which offer similar functionality.

Medical devices play a significant role in achieving the recent health improvement while becoming more affordable. As a result, more and more patients use them. The market size of the medical devices all around the world was around 210 billion USD in 2006 and this number increases each year constantly. To give an example, the number of hip replacement surgeries (a surgery which a hip joint that lost its functionality is replaced by an implant) in the United States increased dramatically from 138700 in 2000 to 310800 in 2010 [3].

The term Medical device is a broad term and applies to any instrument, apparatus, appliance, or software that is used either for diagnostic purposes or therapeutic purposes. According to the US Food and Drug Administration (FDA), three major classes are defined for medical devices. Class I devices such as reusable surgical instruments are categorized as low risk products. Class II devices such as acupuncture needles are defined as medium to higher risk devices and need more than general control to guarantee their safety. Class III devices are the most critical devices with the highest risk which clear authorization is required before being in the market. Implantable devices are mainly considered in this category.

Not all the materials are qualified to be implanted in a human body, there are some criteria which need to be met, among which biocompatibility is a key criterion. Biocompatibility is defined as an ability of a material to function with a proper response in living tissue. Materials have therefore be selected or occasionally developed such that they are non-toxic, non-immunogenic, non-carcinogenic, non-irritant, and so on [4].

The main biocompatible materials (biomaterials) are metals (i.e. titanium), ceramics (i.e. zirconia), and polymers (i.e. collagen) (figure 1-1) [5].

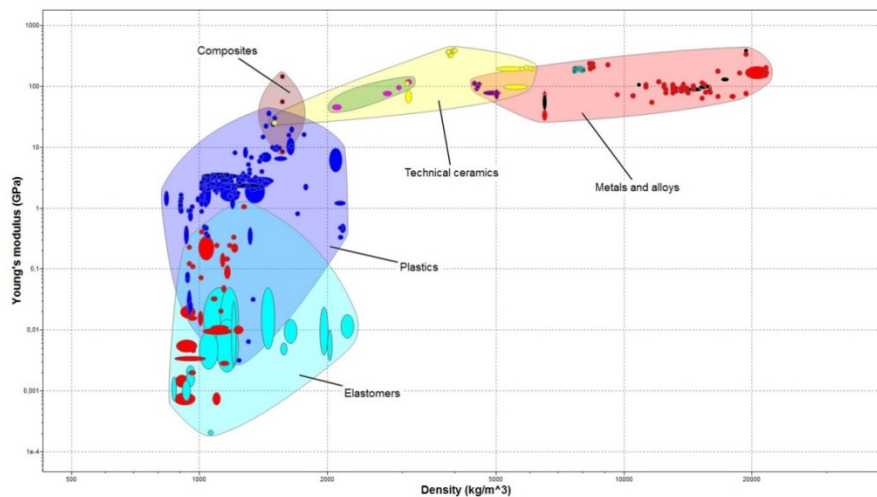


Figure 1-1. Biomaterials classification

However, not all of the above-mentioned biomaterials are proper candidates for bone substituting implants. Although some progress has been made in the development of biopolymers and bioceramics, biometals remain the most promising orthopaedic materials due to their strength and wear resistance. For instance, titanium is accepted as one of the best biocompatible metals given its resistance to body fluid effects and great strength-to-weight ratio [6]. Co-Cr-Mo alloys have been also widely used as an orthopaedic implant material in joint replacement prostheses owed to their excellent biocompatibility, mechanical properties, and wear resistance [7].

Metal orthopaedic implants show significant success with a low failure rate in their short-term clinical performance [8]. There are a series of issues affecting the long-term performance of the implants such as late infection and mechanical failure. To avoid late infections, implant surface could be functionalized [9]. Dealing with the mechanical failure at the interface of bone and implant is, however, more challenging.

In order to reduce mechanical failure first, a clearer understanding of failure causes is needed. Clinical studies show that there are two main failure reasons, namely stiffness mismatch between the bone and implant and poor bonding between them.

Stiffness

The mechanical properties of bone tissue are highly dependent on the microstructure, orientation, and anatomic location of bone. In general, trabecular bone is less stiff than cortical bone. In the literature, the elastic modulus of bone has been reported to be in the range of 0.76 to 19.6 GPa (Table 1-1) [10].

Table 1-1. Elastic modulus of bone (estimated)

Source	Test method	Estimate of elastic modulus (GPa)
Wolff (1982)	Hypothesis	17-20
Runke and Pugh (1975)	Buckling	8.69 ± 3.17
Towmsend et al. (1975)	Inelastic buckling	11.38
Williams et al. (1982)	FE models	11.3
Ashman and Rho (1988)	Ultrasound	12.7 ±2.0
Kuhn et al. (1989)	3 points bending	3.81
Rho et al (1993)	Tensile testing	14.8 ±1.4

Metallic implants are often much stiffer than bone. The weakest biometal, a shape memory alloy Nitinol, has a stiffness of 29-41 GPa while cobalt-based implants, which are considered to be the stiffest metallic implants have an elastic modulus in the range of 220 to 230 GPa (table 1-2) [11].

Table 1-2. Mechanical properties of several biometals

Materials	E(GPa)	σ_{yield} (Mpa)	σ_{ult} (MPa)	% Elong
SS 316L type	193	172-690	485-860	12-40
Tantalum	188-190	138-345	205-517	1-30
Cp-Ti	100-115	170-483	240-550	15-24
Ti6Al4V	110	860	930	10-15
Co-based	220-230	450-1500	655-1900	5-30
NiTi	29-41	70-140	700-1100	10

The mismatch between the stiffness values of bone and implants could result in a reduction of bone density around the implant, because the biomechanical load transfers through the stiffer part (implant), resulting in reduced bone loading. Consequently, the bone tissue then becomes less dense, because there is not enough stimulus for continued remodelling required for maintaining bone mass (stress shielding) [12].

Bonding

Many implants fail due to weak bonding between implants and bone. Although existing metallic implants are either bioactive or possess treated surfaces which make them appealing for bone ongrowth (bone growth onto implants surface), yet, as long as this connection has to depth (only surface to surface bonding), any intense periodic load may eventuate to implant failure.

Furthermore, the mechanical properties of bone surrounding implant may change in time due to age, nutrition and physical activity. Since for the conventional implants, the bonding is only limited to surfaces and not into an implant structure, the chance of implant dislocation and eventually failure is much higher compared to structures with a possibility of bone ingrowth.

1.2 Central theme of this thesis

To overcome these two complications, in this thesis a novel idea has been proposed: a porous metallic structure with the aim of additive manufacturing (AM) techniques. Additive manufacturing is a formal term for what is widely called 3D printing and describe a technique which fabricates a three-dimensional computer-aided design (CAD model) directly without the need for process planning. Typically, parts are fabricated by adding materials in layers; each layer has a thin thickness a cross-section of the part resulting from the 3D CAD model [13].

In this thesis, all the parts have been fabricated by selective laser melting (SLM) machines. SLM is one of the common AM techniques, which selectively melting successive layers of metal powder on top of each other, using laser beams [14]. SLM enables us to manufacture complex design which makes it the unsurpassed candidate to print porous structures.

In order to determine proper porous structures which mimic bone, different geometries and biomaterials have been selected. These structures fulfil mechanical requirements of load-bearing and non-load bearings bone implants while their pore size is optimized for bone ingrowth.

1.3 Thesis outline

This thesis consists of nine chapters. The middle chapters are based on scientific articles, which are published or to be published in peer-reviewed journals. The first chapter is an introduction to the thesis and the final chapter present some concluding remarks and future work suggestions.

Chapter 2: In this chapter, first, analytical solutions are presented that could predict the mechanical properties of the diamond-type cellular solids such as elastic gradient, Poisson's ratio, yield stress, and critical buckling load. Then, a finite element model is used for estimating the mechanical properties of the diamond-type cellular solids. Finally, a series of experiments are carried out to determine the mechanical behavior of selective laser melted porous titanium structures made of the diamond lattice unit cell. The results of the presented analytical solutions, finite element model, and experimental study are compared with each other to study the ability of analytical and numerical solutions to capture the experimentally observed mechanical behavior.

Chapter 3: In this chapter, the SLM technology is used to manufacture porous structures from commercially pure (CP) grade 1 titanium. The use of CP Ti has some major advantages over alloyed titanium that can potentially bring additively manufactured CP Ti back in the scope of medical device manufacturers. First of all, CP Ti has the advantage of having no potentially hazardous or toxic alloying components such as V or Al. Secondly, the high ductility that provides CP Ti with the sometimes necessary deformability in certain applications like e.g. bone plates, could be an interesting property of porous metals that could be deformed intra operatively to the patient specific bone defect.

Therefore, the aim of this chapter is to investigate whether CP Titanium can have a revival in orthopedics as a raw material for SLM processed porous implants. This is the first study that presents and discusses the mechanical properties of additively manufactured porous structures made of CP Ti grade 1 and compares them with those of additively manufactured Ti6Al4V ELI and Ta structures. This could be useful for facilitating proper selection of the most appropriate material for the envisioned implant application.

Chapter 4: In this chapter, six different reputable unit cell configurations, namely, cubic, diamond, truncated cube, truncated cuboctahedron, rhombic dodecahedron, and rhombicuboctahedron are selected and fabricated by the SLM technology. Micro-CT imaging and compression testing were performed to determine the morphological and mechanical properties of the porous materials and to study the relationship between these parameters.

The objective of this chapter is to ascertain whether the mechanical properties of additively manufactured porous biomaterials are dependent on the type of unit cell from which they are made or not.

Chapter 5: The aim of this chapter is to contribute towards understanding the relationship between the geometrical design of AM porous biomaterials at the small-scale and their fatigue properties. Selective laser melted (SLM) porous titanium structures based on three different types of space-filling unit cells including cube, diamond, and truncated cuboctahedron were considered. The relationship between the type of the unit cell and porosity on the one hand and the fatigue behavior of porous structures, on the other hand, is not yet well understood. In this chapter, we study the relationship between the geometrical design of porous structures including the type of unit cell and porosity and their fatigue behavior.

Chapter 6: In this chapter, we intend to find out how the processing parameters of laser beam (i.e. laser power and exposure time) affect the geometrical and mechanical properties of porous biomaterials manufactured based on vectors. To reach this aim, several cylindrical porous structures were additively manufactured with a wide range of exposure time and laser power and the effect of these parameters on the surface roughness, strut diameter, relative density, elastic modulus, yield stress, first maximum stress, and plateau stress of the porous structures was studied.

Chapter 7: In this chapter, a selective laser melting (SLM) is used to manufacture porous metallic biomaterials from Co-Cr with three different type of repeating unit cells and three to four porosities. The topological features and compressive mechanical properties of the obtained specimens are then determined using respectively micro-computed tomography (μ CT) and mechanical testing. In previous chapters, we had additively manufactured, topologically characterized, and mechanically tested similar (same unit cell designs) porous structures from other types of materials including the titanium alloy Ti-6Al-4V, pure titanium, and tantalum. The entire dataset of four different types of materials, three types of repeating unit cells, and multiple porosities is then used to determine whether or not there is a modulation between the material type and topology in determining the normalized mechanical properties of additively manufactured porous biomaterials.

Chapter 8: The aim of this chapter is to investigate the isolated and modulated effects of topological design and material type on the compressive-compressive fatigue behavior of bone-mimicking metallic meta-biomaterials. A large dataset of different topological designs and material types is needed to answer the research questions presented above. We, therefore, determine the compression-compression S-N curves for a large set of different topological designs of a Co-Cr alloy. The topological designs included three different types of repeating unit cells and three/four porosities for each type of repeating unit cell. The generated data is used in combination with the S-N curves available for bone-mimicking from previous chapters on the fatigue behavior of bone-mimicking meta-biomaterials made from Ti-6Al-4V, pure titanium, and tantalum.

1.4 References

- [1] Wang H, Dwyer-Lindgren L, Lofgren KT, Rajaratnam JK, Marcus JR, Levin-Rector A, et al. Age-specific and sex-specific mortality in 187 countries, 1970–2010: a systematic analysis for the Global Burden of Disease Study 2010. *The Lancet* 2013;380:2071-94.
- [2] Kontis V, Bennett JE, Mathers CD, Li G, Foreman K, Ezzati M. Future life expectancy in 35 industrialised countries: projections with a Bayesian model ensemble. *The Lancet* 2017.
- [3] Wolford M, Palso K, Bercovitz A. Hospitalization for Total Hip Replacement Among in Patients Aged 45 and Over: United States, 2000–2010. NCHS Data Brief, No 186. Hyattsville, MD: National Center for Health Statistics, 2015. 2016.
- [4] Williams DF. On the mechanisms of biocompatibility. *Biomaterials* 2008;29:2941-53.
- [5] Mihov D, Katerska B. Some biocompatible materials used in medical practice. *Trakia Journal of Sciences* 2010;8:119-25.
- [6] Niinomi M. Mechanical properties of biomedical titanium alloys. *Materials Science and Engineering: A* 1998;243:231-6.

-
- [7] Chiba A, Kumagai K, Takeda H, Nomura N. Mechanical properties of forged low Ni and c-containing Co-Cr-Mo biomedical implant alloy. *Materials Science Forum: Trans Tech Publ*; 2005. p. 2317-22.
- [8] Khan SK, Malviya A, Muller SD, Carluke I, Partington PF, Emmerson KP, et al. Reduced short-term complications and mortality following Enhanced Recovery primary hip and knee arthroplasty: results from 6,000 consecutive procedures. *Acta orthopaedica* 2014;85:26-31.
- [9] Geesink RG, De Groot K, Klein CP. Chemical Implant Fixation Using Hydroxyl-Apatite Coatings: The Development of a Human Total Hip Prosthesis for Chemical Fixation to Bone Using Hydroxyl-Apatite Coatings on Titanium Substrates. *Clinical orthopaedics and related research* 1987;225:147-70.
- [10] Rho J-Y, Kuhn-Spearing L, Zioupos P. Mechanical properties and the hierarchical structure of bone. *Medical Engineering & Physics* 1998;20:92-102.
- [11] Wu S, Liu X, Yeung KW, Liu C, Yang X. Biomimetic porous scaffolds for bone tissue engineering. *Materials Science and Engineering: R: Reports* 2014;80:1-36.
- [12] Sumner D. Long-term implant fixation and stress-shielding in total hip replacement. *Journal of biomechanics* 2015;48:797-800.
- [13] Gibson I, Rosen DW, Stucker B. *Additive manufacturing technologies*: Springer; 2010.
- [14] Vandenbroucke B, Kruth J-P. Selective laser melting of biocompatible metals for rapid manufacturing of medical parts. *Rapid Prototyping Journal* 2007;13:196-203.

Chapter 2 Mechanical behavior of regular open-cell porous biomaterials made of diamond lattice unit cells

This chapter has been published as:

SM Ahmadi, G Campoli, S Amin Yavari, B Sajadi, Ruben Wauthlé, Jan Schrooten, H Weinans, AA Zadpoor, *Mechanical behavior of regular open-cell porous biomaterials made of diamond lattice unit cells*, Journal of the mechanical behavior of biomedical materials, 2015. P. 106-115

2.1 Abstract

Cellular structures with highly controlled micro-architectures are promising materials for orthopedic applications that require bone-substituting biomaterials or implants. The availability of additive manufacturing techniques has enabled manufacturing of biomaterials made of one or multiple types of unit cells. The diamond lattice unit cell is one of the relatively new types of unit cells that are used in manufacturing of regular porous biomaterials. As opposed to many other types of unit cells, there is currently no analytical solution that could be used for prediction of the mechanical properties of cellular structures made of the diamond lattice unit cells. In this paper, we present new analytical solutions and closed-form relationships for predicting the elastic modulus, Poisson's ratio, critical buckling load, and yield (plateau) stress of cellular structures made of the diamond lattice unit cell. The mechanical properties predicted using the analytical solutions are compared with those obtained using finite element models. A number of solid and porous titanium (Ti6Al4V) specimens were manufactured using selective laser melting. A series of experiments were then performed to determine the mechanical properties of the matrix material and cellular structures. The experimentally measured mechanical properties were compared with those obtained using analytical solutions and finite element (FE) models. It has been shown that, for small apparent density values, the mechanical properties obtained using analytical and numerical solutions are in agreement with each other and with experimental observations. The properties estimated using an analytical solution based on the Euler–Bernoulli theory markedly deviated from experimental results for large apparent density values. The mechanical properties estimated using FE models and another analytical solution based on the Timoshenko beam theory better matched the experimental observations.

2.2 Introduction

Cellular structures possess certain combinations of geometrical features, mechanical properties, and physical properties [2] that make them suitable for many applications in industry as well as in medicine. One of the most important applications of cellular solids is in orthopedic surgery where orthopedic implants are needed to replace bone and integrate with the host bony tissue [3-6]. In such applications, a biomaterial is needed that has mechanical properties similar to that of the bone it replaces. Moreover, the biomaterial should be biocompatible, allow for bone ingrowth and optimal osseointegration, and have the ability to deliver therapeutic agents.

Partly because of their high porosity and huge surface to volume ratio, cellular metallic biomaterials such as cellular titanium alloys satisfy all the above-mentioned criteria. For example, the elastic properties of porous titanium are shown to be similar to that of bone [7-11]. Moreover, titanium alloys are biocompatible and corrosion resistant [12]. Porous titanium is also shown to allow for bone ingrowth and osseointegration [5, 13]. Finally, the ample pore space and large surface area of porous biomaterials have been used for delivery of therapeutic agents such as growth factors [6, 14].

Cellular structures such as cellular biomaterials are made of either two-dimensional unit cells such as honeycombs [15, 16] or are based on three-dimensional unit cells such as tetradecahedron (Kelvin unit cell) [17-20], rhombic dodecahedron [21], cubic [22, 23], or diamond lattice [24, 25]. The type of the unit cell and its dimensions are shown to determine the mechanical properties of the cellular structure [8, 26, 27]. It is therefore important to study how the mechanical properties of cellular biomaterials change with the type and dimensions of the unit cell.

Many of the above-mentioned unit cells have been extensively studied before, and analytical relationships are presented for prediction of the mechanical properties of cellular structures made of those unit cells. The availability of additive manufacturing techniques such as selective laser melting [28-31], selective laser sintering [32, 33], and selective electron beam melting [34] has enabled manufacturing of porous structures based on any arbitrary type of unit cells including a number of relatively new unit cells.

The mechanical properties and permeability of cellular structures are dependent on their morphological features such as the type of unit cell, porosity, and pore size [35, 36]. The biological performance of cellular structures such as cell attachment, growth, and differentiation are also dependent on the pore shape, pore size, and porosity [37]. It is therefore important to study the mechanical properties, fluid flow properties, and biological performance of a wide range of unit cells in order to generate a library of different unit cell types that could be used for optimal design of implants and tissue engineering scaffolds. The diamond lattice unit cell is one of the relatively new types of unit cells that have not been extensively studied before. In an experimental study, the mechanical properties of a specific design of the diamond-type cellular structures (Ti-6Al-4V alloy, selective electron beam melting) were found to be close to those of trabecular bone [35]. However, there are currently no analytical relationships for predicting the mechanical properties of cellular structures made of the diamond unit cell.

In this paper, we study the mechanical properties of cellular titanium solids made of diamond unit cells. First, analytical solutions are presented that could predict the mechanical properties of the diamond-type cellular solids including their Young's modulus, Poisson's ratio, yield stress, and critical buckling load. Then, a finite element model is used for estimating the mechanical properties of the diamond-type cellular solids. Finally, the mechanical behavior of selective laser melted porous titanium structures made of the diamond lattice unit cell is studied experimentally. The results of the presented analytical solutions, finite element model, and experimental study are compared with each other to study the ability of analytical and numerical solutions in capturing the experimentally observed mechanical behavior.

2.3 Materials and methods

2.3.1 Analytical model

Diamond cubic unit cell is an isotropic geometry that has fourteen vertices and sixteen equal edges (Figure 2-1). Each node is connected to four other nodes and the angle between every two struts is 109.5° . The length of each strut (L), length of the unit cell (a), and the angle between struts and the horizontal plane, θ , are related to each other through the following relationships:

$$a = 2\sqrt{2} L \cos \theta, a = \frac{4\sqrt{3}}{3} L, \theta = 35.26^\circ \quad (1)$$

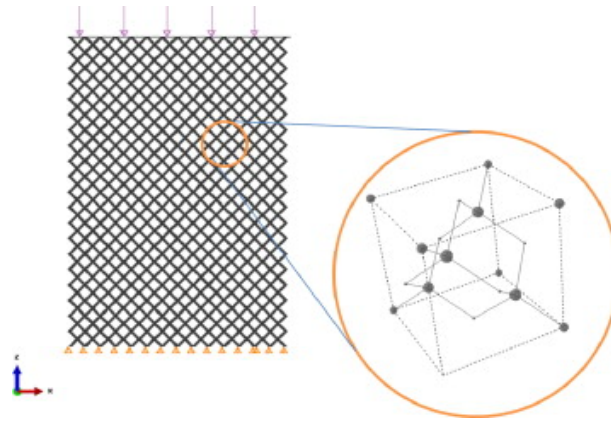


Figure 2-1. The loads, boundary conditions, and one of the unit cells used in the diamond-type cellular structures simulated using three-dimensional finite element models

In this study, we present analytical formulas for three different strut shapes: circle, square, and equilateral triangle. All equations are presented for the circular strut shape. Equations for two other strut shapes can be found in the supplementary material (Appendix A).

Apparent density or relative density is defined as the ratio of foam density to the density of the solid material or the ratio of total volume of the foam to the volume of the corresponding solid material. Since every diamond unit cell is connected to other unit cells by border nodes and there is no shared strut among unit cells, the apparent density calculated for one-unit cell represents that of the cellular solid as well. The volume of the cubic unit cell, V_1 , is given by:

$$V_1 = \frac{64\sqrt{3}}{9} L^3 \quad (2)$$

For circular strut cross-sections, the total volume of all struts in one-unit cell is given by:

$$V_{st-c} = 4\pi d^2 L \quad (3)$$

The apparent density is therefore given by:

$$\rho = \frac{V_{st-c}}{V_1} = \frac{3\pi\sqrt{3}d^2}{16L^2} \cong 1.02 \frac{d^2}{L^2} \quad (4)$$

where d is the strut diameter. The mechanical properties of the diamond-type cellular solids are calculated using the structural theories developed for high porosity materials [38]. The solid material is assumed to be linear elastic, and the deformations are assumed to be small. Since the diamond cubic unit cell is an isotropic geometry, the mechanical properties are the same in different directions and the cellular structure is an isotropic structure mechanically. The elastic modulus of the diamond-type cellular structures is calculated using two theories, namely the Euler-Bernoulli and Timoshenko beam theories. The other mechanical properties of the diamond-type cellular structures are only calculated using the Euler-Bernoulli beam theory.

2.3.1.1 Elastic modulus

2.3.1.1.1 Euler-Bernoulli beam theory

The aim of this section is to derive equations that relate the elastic modulus and Poisson's ratio of the diamond-type cellular structures to the elastic modulus of the matrix material (E_s) and the apparent density of the porous structure (ρ). Let P be the compression force in the y direction transmitted to an arbitrary unit cell (Figure 2). Due to symmetry, there is no difference between the struts of the unit cell and each carries $F = P/4$ together with the resulting bending moment $M = \frac{1}{2}FL\cos\theta$.

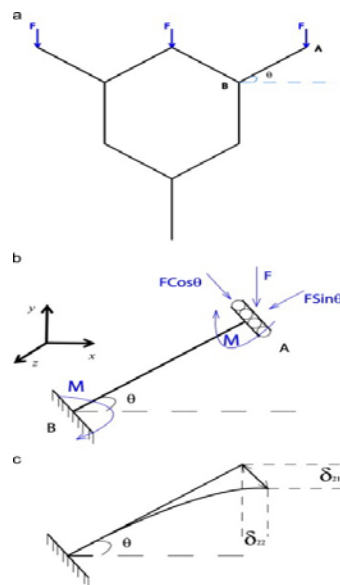


Figure 2-2. An arbitrary unit cell under uniaxial compression (a). The free body diagram and deformations of an arbitrary strut in y (b) and x (c) directions.

In order to find the effective elastic modulus of the diamond unit cell, we need to calculate the total deformation of a unit cell in the y direction (Figure 2) that consists of the deformations of four struts. For every strut, there are two types of deformations, namely the deformation caused by the bending moment and the one caused by axial force.

As for the bending moment, the Euler-Bernoulli beam equation can be written as:

$$\frac{\partial^4 w}{\partial x^4} = 0 \quad (5)$$

where w is the deflection. The solution to this differential equation can be expressed as:

$$w = c_0 + c_1 x + c_2 x^2 + c_3 x^3 \quad (6)$$

where constants c_0 to c_3 need to be determined by applying certain boundary conditions. By applying boundary conditions, and replacing the force term with $F \cos \theta$, the deflection caused by the moment in the y direction, $\delta_{22,b}$, is obtained as:

$$\delta_{22,b} = \frac{FL^3 \cos^2 \theta}{12E_s I} \quad (7)$$

where E_s is elastic modulus of the matrix material and I is the second moment of inertia.

The deformation of a strut in the y direction as result of the axial force, $\delta_{22,a}$, is given by:

$$\delta_{22,a} = \frac{F \sin \theta L}{E_s A} \times \sin \theta = \frac{FL \sin^2 \theta}{E_s A} \quad (8)$$

where A is the cross section area of the strut. The total deformation in the y direction is then obtained as sum of both above-mentioned deformations as:

$$\delta_{22} = \delta_{22,b} + \delta_{22,a} = \frac{FL^3 \cos^2 \theta}{12E_s I} + \frac{FL \sin^2 \theta}{E_s A} \quad (9)$$

The total deformation of the unit cell in the y direction is the sum of the deformations of each of the four struts in the y direction and is therefore given by:

$$\delta_{22,UC} = 4 \left(\frac{PL^3 \cos^2 \theta}{48E_s I} + \frac{PL \sin^2 \theta}{4E_s A} \right) = \frac{PL^3 \cos^2 \theta}{12E_s I} + \frac{PL \sin^2 \theta}{E_s A} \quad (10)$$

On the other hand, the stress-strain relationship for a unit cell can be written as:

$$\sigma_{UC} = E_{UC} \varepsilon_{22,UC} \quad (11)$$

The unit cell stress is calculated by dividing the applied force by the effective area of the unit cell:

$$\sigma_{UC} = \frac{P}{A_{UC}} = \frac{P}{8L^2 \cos^2 \theta} \quad (12)$$

As for the unit cell strain, it can be calculated by dividing the deformation of the unit cell in the y direction by the length of the unit cell:

$$\varepsilon_{22,UC} = \frac{\delta_{22,UC}}{a} \quad (13)$$

The deformation of the unit cell is given by the following relationship:

$$\delta_{22,UC} = \frac{\sqrt{2}P}{4LE_u \cos \theta} \quad (14)$$

Combining equations 10 and 14, it is possible to derive the ratio of the elastic modulus of the unit cell to the elastic modulus of the matrix material as:

$$\frac{E_{UC}}{E_s} = \frac{\sqrt{6}\rho^2}{3\pi + 2\sqrt{3}\rho} = \frac{\rho^2}{3.85 + 1.41\rho} \quad (15)$$

For low density structures, the axial force is ignored and only the bending force is taken into account, we can derive a simplified version of Equation 15:

$$\frac{E_{UC}}{E_s} \approx \frac{\sqrt{6}}{3\pi} \rho^2 \cong 0.26 \rho^2 \quad (16)$$

Since none of the edges are shared between the unit cells in the diamond-type cellular structure, the elastic modulus of an infinitely large cellular structure is the same as that of a single unit cell. We can therefore conclude that the elastic modulus of the diamond-type cellular structure, E_p , is given by:

$$\frac{E_p}{E_s} = \frac{\rho^2}{3.85 + 1.41\rho} \quad (17)$$

2.3.1.1.2 Timoshenko beam theory

The difference between the Euler-Bernoulli and Timoshenko beam theories is that the Timoshenko beam theory takes shear deformation and rotational inertia effects into account. For static loading, the Timoshenko beam theory has one additional term:

$$\frac{dw}{dx} = q(x) - \frac{1}{\kappa AG} \frac{d}{dx} \left(EI \frac{d\varphi}{dx} \right) \quad (18)$$

The deformation of a cantilever beam at its endpoint is therefore given as:

$$\delta = \frac{PL^3}{3EI} + \frac{PL}{\kappa AG} \quad (19)$$

where κ is the shear coefficient factor and for circular cross sections is given by $\frac{6(1+\nu)}{7+6\nu}$. By applying the boundary conditions and replacing the force term with $F \cos \theta$, the deflection caused by the moment in the y direction, $\delta_{22,b-Timoshenko}$, can be obtained as:

$$\delta_{22,b-Timoshenko} = \frac{FL^3 \cos^2 \theta}{12E_s I} + \frac{PL}{\kappa AG} \times \frac{\cos^2 \theta}{4} \quad (20)$$

The deformation of a strut in the y direction as result of the axial force, $\delta_{22,a-Timoshenko}$, is the same as before:

$$\delta_{22,a-Timoshenko} = \frac{FL\sin^2\theta}{E_s A} \quad (21)$$

The total deformation of the unit cell in the y direction according to the Timoshenko beam theory is therefore given as:

$$\delta_{22,UC-Timoshenko} = 4 \left(\frac{PL^3\cos^2\theta}{48E_s I} + \frac{PL\sin^2\theta}{4E_s A} + \frac{PL}{\kappa AG} \times \frac{\cos^2\theta}{4} \right) = \frac{PL^3\cos^2\theta}{12E_s I} + \frac{PL\sin^2\theta}{E_s A} + \frac{PL\cos^2\theta}{\kappa AG} \quad (22)$$

$$\delta_{22,UC-Timoshenko} = \delta_{22,UC-Euler-Bernoulli} + \frac{PL\cos^2\theta}{\kappa AG} \quad (23)$$

$$\varepsilon_{Timoshenko} = \frac{\delta_{22,UC-Timoshenko}}{a} = \varepsilon_{Euler-bernoulli} (1 + \beta) \quad (24)$$

where

$$\beta = \frac{\frac{PL\cos^2\theta}{\kappa AG}}{\delta_{22,UC-Euler-Bernoulli}} = \frac{\frac{PL\cos^2\theta}{\kappa AG}}{\frac{PL^3\cos^2\theta}{12E_s I} + \frac{PL\sin^2\theta}{E_s A}} = \frac{\rho}{0.46 + 0.17\rho} \quad (25)$$

The elastic modulus according to the Timoshenko beam theory can be therefore given as:

$$E_{UC-Timoshenko} = \frac{\sigma_{UC}}{\varepsilon_{Timoshenko}} = \frac{\sigma_{UC}}{\varepsilon_{Euler-bernoulli} (1 + \beta)} = \frac{E_{UC-Euler-Bernoulli}}{(1 + \beta)} \quad (26)$$

The ratio of the elastic moduli calculated using both theories can be related to the density of the cellular structure as:

$$\frac{E_{UC-Timoshenko}}{E_{UC-Euler-Bernoulli}} = \frac{1}{(1 + \beta)} = \frac{1}{1 + \frac{\rho}{0.46 + 0.17\rho}} = \frac{0.46 + 0.17\rho}{0.46 + 1.17\rho} \quad (27)$$

If Equations 17 and 27 are combined, the elastic modulus of the diamond-type cellular structure based on the Timoshenko beam theory, $E_{P-Timoshenko}$, can be obtained as a function of the density of the cellular structure and the elastic modulus of the matrix material:

$$E_{p\text{-Timoshenko}} = \frac{(0.46 + 0.17\rho)\rho^2}{(0.46 + 1.17\rho)(3.85 + 1.41\rho)} E_s \quad (28)$$

2.3.1.2 The Poisson's ratio

We can apply a similar procedure to calculate the Poisson's ratio of the cellular structure based on the Euler-Bernoulli beam theory. The only difference is that the deformation relationships need to be written for the x direction. The deformation caused by the bending moment in the x direction is given by:

$$\delta_{21,b} = \frac{F \cos \theta L^3}{12 E_s I} \times \sin \theta \times \sin \frac{\pi}{4} = \frac{\sqrt{2} F L^3 \sin 2\theta}{48 E_s I} \quad (29)$$

As for the axial force, we have

$$\delta_{21,a} = \frac{F \sin \theta L}{E_s A} \times \cos \theta \times \sin \frac{\pi}{4} = \frac{\sqrt{2} F L \sin 2\theta}{4 E_s A} \quad (30)$$

The total deformation in x direction is then given by:

$$\delta_{21} = \delta_{21,b} + \delta_{21,a} = -\frac{\sqrt{2} F L^3 \sin 2\theta}{48 E_s I} + \frac{\sqrt{2} F L \sin 2\theta}{4 E_s A} \quad (31)$$

The Poisson's ratio is then calculated as:

$$\nu_{12} = -\frac{\varepsilon_{21}}{\varepsilon_{22}} = -\frac{\delta_{21}}{\delta_{22}} \quad (32)$$

Therefore, for struts with circular shape of the cross section, the Poisson's ratio is given by:

$$\nu_{12} = \frac{\left(\frac{\sqrt{2} P L^3 \sin 2\theta}{48 E_s I} - \frac{\sqrt{2} P L \sin 2\theta}{4 E_s A} \right)}{\left(\frac{P L^3 \cos^2 \theta}{12 E_s I} + \frac{P L \sin^2 \theta}{E_s A} \right)} = \frac{4L^2 - 3d^2}{8L^2 + 3d^2} \quad (33)$$

Since $\rho \cong 1.02d^2 / L^2$, the Poisson's ratio can be expressed in terms of apparent density as:

$$g_{12} \cong 0.5 \left(\frac{1 - 0.735\rho}{1 + 0.368\rho} \right) \quad (34)$$

2.3.1.3 Elastic buckling limit and yield stress

The elastic buckling limit of the cellular structure can be calculated using the classical Euler's buckling theory. According to this theory, the buckling load of a column, P_{cr} , is given by the following relationship:

$$P_{cr} = \frac{n^2 \pi^2 EI}{L^2} \quad (35)$$

For the boundary conditions presented in Figure 2, the critical buckling load for the first buckling mode of struts with circular strut cross section can be calculated as:

$$P_{cr,UC} = \frac{\pi^3 E_s d^4}{64 L^2 \sin \theta} \quad (36)$$

The critical stress under which the cellular structure will buckle, σ_{cr} , is therefore given by:

$$\frac{\sigma_{cr}}{E_s} = \frac{3\sqrt{3}\pi^3 d^4}{2^{10} L^4} = \frac{\pi\sqrt{3}}{36} \rho^2 \cong 0.15 \rho^2 \quad (37)$$

According to the international standard for mechanical testing of cellular metals (ISO 13314) [39], there is not a single definition for the yield stress of cellular materials. The plateau stress that is the arithmetical mean of stresses at 20% and 30% compressive strain or at 20% and 40% compressive strain is generally used in place of yield stress. For the diamond type cubic unit cells, the maximum stress in one of the struts of the unit cells is given by:

$$\sigma = \sigma_b + \sigma_a = \frac{Md}{4I} + \frac{P \sin \theta}{A} = \frac{PLd \cos \theta}{8I} + \frac{3P \sin \theta}{16L^2}, I = \pi d^4 / 64 \quad (38)$$

where indices b and a respectively refer to the stresses caused by the bending moment and axial force. The axial term can be, however, neglected when the bending moment reaches the plastic

zone. For such a simplified case, the ratio of the plateau stress, σ_{pl} , to the yield stress of the matrix material is given by the following relationship:

$$\frac{\sigma_{pl}}{\sigma_s} = \frac{9\pi d^3}{32\sqrt{6}L^3} \cong 0.35\rho^{1.5} \quad (39)$$

2.3.2 Finite element model

Finite element (FE) models were generated for estimating the mechanical properties of the diamond-type porous biomaterials. The FE modeling process was similar to the one reported elsewhere [8]. A summary of the modeling procedure is, however, presented here for completeness. The nonlinear implicit solver of a commercial FE package (Abaqus 6.10, Dassault Systems Simulia) was used for solving the equations of the FE model used in the current study.

The struts of the cellular structure were discretized using Timoshenko beam elements, i.e. a 2-node linear integration element (type B31), to capture the shear effects that cannot be captured using Euler-Bernoulli beam elements. The shear effects are more important for thicker struts. A convergence study was conducted to determine the minimum number of elements per strut and the minimum number of unit cells. When comparing the results of the FE models with experimental results, a structure with approximately the same number of unit cells as in the experiments was generated for FE modeling.

The applied boundary conditions mimicked the compression test conditions (Figure 1). One of the planes in the loading direction was displaced such that a homogenized strain of 2% was applied in the porous structure. After applying the displacement, the FE solver computed the reaction force and the homogenized stress value by dividing the total reaction force by the total area of the loading plane. The Poisson's ratio was then calculated by dividing the strain induced in the other direction by the applied strain in the loading direction. The apparent density (AD) of the porous structure was calculated by dividing the sum of the volumes of all beam elements by the total volume of the structure. For both analytical and FE models, it was necessary to correct the apparent density for quadruple-counted beam ends at the intersection of struts. The sum of the volume of quadruple-

counted beam elements was therefore deducted from the total volume of beam elements using a method similar to the one used in reference [40].

2.3.3 Experiments

The selective laser melting technique (SLM) was used for manufacturing cylindrical samples ($\phi 10$ mm \times 15 mm) made of the titanium alloy Ti6Al4V ELI, according to ASTM B348, grade 23. The specifications of the material, the details of the manufacturing process, and the involved parameters are presented elsewhere [7, 8]. Two types of cylindrical samples were produced: solid specimens and cellular specimens. A sample of the STL file used for manufacturing of the porous specimens and the resulting specimen are depicted in Figure 2-3. The solid specimens were used to determine the mechanical behavior of the matrix material while the diamond-type cellular specimens were used for determining the mechanical properties of the porous structures.

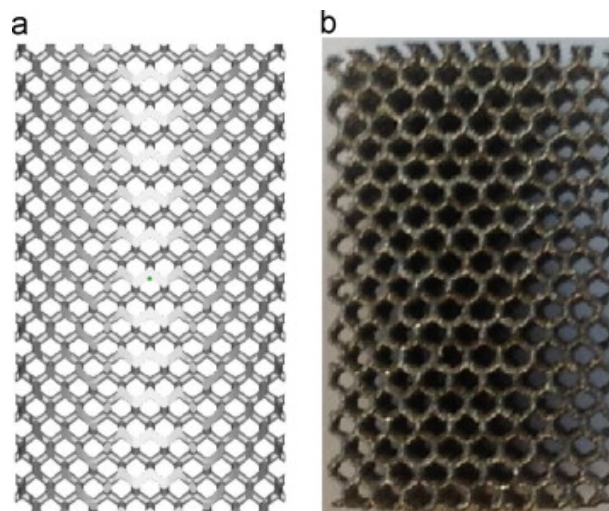


Figure 2-3. The STL file used for manufacturing of the diamond-type cellular structures (a) and a sample of the resulting structures (b).

Five solid specimens were tested under compression using a static test machine (Instron 5985, 100 kN load cell). A constant deformation rate of 1.8 mm/min was used. The obtained stress-strain curves were used for calculating the mechanical properties of the solid material. The density of the solid samples was determined using the Archimedes technique.

Four diamond-type cubic cellular structures with different strut diameters and, thus, different ratios of strut length to strut diameter were manufactured and tested under compression in accordance with the ISO standard for mechanical testing of porous metallic materials, ISO [39]. The strut length to strut diameter, L/D , varied between 1.67 and 5. The same mechanical testing machine as for solid specimens was used for testing the porous samples under a constant deformation rate of 1.8 mm/min. The tests were continued until specimens experienced 80% strain. From every variation of the porous structure, four specimens were tested and similar to solid samples, apparent density of the solid samples was determined using the Archimedes technique. The obtained strain-stress curves were used to determine the mechanical properties of the porous structures such as plateau stress (σ_{pl}) and elastic gradient ($E_{\sigma_{20-70}}$) (Table 2-1). To simplify comparison between the results presented here and those of other studies, we assume that the plateau stress (the arithmetical mean of the stresses between 20% and 40% compressive strains) and elastic gradient (the gradient of the elastic straight line between σ_{70} and σ_{20}) respectively represent yield stress and Young's modulus. A more detailed discussion of these two concepts and their relationships with yield stress and Young's modulus can be found in [7, 8].

Table 2-1. The summary of the mechanical properties of the diamond-type cellular structures with different apparent densities measured using compression tests. Both mean and standard deviation values are presented.

L/D	σ_{pl} (MPa)	$E_{\sigma_{20-70}}$ (GPa)	AD
1.67			
Mean	99.64	4.24	0.36
SD	8.91	0.07	0.004
2			
Mean	62.92	2.64	0.265
SD	5.03	0.03	0.005
2.5			
Mean	25.57	1.22	0.181
SD	2.62	0.14	0.001
5			
Mean	8.2	0.37	0.105
SD	0.44	0.03	0.002

2.4 Results

As the number of unit cells used in x , y , and z directions increased from 5 to 20, the cellular structure exhibited a stiffer response until the elastic modulus and the Poisson's ratio converged to those calculated using the analytical solution. Using 15 unit cells in every direction changed the calculated mechanical properties by less than 1% as compared to the properties calculated with 14 unit cells. It was therefore concluded that 14 unit cells in every direction (2744 unit cells in total) are sufficient for estimating the mechanical properties of the cellular structure with infinite number of unit cells. As the number of elements used for discretizing every strut was increased from 1 to 12, the calculated elastic modulus initially dropped but then rapidly converged for the number of elements larger than 5. The mechanical properties estimated using 15 elements per strut differed by less than 0.6% from those estimated by 5 elements per strut. It was therefore concluded that 5 elements per strut is sufficient for obtaining accurate estimations of the mechanical properties of the cellular structure with infinite number of unit cells.

The Young's modulus and yield stress of the solid specimens were respectively found to be 122.3 ± 2.5 GPa (mean \pm SD) and 980 ± 35 MPa (Figure 2-4a). These values were used for calculating the elastic modulus, elastic buckling limit, and yield stress of the cellular structure based on the equations derived in section 2.1. The stress-strain curves of the cellular structures showed the typical features of cellular solids with a starting linear behavior, a clear plateau, and a shift to fluctuating stress-strain behavior (Figure 2-4b-c). The stress-strain showed the typical stiffening behavior for large strains after the plateau (Figure 2-4b-c).

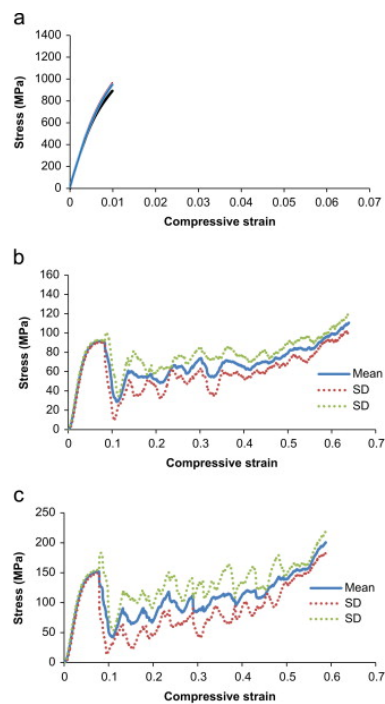


Figure 2-4. Experimentally measured stress–strain curves for solid specimens (a) and two of the cellular structures tested in the current study: one structure with a strut length of 0.65 mm and mean strut diameter of 0.347 mm (b) and one structure with a strut length of 0.65 mm and a mean strut diameter of 0.419 mm (c).

Comparison between the analytical, numerical, and experimental results shows that for small values of the apparent density, all methods yield very similar results (Figure 2-5a). As the apparent density increases, there is a difference between the elastic properties obtained using the different approaches. The Young's moduli estimated using the FE model match the experimental results very well even for large apparent density values (Figure 2-5a). For large apparent density values, the analytical solution based on the Euler-Bernoulli beam theory exhibits large differences from the experimental results (Figure 2-5a). The analytical solution based on the Timoshenko beam theory is much closer to the experimental results (Figure 2-5a). While the analytically estimated values of the Young's modulus are larger than the experimental results for the Euler-Bernoulli theory, they are below the experimental results for the Timoshenko beam theory (Figure 2-5a). Comparison between the analytically and numerically calculated values of the Poisson's ratio shows that they are in excellent agreement for small apparent densities but as the apparent density increases they gradually deviate from each other (Figure 2-5b). The yield stress values calculated using the analytical approach (Euler-Bernoulli) are also quite close to the experimentally measured values for

small apparent density values (Figure 2-5c). There is a relatively large difference between the analytically estimated and experimentally measured yield stresses for large apparent density values (Figure 2-5c).

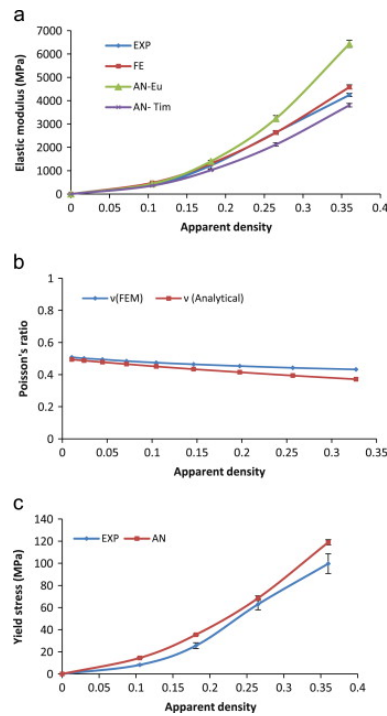


Figure 2-5. Comparison between the elastic modulus (a) Poisson's ratio (b), and yield stress (c) values obtained using different approaches including analytical, numerical, and experimental approaches (AN-Eu: analytical solution based on the Euler–Bernoulli theory, AN-Tim: analytical solution based on the Timoshenko theory, EXP: experimental results, FE: finite element solution).

2.5 Discussion

One of the most important contributions of the current study is presenting analytical solutions that could be used for easy and fast prediction of the mechanical properties of cellular structures made

of the diamond lattice unit cells. In addition, these analytical solutions serve as reference solutions against which finite element solutions can be (cross-) validated. The analytical solutions presented here include relationships for estimating the elastic modulus, Poisson's ratio, elastic buckling limit, and yield stress of the diamond-type cellular structures. We validated the mechanical properties estimated using analytical solutions against numerical solutions and experiments. The only analytical solution that was not validated is the elastic buckling limit for which no validation data was available.

The results of above-mentioned validations show that both analytical solutions are in agreement with the numerical solutions and experimental results particularly for low apparent density values. For small apparent density values, the elastic moduli obtained using the analytical and numerical solutions are practically overlapping. That is expected because the difference between the Euler-Bernoulli beam theory used in the derivation of one of the analytical solutions and the Timoshenko beam theory used in the other analytical solution and the FE models appears only for larger strut diameters that translate to higher apparent density values. For thicker beams, the shear and rotational inertia effects, that are taken into account in the Timoshenko beam theory but are neglected in the Euler-Bernoulli theory, start to play important roles. That is why the solutions based on both theories start to deviate from each other for large apparent density values. In general, the shear and rotational inertia effects cause the beam to behave less stiffly and that is why, for less porous structures, the elastic moduli calculated using the Euler-Bernoulli analytical solution are significantly larger than those calculated using finite element models and the analytical solution based on the Timoshenko beam theory.

In order to understand the failure mechanism of the diamond-type cellular structures, it is important to study whether buckling or yielding occurs first. Combining Equations 37 and 39, one could express

the ratio of the buckling stress to yield stress for Ti-6Al-4V alloy as $\frac{\sigma_{cr}}{\sigma_{pl}} = 52.48\rho^{0.5}$. Except for very

small densities ($\rho < 0.0004$), the ratio of the buckling stress to yield stress will be larger than one. For density values as low as 0.04, the ratio of buckling stress to yield stress will be as high as 10, meaning that yielding will occur far before buckling for most cellular structures of practical relevance. Since the analytical solutions are relatively simple and neglect some important mechanisms, it is important to validate their predictions for the buckling and yield stresses. We

performed some additional finite element simulations (see Appendix B, electronic supplementary material) to check the validity of the predictions of the analytical solutions. The predictions of the analytical solutions regarding the ratio of the buckling stress to yield stress showed good agreement with those obtained using finite element simulations.

The availability of additional types of unit cells is important for design of effective bone implants or bone grafting materials. As opposed to traditional porous biomaterials that are limited in the design of their microarchitecture, the micro-architecture of porous biomaterials manufactured using additive manufacturing techniques such as selective laser melting can be very precisely controlled. Since the diamond unit cell has a simpler structure as compared to many other types of open unit cells geometries such as truncated octahedron or rhombic dodecahedron, it is easier to fabricate using additive manufacturing techniques.

Using additive manufacturing techniques, it is possible to manufacture biomaterials such that they have different regions with different micro-architecture and, thus, different mechanical properties. Since bone generation/resorption and osseointegration are dependent on mechanical forces [41-44], the distribution of mechanical properties within the implant or bone substitute can be used for regulating bone regeneration and implant osseointegration and reducing the chance of aseptic loosening.

Since so many options are available in the design and manufacturing of biomaterials based on additive manufacturing and three-dimensional printing techniques, it is important to have analytical and numerical tools that could be used for optimizing the distribution of mechanical properties within the biomaterial. The new analytical solution proposed here for the diamond-type unit cell is an addition to the arsenal of tools that are available for such an optimization effort. The analytical formulas and FE models developed here could be integrated within improved versions of currently available patient-specific modeling platforms [45-47] and need to combine statistical shape and appearance models [48] with large-scale musculoskeletal models [49-51] or mass-spring-damper models [52, 53] to be able to yield patient-specific optimal implants. The accuracy of the models that are used for predicting the mechanical properties of cellular structures is very important, because it would be next to impossible to find the optimal distribution of type and dimensions of unit cells within the biomaterials without analytical and/or numerical models that could accurately predict the

mechanical properties of cellular structures. It is therefore important to thoroughly study the accuracy of the analytical and numerical models such as the ones presented in the current study before proceeding to use the models in the design of cellular biomaterials.

2.6 Conclusion

The mechanical properties of cellular solids made of the diamond lattice unit cell were studied in this paper. Analytical solutions were presented that could predict the elastic modulus, Poisson's ratio, elastic buckling limit, and yield stress of cellular structures with that type of unit cell. The predictions of the analytical solutions were compared with those based on finite element modeling and experimental observations. It is concluded that the analytical and numerical solutions are in good agreement with experimental observations for small apparent density values. For large apparent densities, the results of the analytical solution based on the Euler-Bernoulli beam theory significantly deviate from the experimental results while the mechanical properties predicted with FE models and the analytical solution based on the Timoshenko beam theory, though less accurate than for small apparent density values, are relatively closer to experimental observations.

2.7 References

- [1] Junca D, Ribeaute D. Comment rédiger les bibliographies. Paris: Adventure Works Press; 2006.
- [2] Thiyagasundaram P, Sankar BV, Arakere NK. Elastic properties of open-cell foams with tetrakaidecahedral cells using finite element analysis. *AIAA Journal* 2010;48:818-28.
- [3] Kujala S, Ryhänen J, Danilov A, Tuukkanen J. Effect of porosity on the osteointegration and bone ingrowth of a weight-bearing nickel–titanium bone graft substitute. *Biomaterials* 2003;24:4691-7.
- [4] Mullen L, Stamp RC, Brooks WK, Jones E, Sutcliffe CJ. Selective Laser Melting: A regular unit cell approach for the manufacture of porous, titanium, bone in-growth constructs, suitable for orthopedic applications. *Journal of Biomedical Materials Research Part B: Applied Biomaterials* 2009;89:325-34.

-
- [5] Van der Stok J, Van der Jagt O, Amin Yavari S, De Haas M, Waarsing J, Jahr H, et al. Selective laser melting-produced porous titanium scaffolds regenerate bone in critical size cortical bone defects. *Journal of Orthopaedic Research* 2012;31:792–9.
- [6] Van der Stok J, Wang H, Amin Yavari S, Siebelt M, Sandker M, Waarsing JH, et al. Enhanced bone regeneration of cortical segmental bone defects using porous titanium scaffolds incorporated with colloidal gelatin gels for time-and dose-controlled delivery of dual growth factors. *Tissue Engineering Part A* 2013;in press.
- [7] Amin Yavari S, Wauthle R, van der Stok J, Riemsdag A, Janssen M, Mulier M, et al. Fatigue behavior of porous biomaterials manufactured using selective laser melting. *Materials Science and Engineering: C* 2013;33:4849-58.
- [8] Campoli G, Borleffs M, Amin Yavari S, Wauthle R, Weinans H, Zadpoor A. Mechanical properties of open-cell metallic biomaterials manufactured using additive manufacturing. *Materials & Design* 2013;49:957–65.
- [9] Greiner C, Oppenheimer SM, Dunand DC. High strength, low stiffness, porous NiTi with superelastic properties. *Acta Biomaterialia* 2005;1:705-16.
- [10] Oh I-H, Nomura N, Masahashi N, Hanada S. Mechanical properties of porous titanium compacts prepared by powder sintering. *Scripta Materialia* 2003;49:1197-202.
- [11] Wen C, Yamada Y, Shimojima K, Chino Y, Hosokawa H, Mabuchi M. Novel titanium foam for bone tissue engineering. *Journal of Materials Research* 2002;17:2633-9.
- [12] Long M, Rack H. Titanium alloys in total joint replacement—a materials science perspective. *Biomaterials* 1998;19:1621-39.
- [13] Pilliar R. Powder metal-made orthopedic implants with porous surface for fixation by tissue ingrowth. *Clinical Orthopaedics and Related Research* 1983;176:42-51.
- [14] Jansen J, Vehof J, Ruhe P, Kroeze-Deutman H, Kuboki Y, Takita H, et al. Growth factor-loaded scaffolds for bone engineering. *Journal of Controlled Release* 2005;101:127-36.

-
- [15] Gibson LJ, Ashby MF, Schajer GS, Robertson CI. The Mechanics of Two-Dimensional Cellular Materials. *Proceedings of the Royal Society of London Series A, Mathematical and Physical Sciences* 1982;382:25-42.
- [16] Li X, Wang C, Zhang W, Li Y. Fabrication and compressive properties of Ti6Al4V implant with honeycomb-like structure for biomedical applications. *Rapid Prototyping Journal* 2010;16:44-9.
- [17] Roberts AP, Garboczi EJ. Elastic properties of model random three-dimensional open-cell solids. *Journal of the Mechanics and Physics of Solids* 2002;50:33-55.
- [18] Jang W-Y, Kraynik AM, Kyriakides S. On the microstructure of open-cell foams and its effect on elastic properties. *International Journal of Solids and Structures* 2008;45:1845-75.
- [19] Sullivan RM, Ghosn LJ, Lerch BA. A general tetrakaidecahedron model for open-celled foams. *International Journal of Solids and Structures* 2008;45:1754-65.
- [20] Lalvani H. Non-periodic space structures. *International Journal of Space Structures* 2011;26:139-54.
- [21] Babae S, Jahromi BH, Ajdari A, Nayeb-Hashemi H, Vaziri A. Mechanical properties of open-cell rhombic dodecahedron cellular structures. *Acta Materialia* 2012;60:2873-85.
- [22] Parthasarathy J, Starly B, Raman S. A design for the additive manufacture of functionally graded porous structures with tailored mechanical properties for biomedical applications. *Journal of Manufacturing Processes* 2011;13:160-70.
- [23] Parthasarathy J, Starly B, Raman S, Christensen A. Mechanical evaluation of porous titanium (Ti6Al4V) structures with electron beam melting (EBM). *Journal of the Mechanical Behavior of Biomedical Materials* 2010;3:249-59.
- [24] Heintz P, Körner C, Singer RF. Selective electron beam melting of cellular titanium: Mechanical properties. *Advanced Engineering Materials* 2008;10:882-8.
- [25] Campoli G, Borleffs MS, Amin Yavari S, Wauthle R, Weinans H, Zadpoor AA. Mechanical properties of open-cell metallic biomaterials manufactured using additive manufacturing. *Materials & Design* 2013;49:957-65.

-
- [26] Gibson LJ, Ashby MF. Cellular solids: structure and properties: Cambridge University Press; 1999.
- [27] Li H, Oppenheimer SM, Stupp SI, Dunand DC, Brinson LC. Effects of pore morphology and bone ingrowth on mechanical properties of microporous titanium as an orthopaedic implant material. *Materials Transactions* 2004;45:1124-31.
- [28] Barbas A, Bonnet AS, Lipinski P, Pesci R, Dubois G. Development and mechanical characterization of porous titanium bone substitutes. *Journal of the Mechanical Behavior of Biomedical Materials* 2012;9:34-44.
- [29] Kruth J-P, Mercelis P, Van Vaerenbergh J, Froyen L, Rombouts M. Binding mechanisms in selective laser sintering and selective laser melting. *Rapid Prototyping Journal* 2005;11:26-36.
- [30] Lin CY, Wirtz T, LaMarca F, Hollister SJ. Structural and mechanical evaluations of a topology optimized titanium interbody fusion cage fabricated by selective laser melting process. *Journal of Biomedical Materials Research Part A* 2007;83:272-9.
- [31] Warnke PH, Douglas T, Wollny P, Sherry E, Steiner M, Galonska S, et al. Rapid prototyping: porous titanium alloy scaffolds produced by selective laser melting for bone tissue engineering. *Tissue Engineering Part C: Methods* 2008;15:115-24.
- [32] Traini T, Mangano C, Sammons R, Mangano F, Macchi A, Piattelli A. Direct laser metal sintering as a new approach to fabrication of an isoelastic functionally graded material for manufacture of porous titanium dental implants. *Dental Materials* 2008;24:1525-33.
- [33] Williams JM, Adewunmi A, Schek RM, Flanagan CL, Krebsbach PH, Feinberg SE, et al. Bone tissue engineering using polycaprolactone scaffolds fabricated via selective laser sintering. *Biomaterials* 2005;26:4817-27.
- [34] Hrabe NW, Heinel P, Flinn B, Körner C, Bordia RK. Compression-compression fatigue of selective electron beam melted cellular titanium (Ti-6Al-4V). *Journal of Biomedical Materials Research - Part B Applied Biomaterials* 2011;99 B:313-20.

-
- [35] Heini P, Müller L, Körner C, Singer RF, Müller FA. Cellular Ti–6Al–4V structures with interconnected macro porosity for bone implants fabricated by selective electron beam melting. *Acta Biomaterialia* 2008;4:1536-44.
- [36] Truscetto S, Kerckhofs G, Van Bael S, Pyka G, Schrooten J, Van Oosterwyck H. Prediction of permeability of regular scaffolds for skeletal tissue engineering: A combined computational and experimental study. *Acta Biomaterialia* 2012;8:1648-58.
- [37] Van Bael S, Chai YC, Truscetto S, Moesen M, Kerckhofs G, Van Oosterwyck H, et al. The effect of pore geometry on the in vitro biological behavior of human periosteum-derived cells seeded on selective laser-melted Ti6Al4V bone scaffolds. *Acta Biomaterialia* 2012;8:2824-34.
- [38] Thelen S, Barthelat F, Brinson LC. Mechanics considerations for microporous titanium as an orthopedic implant material. *Journal of Biomedical Materials Research Part A* 2004;69A:601-10.
- [39] 13314:2011 I. Mechanical testing of metals -- Ductility testing -- Compression test for porous and cellular metals. 2011.
- [40] Borleffs MS. Finite element modeling to predict bulk mechanical properties of 3D printed metal foams. Delft: Delft University of Technology; 2012.
- [41] Campoli G, Weinans H, Zadpoor AA. Computational load estimation of the femur. *Journal of the Mechanical Behavior of Biomedical Materials* 2012;10:108-19.
- [42] Checa S, Prendergast PJ. Effect of cell seeding and mechanical loading on vascularization and tissue formation inside a scaffold: a mechano-biological model using a lattice approach to simulate cell activity. *Journal of Biomechanics* 2010;43:961-8.
- [43] Hoshaw SJ, Brunski JB, Cochran GV. Mechanical loading of Branemark implants affects interfacial bone modeling and remodeling. *International Journal of Oral and Maxillofacial Implants* 1994;9:345-60.
- [44] Zadpoor AA, Campoli G, Weinans H. Neural network prediction of load from the morphology of trabecular bone. *Applied Mathematical Modelling* 2013;37:5260–76.

-
- [45] Harrysson OL, Hosni YA, Nayfeh JF. Custom-designed orthopedic implants evaluated using finite element analysis of patient-specific computed tomography data: femoral-component case study. *BMC Musculoskeletal Disorders* 2007;8:91.
- [46] Poelert S, Valstar E, Weinans H, Zadpoor AA. Patient-specific finite element modeling of bones. *Proceedings of the Institution of Mechanical Engineers, Part H: Journal of Engineering in Medicine* 2013;227:464-78.
- [47] Viceconti M, Davinelli M, Taddei F, Cappello A. Automatic generation of accurate subject-specific bone finite element models to be used in clinical studies. *Journal of Biomechanics* 2004;37:1597-605.
- [48] Zheng G, Gollmer S, Schumann S, Dong X, Feilkas T, González Ballester MA. A 2D/3D correspondence building method for reconstruction of a patient-specific 3D bone surface model using point distribution models and calibrated X-ray images. *Medical Image Analysis* 2009;13:883-99.
- [49] Chao E. Graphic-based musculoskeletal model for biomechanical analyses and animation. *Medical engineering & physics* 2003;25:201-12.
- [50] Pearce A, Richards R, Milz S, Schneider E, Pearce S. Animal models for implant biomaterial research in bone: a review. *Eur Cell Mater* 2007;13:1-10.
- [51] Shelburne KB, Pandy MG. A musculoskeletal model of the knee for evaluating ligament forces during isometric contractions. *Journal of Biomechanics* 1997;30:163-76.
- [52] Nikooyan AA, Zadpoor AA. An improved cost function for modeling of muscle activity during running. *Journal of Biomechanics* 2011;44:984-7.
- [53] Nikooyan AA, Zadpoor AA. Effects of muscle fatigue on the ground reaction force and soft-tissue vibrations during running: a model study. *IEEE Transactions on Biomedical Engineering* 2012;59:797-804.

Chapter 3 Revival of pure titanium for dynamically loaded porous implants using additive manufacturing

This chapter has been published as:

R Wauthle, **SM Ahmadi**, S Amin Yavari, M Mulier, AA Zadpoor, H Weinans, J Van Humbeeck, JP Kruth, J Schrooten, *Revival of pure titanium for dynamically loaded porous implants using additive manufacturing*, Materials Science and Engineering: C, 2015. P. 94-100

3.1 Abstract

Additive manufacturing techniques are getting more and more established as reliable methods for producing porous metal implants thanks to the almost full geometrical and mechanical control of the designed porous biomaterial. Today, Ti6Al4V ELI is still the most widely used material for porous implants, and none or little interest goes to pure titanium for use in orthopedic or load-bearing implants. Given the special mechanical behavior of cellular structures and the material properties inherent to the additive manufacturing of metals, the aim of this study is to investigate the properties of selective laser melted pure unalloyed titanium porous structures. Therefore, the static and dynamic compressive properties of pure titanium structures are determined and compared to previously reported results for identical structures made from Ti6Al4V ELI and tantalum. The results show that porous Ti6Al4V ELI still remains the strongest material for statically loaded applications, whereas pure titanium has a mechanical behavior similar to tantalum and is the material of choice for cyclically loaded porous implants. These findings are considered to be important for future implant developments since it announces a potential revival of the use of pure titanium for additively manufactured porous implants.

3.2 Introduction

Porous metal structures in orthopedics were first reported in the late sixties, and ever since then the interest has only increased [1-3]. The reasons for this trend in reconstructive surgery are obvious: coming from solid metal implants with high strength and stiffness, porous metals are optimal for uncemented use since they allow for bone in-growth through the open porosities, have an improved fixation thanks to the high roughness and corresponding coefficient of friction and have in addition a lower stiffness and thus avoid stress-shielding [4]. Today, one of the most well-known porous metal bone replacement structures is *Trabecular Metal™* (Zimmer, Warsaw, IN, USA), which is a highly porous carbon matrix coated with tantalum (Ta) [1], [5-9]. But due to the high density and high cost of Ta and its difficulty to process, most orthopedic device manufacturers choose to use porous

biomaterials based on titanium or titanium alloys [2], [3] and [10]. These titanium porous structures are usually manufactured using conventional techniques such as furnace sintering, plasma spraying, lost wax casting and vapor deposition [10-13]. Recently, additive manufacturing (AM) techniques such as selective laser melting (SLM, [14]) and electron beam melting (EBM) are breaking new ground in implant manufacturing and more specifically in the manufacturing of porous metal bone replacement structures. AM allows for almost full design freedom, giving the possibility to manufacture regular open porous structures with high repeatability and thus full control over both geometrical and mechanical properties. The design freedom and reproducibility are important features when there is a need for implant performance simulations and outcome predictions [15-16]. Also, using AM has the advantage to manufacture implants with both porous and solid sections in one step (monolithic design), with less material consumption since the non-used powder can be recycled for future use, when the chemical composition is still fulfilling the required specifications and when the recycling process is free from contamination. Finally, materials like Ta that are difficult to process conventionally, could be also processed using AM, creating a whole range of new opportunities [17].

In the current study, the SLM technology was used to manufacture porous structures from commercially pure (CP) grade 1 titanium. Previous studies mostly dealt with porous structures in Ti6Al4V (grade 5 or grade 23), either using SLM [15-30] or EBM [13], [31-36]. This biocompatible titanium alloy is the material of choice for load-bearing applications since it has a high strength to weight ratio. Commercially pure titanium (CP Ti), on the other hand, has a lower strength and therefore its use is often limited to non-load bearing applications like cranio-maxilla-facial implants [37]. A general overview of these mechanical properties of different grades of titanium and Ta can be found in Table 3-1.

Table 3-1. Literature values of the density and mechanical properties of standard annealed wrought titanium grades [38] and tantalum [39] and [40]: The density, yield strength (YS), the ultimate tensile strength (UTS), Young's modulus (E) and the elongation (e). Fatigue data are taken from [1].

Material	Density[g/cm ³]	YS[MPa]	UTS[MPa]	E[GPa]	e[%]	Fatigue[MPa]
CP Ti grade 1	4.51	170-241	240-331	103	30	270
CP Ti grade 2	4.51	280-345	340-434	103	28	330
CP Ti grade 3	4.51	380-448	450-517	103	25	350
CP Ti grade 4	4.51	480-586	550-662	104	20	376
Ti6Al4V grade 5	4.43	830-924	900-993	114	14	500
Ti6Al4V ELI grade 23	4.43	760-827	830-896	114	15	n.a.
Tantalum	16.6	165-220	200-390	186	20-50	n.a.

Also, only few publications about additively manufactured CP Ti are available, all of them covering SLM of CP Ti grade 2 [41-45] and none were found that deal with CP Ti grade 1. Nevertheless, the use of CP Ti has some major advantages over alloyed titanium that can potentially bring additively manufactured CP Ti back in the scope of medical device manufacturers. First of all, CP Ti has the advantage of having no potential hazardous or toxic alloying components such as V or Al [1]. Secondly, the high ductility that provides CP Ti with the sometimes necessary deformability in certain applications like e.g. bone plates, could be an interesting property of porous metals that could be deformed intra operatively to the patient specific bone defect. And finally, in a previous study on porous Ta structures, the ductile behavior of the Ta material led to a very high fatigue strength compared to similar Ti6Al4V ELI structures and a preferential load transfer and bone in growth in an animal study [17]. It was proposed that the mechanical behavior of the porous Ta including its high ductility was partly responsible for the excellent *in vivo* performance of Ta. Therefore, the aim of this study is to investigate whether CP Titanium can have a revival in orthopedics as a raw material for SLM processed porous implants. This is the first study that presents and discusses the mechanical properties of additively manufactured porous structures made of CP Ti grade 1 and compares them with those of additively manufactured Ti6Al4V ELI and Ta structures. This could be useful for facilitating proper selection of the most appropriate material for the envisioned implant application.

3.3 Materials and Methods

The materials and methods section describes the details of the new porous CP grade 1 Ti samples, manufactured and analyzed in the current study. The properties of identical porous structures made from Ti6Al4V ELI and Ta to which the CP Ti samples will be compared were published elsewhere, unless otherwise implied [17] and [23].

3.3.1 Materials and manufacturing

Porous CP Ti grade 1 structures were manufactured from CP Ti grade 1 powder using the selective laser melting technology (3D Systems - Layerwise NV, Leuven, Belgium). The details of the laser processing method were similar to the ones presented in previous studies [19-21] and [23]. The unit cell used as the micro-architecture of these porous structures was in all cases dodecahedron, in four different porosities as seen on Fig. 3-1. This specific unit cell, pore and strut sizes were chosen in order to compare the results with those of a previous study that used identical dodecahedron structures made by SLM out of Ti6Al4V ELI powder [23]. The used nomenclature in Fig 3-1 refers to the theoretical strut and pore size; e.g. Ti 120 – 500 has a theoretical strut size of 120 μm and pore size of 500 μm . In this work, spherical commercially pure grade 1 Ti powder (chemical composition according to ASTM F67, further referred to as CP Ti) with particle size ranging from 10 μm to 45 μm was used. The production was performed in an inert atmosphere and the samples were built on top of a solid Ti substrate. After production, the samples were removed from the substrate using wire electro discharge machining (EDM). Cylindrical porous specimens with a diameter of 10 mm and height of 15 mm were manufactured for morphological analysis, static and dynamic mechanical testing. The chemical composition of the porous specimens after SLM manufacturing was measured using IGA (Interstitial Gas Analysis) and ICP-OES (Inductively Coupled Plasma Optical Emission Spectrometry). With measured concentrations of C (0.0075 % wt), N (0.0100 % wt), O (0.1600 % wt), H (0.0036 % wt) and Fe (0.040 % wt), the specifications of ASTM F67 for CP Ti grade 1 are fulfilled.

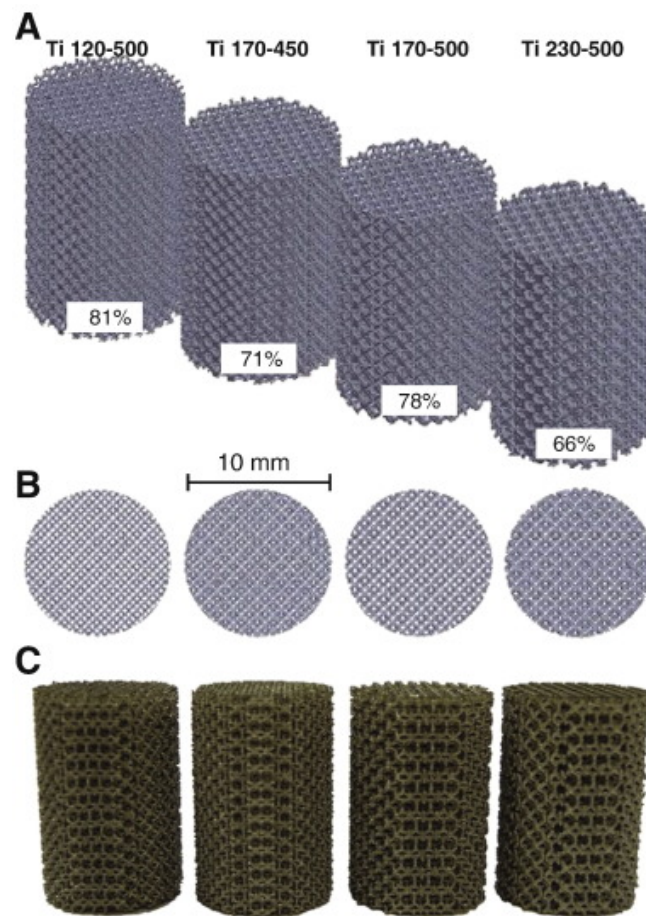


Figure 3-1. Additively manufactured porous CP Ti structures: 3D CAD visual representation of the four different structures in isometric (A) and top (B) view and a picture after manufacturing (C).

3.3.2 Morphological analysis

Overall open porosity was measured using dry weighing and Archimedes measurements on five different cylindrical samples prior to being used for mechanical testing. Dry weighing occurred under normal atmosphere conditions and overall porosity was calculated by dividing the actual weight by the theoretical weight of the macro volume using a theoretical density of 4.507 g/cm^3 for pure Ti [39]. Archimedes measurements are based on a combination of dry weighing and weighing in pure ethanol. The absolute density (ρ_{abs}) of each porous specimen was calculated using the equation:

$$\rho_{\text{abs}} = \frac{m_{\text{air}}(\rho_{\text{ethanol}} - 0.0012)}{m_{\text{air}} - m_{\text{ethanol}}} + 0.0012$$

Where m_{air} is the weight of the porous specimen in air, m_{ethanol} the weight of the porous specimen while immersed in ethanol and ρ_{ethanol} is the density of ethanol. Dividing the weight in air by the absolute density resulted in the actual volume, while the overall porosity was then calculated by dividing the actual volume by the macro volume. All weighing measurements were performed on an OHAUS Pioneer balance.

3.3.3 Mechanical testing

3.3.3.1 Static mechanical testing

Static mechanical testing of five cylindrical samples of each of the four series of porous structures was carried out in accordance with the standard ISO 13314 [46]. All tests were done using an INSTRON 5985 mechanical testing machine (30 kN load cell) by applying a constant deformation rate of 1.8 mm/min. Each static compression test resulted in a stress–strain curve (Fig 3-3 for which the following values were calculated: plateau stress (σ_{pl}) as the arithmetical mean of the stresses between 20% and 40% compressive strain, plateau end stress (σ_{130}) and strain (e_{ple}) as the point in the stress–strain curve at which the stress is 1.3 times the plateau stress, the quasi-elastic gradient (E) as gradient of the straight line determined within the linear deformation region at the beginning of the compressive stress–strain curve and the yield strength (σ_y) as the compressive 0.2% offset stress. In this context, the quasi-elastic gradient is closest to the concept of stiffness, which is used for solid materials. In order to facilitate understanding and comparison between the results of this study and those of similar studies on solid and porous materials, the quasi-elastic gradient will be referred to as stiffness. Nevertheless, the exact definitions presented above should be kept in mind when interpreting the data. In the previous study on Ti6Al4V ELI porous structures, it was assumed that the plateau stress was close to the concept of yield stress [23], and this is confirmed by recalculating the yield stress according the 0.2% offset stress explained above (solid and dashed grey lines in Fig 3-2 C). For three out of four data points, there is no significant difference between the yield stress and the plateau stress for Ti6Al4V ELI porous structures, meaning that the assumptions were valid. However, for CP Ti porous structures, there is a significant difference between the yield stress and the plateau stress, and therefore both values were calculated and analyzed separately.

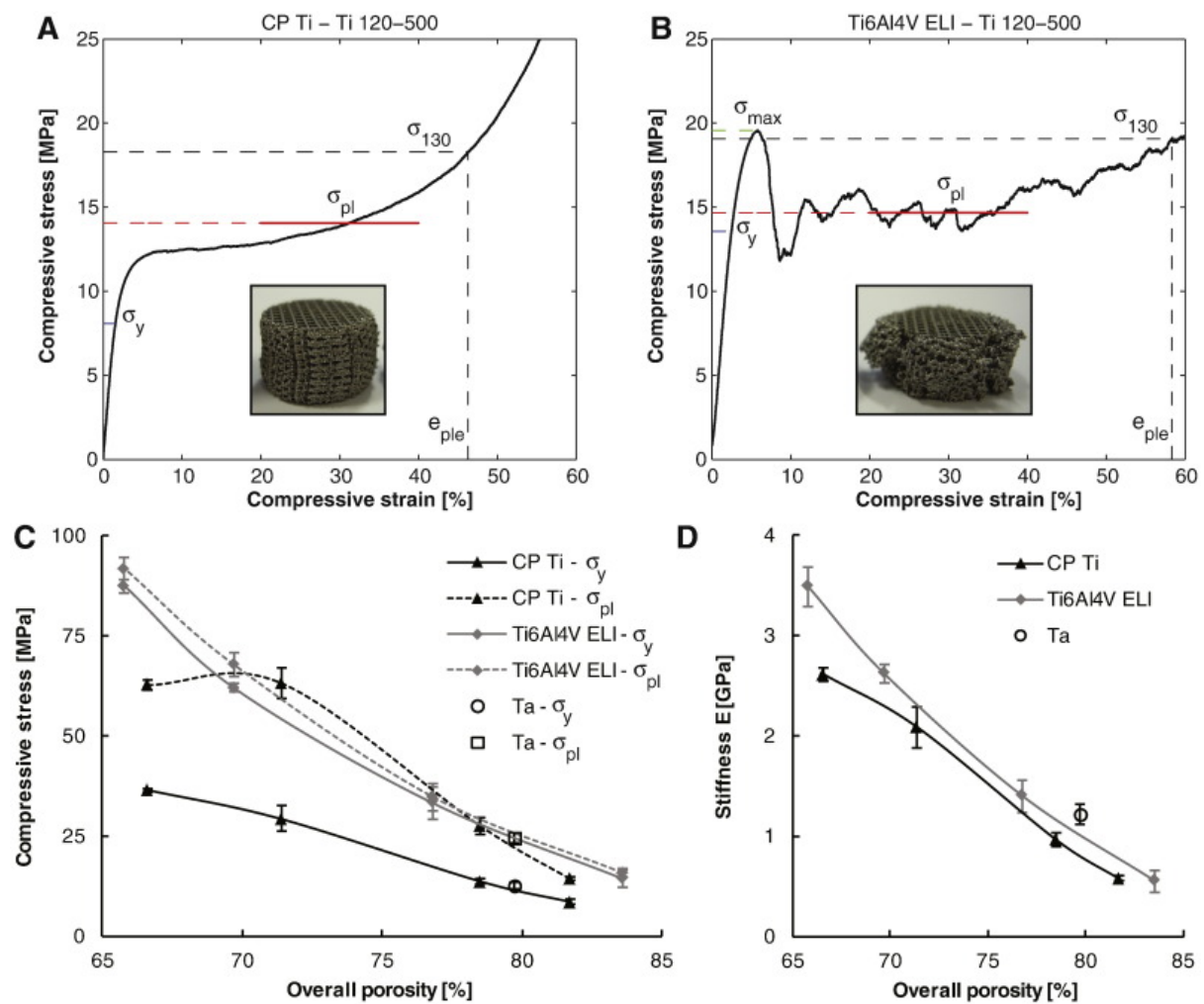


Figure 3-2. Static mechanical properties of open porous SLM processed titanium and tantalum structures: representative compressive stress–strain curve and graphical representation of the calculated values σ_y , σ_{pl} , σ_{130} , e_{ple} for a Ti 120–500 structure in CP Ti (A) and Ti6Al4V ELI (B), both including a picture of a sample after compression testing; and a comparison between the yield strength and plateau stress (C) and stiffness (D) for all three materials versus the actual measured open porosity of each structure

3.3.3.2 Dynamic mechanical testing

Compression-compression fatigue tests were carried out on an identical set-up as reported before [23] using a hydraulic test frame (MTS, Minneapolis, US) with a 25 kN load cell. The loading frequency was fixed at 15 Hz (sinusoidal wave shape) and a constant load ratio, $R = 0.1$ was used

(load ratio is the ratio of the minimum load to the maximum load applied during the cycle). Ten different values of maximum force were chosen for every porous structure (except one, for which only 7 values were tested), resulting in applied stress levels between $0.45 \sigma_y$ and $0.8 \sigma_y$. Two samples were tested for each stress level with 20 samples in total for series Ti 120–500, Ti 170–500 and Ti 230–500 and 14 samples for series Ti 170–450 (see Fig. 3-1 and Table 3-2 for details on the series nomenclature). The samples were considered to have failed once they lost + 90% of their stiffness. The S-N curves of the four tested porous structures were established by plotting both absolute and normalized values of stress versus number of cycles to failure for all tested samples. In case of normalized S-N curves, a power law was fitted to all data points of the normalized S-N curves.

Table 3-2. The geometrical/physical properties of the four different series of porous CP Ti samples tested in the current study

Series	Ti 120-500	Ti 170-450	Ti 170-500	Ti 230-500
Porosity, dry weighing [%]	81.7±0.2	71.4±0.6	78.5±0.3	66.7±0.4
Porosity, Archimedes [%]	81.6±0.2	71.1±0.6	78.4±0.4	66.0±0.6
Strut density, Archimedes [%]	99.8±0.2	99.2±0.1	99.5±0.3	98.0±1.1
Pore size, nominal [μm]	500	450	500	500
Strut size, nominal [μm]	120	170	170	230

3.4 Results

3.4.1 Morphological properties

The measured values for the overall porosity by dry weighing and Archimedes measurements are summarized in Table 3-2. A high repeatability in terms of overall porosity (< 1%) and a high density of the struts (> 98%) was achieved, which is of importance for reproducibility of the mechanical properties.

3.4.2 Mechanical properties

The results of the static compression tests are summarized in Table 3-3. Due to the ductile behavior of the porous CP Ti material, no maximum compressive stress (σ_{max}) and strain at maximum

compressive stress (e_{max}) could be registered. Fig. 3-2 A shows a representative stress–strain curve and the ductile behavior of the porous CP Ti Ti 120–500 structure during static compression testing, including a graphical representation of all calculated properties. The actual values of the static mechanical properties are summarized in Table 3-3 and are visually presented and compared to Ti6Al4V ELI and Ta in Fig. 3-2 C and D, in which the actual open porosity of each porous structure is taken into account. For the Ta values, σ_{pl} was recalculated for the 20-40% strain interval instead of the previously reported 20-30% strain interval.

Table 3-3. The static mechanical properties of the four different series of porous CP Ti samples tested according to ISO 13314.

Series	σ_y [MPa]	σ_{pl} [MPa]	σ_{130} [MPa]	e_{pl} [%]	E[GPa]
Ti 120-500	8.6±0.3	14.3±0.2	18.6±0.3	46.3±0.4	0.58±0.02
Ti 170-450	29.2±2.3	63.2±3.8	82.3±5.2	40.3±0.5	2.08±0.14
Ti 170-500	13.7±0.4	27.6±2.2	36.3±3.4	41.4±2.3	0.96±0.05
Ti 230-500	36.5±0.4	62.7±1.4	81.5±1.9	42.4±0.5	2.61±0.05

The dynamic compression test results are shown through S-N curves in Fig. 3-3 A for absolute and in Fig. 3-3 B for normalized stress values obtained by compression-compression fatigue testing, including the power law for the normalized S-N curves of Ti6Al4V ELI and Ta structures as reported previously [17] and [23]. Power laws were fitted to the normalized data points of all four series and to all series together and are represented in Table 3-4. The coefficient of determination was very high for all fitted power laws, but it should be noted that the series Ti 170–450 and the combined data have a lower coefficient of determination. When multiplying these power laws by the yield strength of each series for both materials, this results in power laws for the absolute stress values as shown in Fig. 3-3 C. The point where the same series in the two materials intersect is marked with an 'X'. It should be noted that Fig. 3-3 C assumes that each of the four series in CP Ti are completely identical to the corresponding series in Ti6Al4V ELI, while in fact there are minor differences in overall open porosities between them, which should be kept in mind while interpreting this figure. In conclusion, Fig. 3-3 D shows the fatigue strength S_f after 10^6 cycles, for CP Ti based on an extrapolation of the fitted power laws in Table 3-4, for Ti6Al4V ELI based on the estimated fatigue strength of $0.12 \sigma_y$ in [23], taking into account the actual overall porosity for both materials and for all four series, and finally for Ta based on the determined fatigue strength of 7.35 MPa (or $0.57 \sigma_y$) for only one porosity mentioned in [17].

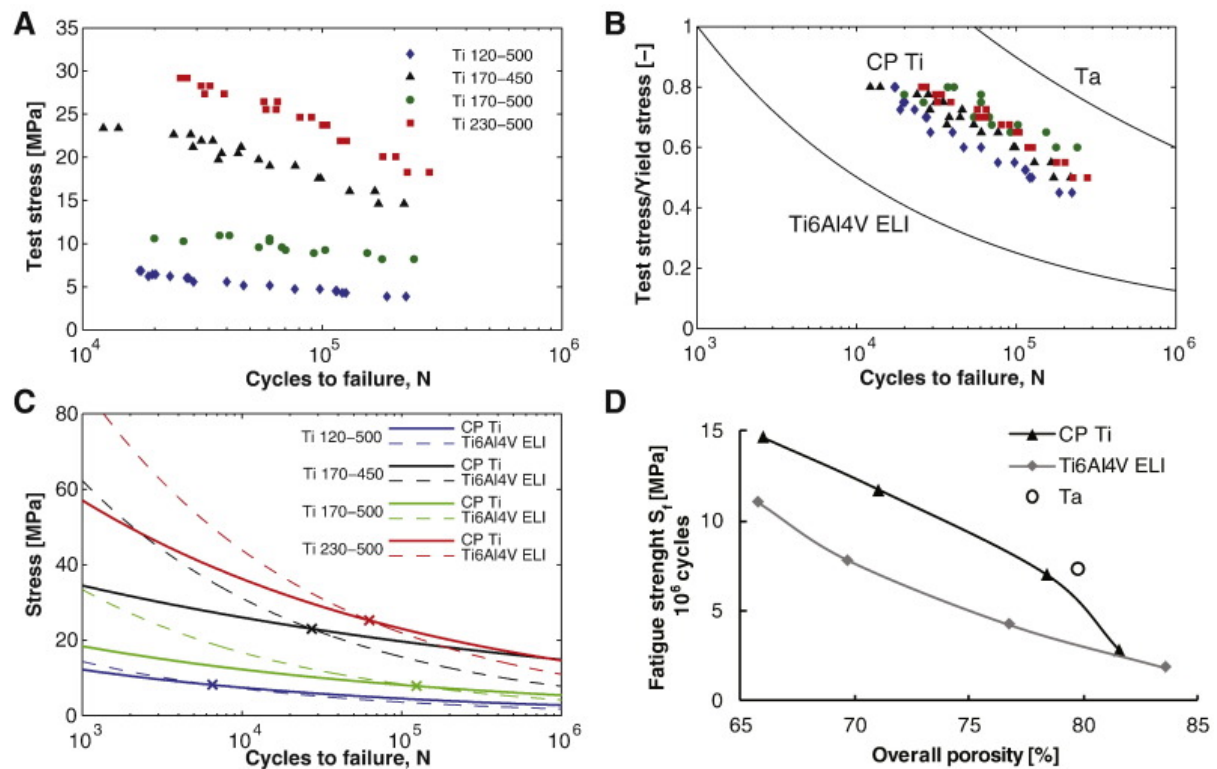


Figure 3-3. Dynamic mechanical properties of open porous SLM processed titanium and tantalum structures: S-N curves obtained by compression-compression fatigue testing of all CP Ti samples using absolute (A) and normalized (B) stress values and a power law representing the results of Ti6Al4V ELI and Ta structures from previous studies (B) [17] and [23]; an overview of all fitted power laws for all four porous structures in both titanium materials using absolute stress values, including the structure intersection points marked by 'X' (C); an extrapolation of the fitted power laws to 10^6 cycles for all four porous structures in both titanium materials and the actual fatigue limit of the Ta structure versus the actual measured open porosity of each structure (D).

Table 3-4. The power laws fitted to the data points of the normalized S-N curves for all four different series of porous CP Ti samples tested. When multiplied by the corresponding value of the yield strength, the power law of the absolute values is obtained. Also the extrapolated values at $N = 10^6$ cycles are listed.

Series	Fitted power law	R2 value	Stress level at 10e6 cycles
Ti 120-500	$\sigma_y \cdot 6.266 \cdot N^{-0.215}$	0.98	0.32 σ_y
Ti 170-450	$\sigma_y \cdot 2.742 \cdot N^{-0.122}$	0.77	0.51 σ_y
Ti 170-500	$\sigma_y \cdot 4.465 \cdot N^{-0.177}$	0.93	0.39 σ_y
Ti 230-500	$\sigma_y \cdot 6.095 \cdot N^{-0.197}$	0.95	0.40 σ_y
All series	$\sigma_y \cdot 4.154 \cdot N^{-0.167}$	0.72	0.41 σ_y

3.5 Discussion

Recently, it has been shown that selective laser melted porous structures made from Ti6Al4V ELI and Ta can be clinically used as implant materials [17] and [24]. Although Ti6Al4V ELI is the current standard for load-bearing implant applications, Ta showed excellent *in vivo* performance and bone ingrowth. The ductile mechanical behavior and the high fatigue strength are believed to be one of the key factors for the performance of porous Ta implants, but due to high material cost, the use of Ta in large orthopedic implants is expected to remain relatively limited. In this study, the SLM technology was used to manufacture porous CP Ti structures based on dodecahedron unit cells with overall porosities ranging from 66% to 82% in order to compare them with previously published data of Ti6Al4V ELI and Ta structures with the same geometrical architecture.

A first part investigates whether CP Ti porous structures have similar static and dynamic mechanical properties as compared to pure Ta structures. It was observed that CP Ti porous structures continuously deform under increased compressive load, without reaching a first local maximum (Fig. 3-2A). This ductile mechanical behavior of CP Ti porous structures is very similar to what was previously reported for pure Ta [17]. In order to compare the actual measurable static mechanical properties, it is important to take the overall porosity into account. It was concluded that for both the yield strength and the plateau stress, there is no significant difference between the values of porous Ta and the trend lines of porous CP Ti obtained in this study (Fig. 3-2 C and D). To explain this resemblance, the properties of the solid pure metals Ta and CP Ti should be compared. Both metals are one phase metals, but they do have a different crystal structure; Ta has a cubic BCC structure and Ti has a close packed hexagonal HCP structure [39]. In terms of yield strength both Ta and CP Ti have similar bulk properties (Table 3-1). Since both metals are single phase ductile materials with similar yield strength, the resembling mechanical behavior of Ta and CP Ti as a porous structure can be explained. The stiffness of porous Ta does however appear to be different from the trend line of porous CP Ti stiffness values (Fig. 3-2 D). This difference can be explained by the fact that the stiffness of pure Ta is higher than that of CP Ti (Table 3-1). Regarding the dynamic mechanical properties it was observed that porous Ta has a higher relative fatigue strength ($0.58 \sigma_y$ vs. $0.41 \sigma_y$)

and since there is no significant difference in yield strength, this resulted in a slightly higher absolute fatigue strength for porous Ta compared to CP Ti (Fig. 3-3 D). In conclusion it can be stated that porous CP Ti has a comparable mechanical behavior compared to porous Ta, except that CP Ti has a slightly lower stiffness and absolute fatigue strength after 10^6 cycles. This is a very interesting finding, since in a previous study it was shown that the mechanical behavior of porous Ta was likely responsible for the excellent *in vivo* performance, which could now be replaced by the much cheaper, more commonly available and easier to process CP Ti. Therefore, the authors suggest for future research to evaluate porous CP Ti implants in an *in vivo* animal study and compare the results with those obtained for porous Ta.

In the second part, identical porous structures in CP Ti and Ti6Al4V ELI have to be compared in order to understand their differences in static and dynamic mechanical properties. To do so, the researchers aimed to manufacture porous CP Ti structures with nearly identical geometrical properties as reported before for Ti6Al4V ELI [23]. The results show that the morphological properties of the CP Ti structures are very close to those of Ti6Al4V ELI, but nevertheless the small differences should be taken into account wherever possible because small changes in overall porosity can have significant influence on the mechanical properties. Firstly, comparing the mechanical behavior during compression testing already reveals a significant difference between both materials. While porous CP Ti continuously deforms during compression without fracture, Ti6Al4V ELI reaches a maximum compression point, after which the structure starts to fail locally. Due to the geometry of the Ti6Al4V ELI structure, non-failed parts of the structure continue to deform until they fail. This compressive failure behavior continues until a plateau is reached and full compression occurs. The difference in mechanical deformation or failure can also be seen on the test sample images after compression. The porous CP Ti sample is completely deformed (Fig. 3-2 A), whereas the Ti6Al4V ELI structure failed during compression testing (Fig. 3-2 B). This also explains the difference between the values of the plateau end e_{ple} , which occurs between 40 and 47 % strain for CP Ti and between 56 and 76% strain for Ti6Al4V ELI [23]. Because of the pure deformation of CP Ti structures, full or final compression occurs at lower strains. The yield strength is lower for CP Ti compared to Ti6Al4V ELI. This is also expected since the yield strength of wrought Ti6Al4V ELI is about four times the strength of CP Ti (Table 3-1). However, for the porous structures compared in this study, the Ti6Al4V ELI structures have a yield strength that is only 1.7 to 2.4 times more than

that of CP Ti, as would be expected for standard grade 3 or 4 titanium, so the reference values of wrought titanium do not hold true for SLM processed porous titanium. If, on the other hand, strength values of as-manufactured selective laser melted solid Ti6Al4V ELI (1110 MPa[47]) and CP Ti (555 MPa [48]) are used, it should be noted that SLM Ti6Al4V ELI is 40% and CP Ti is 170% stronger compared to their conventionally processed counterparts. By doing so, a yield strength ratio of 2.0 is obtained, which is closer to the values that were actually observed for both porous materials. The plateau stress is not significantly different in the range of 70-80% overall porosity, but it tends to be lower for CP Ti outside this interval. Also a strange curve in the trend line for CP Ti is noticeable for the Ti 170–450 series data point. Since this is the only series with smaller pore size compared to the others (450 μm vs. 500 μm) and since porous CP Ti continuously deforms as a whole instead of failing by local fracturing, it is assumed that these two factors are the reason for the particular curve in the trend line of the plateau stress of porous CP Ti. Given the ductile deformation behavior and the sensitivity of the plateau stress to the pore size, it is important to carefully interpret and compare plateau stress for CP Ti, since the calculated values do not represent an actual plateau as is reached with Ti6Al4V ELI. The authors therefore suggest including the deformation mechanism for pure and ductile metals and corresponding definitions of representative values in a next revision of the ISO 13314 standard. The stiffness of porous CP Ti structures shows to be lower, but not significantly different for porosities > 70%, compared to Ti6Al4 ELI. Since solid CP Ti has a lower stiffness compared to Ti6Al4V ELI (Table 3-1), and since both the overall porosity and deformation mechanism influence the stiffness of a cellular metal [49] and [50], the small differences for the porous structures in Fig. 3-2 D are justified. Summarizing the differences in static mechanical properties between porous CP Ti and Ti6Al4V ELI structures, it can be stated that selective laser melted porous CP Ti has about half the yield strength and a more ductile deformation mechanism compared to Ti6Al4V ELI, while the stiffness remains the same. When the normalized stress levels of the dynamic properties are compared, it can be concluded that CP Ti has a higher normalized fatigue strength, and an overall normalized fatigue strength after 10^6 cycles of $0.41 \sigma_y$, which is 3.4 times higher than the normalized fatigue strength of Ti6Al4V ELI (Fig. 3-3 B, Table 3-4 and [23]). The S-N curves obtained by fitting power laws through all data series for absolute stress levels, reveal that the S-N curves of CP Ti and Ti6Al4V ELI for each separate series intersect at some point (Fig. 3-3 C). Keeping in mind that the porosities were not exactly the same for both materials, which will cause a shift in the intersection point of Ti 120–500 to the right and of Ti 170–500 to the left, it can be

reasonably stated that all intersection points lie in the interval $10^4 - 10^5$ cycles. Hence the general observation and conclusion is that Ti6Al4V ELI porous structures are mechanically stronger for static or low cycle fatigue ($< 10^4$ cycles) applications, whereas commercially pure CP Ti structures are mechanically superior for high cycle fatigue ($> 10^5$ cycles) applications. This statement is ratified by the extrapolated values at 10^6 cycles for both materials and for the full range of tested porosities, which show superior fatigue strength for porous CP Ti structures compared to Ti6Al4V ELI (Fig. 3-3 D). In general, titanium is known to have a very good fatigue resistance, and properties like crack initiation and crack propagation or growth are often used to explain or predict the fatigue behavior of a material. But for porous structures the situation is more complex, since it is a combination of actual material properties and the architectural properties of the structure itself. Assuming the structures do have identical geometrical morphology, it is reasonable to say that the ductile deformation behavior of porous CP Ti is likely to be the reason for the excellent high cycle fatigue performance, because ductile materials have a lower crack initiation and propagation by softening the material when loaded [51]. This, however, remains a remarkable observation since the wrought titanium alloys generally have a superior fatigue strength compared to commercially pure titanium grades (Table 3-1). Since little is known about the fatigue mechanism for porous metals in general and given that fatigue properties of additively manufactured solid Ti6Al4V ELI reported elsewhere are non-consistent [52-54], the authors consider it as future research to further investigate more in detail the fatigue behavior mechanism of porous metals manufactured by AM and how processing conditions (e.g. build direction) and post process heat treatments can influence these results. Heat treatments are often applied on parts made by SLM to reduce residual stresses in bulky parts or to improve the mechanical properties. The results discussed here are without any heat treatment and can change the static and dynamic properties of porous structures [55].

3.6 Conclusion

In this study the additive manufacturing technology selective laser melting was used to manufacture highly open porous (66-82%) CP grade 1 Ti structures. After a morphological characterization, both static and dynamic compression tests were done on four series of porous structures based on the dodecahedron unit cell architecture. The results were compared to previously reported data on

identical porous structures in Ta[17] and Ti6Al4V ELI [23]. Based on the experimental results obtained in this study and the comparison with the other two already established orthopedic porous metals, it can be concluded that CP Ti is an excellent material for dynamically loaded porous implants. At first, it has almost identical mechanical behavior and properties compared to porous Ta, which has proven excellent *in vivo* performance, likely thanks to these properties. Secondly, for high cycle fatigue strength ($> 10^5$ cycles), CP Ti outperforms Ti6Al4V ELI, but for statically loaded or low cycle fatigue applications ($< 10^4$ cycles), Ti6Al4V ELI remains the preferred material. These conclusions can have a potential huge impact on the medical device industry, because it brings CP Ti back in the scope of implant designers, has a lower cost compared to Ta and has the advantage of no potential hazardous or toxic alloying components like the presently applied titanium alloys. However, no comparative *in vitro* and *in vivo* data between additively manufactured CP Ti and Ti6Al4V ELI is available and the authors suggest to investigate this in future research.

3.7 Acknowledgements

This research was established by funding of the agency for Innovation by Science and Technology (IWT) of the Flemish government through Baekeland mandate 'IWT 100228'.

3.8 References

- [1] J.A. Helsen, Y. Missirlis. Biomaterials - A Tantalus Experience. Springer (2010)
- [2] B.R. Levine, D.W. Fabi. Porous metals in orthopedic applications - A review [Poröse Metalle in orthopädischen Anwendungen - Eine Übersicht]. Mater. Werkst., 41 (2010), pp. 1001–1010
- [3] B. Levine. A New Era in Porous Metals: Applications in Orthopaedics. Adv. Eng. Mater., 10 (2008), pp. 788–792
- [4] M.T. Andani, N.S. Moghaddam, C. Haberland, D. Dean, M.J. Miller, M. Elahinia. Metals for bone implants. Part 1. Powder metallurgy and implant rendering. Acta Biomater., 10 (10) (2014), pp. 4058–4070

-
- [5] J.D. Bobyn, G.J. Stackpool, S.A. Hacking, M. Tanzer, J.J. Krygier. Characteristics of bone ingrowth and interface mechanics of a new porous tantalum biomaterial. *J. Bone Joint Surg. Br. Vol.*, 81 (1999), pp. 907–914
- [6] L.D. Zardiackas, D.E. Parsell, L.D. Dillon, D.W. Mitchell, L.A. Nunnery, R. Poggie. Structure, metallurgy, and mechanical properties of a porous tantalum foam. *J. Biomed. Mater. Res.*, 58 (2001), pp. 180–187 |
- [7] D.A. Shimko, V.F. Shimko, E.A. Sander, K.F. Dickson, E.A. Nauman. Effect of porosity on the fluid flow characteristics and mechanical properties of tantalum scaffolds. *J. Biomed. Mater. Res. B Appl. Biomater.*, 73 (2005), pp. 315–324
- [8] B.R. Levine, S. Sporer, R.A. Poggie, C.J. Della Valle, J.J. Jacobs. Experimental and clinical performance of porous tantalum in orthopedic surgery. *Biomaterials*, 27 (2006), pp. 4671–4681
- [9] B. Levine, C.J. Della Valle, J.J. Jacobs. Applications of porous tantalum in total hip arthroplasty. *J. Am. Acad. Orthop. Surg.*, 14 (2006), pp. 646–655
- [10] G. Lewis. Properties of open-cell porous metals and alloys for orthopaedic applications. *J. Mater. Sci. Mater. Med.*, 24 (2013), pp. 2293–2325
- [11] E. Marin, L. Fedrizzi, L. Zagra. Porous metallic structures for orthopaedic applications: a short review of materials and technologies. *Eur. Orthop. Traumatol.*, 1 (2010), pp. 103–109
- [12] B. Vandenbroucke, J.-P. Kruth. Selective laser melting of biocompatible metals for rapid manufacturing of medical parts. *Rapid Prototyp. J.*, 13 (2007), pp. 196–203
- [13] P. Heintl, L. Muller, C. Korner, R.F. Singer, F.A. Muller. Cellular Ti-6Al-4 V structures with interconnected macro porosity for bone implants fabricated by selective electron beam melting. *Acta Biomater.*, 4 (2008), pp. 1536–1544
- [14] J.P. Kruth, G. Levy, F. Klocke, T.H.C. Childs. Consolidation phenomena in laser and powder-bed based layered manufacturing. *CIRP Ann. Manuf. Technol.*, 56 (2007), pp. 730–759

-
- [15] G. Campoli, M.S. Borleffs, S. Amin Yavari, R. Wauthle, H. Weinans, A.A. Zadpoor. Mechanical properties of open-cell metallic biomaterials manufactured using additive manufacturing. *Mater. Des.*, 49 (2013), pp. 957–965
- [16] S.M. Ahmadi, G. Campoli, S. Amin Yavari, B. Sajadi, R. Wauthle, J. Schrooten, *et al.*. Mechanical behavior of regular open-cell porous biomaterials made of diamond lattice unit cells. *J. Mech. Behav. Biomed. Mater.*, 34C (2014), pp. 106–115
- [17] R. Wauthle, J. van der Stok, S. Amin Yavari, J. Van Humbeeck, J.P. Kruth, A.A. Zadpoor, *et al.*. Additively manufactured porous tantalum implants. *Acta Biomater.*, 14 (2015), pp. 217–225
- [18] C. Emmelmann, P. Scheinemann, M. Munsch, V. Seyda. Laser Additive Manufacturing of Modified Implant Surfaces with Osseointegrative Characteristics. *Phys. Procedia*, 12 (2011), pp. 375–384
- [19] S. Van Bael, G. Kerckhofs, M. Moesen, G. Pyka, J. Schrooten, J.P. Kruth. Micro-CT-based improvement of geometrical and mechanical controllability of selective laser melted Ti6Al4V porous structures. *Mater. Sci. Eng. A*, 528 (2011), pp. 7423–7431
- [20] S. Van Bael, Y.C. Chai, S. Truscello, M. Moesen, G. Kerckhofs, H. Van Oosterwyck, *et al.*. The effect of pore geometry on the in vitro biological behavior of human periosteum-derived cells seeded on selective laser-melted Ti6Al4V bone scaffolds. *Acta Biomater.*, 8 (2012), pp. 2824–2834
- [21] G. Pyka, A. Burakowski, G. Kerckhofs, M. Moesen, S. Van Bael, J. Schrooten, *et al.*. Surface Modification of Ti6Al4V Open Porous Structures Produced by Additive Manufacturing. *Adv. Eng. Mater.*, 14 (2012), pp. 363–370
- [22] J. Wieding, A. Jonitz, R. Bader. The Effect of Structural Design on Mechanical Properties and Cellular Response of Additive Manufactured Titanium Scaffolds. *Materials*, 5 (2012), pp. 1336–1347
- [23] S. Amin Yavari, R. Wauthle, J. van der Stok, A.C. Riemsdag, M. Janssen, M. Mulier, *et al.*. Fatigue behavior of porous biomaterials manufactured using selective laser melting. *Mater. Sci. Eng.*, C, 33 (2013), pp. 4849–4858

-
- [24] J. van der Stok, H. Wang, S. Amin Yavari, M. Siebelt, M. Sandker, J.H. Waarsing, *et al.*. Enhanced bone regeneration of cortical segmental bone defects using porous titanium scaffolds incorporated with colloidal gelatin gels for time- and dose-controlled delivery of dual growth factors. *Tissue Eng. A*, 19 (2013), pp. 2605–2614
- [25] J. Van der Stok, O.P. Van der Jagt, S. Amin Yavari, M.F. De Haas, J.H. Waarsing, H. Jahr, *et al.*. Selective laser melting-produced porous titanium scaffolds regenerate bone in critical size cortical bone defects. *J. Orthop. Res.*, 31 (2013), pp. 792–799
- [26] S. Amin Yavari, J. van der Stok, Y.C. Chai, R. Wauthle, Z. Tahmasebi Birgani, P. Habibovic, *et al.*. Bone regeneration performance of surface-treated porous titanium. *Biomaterials*, 35 (2014), pp. 6172–6181
- [27] F. Brenne, T. Niendorf, H.J. Maier. Additively manufactured cellular structures: Impact of microstructure and local strains on the monotonic and cyclic behavior under uniaxial and bending load. *J. Mater. Process. Technol.*, 213 (2013), pp. 1558–1564
- [28] E. Sallica-Leva, A.L. Jardini, J.B. Fogagnolo. Microstructure and mechanical behavior of porous Ti-6Al-4 V parts obtained by selective laser melting. *J. Mech. Behav. Biomed. Mater.*, 26 (2013), pp. 98–108
- [29] J. Sun, Y. Yang, D. Wang. Mechanical properties of a Ti6Al4V porous structure produced by selective laser melting. *Mater. Des.*, 49 (2013), pp. 545–552
- [30] V.J. Challis, X. Xu, L.C. Zhang, A.P. Roberts, J.F. Grotowski, T.B. Sercombe. High specific strength and stiffness structures produced using selective laser melting. *Mater. Des.*, 63 (2014), pp. 783–788
- [31] L.E. Murr, S.M. Gaytan, F. Medina, M.I. Lopez, E. Martinez, R.B. Wicker. Additive Layered Manufacturing of Reticulated Ti-6Al-4 V Biomedical Mesh Structures by Electron Beam Melting
A. McGoron, C.-Z. Li, W.-C. Lin (Eds.), 25th Southern Biomedical Engineering Conference 2009, 15–17 May 2009, Springer Berlin Heidelberg, Miami, Florida, USA (2009), pp. 23–28

-
- [32] J. Parthasarathy, B. Starly, S. Raman, A. Christensen. Mechanical evaluation of porous titanium (Ti6Al4V) structures with electron beam melting (EBM). *J. Mech. Behav. Biomed. Mater.*, 3 (2010), pp. 249–259
- [33] S.J. Li, L.E. Murr, X.Y. Cheng, Z.B. Zhang, Y.L. Hao, R. Yang, *et al.*. Compression fatigue behavior of Ti–6Al–4 V mesh arrays fabricated by electron beam melting. *Acta Mater.*, 60 (2012), pp. 793–802
- [34] X.Y. Cheng, S.J. Li, L.E. Murr, Z.B. Zhang, Y.L. Hao, R. Yang, *et al.*. Compression deformation behavior of Ti-6Al-4 V alloy with cellular structures fabricated by electron beam melting. *J. Mech. Behav. Biomed. Mater.*, 16 (2012), pp. 153–162
- [35] T.J. Horn, O.L.A. Harrysson, D.J. Marcellin-Little, H.A. West, B.D.X. Lascelles, R. Aman. Flexural properties of Ti6Al4V rhombic dodecahedron open cellular structures fabricated with electron beam melting. *Addit. Manuf.*, 1–4 (2014), pp. 2–11
- [36] S.J. Li, Q.S. Xu, Z. Wang, W.T. Hou, Y.L. Hao, R. Yang, *et al.*. Influence of cell shape on mechanical properties of Ti-6Al-4 V meshes fabricated by electron beam melting method. *Acta Biomater.*, 10 (2014), pp. 4537–4547
- [37] D.M. Brunette, P. Tengvall, M. Textos, P. Thomsen. *Titanium in Medicine*. Springer, Berlin Heidelberg (2001)
- [38] S. Lampman. *Wrought Titanium and Titanium Alloys. Properties and Selection: Nonferrous Alloys and Special-Purpose Materials*, ASM Handbook, ASM International (1990), pp. 592–633
- [39] W.S. Lyman. *Properties of Pure Metals. Properties and Selection: Nonferrous Alloys and Special-Purpose Materials*, ASM Handbook, ASM International (1990), p. 1099-201
- [40] L. Thijs, M.L. Montero Sistiaga, R. Wauthle, Q. Xie, J.-P. Kruth, J. Van Humbeeck. Strong morphological and crystallographic texture and resulting yield strength anisotropy in selective laser melted tantalum. *Acta Mater.*, 61 (2013), pp. 4657–4668
- [41] L. Mullen, R.C. Stamp, W.K. Brooks, E. Jones, C.J. Sutcliffe. Selective Laser Melting: a regular unit cell approach for the manufacture of porous, titanium, bone in-growth constructs, suitable for orthopedic applications. *J. Biomed. Mater. Res. B Appl. Biomater.*, 89 (2009), pp. 325–334

-
- [42] L. Mullen, R.C. Stamp, P. Fox, E. Jones, C. Ngo, C.J. Sutcliffe. Selective laser melting: a unit cell approach for the manufacture of porous, titanium, bone in-growth constructs, suitable for orthopedic applications. II. Randomized structures. *J. Biomed. Mater. Res. B Appl. Biomater.*, 92 (2010), p. 178-88
- [43] A. Barbas, A.S. Bonnet, P. Lipinski, R. Pesci, G. Dubois. Development and mechanical characterization of porous titanium bone substitutes. *J. Mech. Behav. Biomed. Mater.*, 9 (2012), pp. 34–44
- [44] M. de Wild, R. Schumacher, K. Mayer, E. Schkommodau, D. Thoma, M. Bredell, *et al.*. Bone regeneration by the osteoconductivity of porous titanium implants manufactured by selective laser melting: a histological and micro computed tomography study in the rabbit. *Tissue Eng. A*, 19 (2013), pp. 2645–2654
- [45] P. Lipinski, A. Barbas, A.S. Bonnet. Fatigue behavior of thin-walled grade 2 titanium samples processed by selective laser melting. Application to life prediction of porous titanium implants. *J. Mech. Behav. Biomed. Mater.*, 28 (2013), pp. 274–290
- [46] ISO 13314. Mechanical testing of metals – Ductility testing – Compression test for porous and cellular metals. (2011)
- [47] B. Vrancken, L. Thijs, J.-P. Kruth, J. Van Humbeeck. Heat treatment of Ti6Al4V produced by Selective Laser Melting: Microstructure and mechanical properties. *J. Alloys Compd.*, 541 (2012), pp. 177–185
- [48] H. Attar, M. Calin, L.C. Zhang, S. Scudino, J. Eckert. Manufacture by selective laser melting and mechanical behavior of commercially pure titanium. *Mater. Sci. Eng. A*, 593 (2014), pp. 170–177
- [49] H.-P. Degischer, B. Kriszt. *Handbook of Cellular Metals: Production, Processing, Applications*. Wiley-VCH Verlag GmbH & Co. KGaA (2002)
- [50] L.J. Gibson, M.F. Ashby. *Cellular Solids - Structure and Properties*. Cambridge University Press (1999)

[51] R.O. Ritchie. Mechanisms of fatigue-crack propagation in ductile and brittle solids. *Int. J. Fract.*, 100 (1999), pp. 55–83

[52] K.S. Chan, M. Koike, R.L. Mason, T. Okabe. Fatigue Life of Titanium Alloys Fabricated by Additive Layer Manufacturing Techniques for Dental Implants. *Metall. Mater. Trans. A*, 44 (2012), pp. 1010–1022

[53] S. Leuders, M. Thöne, A. Riemer, T. Niendorf, T. Tröster, H.A. Richard, *et al.*. On the mechanical behaviour of titanium alloy TiAl6V4 manufactured by selective laser melting: Fatigue resistance and crack growth performance. *Int. J. Fatigue*, 48 (2013), pp. 300–307

[54] P. Edwards, M. Ramulu. Fatigue performance evaluation of selective laser melted Ti–6Al–4 V. *Mater. Sci. Eng. A*, 598 (2014), pp. 327–337

[55] R. Wauthle, B. Vrancken, B. Beynaerts, K. Jorissen, J. Schrooten, J.-P. Kruth, *et al.*. Effects of build orientation and heat treatment on the microstructure and mechanical properties of selective laser melted Ti6Al4V lattice structures. *Addit. Manuf.*, 5 (2015), pp. 77–84.

Chapter 4 Additively manufactured open-cell porous biomaterials made from six different space-filling unit cells: the mechanical and morphological properties

This chapter has been published as:

SM Ahmadi, S Amin Yavari, R Wauthle, B Pouran, J Schrooten, H Weinans, AA Zadpoor, *Additively manufactured open-cell porous biomaterials made from six different space-filling unit cells: The mechanical and morphological properties*, *Materials*, 2015. P. 1871-1896.

4.1 Abstract

The mechanical properties of bone-mimicking porous biomaterials are known to be a function of the morphological properties of the porous structure including the type and dimensions of the repeating unit cell from which they are made. This relationship is not studied for many important types of space-filling unit cells in the past, primarily because it was not possible to manufacture porous biomaterials with arbitrarily complex morphological designs. In this study, we studied the relationship between morphological and mechanical properties of additively manufactured porous titanium biomaterials based on six different types of unit cells including cubic (C), diamond (D), truncated cube (TC), truncated cuboctahedron (TCO), rhombic dodecahedron (RD), and rhombicuboctahedron (RCO). Porous structures with different porosities were manufactured using the selective laser melting technique from Ti6Al4V-ELI powder and were mechanically tested in compression. Porous structures based on different types of unit cells exhibited very different mechanical properties and failure mechanisms, but the diamond unit cell consistently showed the lowest mechanical properties. In unit cells with vertical struts, the entire unit cell collapsed at once, causing the force to momentarily drop to near-zero values. The mechanical properties of all porous structures increased with apparent density. The comparative performance of different unit cells was in many cases different for small and large values of apparent density (AD) with a separating AD of 0.15-0.2. The unit cells were divided into a stiff group including TC, TCO, RCO, and C and a compliant group including D and RD. However, truncated cube showed remarkably higher stiffness values than its other group members for $AD > 0.2$. The data provided in this study are important for understanding the mechanical behavior of porous biomaterials made from different types of unit cells and for corroborating analytical and computational models developed for estimation of the mechanical properties of those structures.

4.2 Introduction

In orthopaedic surgery, cellular structures are used as three-dimensional porous biomaterials that try to mimic the structure and function of bone [1]. The porous biomaterial could be used either as a bone substitute or a cell-seeded scaffold used as a part of a tissue engineering approach. In either case, the porous biomaterial should be designed such that its mechanical properties match those of bone, while considering the other factors that maximize bone ingrowth. For example, the permeability of the porous structures used in bone tissue engineering could influence cell migration and mass transport and should be carefully designed [2,3]. During the last two decades, several design principles have been proposed for the design of bone tissue engineering scaffolds that consider the mechanical properties, biocompatibility, biodegradability, and bio-functionality of the scaffold biomaterials [4,5,6,7,8,9].

In this study, we focused on the compressive properties of porous titanium biomaterials aimed for application in orthopaedic surgery. Solid titanium alloys are often very stiff, exceeding the mechanical properties of bone by up to one order of magnitude [10,11]. The mismatch between the mechanical properties of bone and those of the biomaterial could hinder bone ingrowth, result in stress shielding, bone resorption, and ultimately cause loosening of orthopaedic implants [12,13,14,15]. Creating porous structures out of bulk materials, however, results in much lower stiffness values that are comparable with those of bone [10,16,17]. Traditionally, various techniques have been used for fabrication of porous biomaterials including space-holder method, hot isostatic pressing, gel casting, and chemical vapor deposition/infiltration [18,19,20,21]. Recently, additive manufacturing techniques have been introduced for manufacturing of porous biomaterials and have several advantages over conventional techniques including their ability to create arbitrarily complex 3D structures, highly accurate and predictable porous structure, and wide materials selection [22,23,24,25]. Two widely used AM methods are selective laser melting [26,27,28,29,30] and electron beam melting [31,32,33,34]. In addition to favorable mechanical properties, highly porous biomaterials have a large pore space that could be used for controlled release of growth factors [35] as well as huge surface area that could be treated using chemical and electrochemical techniques for obtaining desired bio-functional properties [36,37,38,39].

The mechanical properties of additively manufactured porous biomaterials are highly dependent on the type of unit cell from which they are made [40,41,42,43,44,45]. Optimizing the mechanical properties of porous biomaterials for different applications may require combining various types and dimensions of unit cells in one single porous structure. It is therefore important to have a good understanding of the relationship between the type and dimensions of unit cell and the resulting mechanical properties of the porous structure [46]. Many different types of unit cells are available. However, data on the mechanical properties of porous structures from many different unit cell configurations are limited.

In the present work, we used six different unit cell configurations, namely, cubic, diamond, truncated cube, truncated cuboctahedron, rhombic dodecahedron, and rhombicuboctahedron are considered in the current study. For each of these configurations, we used selective laser melting to manufacture porous structures with different porosities. Micro-CT imaging and compression testing were performed to determine the morphological and mechanical properties of the porous materials and to study the relationship between these parameters.

4.3 Materials and methods

4.3.1 Materials and manufacturing

Selective laser melting (SLM) method (Layerwise NV, Leuven, Belgium) was used for processing of Ti6Al4V-ELI powder (according to ASTM B348, grade 23) on top of a solid titanium substrate and in an inert atmosphere. Porous titanium structures were thereby manufactured based on six different unit cells configurations, namely, cubic, diamond, truncated cube, rhombicuboctahedron, rhombic dodecahedron, and truncated cuboctahedron (Figure 4-1). The details of the laser process technique were reported in our previous studies [10,16,40,47,48]. For each unit cell, different porosities were achieved by changing the strut thickness and pore size (Table 1). Cylindrical specimens with the length of 15 mm, diameter of 10 mm and unit cell size of 1.5 mm were manufactured for static compression testing (Figure 4-2). After fabrication, electro discharge machining (EDM) was used to remove the specimens from the substrate.

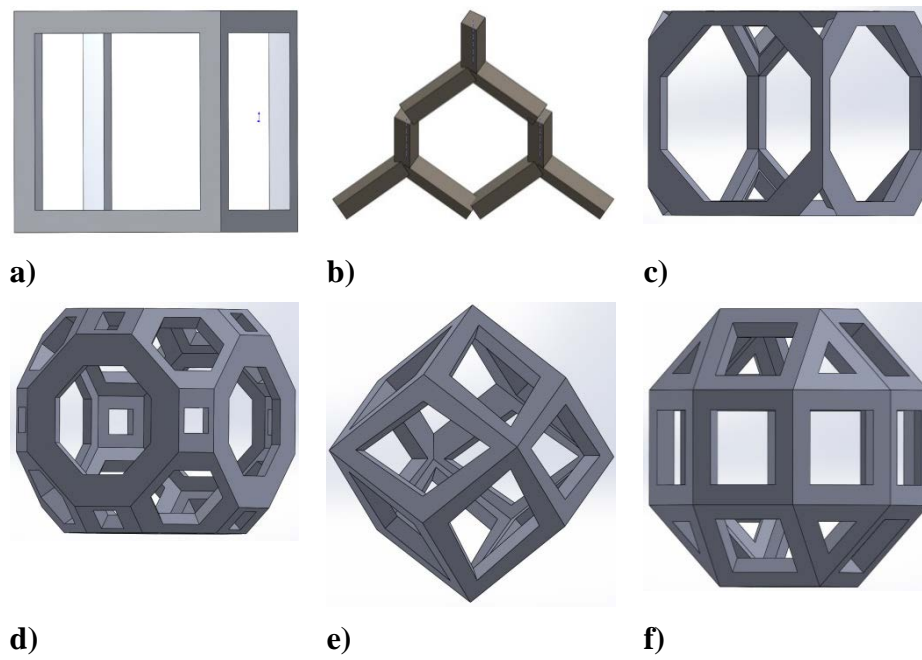


Figure 4-1. Schematic drawings of the unit cells used in the porous structure: (a) Cubic; (b) Diamond; (c) Truncated cube; (d) Truncated cuboctahedron; (e) Rhombic dodecahedron; (f) Rhombicuboctahedron.

Table 4-1. Morphological properties of the porous structures used.

	Strut diameter		Pore size	
	(μm)		(μm)	
	Nominal	$\mu\text{CT}(\text{SD})$	Nominal	$\mu\text{CT}(\text{SD})$
Cubic (C)				
C-1	348	451(147)	1452	1413(366)
C-2	540	654(190)	1260	1139(359)
C-3	612	693(200)	1188	1155(354)
C-4	720	823(230)	1080	1020(311)
Diamond (D)				
D-1	277	240(46)	923	958(144)
D-2	450	416(65)	750	780(141)
D-3	520	482(70)	680	719(130)
D-4	600	564(76)	600	641(137)
Truncated cube (TC)				
TC-1	180	331(76)	1720	1625(398)
TC-2	240	363(80)	1660	1615(392)
TC-3	304	395(88)	1596	1593(382)
TC-4	380	463(126)	1520	1535(370)
TC-5	460	568(183)	1440	1497(360)
TC-6	530	620(200)	1370	1426(357)
Truncated cubeoctahedron (TCO)				
TCO-1	324	350(60)	876	862(349)
TCO-2	460	416(64)	1040	1142(383)
TCO-3	520	452(65)	980	1098(386)
TCO-4	577	482(70)	923	1079(391)
TCO-5	621	516(82)	862	1065(361)
TCO-6	693	564(76)	807	1049(383)
Rhombicdodecahedron (RD)				
RD-1	250	246(53)	1250	1299(449)
RD-2	310	305(97)	1190	1224(455)
RD-3	370	440(126)	1130	1168(364)
RD-4	430	461(163)	1070	1305(554)
RD-5	490	430(122)	1010	920(300)

RD-6	550	506(144)	950	1058(356)
Rhombic cubeoctahedron (RCO)				
RCO-1	380	348(59)	820	877(355)
RCO-2	410	369(59)	790	847(349)
RCO-3	440	486(113)	760	1089(402)
RCO-4	470	437(61)	730	754(359)
RCO-5	500	539(120)	700	1043(401)
RCO-6	530	438(61)	670	794(368)

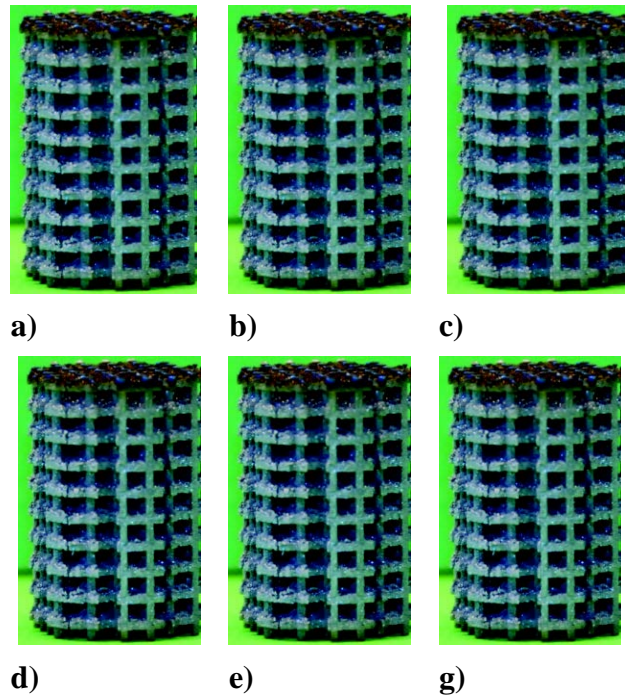


Figure 4-2. Sample specimens from the porous structures based on different types of unit cells: (a) Cubic; (b) Diamond; (c) Truncated cube; (d) Truncated cuboctahedron; (e) Rhombic dodecahedron; (f) Rhombicuboctahedron.

4.3.2 Morphological characterization

For morphological characterization, we scanned the titanium scaffolds using a micro-CT (Quantum FX, Perkin Elmer, Waltham, MA, USA). The scans were made under tube voltage of 90 kV, tube current of 180 μ A, scan time of 3 min, and resolution of 42 μ m. The 3D images of the porous

structures were automatically reconstructed using the in-built software of the micro-CT. The reconstructed images were then transferred to the Caliper Analyze 11.0 (provided by the manufacturer) to align the geometry along the major axis of the specimens and to acquire 2D slices. The 2D slices contained transverse views of the scaffolds, i.e., circular cross-sections. The 2D slices were then imported into the ImageJ 1.47v (<http://imagej.nih.gov/ij/>) in order to create region of interests (ROIs) and segment the titanium volume using the optimal thresholding algorithm available in the boneJ [49] plugin of ImageJ 1.47v (16 bit images). Segmented images were then exported to the boneJ plugin to calculate the ratio of the void volume to the 3D ROI volume that was ultimately reported as the structure relative density of the porous structures.

In addition, the Archimedes technique and dry weighing were used for determining the structure relative density of the specimens (Table 2) using five specimens from each porous type of porous structure, except for the case of rhombic dodecahedron unit cells that only 2 samples were used for measurement of the Archimedes porosity values. In both cases, an OHAUS Pioneer balance was used for weight measurements that were performed in normal atmospheric conditions in room temperature. As for the dry weighing, the weight of the porous specimens was divided by the theoretical weight of the corresponding solid specimens assuming a theoretical density of 4.42 g/cm³ for Ti6Al4V-ELI [50]. In the Archimedes technique, the specimens were weighed both in dry conditions and in pure ethanol to determine the actual and macro volume and calculating overall porosity of the porous structures.

4.3.3 Mechanical testing

The mechanical properties of the porous structures were obtained by static compression test using a static test machine (INSTRON 5985, 100 kN load cell) by applying a constant deformation rate of 1.8 mm/min. The compression test was carried out in accordance with ISO standard 13314:2011 [51] which refers to mechanical testing of porous and cellular metals. The tests were continued until 60% strain was applied to the specimens. Five specimens were tested for every variation of the porous structures. The stress-strain curves were obtained and the mean and standard deviation of each of five compressive properties were determined. According to the above-mentioned standard, the elastic gradient ($E_{\sigma 20-70}$) was calculated as the gradient of the elastic straight line between two

stress values, namely σ_{70} and σ_{20} . The first maximum compressive strength (σ_{max}) that corresponds to the first local maximum in the stress-strain curve was also calculated. The plateau stress (σ_y) was defined according to the same standard as the arithmetical mean of the stresses between 20% and 40% compressive strain and was calculated for all specimens. [40,51]. Energy absorption, which is defined as the energy required for deforming a specimen to a strain (ϵ), was calculated from the area under the strain-stress curve up to 50% strain [52,53].

In order to analyze the compressive properties of porous structures more systematically, power laws relating structure relative density (the weight per unit volume of a material, including voids that exist in the tested material" as defined in ASTM D1895) to different compressive properties were fitted to the measured experimental data:

$$X = a\rho^b$$

(1)

Where X is any of the above-mentioned mechanical properties measured for the porous structures and ρ is apparent density. The parameters a and b are dependent on the type of the unit cell.

Correlational analysis

MATLAB and Simulink R2014a, The MathWorks Inc., Natick, MA, USA, and Microsoft Excel, Microsoft Corporation, Redmond, WA, USA, were used to determine the correlation between the compressive properties of specimens and relevant density. Closeness of the data to the fitted regression line was measured by coefficient of determination.

4.4 Results

The structure relative density of each unit cell configuration is presented in Table 2. The trends observed in the stress strain curves of the specimens with different types of unit cells were quite different (Figure 4-3 to 4-8). There were also differences in the shape of stress-strain curves of specimens with the same type of unit cell configuration but different relative density (RD) (Figure 3-8). In many cases, the typical stress-strain response of porous alloy was observed including the initial linear response that was followed by a plateau region and the subsequent fluctuations of the stress-

strain curve (Figure 4-3 to 4-8). The final part of the stress-strain curves was often associated with stiffening of the porous structure (Figure 4-3 to 4-8). In general, the level of fluctuations following the plateau region tended to decrease as the structure relative density of the porous structures increased (Figure 4-3 to 4-8). However, this was not the case for porous structures based on the truncated cube unit cell (Figure 4-8).

Table 4-2. Summary of the structure relative density results (in %).

	Apparent density (%)			
	Nominal	Dry weighing(SD)	Archimedes(SD)	μ CT
Cubic (C)				
C-1	10	11(0.1)	12(0.1)	13
C-2	22	21(0.2)	22(0.2)	24
C-3	27	26(0.2)	26(0.2)	28
C-4	35	34(0.1)	34(0.2)	37
Diamond (D)				
D-1	11	11(0.1)	11(0.2)	11
D-2	21	20(0.2)	21(0.1)	21
D-3	28	26(0.4)	27(0.3)	28
D-4	37	34(0.3)	35(0.4)	36
Truncated cube (TC)				
TC-1	6	7(0.1)	7(0.1)	9
TC-2	9	9(0.1)	9(0.1)	11
TC-3	12	12(0.1)	12(0.1)	12
TC-4	16	14(0.2)	15(0.2)	14
TC-5	21	17(0.2)	18(0.1)	17
TC-6	24	20(0.2)	20(0.2)	20
Truncated cubeoctahedron (TCO)				
TCO-1	18	20(0.4)	20(0.4)	19
TCO-2	21	23(0.2)	23(0.2)	21
TCO-3	26	25(0.5)	25(0.5)	23
TCO-4	31	28(0.2)	28(0.3)	28
TCO-5	34	31(0.3)	31(0.3)	32

TCO-6	36	34(0.2)	35(0.3)	36
<hr/>				
Rhombicdodecahedron (RD)				
RD-1	10	11(0.3)	11(0.4)	11
RD-2	15	17(0.2)	17(0.1)	16
RD-3	20	23(0.2)	23(0.1)	22
RD-4	25	27(0.1)	27(0.2)	27
RD-5	29	28(0.3)	28(0.3)	28
RD-6	34	33(0.3)	33(0.2)	32
<hr/>				
Rhombic cubeoctahedron (RCO)				
RCO-1	16	18(0.2)	18(0.2)	18
RCO-2	18	21(0.2)	21(0.2)	21
RCO-3	21	23(0.3)	23(0.3)	24
RCO-4	26	25(0.3)	26(0.4)	25
RCO-5	31	29(0.4)	29(0.4)	27
RCO-6	36	32(0.3)	33(0.5)	31

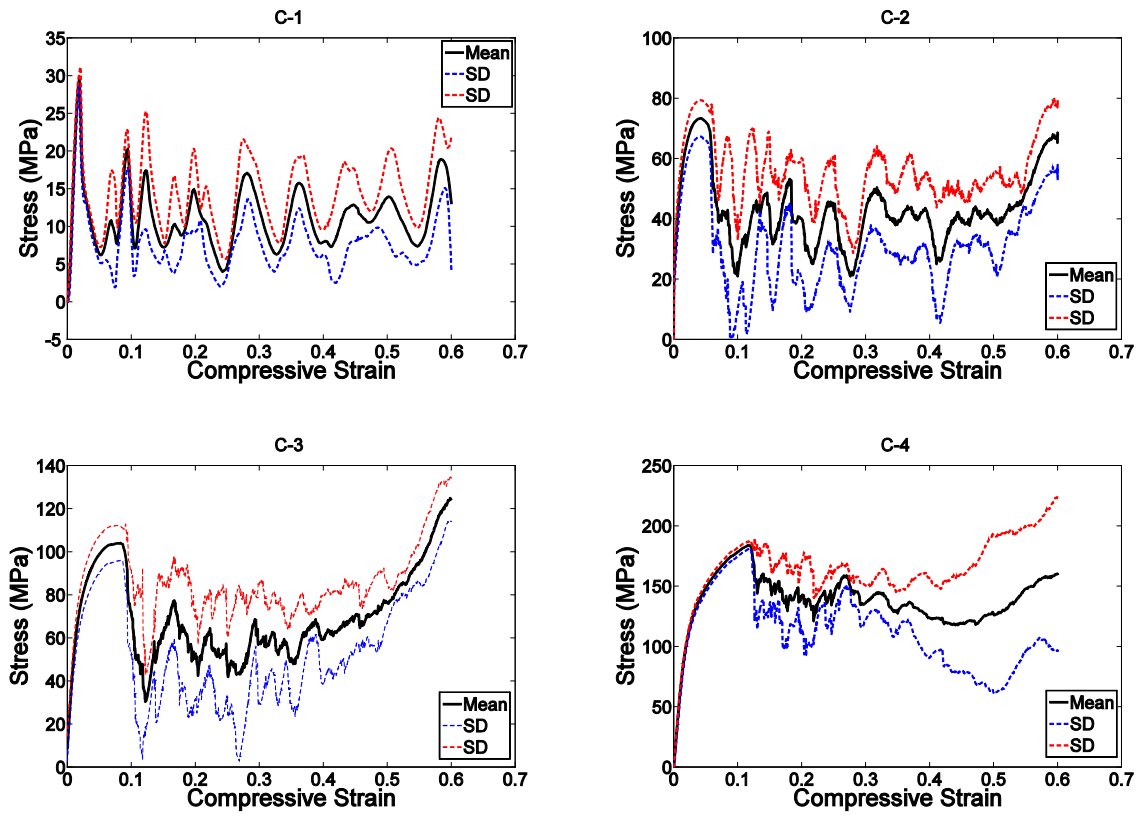


Figure 4-3. Compressive stress-versus-compressive strain curves for specimens based on the cube unit cell and with different porosities (see Table 2).

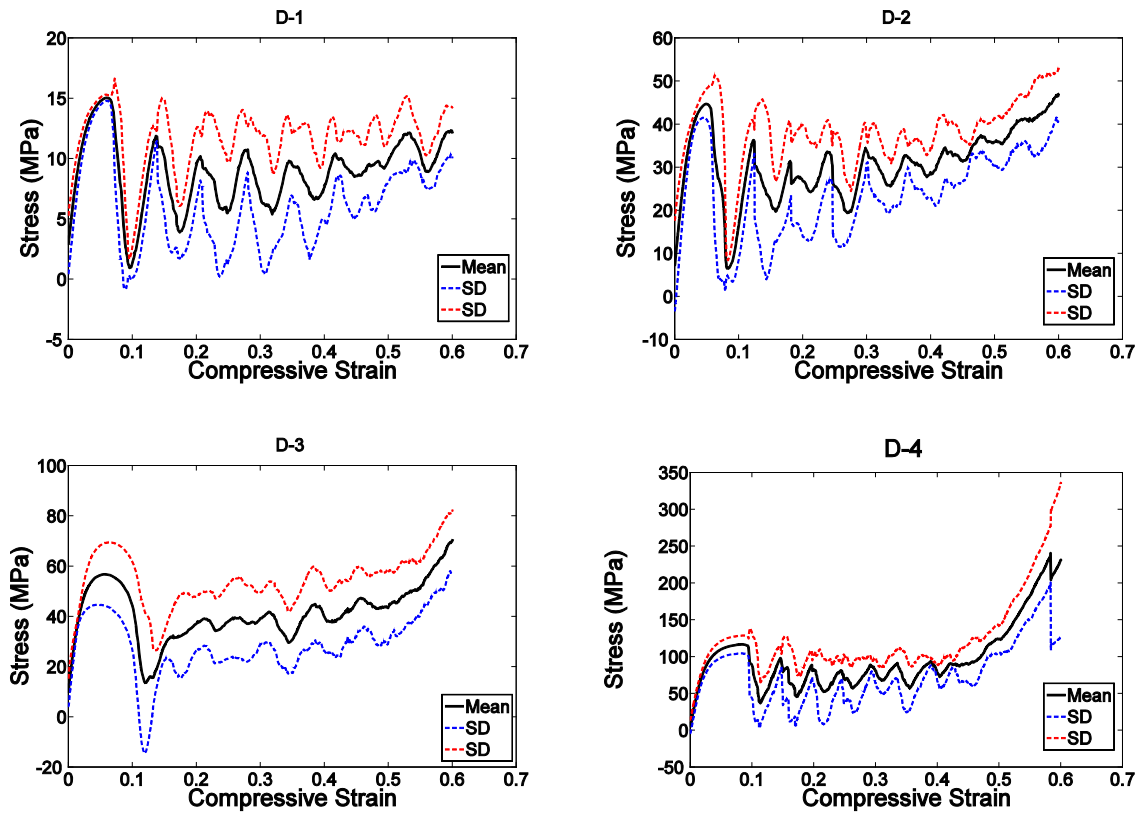


Figure 4-4. Stress-strain curves for specimens based on the diamond unit cell and with different porosities (see Table 2).

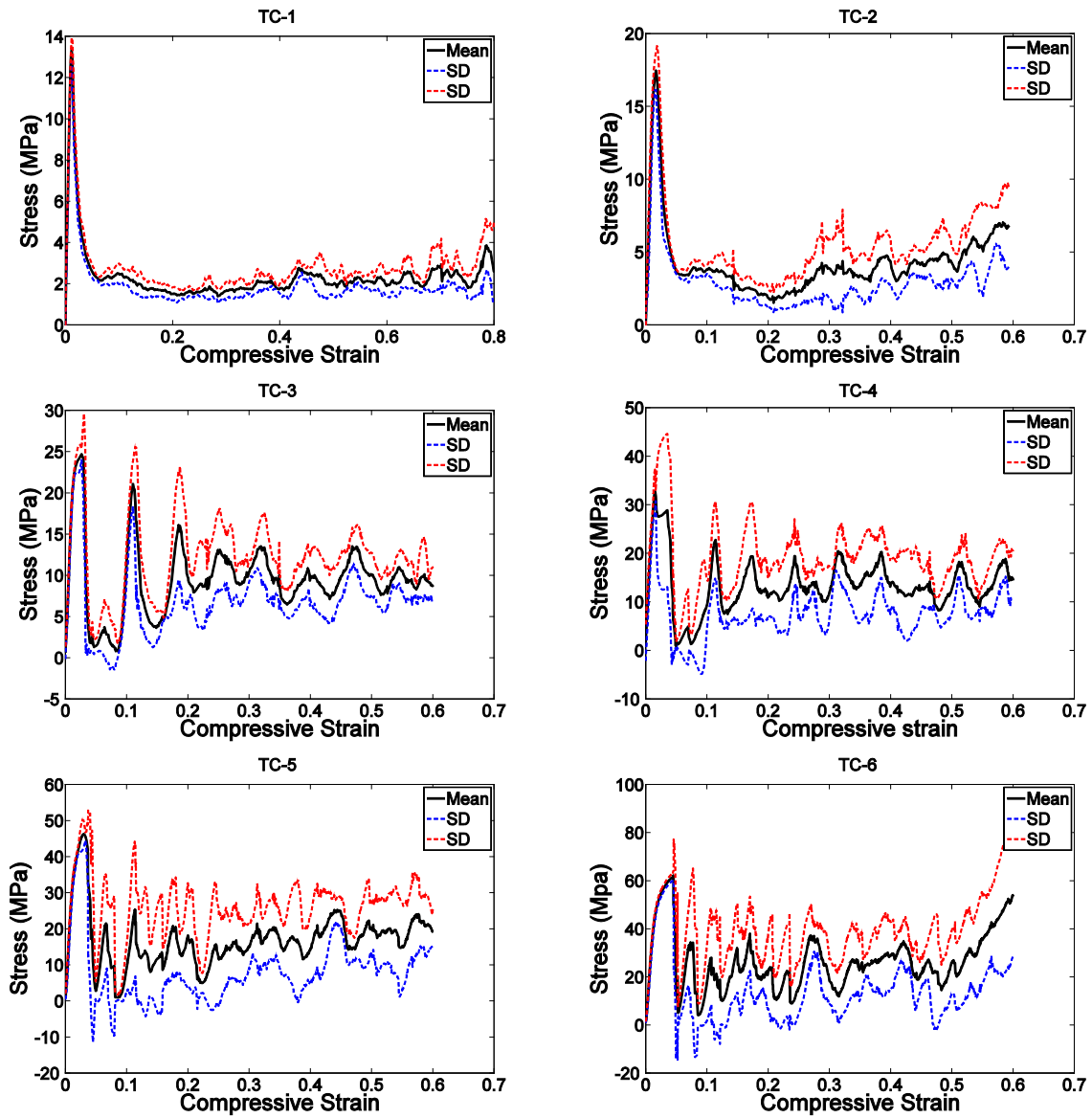


Figure 4-5. Compressive stress-versus-compressive strain curves for specimens based on the truncated cube unit cell and with different porosities (see Table 2).

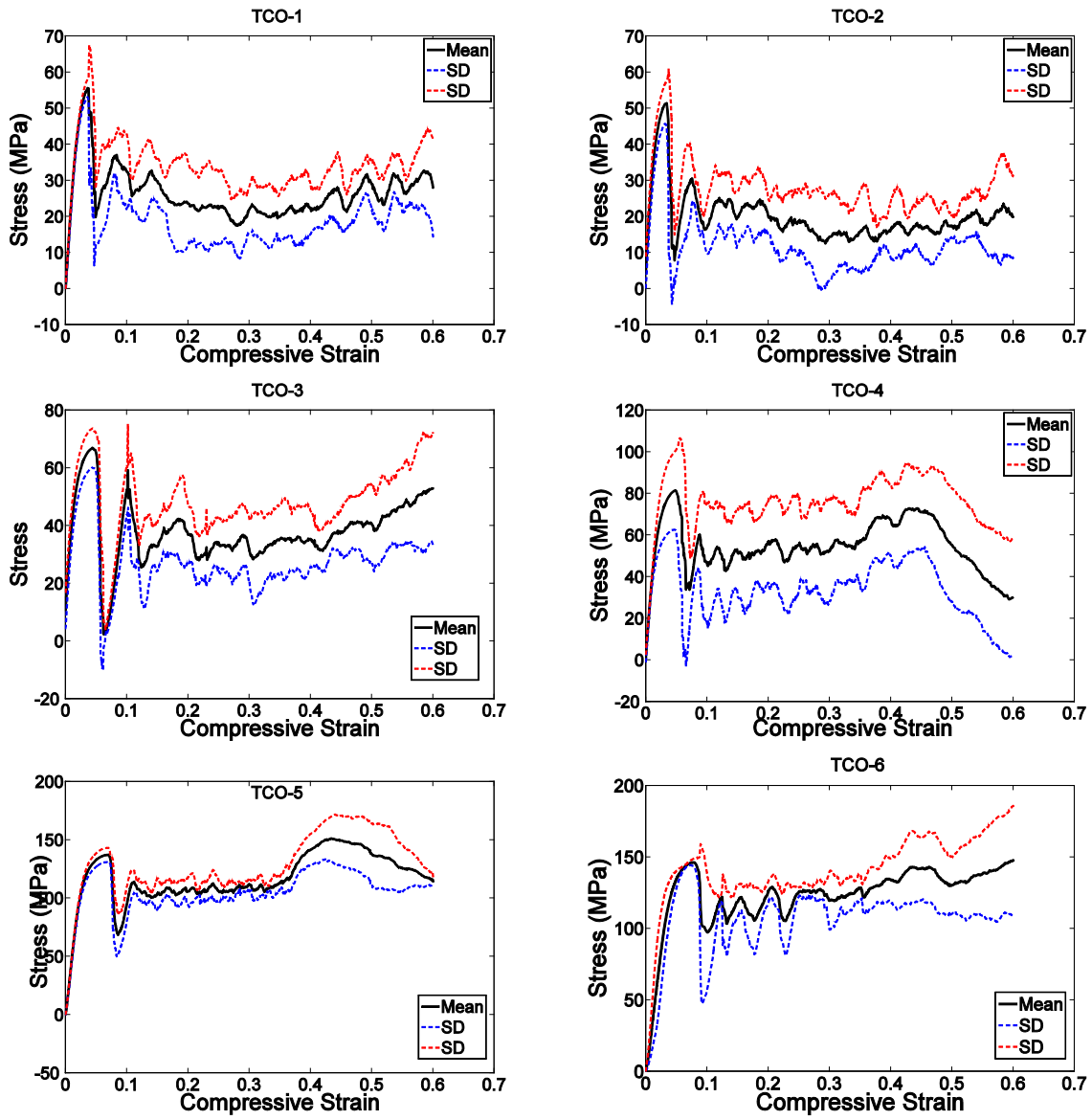


Figure 4-6. Compressive stress-versus-compressive strain curves for specimens based on the truncated cuboctahedron unit cell and with different porosities (see Table 2)

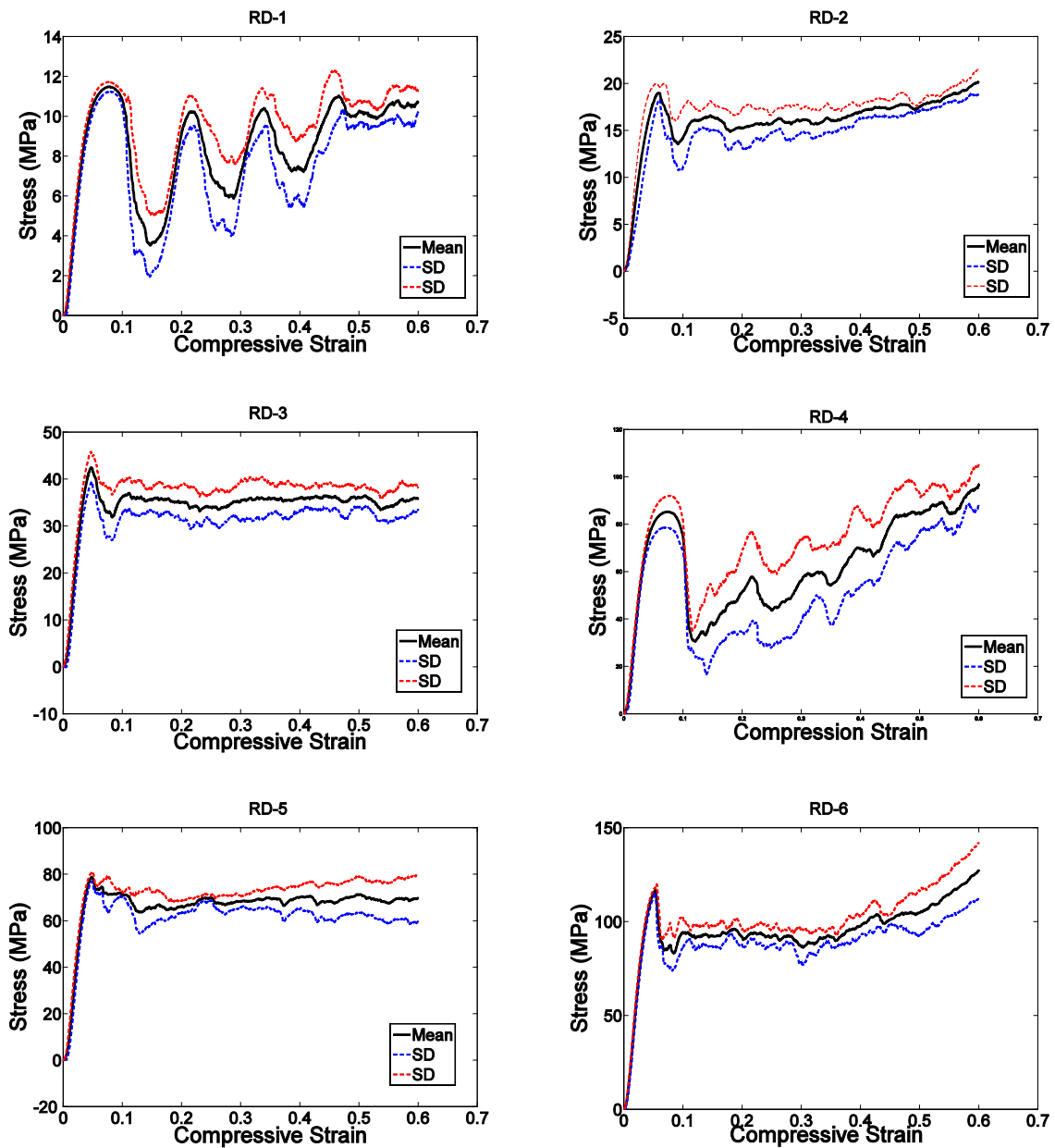


Figure 4-7. Compressive stress-versus-compressive strain for specimens based on the rhombic dodecahedron unit cell and with different porosities (see Table 2).

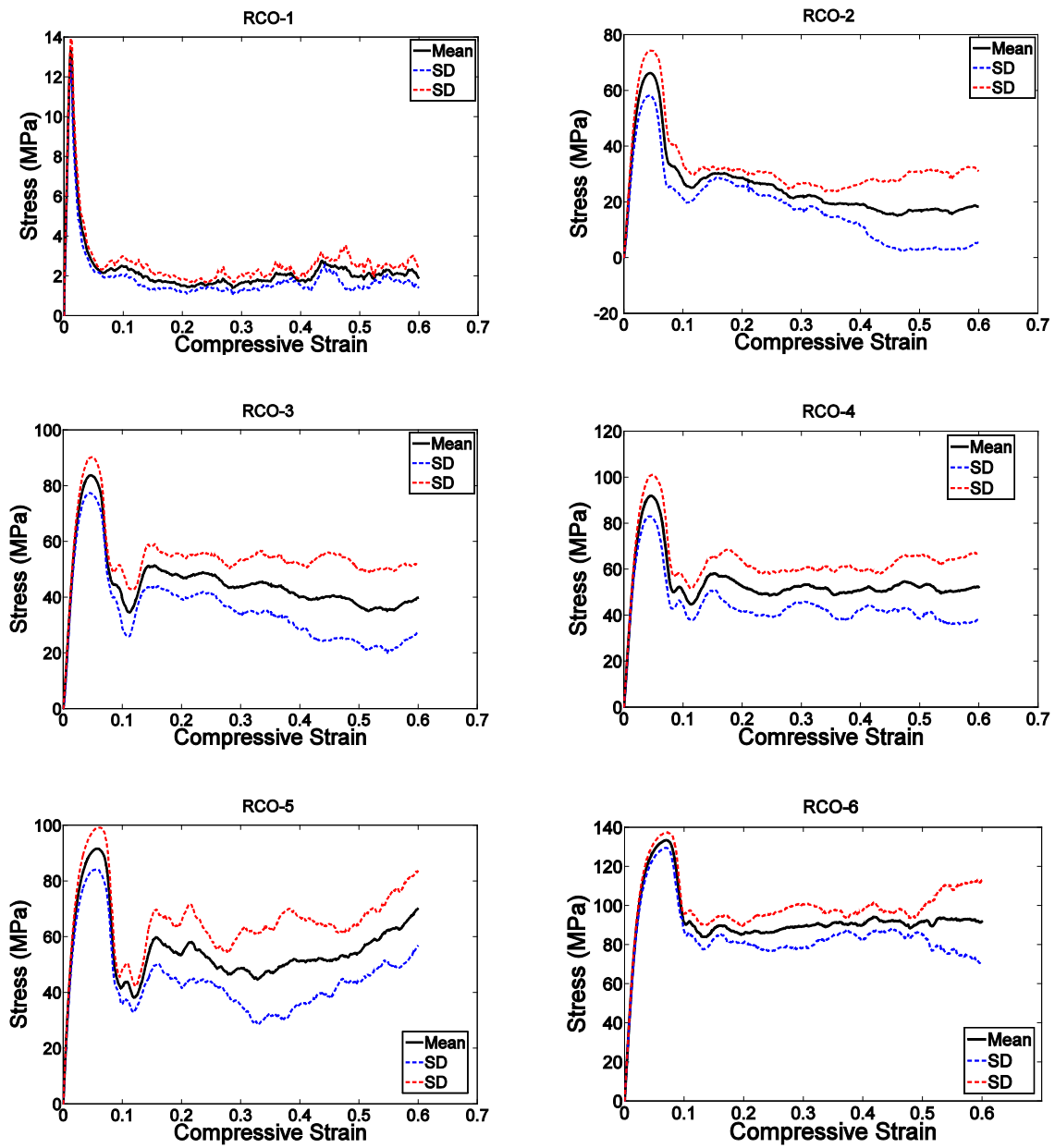


Figure 4-8. Compressive stress-versus-compressive strain curves for specimens based on the rhombicuboctahedron unit cell and with different porosities (see Table 2).

As expected, each of the compressive properties increased with increase in structure relative density (Figure 4-9 to 4-13). The exponent of the power law fitted to the experimental data points (Figure 4-9 to 4-13) varied between 0.93 and 2.34 for the elastic gradient (Figure 9), between 1.28 and 2.15 for the first maximum stress (Figure 4-10), between 1.75 and 3.5 for the plateau stress (Figure 4-11), between 1.21 and 2.31 for the yield stress (Figure 4-12), and between 2.18 and 73 for energy absorption (Figure 4-13).

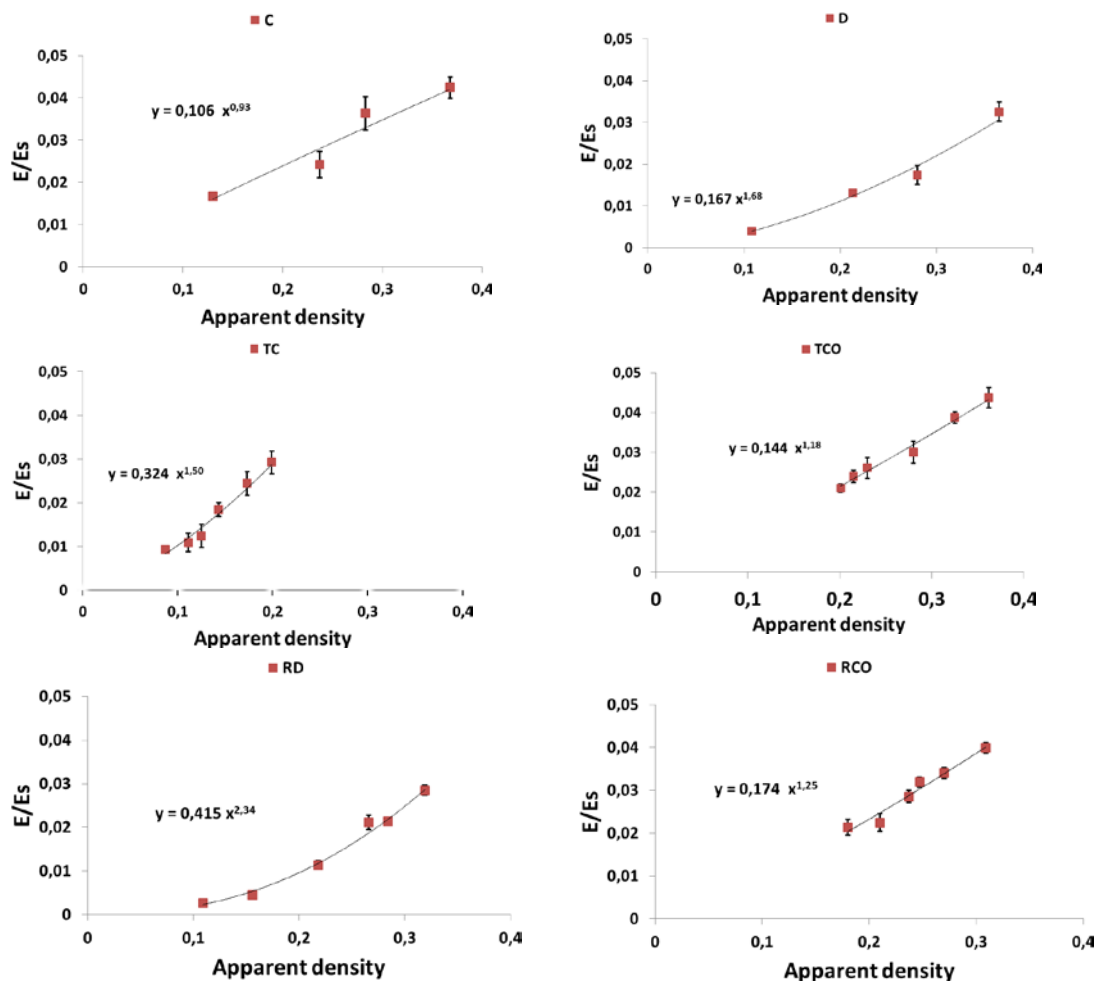


Figure 4-9. Summary of the elastic gradient results for porous structures based on different types of unit cell configurations (cubic (C); diamond (D); truncated cube (TC); truncated cuboctahedron (TCO); rhombic dodecahedron (RD); rhombicuboctahedron (RCO)) and different structure relative densities (see Table 2) (E_s indicates the elastic gradient of the structure if it was solid).

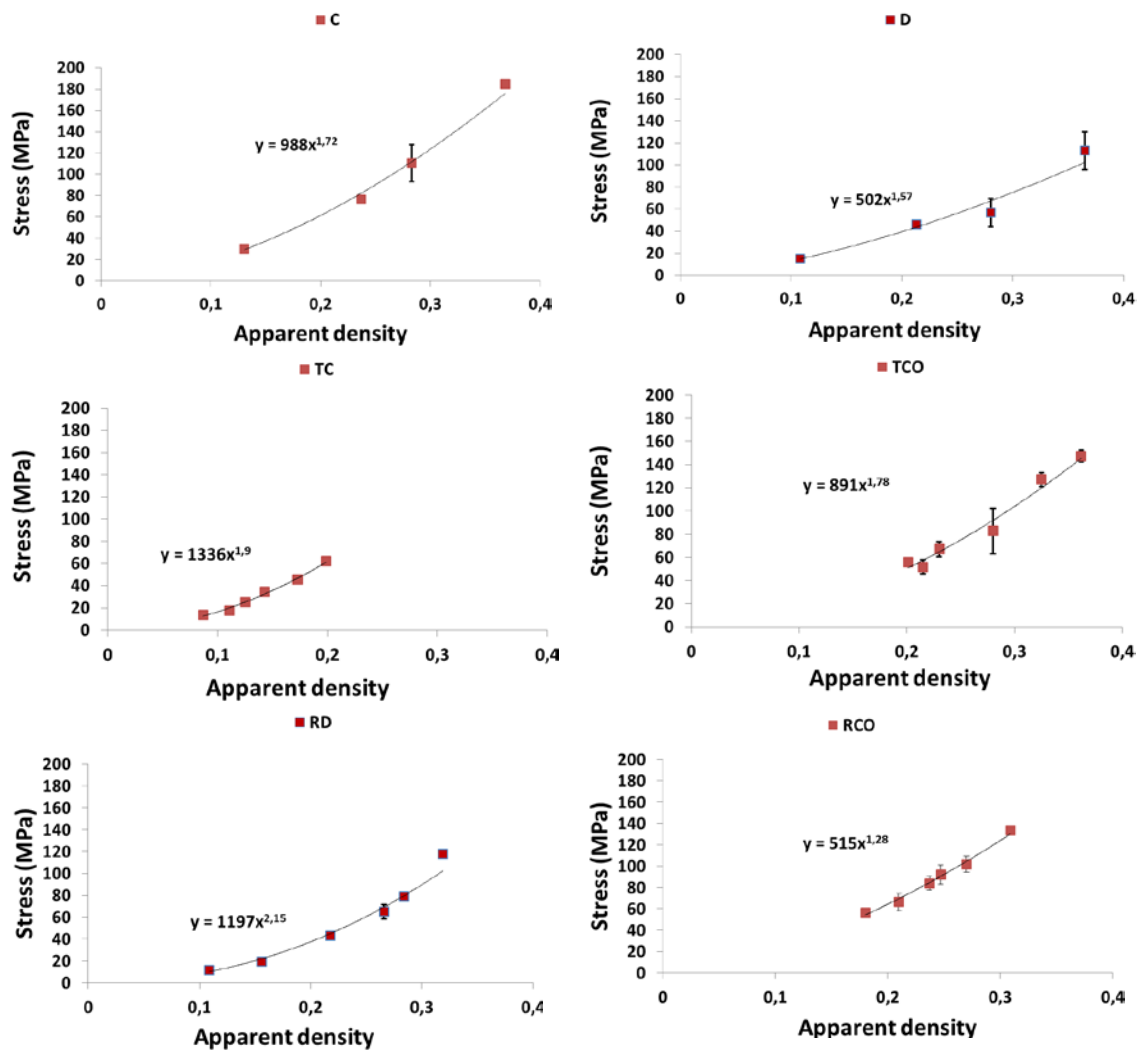


Figure 4-10. Summary of the first maximum stress results for porous structures based on different types of unit cell configurations (cubic (C); diamond (D); truncated cube (TC); truncated cuboctahedron (TCO); rhombic dodecahedron (RD); rhombicuboctahedron (RCO)) and different structure relative densities (see Table 2).

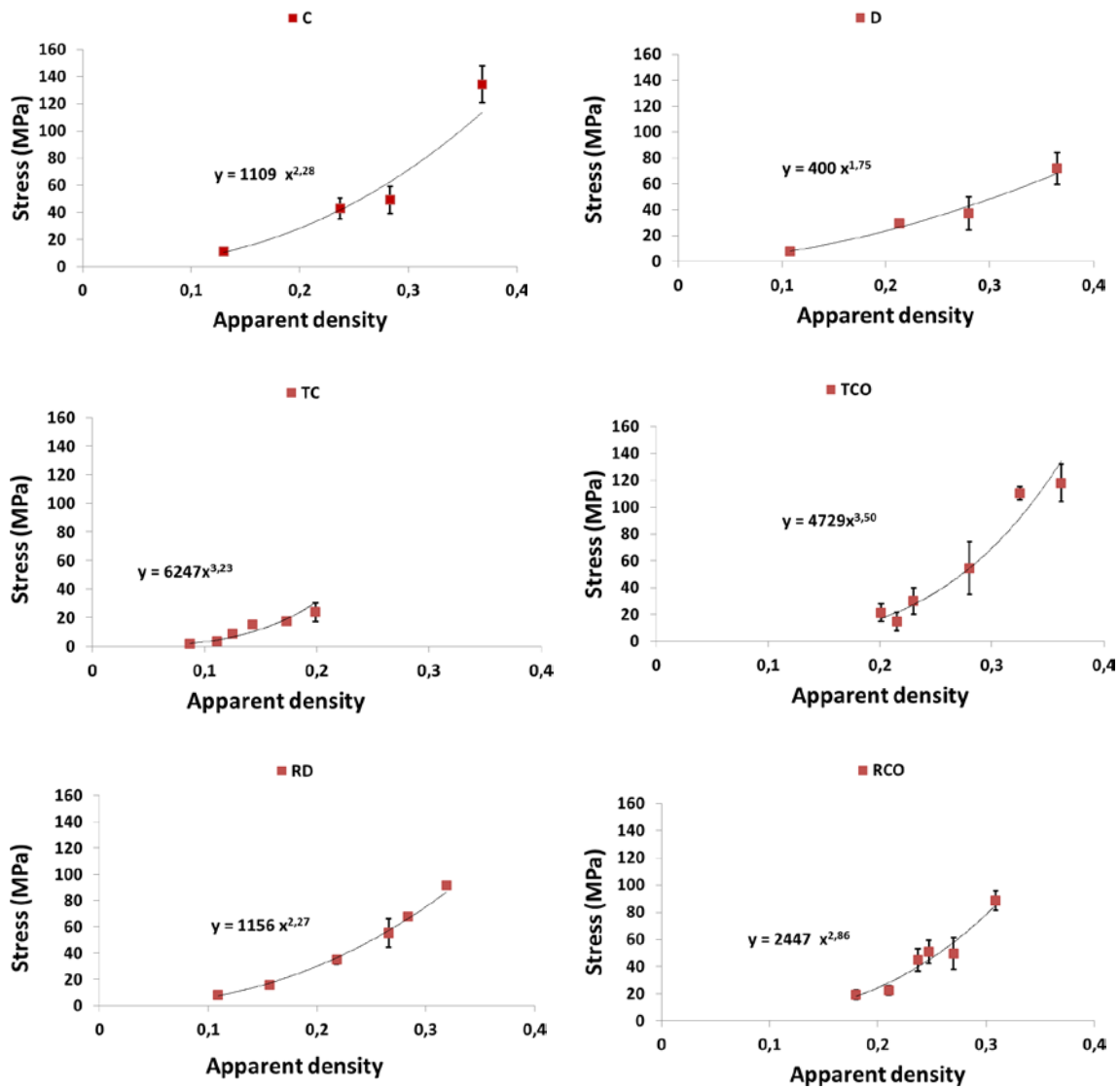


Figure 4-11. Summary of the plateau stress results for porous structures based on different types of unit cell configurations (cubic (C); diamond (D); truncated cube (TC); truncated cuboctahedron (TCO); rhombic dodecahedron (RD); rhombicuboctahedron (RCO)) and different structure relative densities (see Table 2).

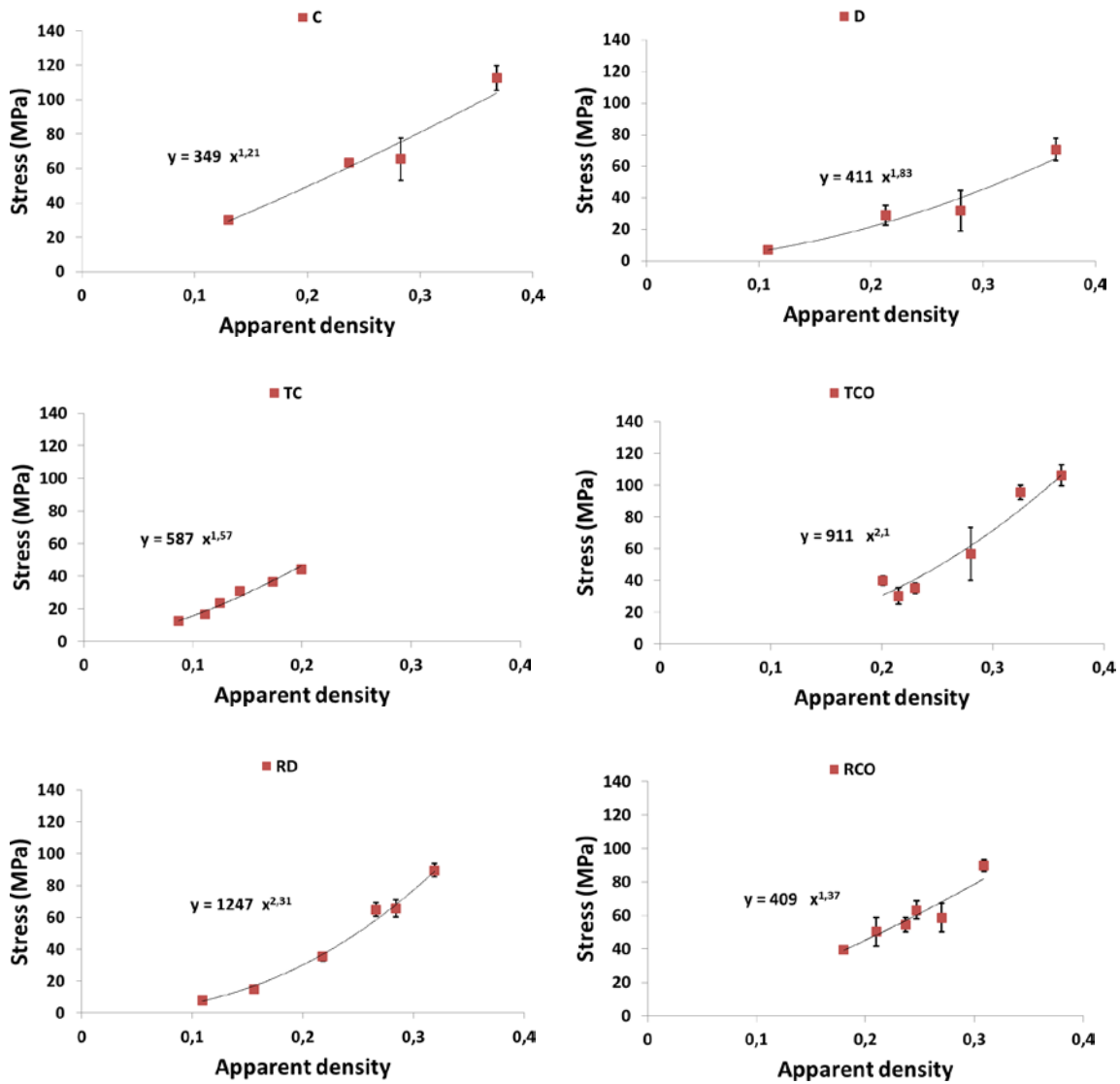


Figure 4-12. Summary of the yield stress results for porous structures based on different types of unit cell configurations (cubic (C); diamond (D); truncated cube (TC); truncated cuboctahedron (TCO); rhombic dodecahedron (RD); rhombicuboctahedron (RCO)) and different structure relative densities (see Table 2).

Among all the unit cells studied here, the structure with the diamond unit cell was the most compliant, especially at $RD > 0.15$, whereas the stiffest structure was that having a truncated cube unit cell, especially when $RD > 0.30$ (Figure 9). When RD was small ($RD < 0.2$) the structures may be divided into two groups, with those in the first group (truncated cube, truncated cuboctahedron, rhombicuboctahedron, and cube unit cells) having larger stiffness than those in the second group (diamond and rhombic dodecahedron unit cells) (Figure 4- 9 and Figure 4-14a).

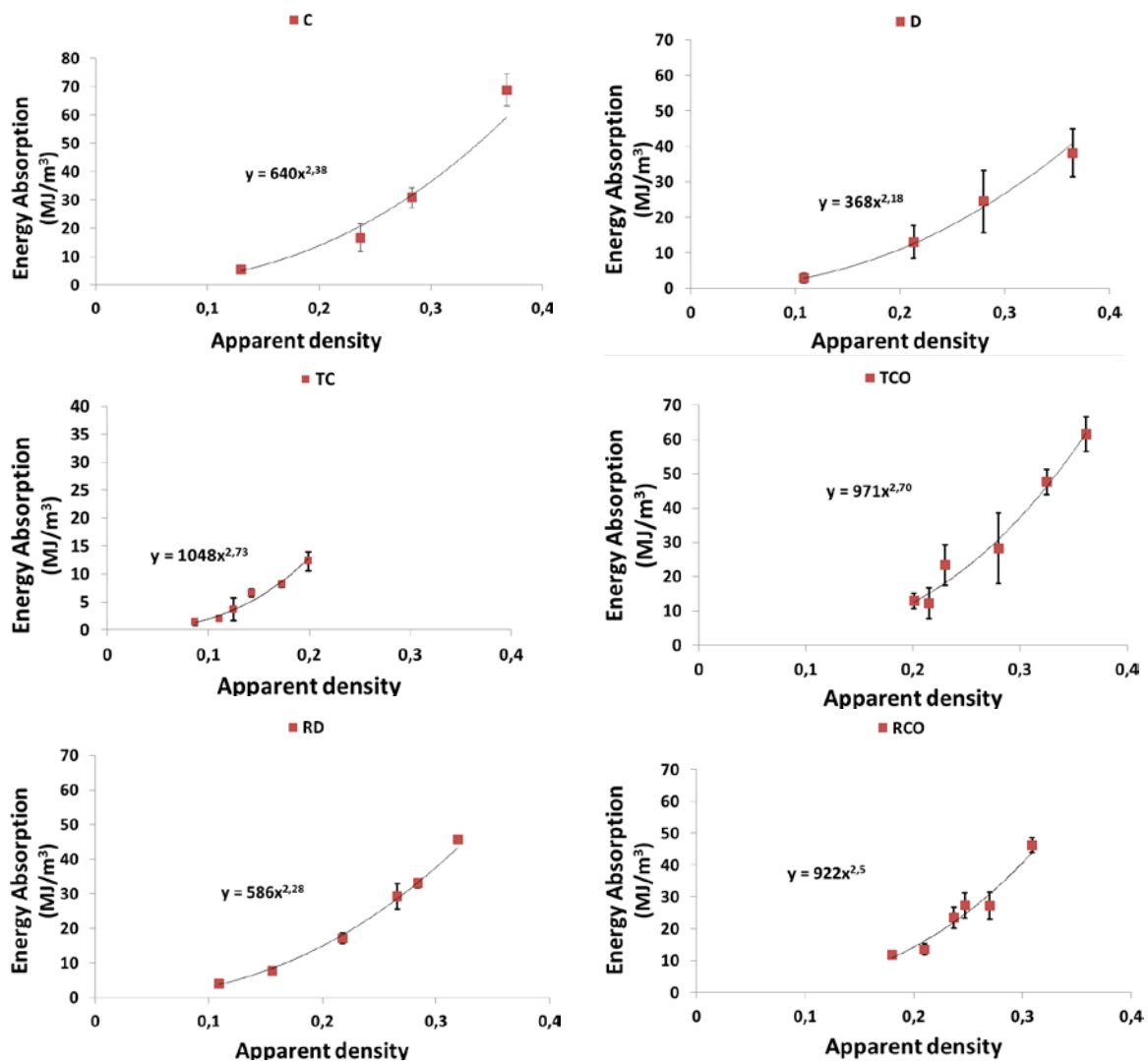


Figure 4-13. Summary of the energy absorption results for porous structures based on different types of unit cell configurations (cubic (C); diamond (D); truncated cube (TC); truncated cuboctahedron (TCO); rhombic dodecahedron (RD); rhombicuboctahedron (RCO)) and different structure relative densities (see Table 2).

With regard to σ_{max} , there is also separation of the structures into two groups. When $RD < 0.2$, the structures with the highest and lowest value of this compressive property were built using rhombicuboctahedron and rhombic dodecahedron unit cells, respectively (Figure 4-10). However, when $RD > 0.2$, the structures with the highest and lowest value of this compressive property were built using the truncated cube and diamond unit cells, respectively (Figure 4-10 and Figure 4-14b). When $RD < 0.2$, there is no difference in plateau stress between the different structures, but, when $RD > 0.2$, the highest and lowest value of this compressive property were built using the truncated cube and diamond unit cells, respectively (Figure 4-11 and Figure 4-14c). The four remaining unit cells are relatively close in terms of the plateau stress values they exhibit (Figure 4-11 and Figure 4-14c).

Regarding σ_y , structures with the diamond unit cell show the lowest value throughout the RD range (Figure 4-12 and Figure 4-14d). The one group comprising structures having the truncated cube rhombicuboctahedron, and cube and cube and the other group comprising structures having truncated cuboctahedron and rhombic dodecahedron, When $RD < 0.2$, the former group has clearly higher yield stress values as compared to the latter group, but, when $RD > 0.2$, the results for the two groups overlapped (Figure 4-12 and Figure 4-14d). When $RD < 0.2$, Energy absorption (EA) for the structures with different unit cell configurations are practically the same, but, at higher RD, EA of structure with diamond unit cell is much lower than that of a structure with any other type of unit cell configuration (Figure 4-13 and Figure 4-14e).

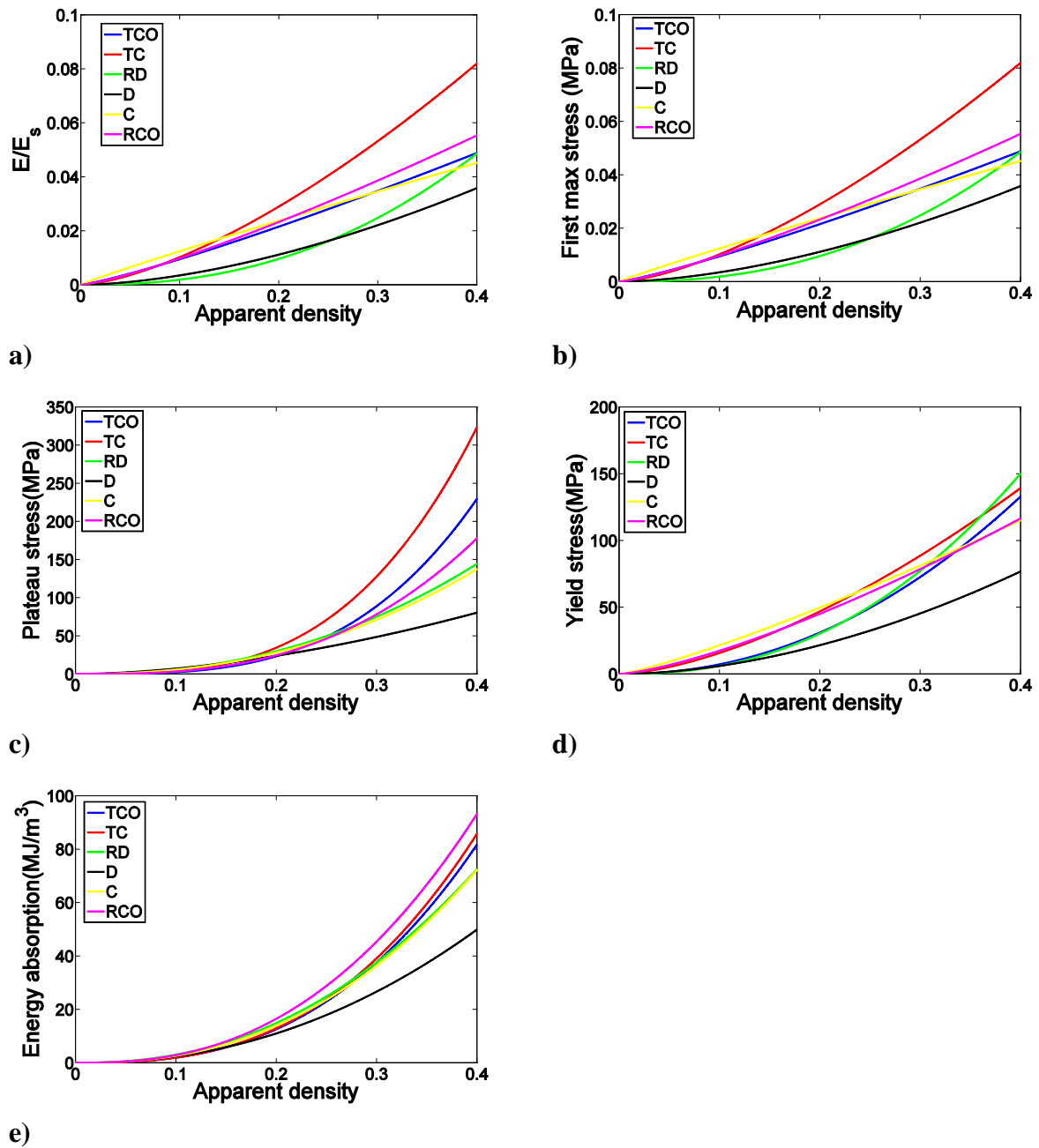


Figure 4-14. Comparison between the mechanical properties measured for different types of porous structures based on the six different unit cells studied here including (a) Elastic gradient; (b) First maximum stress. (c) Plateau stress; (d) Yield stress; (e) Energy absorption. In these figures, the power laws fitted to the experimental data points, and not the experimental data points themselves, are compared with each other.

The ratio of plateau stress to yield stress was more or less constant and close to one for the diamond and rhombic dodecahedron unit cells (Figure 4-15a). For the other types of unit cells, the ratio of

plateau stress to yield stress remarkably increased with the relative density (Figure 4-15a). As for the ratio of plateau stress to first maximum stress, it was relatively stable for diamond, rhombic dodecahedron, and rhombicuboctahedron (Figure 4-15b). For the three remaining types of unit cells, the ratio of plateau stress to first maximum stress drastically increased with the relative density (Figure 4-15b).

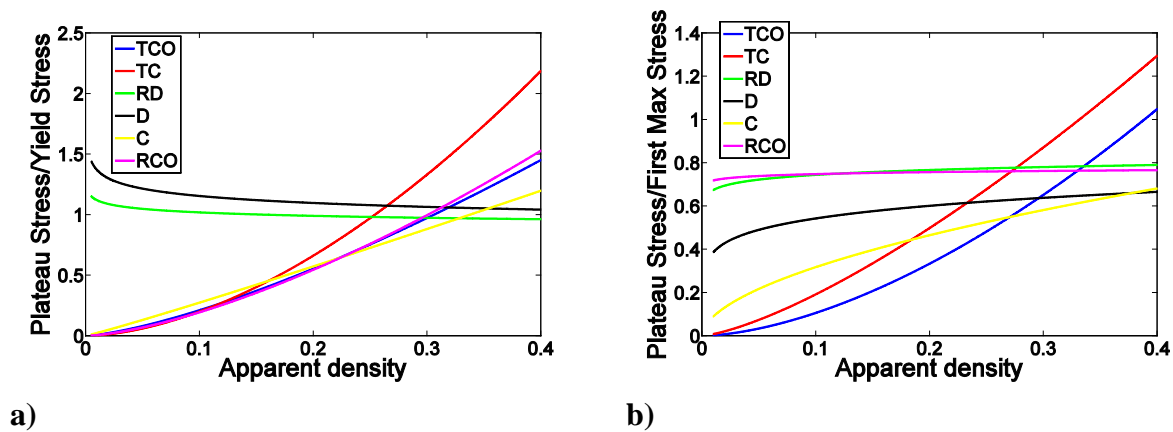


Figure 4-15. (a) The ratio of plateau stress to yield stress as well as (b) the ratio of plateau stress to first maximum stress for different types of unit cells. In these figures, the power laws fitted to the experimental data points, and not the experimental data points themselves, are compared with each other.

4.5 Discussion

The results of this study clearly show the difference between the porous structures made using different types of unit cells. Not only do the mechanical properties of the porous structures differ drastically between the various unit cells studied here, the deformation and failure mechanisms change as well particularly at the plateau region as well as in the succeeding regions of the stress-strain curves. These different failure mechanisms are reflected in the different shapes of stress-strain curves.

4.5.1 Comparison between the Different Types of Unit Cells

Since all other parameters are kept constant during the manufacturing of the specimens, the only factor that differentiates the different classes of porous structures from each other is the geometry

of unit cell. For example, it was observed that the unit cells that include vertical struts, exhibit a different failure mechanism as compared to the other unit cells. In the unit cells with vertical struts, failure of one (vertical) strut usually resulted in the collapse of the entire unit cell, causing a sudden drop of the measured force to values close to zero. Once one-unit cell, that is often the weakest link in the remaining porous structure, has collapsed, the other unit cells take over the force-carrying function of the missing unit cell and the force increases again. This will continue until the next weakest link in the remaining porous structure has collapsed and the force drops to near-zero values again. The presence of vertical struts could not, however, explain all the cases where force repeatedly dropped to near-zero values. An important exception was the diamond unit cell. In this unit cell, the geometry of the unit cell is such that the failure of one strut could easily cause the collapse of the entire unit cell, as the shape of the unit cell is relatively simple and the different struts provide only limited support to each other. This could be also found back in all of the compressive properties measured for the diamond unit cell. Comparatively speaking, the diamond unit cell showed the lowest values of the compressive properties for the entire range of apparent densities. There are only two exceptions, elastic gradient and first maximum stress, where rhombic dodecahedron shows slightly lower compressive properties for the lowest values of the structure relative density.

The stiffness of the porous structures made from different types of unit cells is probably the most important property of these structures when they are used as bone-mimicking biomaterials. The elastic gradient is the best indicator of the stiffness of the porous structure, among all the compressive properties presented here. For small apparent densities, i.e., < 0.15 , one could speak of two groups of unit cells, namely strong unit cells and weak unit cells. The strong unit cells group includes truncated cube, truncated cuboctahedron, rhombicuboctahedron, and cube, while the weak unit cell group includes diamond and rhombic dodecahedron. Within each of the groups, there is not much difference between the different types of unit cells for small structure relative density values, meaning that they are interchangeable from mechanical viewpoint. The other considerations such as permeability [3,9] could therefore play more important role when deciding which of those unit cells is used in bone regeneration applications. For larger structure relative density values, i.e., > 0.15 , the truncated cube unit cell shows remarkably higher stiffness values and could therefore be used in the applications where high stiffness values are required. Since cube and truncated cube are

relatively similar unit cells, it is remarkable that such small variation in the geometry of the cubic unit cells results in such improvement in the stiffness values for relatively large apparent densities. One could explain this by noting that in the cube unit cell force transmission occurs at a few junction points that are also prone to stress concentration. Truncated cube replaces the single junction of the cubic unit cell with a supporting structure that could better distribute and transmit the forces. This improves the stiffness of the porous structure particularly for higher apparent densities where the thick struts at the truncation region of the truncated cube unit cell are particularly closed-pack and support the porous structure very efficiently.

4.5.2 Ratio of Plateau Stress to Yield Stress

One of the important findings of the current study is the point that the relationship between the plateau stress and yield stress is very different for different types of unit cells. In general, plateau stress has received more attention in the recent literature, partly because of the emphasis and explicit definition of the concept in the new ISO standard for the mechanical testing of metallic porous materials [51]. In comparison, there is less emphasis on the concept of yield (or compressive offset) stress in the standard, demoting it to the status of “optional information” in the standard test report [51]. As a consequence, a number of recent studies including our studies on porous structures made from the rhombic dodecahedron unit cell [16,40] and one study of the mechanical behavior of porous structures based on the diamond unit cell [10] have used the concept of plateau stress as a replacement for the yield stress. The results of the current study show that, interestingly, for both types of unit cells used in our previous studies, the plateau and yield stress are very close. Moreover, the ratio of plateau stress to yield stress is largely independent from the structure relative density. This justifies the use of plateau stress as a replacement for the yield stress for the porous structures based on those two types of unit cells. The results of this study, however, show that this is not necessarily the case for the other types of unit cells. Not only the plateau and yield stress are not close to each other for the other types of unit cells, their ratio could be very much dependent on the structure relative density. This is an important point in all future studies where one needs to choose a specific parameter for representing the elastic limit of additively manufactured porous structures based on the different types of unit cells.

4.5.3 Energy Absorption

Fracture toughness of bone is defined as the resistance to crack growth before the final fracture [54] and several studies on what can influence on fracture toughness of the human bone, cortical and trabecular [55,56,57,58] show the importance of this definition. Although tough bone resists more to fracture but it may have lower yield point and be considered weaker [59]. It is therefore important to select the right type of unit cell for bone-mimicking porous structure by comparing the energy absorption values of the porous structures based on the different types of unit cells with that of bone they are aimed to replace. This is an important design aspect has received less attention in the previous studies that look into the mechanical properties of bone-mimicking porous biomaterials and how they are related to those of bone.

4.5.4 Anisotropy

The mechanical properties of porous structures based on some of the unit cells included in the current study are anisotropic. In the current study, we only studied the mechanical properties of the porous structures in one direction (Figure 1). The mechanical properties of the porous structures may be therefore very different in the directions not tested in the current study. One needs to be careful when interpreting the results presented here, as they only pertain to specific directions of unit cells. The experiment required for characterizing the mechanical properties of the porous structures in all relevant directions is formidably large and expensive. A more feasible approach would be to develop analytical and computational models that are first validated against the experimental data presented here and could then be used for estimating the mechanical properties of the porous structures in all possible directions. In addition to the anisotropy caused by the geometry of the unit cells, the manufacturing process could also cause some directionality in the porous structure [44]. This directionality, which is dependent on the geometry of the unit cell, could also induce some additional anisotropy in the mechanical behavior of the porous structures.

4.5.5 Applications in the Design of Implants and Tissue Engineering Scaffolds

The main application of the results presented in the current study is in the design of porous biomaterials used for bone substitution either as an implant or as a part of a bone tissue engineering scheme. The mechanical properties of the porous biomaterials are important from several viewpoints. First, one needs to ensure that there is a good match between the stiffness of porous biomaterial and those of the bone they replace. This could help in avoiding stress shielding. The elastic gradient values reported here for the different types of unit cells could be important in that context. Second, it is important to make sure that the porous biomaterials are capable of providing enough mechanical support and do not fail under the mechanical loading they are exposed to. The plateau stress as well as yield and first maximum stress values reported here could play important roles in that regard.

From a design viewpoint, one needs to ensure that the mechanical properties of the porous biomaterials are favorable for bone regeneration and ingrowth. That is because bone tissue formation is known to be largely driven by mechanical loading [60,61,62,63]. The results of the current study clearly show that, for the same structure relative density, the mechanical properties of bone-mimicking porous biomaterials are very much dependent on the morphology of the porous structure including the type of unit cell and the unit cell dimensions. On the other hand, the same morphological properties determine the other important properties of the porous biomaterials such as permeability and diffusivity [2,3,8,9]. The design of porous biomaterials for bone regeneration applications can therefore be defined as a multi-objective optimization problem. There are additional patient-specific aspects that need to be taken into account. It is therefore important to combine the computer models for optimal design of porous biomaterials with patient-specific finite element models of bones [64,65,66]. The complex and multi-objective nature of such an optimal design problem requires a high degree of flexibility in the design space. Studies such as the present study that help to establish the relationship between the morphological design and the different types of properties of porous biomaterials based on various types of unit cells are helpful in this context. That is because they enable the designers to use a larger library of unit cells for which the different types of properties including mechanical properties are known, thereby enlarging the design space for optimal design of bone substituting implants and tissue engineering scaffolds. Given

the production flexibility offered by advanced additive manufacturing techniques such as selective laser melting, different types of unit cells could be combined in one single implant or scaffold so as to optimally distribute the properties within the entire implant or scaffold.

The results presented in this study are also valuable for corroboration of analytical and numerical models that are developed used for prediction of the mechanical properties of porous structures given their designed morphology. This type of experimental data is not currently available in the literature particularly for some of the unit cells studied here.

4.5.6 Future research

In this study, all the manufacturing parameters such as building orientation and post processing of the samples [44] or laser power or energy density of the specimens processed by SLM [30] considered to be constant. Changing in any of these parameters will influence the results [42]. It is clear from the results of this study that the deformation and failure mechanisms of porous structures based on the considered unit cells are very different. Even though certain aspects of the deformation and failure mechanisms were studied in the current study, it was not the main focus of the paper. It is suggested that future studies should focus on the detailed deformation and failure mechanisms of additively manufactured porous biomaterials based on different types of unit cells. In particular, it would be useful to perform full-field strain measurement [67,68,69,70] during the mechanical testing of the structures, for example, using optical techniques such as digital image correlation (DIC). DIC has been previously used for measurement of strain in engineering [71,72,73,74] and biological materials [75,76,77] and is shown to be capable of capturing the detailed deformation and fracture mechanisms of both types of materials. For determining the mechanical properties only static compressive properties were determined in the present work. In future studies, other relevant mechanical properties, such as static bending strength [46], static torsional strength [46] and fatigue life [50], should be determined.

4.6 Conclusion

The relationship between morphological and mechanical properties of selective laser melted porous titanium alloy biomaterials based on six different types of space-filling unit cells were studied. It was observed that the mechanical behavior, mechanical properties, and failure mechanisms of the porous structures are highly dependent on the type and dimensions of the unit cells out of which the porous structures are made. As expected, compressive properties of all the porous structures increased with structure relative density. Moreover, for a given compressive property of a porous structure, the dependence on the structure relative density was of the power type. The exponent could be used for generalizing the relationships between structure relative density and the compressive properties of porous structures with different types of unit cells. When comparing the compressive properties of the porous structures based on the different types of unit cells, it was found that in many cases the comparative performance of the structures is different for low and high values of structure relative density with a separating structure relative density of 0.15–0.2. Among all unit cells, the diamond unit cell consistently showed lower compressive properties. Regarding the stiffness values, the unit cells were divided into a high stiffness group including truncated cube, truncated cuboctahedron, rhombicuboctahedron, and cube and a low stiffness group including diamond and rhombic dodecahedron. However, truncated cube showed remarkably higher stiffness than other members of its group for apparent densities exceeding 0.2. The results obtained in the present study revealed the relationship between the morphological and compressive properties of porous structures based on six different types of unit cells, many of which have been so far largely unexplored. Moreover, it could serve as a basis for validation of analytical and computational models developed for estimation of the mechanical properties of additively manufactured porous biomaterials.

4.7 Author contribution

Seyed Mohammad Ahmadi, Saber Amin Yavari, Jan Schrooten, Harrie Weinans and Amir A. Zadpoor conceived the experiments; Seyed Mohammad Ahmadi and Saber Amin Yavari performed the experiments; Seyed Mohammad Ahmadi and Amir A. Zadpoor analyzed the data; Ruben Wauthle,

Behdad Pouran contributed materials and analysis tools; each of the authors reviewed the manuscript for intellectual content.

4.8 Conflicts of interest

The authors declare no conflict of interest.

4.9 References

1. Butscher, A.; Bohner, M.; Holmann, S.; Gauckler, L.; Muller, R. Structural and material approaches for bone tissue engineering in powder based 3D printing. *Acta Biomater.* 2013, 7, 907–920.
2. Hollister, S.J. Porous scaffold design for tissue engineering. *Nat. Mater.* 2005, 4, 518–524.
3. Hollister, S.J. Scaffold design and manufacturing: From concept to clinic. *Adv. Mater.* 2009, 21, 3330–3342.
4. Hutmacher, D.W. Scaffold design and fabrication technologies for engineering tissues—State of the art and future perspectives. *J. Biomater. Sci. Polym. Ed.* 2001, 12, 107–124.
5. Cook, S.; Dalton, J. Biocompatibility and biofunctionality of implanted materials. *Alpha Omegan* 1991, 85, 41–47.
6. Gotman, I. Characteristics of metals used in implants. *J. Endourol.* 1997, 11, 383–389.
7. Goulet, R.W.; Goldstein, S.A.; Ciarelli, M.J.; Kuhn, J.L.; Brown, M.B.; Feldkamp, L.A. The relationship between the structural and orthogonal compressive properties of trabecular bone. *J. Biomech.* 1994, 27, 375–377.
8. Dias, M.R.; Guedes, J.M.; Flanagan, C.L.; Hollister, S.J.; Fernandes, P.R. Optimization of scaffold design for bone tissue engineering: A computational and experimental study. *Med. Eng. Phys.* 2014, 36, 448–457.

-
9. Dias, M.R.; Fernandes, P.R.; Guedes, J.M.; Hollister, S.J. Permeability analysis of scaffolds for bone tissue engineering. *J. Biomech.* 2012, 45, 938–944.
 10. Ahmadi, S.M.; Campoli, G.; Yavari, S.A.; Sajadi, B.; Wauthle, R.; Schrooten, J.; Weinans, H.; Zadpoor, A.A. Mechanical behavior of regular open-cell porous biomaterials made of diamond lattice unit cells. *J. Mech. Behav. Biomed. Mater.* 2014, 34, 106–115.
 11. Niinomi, M. Mechanical properties of biomedical titanium alloys. *Mater. Sci. Eng.: A* 1998, 243, 231–236.
 12. Engh, C.; Bobyn, J.; Glassman, A. Porous-coated hip replacement. The factors governing bone ingrowth, stress shielding, and clinical results. *J. Bone Joint Surg. Br.* 1987, 69, 45–55.
 13. Engh, C.A., Jr.; Young, A.M.; Engh, C.A.; Robert, H., Jr. Clinical consequences of stress shielding after porous-coated total hip arthroplasty. *Clin. Orthop. Relat. Res.* 2003, 417, 157–163.
 14. Huiskes, R.; Weinans, H.; van Rietbergen, B. The relationship between stress shielding and bone resorption around total hip stems and the effects of flexible materials. *Clin. Orthop. Relat. Res.* 1992, 274, 124–134.
 15. Nagels, J.; Stokdijk, M.; Rozing, P.M. Stress shielding and bone resorption in shoulder arthroplasty. *J. Shoulder Elbow Surg.* 2003, 12, 35–39.
 16. Amin Yavari, S.; Ahmadi, S.M.; van der Stok, J.; Wauthle, R.; Riemsdag, A.C.; Janssen, M.; Schrooten, J.; Weinans, H.; Zadpoor, A.A. Effects of bio-functionalizing surface treatments on the mechanical behavior of open porous titanium biomaterials. *J. Mech. Behav. Biomed. Mater.* 2014, 36, 109–119.
 17. Van der Stok, J.; van der Jagt, O.P.; Yavari, S.A.; de Haas, M.F.P.; Waarsing, J.H.; Jahr, H.; van Lieshout, E.M.M.; Patka, P.; Verhaar, J.A.N.; Zadpoor, A.A.; et al. Selective laser melting-produced porous titanium scaffolds regenerate bone in critical size cortical bone defects. *J. Orthop. Res.* 2013, 31, 792–799.

-
18. Imwinkelried, T. Mechanical properties of open-pore titanium foam. *J. Biomed. Mater. Res. Part A* 2007, 81, 964–970.
 19. Krishna, B.V.; Bose, S.; Bandyopadhyay, A. Low stiffness porous Ti structures for load-bearing implants. *Acta Biomater.* 2007, 3, 997–1006.
 20. Torres, Y.; Pavón, J.J.; Rodríguez, J.A. Processing and characterization of porous titanium for implants by using NaCl as space holder. *J. Mater. Process. Technol.* 2012, 212, 1061–1069.
 21. Yang, D.; Shao, H.; Guo, Z.; Lin, T.; Fan, L. Preparation and properties of biomedical porous titanium alloys by gelcasting. *Biomed. Mater.* 2011, 6. [CrossRef]
 22. Bartolo, P.; Kruth, J.-P.; Silva, J.; Levy, G.; Malshe, A.; Rajurkar, K.; Mitsuishi, M.; Ciurana, J.; Leu, M. Biomedical production of implants by additive electro-chemical and physical processes. *CIRP Ann. Manuf. Technol.* 2012, 61, 635–655.
 23. Gu, D.; Meiners, W.; Wissenbach, K.; Poprawe, R. Laser additive manufacturing of metallic components: Materials, processes and mechanisms. *Int. Mater. Rev.* 2012, 57, 133–164.
 24. Mironov, V.; Trusk, T.; Kasyanov, V.; Little, S.; Swaja, R.; Markwald, R. Biofabrication: A 21st century manufacturing paradigm. *Biofabrication* 2009, 1. [CrossRef]
 25. Murr, L.; Gaytan, S.M.; Medina, F.; Lopez, H.; Martinez, E.; Machado, B.I.; Hernandez, D.H.; Martinez, L.; Lopez, M.I.; Wicker, R.B.; et al. Next-generation biomedical implants using additive manufacturing of complex, cellular and functional mesh arrays. *Philos. Trans. R. Soc. A: Math. Phys. Eng. Sci.* 2010, 368, 1999–2032.
 26. Louvis, E.; Fox, P.; Sutcliffe, C.J. Selective laser melting of aluminium components. *J. Mater. Process. Technol.* 2011, 211, 275–284.
 27. Mullen, L.; Stamp, R.C.; Brooks, W.K.; Jones, E.; Sutcliffe, C.J. Selective Laser Melting: A regular unit cell approach for the manufacture of porous, titanium, bone in-growth constructs, suitable for orthopedic applications. *J. Biomed. Mater. Res. Part B: Appl. Biomater.* 2009, 89, 325–334.

-
28. Mullen, L.; Stamp, R.C.; Fox, P.; Jones, E.; Ngo, C.; Sutcliffe, C.J. Selective laser melting: A unit cell approach for the manufacture of porous, titanium, bone in-growth constructs, suitable for orthopedic applications. II. Randomized structures. *J. Biomed. Mater. Res. Part B: Appl. Biomater.* 2010, 92, 178–188.
 29. Vandenbroucke, B.; Kruth, J. Selective laser melting of biocompatible metals for rapid manufacturing of medical parts. *Rapid Prototyp. J.* 2007, 13, 196–203.
 30. Attar, H.; Calin, M.; Zhang, L.C.; Scudino, S.; Eckert, J. Manufacture by selective laser melting and mechanical behavior of commercially pure titanium. *Mater. Sci. Eng.: A* 2014, 593, 170–177.
 31. Heintl, P.; Müller, L.; Körner, C.; Singer, R.F.; Müller, F.A. Cellular Ti–6Al–4V structures with interconnected macro porosity for bone implants fabricated by selective electron beam melting. *Acta Biomater.* 2008, 4, 1536–1544.
 32. Li, X.; Wang, C.; Zhang, W.; Li, Y. Fabrication and characterization of porous Ti6Al4V parts for biomedical applications using electron beam melting process. *Mater. Lett.* 2009, 63, 403–405.
 33. Parthasarathy, J.; Starly, B.; Raman, S.; Christensen, A. Mechanical evaluation of porous titanium (Ti6Al4V) structures with electron beam melting (EBM). *J. Mech. Behav. Biomed. Mater.* 2010, 3, 249–259.
 34. Ponader, S.; von Wilmsowky, C.; Widenmayer, M.; Lutz, R.; Heintl, P.; Körner, C.; Singer, R.F.; Nkenke, E.; Neukam, F.W.; Schlegel, K.A. In vivo performance of selective electron beam-melted Ti-6Al-4V structures. *J. Biomed. Mater. Res. Part A* 2010, 92, 56–62.
 35. Van der Stok, J.; Wang, H.; Amin, Y.S.; Siebelt, M.; Sandker, M.; Waarsing, J.H.; Verhaar, J.A.; Jahr, H.; Zadpoor, A.A.; Leeuwenburgh, S.C.; et al. Enhanced bone regeneration of cortical segmental bone defects using porous titanium scaffolds incorporated with colloidal gelatin gels for time-and dose-controlled delivery of dual growth factors. *Tissue Eng. Part A* 2013, 19, 2605–2614.

-
36. Amin Yavari, S.; Wauthle, R.; Böttger, A.J.; Schrooten, J.; Weinans, H.; Zadpoor, A.A. Crystal structure and nanotopographical features on the surface of heat-treated and anodized porous titanium biomaterials produced using selective laser melting. *Appl. Surf. Sci.* 2014, 290, 287–294.
 37. Chen, X.-B.; Li, Y.C.; Du Plessis, J.; Hodgson, P.D.; Wen, C. Influence of calcium ion deposition on apatite-inducing ability of porous titanium for biomedical applications. *Acta Biomater.* 2009, 5, 1808–1820.
 38. Liang, F.; Zhou, L.; Wang, K. Apatite formation on porous titanium by alkali and heat-treatment. *Surf. Coat. Technol.* 2003, 165, 133–139.
 39. Lopez-Heredia, M.A.; Sohier, J.; Gaillard, C.; Quillard, S.; Dorget, M.; Layrolle, P. Rapid prototyped porous titanium coated with calcium phosphate as a scaffold for bone tissue engineering. *Biomaterials* 2008, 29, 2608–2615.
 40. Campoli, G.; Borleffs, M.S.; Amin Yavari, S.; Wauthle, R.; Weinans, H.; Zadpoor, A.A. Mechanical properties of open-cell metallic biomaterials manufactured using additive manufacturing. *Mater. Des.* 2013, 49, 957–965.
 41. Hazlehurst, K.B.; Wang, C.J.; Stanford, M. A numerical investigation into the influence of the properties of cobalt chrome cellular structures on the load transfer to the periprosthetic femur following total hip arthroplasty. *Med. Eng. Phys.* 2014, 36, 458–466.
 42. Lewis, G. Properties of open-cell porous metals and alloys for orthopaedic applications. *J. Mater. Sci.: Mater. Med.* 2013, 24, 2293–2325.
 43. Li, S.; Xu, Q.S.; Wang, Z.; Hou, W.T.; Hao, Y.L.; Yang, R.; Murr, L.E. Influence of cell shape on mechanical properties of Ti-6Al-4V meshes fabricated by electron beam melting method. *Acta Biomater.* 2014, 10, 4537–4547.
 44. Wauthle, R.; Vrancken, B.; Beynaerts, B.; Jorissen, K.; Schrooten, J.; Kruth, J.-P.; van Humbeeck, J. Effects of build orientation and heat treatment on the microstructure and mechanical properties of selective laser melted Ti6Al4V lattice structures. *Addit. Manuf.* 2015, 5, 77–84.

-
45. Wieding, J.; Jonitz, A.; Bader, R. The effect of structural design on mechanical properties and cellular response of additive manufactured titanium scaffolds. *Materials* 2012, 5, 1336–1347.
 46. Wieding, J.; Wolf, A.; Bader, R. Numerical optimization of open-porous bone scaffold structures to match the elastic properties of human cortical bone. *J. Mech. Behav. Biomed. Mater.* 2014, 37, 56–68.
 47. Pyka, G.; Burakowski, A.; Kerckhofs, G.; Moesen, M.; van Bael, S.; Schrooten, J.; Wevers, M. Surface modification of Ti6Al4V open porous structures produced by additive manufacturing. *Adv. Eng. Mater.* 2012, 14, 363–370.
 48. Van Bael, S.; Kerckhofs, G.; Moesen, M.; Pyka, G.; Schrooten, J.; Krutha, J.P. Micro-CT-based improvement of geometrical and mechanical controllability of selective laser melted Ti6Al4V porous structures. *Mater. Sci. Eng. A* 2011, 528, 7423–7431.
 49. Doube, M.; Kłosowski, M.M.; Arganda-Carreras, I.; Cordelières, F.P.; Dougherty, R.P.; Jackson, J.S.; Schmid, B.; Hutchinson, J.R.; Shefelbine, S.J. BoneJ: Free and extensible bone image analysis in ImageJ. *Bone* 2010, 47, 1076–1079.
 50. Amin Yavari, S.; Ahmadi, S.M.; Wauthle, R.; Pouran, B.; Schrooten, J.; Weinans, H.; Zadpoor, A.A. Relationship between unit cell type and porosity and the fatigue behavior of selective laser melted meta-biomaterials. *J. Mech. Behav. Biomed. Mater.* 2015, 43, 91–100.
 51. International Organization for Standardization (ISO). *Mechanical Testing of Metals—Ductility Testing—Compression Test for Porous and Cellular Metals*; ISO: Genva, Switzerland, 2011; Volume ISO 13314:2011.
 52. Kim, H.W.; Knowles, J.C.; Kim, H.E. Hydroxyapatite porous scaffold engineered with biological polymer hybrid coating for antibiotic Vancomycin release. *J. Mater. Sci.: Mater. Med.* 2005, 16, 189–195.
 53. Kenesei, P.; Kádár, C.; Rajkovits, Z.; Lendvai, J. The influence of cell-size distribution on the plastic deformation in metal foams. *Scripta Mater.* 2004, 50, 295–300.

-
54. Yeni, Y.N.; Brown, C.U.; Wang, Z.; Norman, T.L. The influence of bone morphology on fracture toughness of the human femur and tibia. *Bone* 1997, 21, 453–459.
 55. Garrison, J.G.; Gargac, J.A.; Niebur, G.L. Shear strength and toughness of trabecular bone are more sensitive to density than damage. *J. Biomech.* 2011, 44, 2747–2754.
 56. Keaveny, T.M.; Wachtel, E.F.; Guo, X.E.; Hayes, W.C. Mechanical behavior of damaged trabecular bone. *J. Biomech.* 1994, 27, 1309–1318.
 57. Moore, T.L.A.; Gibson, L.J. Fatigue Microdamage in Bovine, Trabecular Bone. *J. Biomech. Eng.* 2003, 125, 769–776.
 58. Black, D.M.; Cummings, S.R.; Karpf, D.B.; Cauley, J.A.; Thompson, D.E.; Nevitt, M.C.; Bauer, D.C.; Genant, H.K.; Haskell, W.L.; Marcus, R.; et al. Randomised trial of effect of alendronate on risk of fracture in women with existing vertebral fractures. *Lancet* 1996, 348, 1535–1541.
 59. Morgan, E.F.; Bouxsein, M. Biomechanics of bone and age-related fractures. In *Principles of Bone Biology*, 3rd ed.; Bilezikian, J.P., Raisz, L.G., Martin, J., Eds.; Elsevier: Amsterdam, The Netherlands, 2008; pp. 29–51.
 60. Adachi, T.; Osako, Y.; Tanaka, M.; Hojo, M.; Hollister, S.J. Framework for optimal design of porous scaffold microstructure by computational simulation of bone regeneration. *Biomaterials* 2006, 27, 3964–3972.
 61. Carter, D.R.; Beaupré, G.S.; Giori, N.J.; Helms, J.A. Mechanobiology of skeletal regeneration. *Clin. Orthop. Relat. Res.* 1998, 355, S41–S55.
 62. Petite, H.; Viateau, V.; Bensaïd, W.; Meunier, A.; de Pollak, C.; Bourguignon, M.; Oudina, K.; Sedel, L.; Guillemin, G. Tissue-engineered bone regeneration. *Nat. Biotechnol.* 2000, 18, 959–963.
 63. Zadpoor, A.A. Open forward and inverse problems in theoretical modeling of bone tissue adaptation. *J. Mech. Behav. Biomed. Mater.* 2013, 27, 249–261.

-
64. Harrysson, O.L.; Hosni, Y.A.; Nayfeh, J.F. Custom-designed orthopedic implants evaluated using finite element analysis of patient-specific computed tomography data: femoral-component case study. *BMC Musculoskelet. Disord.* 2007, 8. [CrossRef]
 65. Poelert, S.; Valstar, E.; Weinans, H.; Zadpoor, A.A. Patient-specific finite element modeling of bones. *Proc. Inst. Mech. Eng. Part H: J. Eng. Med.* 2013, 227, 464–478.
 66. Schileo, E.; Taddei, F.; Malandrino, A.; Cristofolini, L.; Viceconti, M. Subject-specific finite element models can accurately predict strain levels in long bones. *J. Biomech.* 2007, 40, 2982–2989.
 67. Lomov, S.V.; Boisse, P.; Deluycker, E.; Morestin, F.; Vanclooster, K.; Vandepitte, D.; Verpoest, I.; Willems, A. Full-field strain measurements in textile deformability studies. *Compos. Part A: Appl. Sci. Manuf.* 2008, 39, 1232–1244.
 68. Pan, B.; Xie, H.; Guo, Z.; Hua, T. Full-field strain measurement using a two-dimensional Savitzky-Golay digital differentiator in digital image correlation. *Opt. Eng.* 2007, 46. [CrossRef]
 69. Schmidt, T.; Tyson, J.; Galanulis, K. Full-field dynamic displacement and strain measurement using advanced 3d image correlation photogrammetry: Part 1. *Exp. Tech.* 2003, 27, 47–50.
 70. Zadpoor, A.A.; Sinke, J.; Benedictus, R. Experimental and numerical study of machined aluminum tailor-made blanks. *J. Mater. Process. Technol.* 2008, 200, 288–299.
 71. Hild, F.; Roux, S. Digital image correlation: from displacement measurement to identification of elastic properties—A review. *Strain* 2006, 42, 69–80.
 72. McCormick, N.; Lord, J. Digital image correlation. *Mater. Today* 2010, 13, 52–54.
 73. Wattrisse, B.; Chrysochoos, A.; Muracciole, J.-M.; Némot-Gaillard, M. Analysis of strain localization during tensile tests by digital image correlation. *Exp. Mech.* 2001, 41, 29–39.
 74. Zadpoor, A.A.; Sinke, J.; Benedictus, R. Elastoplastic deformation of dissimilar-alloy adhesively-bonded tailor-made blanks. *Mater. Des.* 2010, 31, 4611–4620.

-
75. Thompson, M.; Schell, H.; Lienau, J.; Duda, G.N. Digital image correlation: A technique for determining local mechanical conditions within early bone callus. *Med. Eng. Phys.* 2007, 29, 820–823.
76. Verhulp, E.; Rietbergen, B.V.; Huiskes, R. A three-dimensional digital image correlation technique for strain measurements in microstructures. *J. Biomech.* 2004, 37, 1313–1320.
- Zhang, D.; Arola, D.D. Applications of digital image correlation to biological tissues. *J. Biomed. Opt.* 2004, 9, 691–699.

Chapter 5 Relationship between unit cell type and porosity and the fatigue behavior of selective laser melted meta-biomaterials

This chapter has been published as:

S Amin Yavari, **SM Ahmadi**, R Wauthle, B Pouran, J Schrooten, H Weinans, AA Zadpoor, *Relationship between unit cell type and porosity and the fatigue behavior of selective laser melted meta-biomaterials*, Journal of the mechanical behavior of biomedical materials, 2015.p.91-100.

5.1 Abstract

Meta-materials are structures when their small-scale properties are considered, but behave as materials when their homogenized macroscopic properties are studied. There is an intimate relationship between the design of the small-scale structure and the homogenized properties of such materials. In this article, we studied that relationship for meta-biomaterials that are aimed for biomedical applications, otherwise known as meta-biomaterials. Selective laser melted porous titanium (Ti6Al4V ELI) structures were manufactured based on three different types of repeating unit cells, namely cube, diamond, and truncated cuboctahedron, and with different porosities. The morphological features, static mechanical properties, and fatigue behavior of the porous biomaterials were studied with a focus on their fatigue behavior. It was observed that, in addition to static mechanical properties, the fatigue properties of the porous biomaterials are highly dependent on the type of unit cell as well as on porosity. None of the porous structures based on the cube unit cell failed after 10^6 loading cycles even when the applied stress reached 80% of their yield strengths. For both other unit cells, higher porosities resulted in shorter fatigue lives for the same level of applied stress. When normalized with respect to their yield stresses, the S-N data points of structures with different porosities very well ($R^2 > 0.8$) conformed to one single power law specific to the type of the unit cell. For the same level of normalized applied stress, the truncated cuboctahedron unit cell resulted in a longer fatigue life as compared to the diamond unit cell. In a similar comparison, the fatigue lives of the porous structures based on both truncated cuboctahedron and diamond unit cells were longer than that of the porous structures based on the rhombic dodecahedron unit cell (determined in a previous study). The data presented in this study could serve as a basis for design of porous biomaterials as well as for corroboration of relevant analytical and computational models.

5.2 Introduction

Recent advances in additive manufacturing as well as in other multi-scale manufacturing techniques have enabled production of very complex structures with high precision and controllability down to micrometer scale (Cohen et al., 2010, Dalton et al., 2013, Melchels et al., 2012 and Podshivalov et al., 2013). As a consequence, a new class of materials is emerging that might be called “meta-materials” (Garcia et al., 2012, Méjica and Lantada, 2013 and Zhou, 2013). The concept of meta-materials is an in-between concept halfway from both “materials” and “structures.” A meta-material is a structure as far as its small-scale features and properties are concerned, but behaves like a material when its homogenized properties are evaluated at the large, that is, macro, scale. The rationally-designed small-scale structure of meta-materials may give rise to unprecedented or rarely observed macro-scale properties including acoustic (Christensen and de Abajo, 2012, Liang and Li, 2012 and Park et al., 2011), dielectric (Levy et al., 2007, Schuller et al., 2007, Vynck et al., 2009 and Zhao et al., 2009), and mechanical properties (Fang et al., 2006 and Ju et al.,). Those properties are important for application of meta-materials in different industries including the medical industry. When dealing with additively manufactured meta-materials that are aimed for biomedical applications, the more specific term of “meta-biomaterials” may be used. Although more generic terms such as porous biomaterials have been used in the past for describing this class of biomaterials, it seems important to use a more modern term such as “meta-biomaterials” to clarify the connection of this material with other types of meta-materials and distinguish them from the porous biomaterials manufactured using conventional techniques such as space-holder (Aydoğmuş and Bor, 2009, Kolk et al., 2012, Niu et al., 2009 and Wang et al., 2009) and gas foaming (Harris et al., 1998, Kim et al., 2006, Salerno et al., 2009 and Yoon and Park, 2001). Although conventional techniques could be used for adjusting the composition, pore shape, porosity, and mechanical properties of biomaterials (Li et al., 2009 and Wen et al., 2010), they have limited potential for free-form fabrication of fully interconnected porous biomaterials based on rationally designed repeating unit cells.

One of the applications of meta-biomaterials is in bone tissue regeneration and orthopedic implants. The mechanical properties of meta-materials in general and meta-biomaterials in particular including stiffness values comparable to those of bone (Van der Stok et al., 2013), adjustable

permeability (Dias et al., 2014, Lewis, 2013, Truscello et al., 2012 and Van Bael et al., 2012), huge surface area that could be modified for bio-functionalization (Amin Yavari et al., 2014a, Amin Yavari et al., 2014c, Chai et al., 2011 and Heintl et al., 2008), and negative Poisson's ratio (Greaves et al., 2011) have important applications in orthopedics and skeletal tissue regeneration. However, the different properties of this type of porous biomaterials are not well understood. Of particular importance are the deformation and fracture mechanisms of the different classes of meta-biomaterials. As previously implied, the mechanical properties of meta-biomaterials are highly dependent on the design of their small-scale structure (Zhou, 2013, Campoli et al., 2013, Murr et al., 2011 and Parthasarathy et al., 2011). Recently, a growing number of researchers have tried to study the relationship between the geometrical design of the ultra-structure of meta-biomaterials and their mechanical properties (Campoli et al., 2013, Ahmadi et al., 2014a, Babaei et al., 2012 and Li et al., 2014). However, there are very few studies (Amin Yavari et al., 2013 and Hrabe et al., 2011) on the fatigue behavior of such meta-biomaterials. The aim of the current study is to contribute towards understanding the relationship between the geometrical design of meta-biomaterials at the small-scale and their fatigue properties. Selective laser melted (SLM) porous titanium structures based on three different types of space-filling unit cells including cube, diamond, and truncated cuboctahedron were considered. The relationship between the type of the unit cell and porosity on the one hand and the fatigue behavior of porous structures on the other hand is not yet well understood. In this article, we study the relationship between the geometrical design of porous structures including the type of unit cell and porosity and their fatigue behavior.

5.3 Materials and methods

5.3.1 Manufacturing techniques

An additive manufacturing technique, namely SLM, was used for production of the specimens used for morphological characterization, static mechanical testing, and fatigue experiments. The powder used for laser processing was made of Ti6Al4V- ELI according to ASTM F136 (grade 23). The other details of the manufacturing process and processing parameters have been described elsewhere (Amin Yavari et al., 2014a, Ahmadi et al., 2014a and Amin Yavari et al., 2014b). The specimens were

manufactured on top of a solid titanium substrate and were subsequently removed from the substrate using Electrical Discharge Machining (EDM). All specimens were approximately 15 mm in length and 10 mm in diameter, and had an entirely porous structure based on three types of space-filling unit cells including cube, truncated cuboctahedron, and diamond unit cells (Fig. 5-1). Different porosities were achieved by changing the strut thickness (Table 5-1).

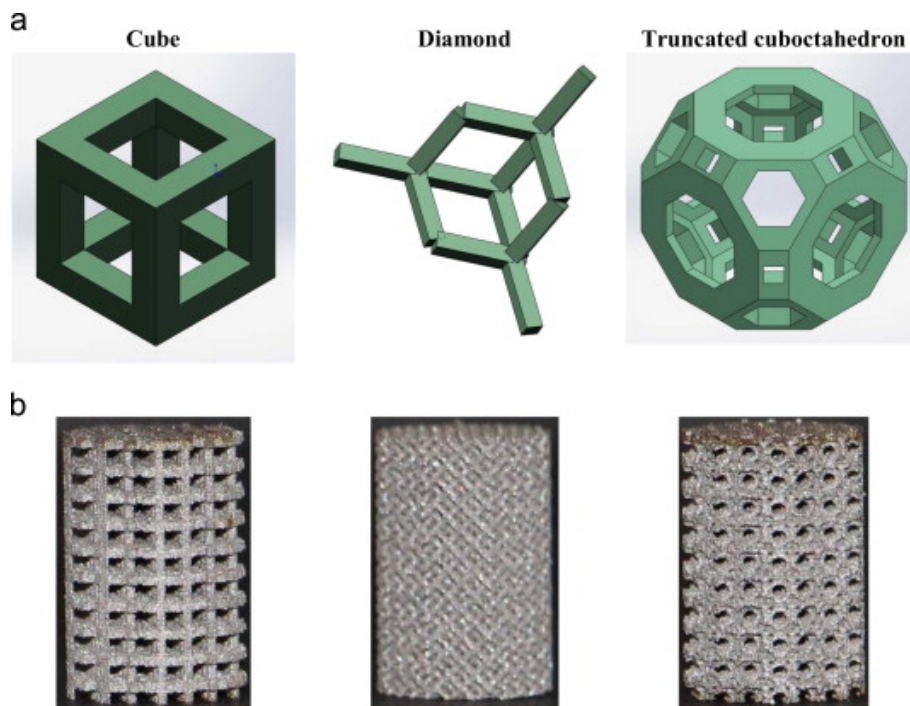


Figure 5-1. Schematic drawings of the unit cells used for manufacturing of porous structures studied here (a) as well as some specimens from the different types of porous structures (b)

Table 5-1. The nominal and actual morphological properties of porous structures made from different types of unit cells (Ahmadi et al., 2014b).

Unit cell type	Porosity (%)		Pore size (μm)		Strut size (μm)	
	Dry weighing	Micro-CT	Nominal	Micro-CT	Nominal	Micro-CT
Diamond						
D1	89 \pm 0.1	89	923	958 \pm 144	277	240 \pm 46
D2	80 \pm 0.2	79	750	780 \pm 141	450	363 \pm 75
D3	74 \pm 0.4	72	680	719 \pm 130	520	472 \pm 108
D4	66 \pm 0.3	64	600	641 \pm 137	600	536 \pm 120
Truncated cuboctahedron						
T1	80 \pm 0.1	83	876	862 \pm 349	234	350 \pm 60
T2	78 \pm 0.2	80	1040	1142 \pm 383	460	416 \pm 64
T3	73 \pm 0.2	73	923	1079 \pm 391	577	482 \pm 70
T4	67 \pm 0.3	64	807	1049 \pm 383	693	564 \pm 76
Cubic						
C1	89 \pm 0.1	87	1452	1413 \pm 366	348	451 \pm 147
C2	79 \pm 0.2	76	1260	1139 \pm 359	540	654 \pm 190
C3	74 \pm 0.2	72	1188	1155 \pm 354	612	693 \pm 200
C4	66 \pm 0.1	63	1080	1020 \pm 311	720	823 \pm 230

5.3.2 Morphological characterization

The actual morphological properties of the porous structures were characterized using four techniques, namely dry weighing, SEM, Archimedes, and micro-CT imaging. As for micro-CT imaging, the porous structures were scanned using Quantum FX (Perkin Elmer, USA). In the scanning protocol, tube voltages of 90 kV, tube currents of 180 μA , scan times of 3 min, and resolutions of 42 μm were used. Subsequently, the acquired 3D images were reconstructed using the in-built algorithms of the scanner. The reconstructed images were then transferred to Caliper Analyze 11.0 (supplied by the manufacturer) to obtain 2D slices that were basically transverse (circular cross-sections) views of the porous structures. ImageJ 1.47v (<http://imagej.nih.gov/ij/>) was used to create regions of interests (ROIs) and segment the metallic volume from air using the optimal thresholding algorithm available

in the boneJ (Doube et al., 2010) plugin of ImageJ. The same plugin was used for calculating the ratio of the metallic volume to total volume and calculating the apparent density.

The morphological characterization of porous structures using dry weighing and the Archimedes technique was performed according to a protocol described elsewhere (Amin Yavari et al., 2014a, Campoli et al., 2013, Ahmadi et al., 2014a, Amin Yavari et al., 2013 and Amin Yavari et al., 2014b). In brief, five specimens were used from each type of porous structures. The weight measurements were performed using an OHAUS Pioneer balance. All dry weighing measurements were performed under normal atmospheric conditions and in room temperature. According to the Archimedes porosity measurement protocol, the specimens were weighed in two conditions, that is, in air and in pure ethanol. The results of the weight measurements were then used to calculate the actual volume. The overall porosity was based on the ratio of the measured volume to the theoretical macro volume. When calculating the porosities using both dry weighing and the Archimedes technique, the theoretical density of Ti6Al4V-ELI was assumed to be 4.42 g/cm³. Furthermore, the porous structures were inspected using a scanning electron microscope (SEM) (JEOL, JSM-6500 F, Japan).

5.3.3 Static mechanical testing

Five specimens from each type of porous structure (different porosities and different types of unit cells, a subset of specimens whose mechanical properties are reported in another study (Ahmadi et al., 2014b)) were mechanically tested under compression using an INSTRON 5985 mechanical testing machine (100 kN load cell). The experiments were conducted according to the ISO standard for the mechanical testing of porous metallic materials, that is, ISO 13314:2011 (ISO 2011).

The same standard was used for calculating the mechanical properties of the porous structures including the maximum compressive strength (σ_{max}), plateau stress (σ_{pl}) (the arithmetical mean of the stresses between 20% and 40% compressive strain), the elastic gradient ($E\sigma_{20-70}$) (the gradient of the elastic straight line between stress values 20 and 70 MPa), and 0.2% offset yield stress (σ_y).

5.3.4 Fatigue mechanical testing

Following a previously published protocol (Amin Yavari et al., 2013), fatigue tests were performed under compression using a hydraulic dynamic testing machine, that is, MTS (Minneapolis, US), equipped with a 25 kN load cell. The shape and frequency of the loading wave were respectively sinusoidal and 15 Hz. A constant load ratio of $R= 0.1$ was used for all the fatigue experiments reported in the current study. The specimens were assumed to have failed once they lost 90% of their initial stiffness. For every series of porous structure and porosity, between 8–10 stress values were selected. All maximum stress values were between $0.2\sigma_y$ and $0.8\sigma_y$ to ensure the specimens are loaded in the elastic region. For all but one specific porosity of one specific unit cell, that is, diamond, two specimens were tested for every value of maximum load. In addition to absolute S-N curves, the normalized S-N curves were calculated by dividing the maximum stress values by the yield stress of the porous structure. Power laws were fitted to the normalized S-N curves. For a number of sample specimens, the fatigue tests were stopped after the specimens had lost 10%, 20%, or 30% of their stiffness. These samples were then photographed so as to document the appearance of the specimens at those levels of stiffness loss.

5.4 Results

The static mechanical properties of all types of porous structures decreased with porosity (Table 5-2). However, the mechanical properties of porous structures with different types of unit cells were different for similar porosities (Table 5-2) (Ahmadi et al., 2014b). The porous structures based on the diamond unit cell had the lowest mechanical properties in general and the lowest strength indicators (e.g. first maximum stress) in particular, as compared to the porous structures based on both other types of unit cells (Table 5-2). The mechanical properties of the porous structures based on the cube and truncated cuboctahedron were more or less similar for similar porosities. Nevertheless, the mechanical properties of the porous structures based on the cube unit cell were slightly higher in most cases (Table 5-2).

Table 5-2. Static mechanical properties of porous structures made from different types of unit cells (Ahmadi et al., 2014b).

Unit cell type	σ_{\max} (MPa)	σ_{pl} (MPa)	σ_y (MPa)	Energy absorption (MJ/m ³)	$E\sigma_{20-\sigma 70}/E_s$
Diamond					
D1	15.1±0.3	7.9±1.3	6.8±2.3	2.8±1.3	0.004±0.000
D2	46.517±2.5	29.2±2.8	28.9±6.2	13.1±4.6	0.013±0.001
D3	57.0±12.8	37.1±12.9	31.7±13.0	14.5±8.8	0.017±0.001
D4	113.0±17.3	71.9±12.5	70.6±7.0	38.1±6.7	0.033±0.002
Truncated cuboctahedron					
T1	55.5±1.7	22.6±4.8	41.4±2.0	13.3±0.8	0.020±0.001
T2	62.2±10.4	30.2±7.1	49.9±18.9	17.1±4.1	0.023±0.001
T3	94.8±6.9	63.4±4.6	66.1±4.0	30.7±2.4	0.030±0.001
T4	147.2±3.7	122.2±8.7	110.1±10.4	60.3±3.3	0.035±0.001
Cubic					
C1	30.2±0.9	11.2±0.5	29.9±0.9	5.5±0.2	0.017±0.000
C2	76.6±2.3	42.7±7.7	63.3±2.2	16.7±5.0	0.024±0.003
C3	110.5±17.4	49.2±10.0	65.6±12.3	30.8±3.6	0.036±0.004
C4	184.8±3.6	134.3±13.4	112.6±7.2	68.8±5.7	0.042±0.003

The results of fatigue experiments showed that both absolute and normalized fatigue behavior of the porous structures considered in the current study are highly dependent on the type of unit cell used in their design. The most remarkable were the porous structures made from the cube unit cell. For those structures, even at the highest load, that is, $0.8\sigma_y$, none of the specimens failed after 106 cycles of loading. This observation held for all porosities. Since 105–106 loading cycles is generally considered the endurance limit of materials, the experiments were stopped when the specimens had endured well over 106 loading cycles. It was therefore not possible to establish an S-N curve for the porous structures made from the cube unit cell.

For the porous structures made from the diamond unit cell, the absolute S-N curves were very much dependent on the porosity of the porous structure. The fatigue life decreased as the porosity of the

structure increased causing a very clear separation between the porous structures with different porosities (Fig. 5-2a). The maximum number of loading cycles was around 1.5×10^5 that occurred for the lowest level of applied stress. In comparison with absolute S-N curves, there was no clear separation between the normalized S-N curves of the porous structures with different porosities (Fig. 5-2b). The normalized S-N data points of the porous structures based on the diamond unit cell conformed very well ($R^2=0.80$) to one single power law (Fig. 5-2b).

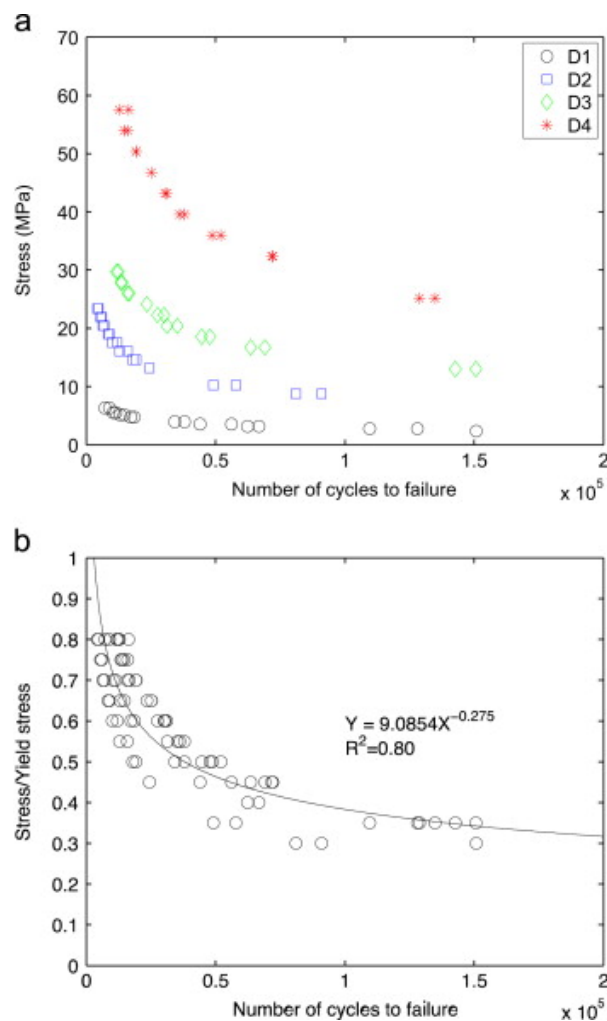


Figure 5-2. Absolute (a) and normalized (b) S-N curves for the porous structures made from the diamond unit cell.

Qualitatively speaking, the fatigue behavior of the porous structures based on the truncated cuboctahedron was similar to the ones based on the diamond unit cell: the absolute S-N curves of the porous structures with different porosities were very different with a very clear separation of S-

N curves and a decrease in fatigue lives with porosity (Fig. 5-3a). The maximum number of loading cycles before failure was slightly less than 2×10^5 and occurred for the lowest level of applied stress (Fig. 5-3a). All the data points in the normalized S-N curves conformed very well ($R^2=0.81$) to one single power law (Fig. 5-3b).

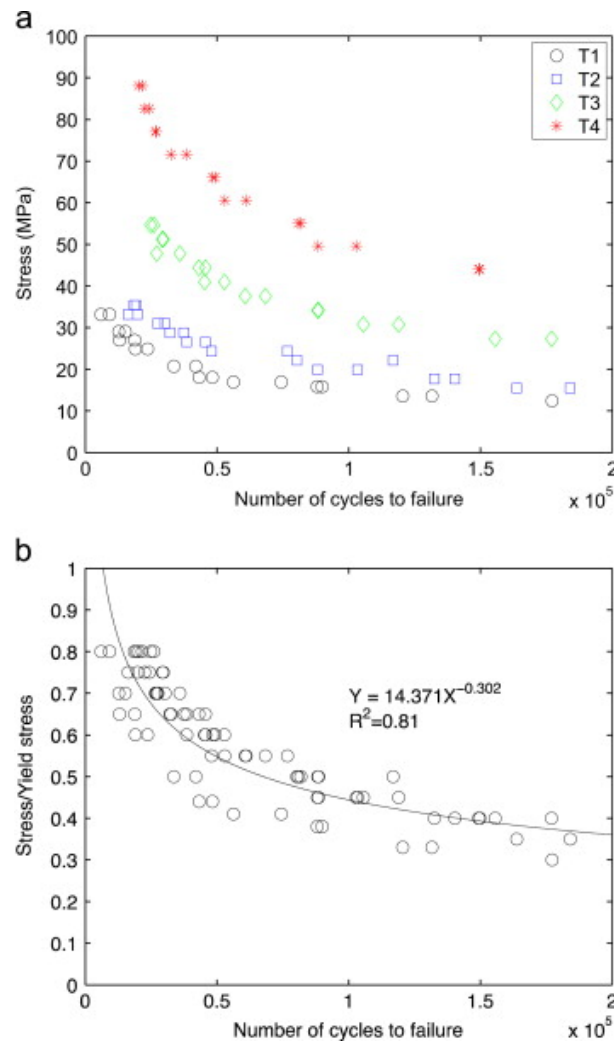


Figure 5-3. Absolute (a) and normalized (b) S-N curves for the porous structures made from the truncated cuboctahedron unit cell.

The normalized S-N curve of the porous structures based on the truncated cuboctahedron unit cell was clearly above that of the porous structures based on the diamond unit cell (Fig. 5-4). Both of the normalized S-N curves of the structures determined in the current study were above that of the

normalized S-N curve of the porous structures based on the rhombic dodecahedron unit cell determined in a previous study (Amin Yavari et al., 2013) (Fig. 5-4).

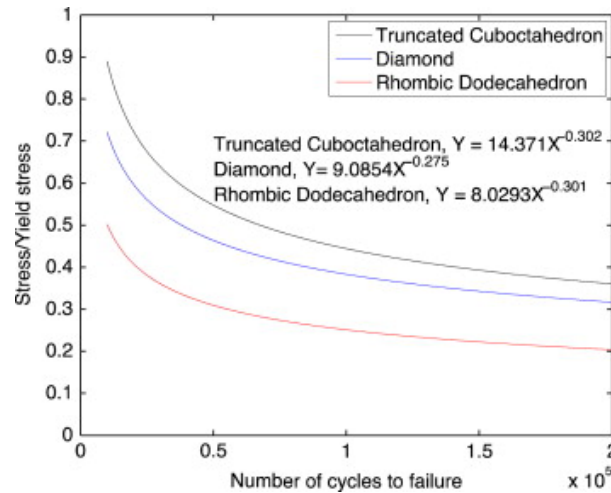


Figure 5-4. Comparison between the normalized S-N curves (fitted power laws) of the porous structures made from diamond, truncated cuboctahedron, and rhombic dodecahedron unit cells.

The stiffness loss was initially not accompanied with major change in the appearance of the specimens (Fig. 5-5). Only in the last stages of stiffness loss, the appearance of the specimens had significantly changed. The transition from intermediate values of stiffness loss to the final loss of stiffness occurred very rapidly, similar to what was previously observed for the porous structures based on the rhombic dodecahedron unit cell (Amin Yavari et al., 2013).

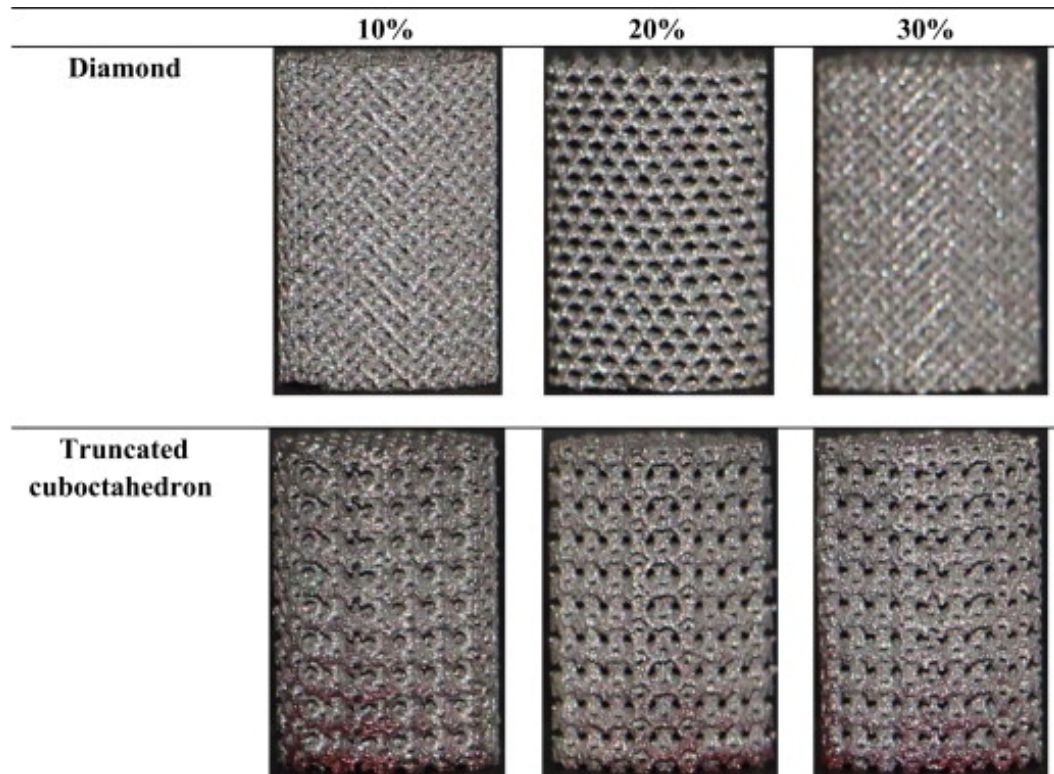


Figure 5-5. Appearance of some sample specimens after partial loss of their stiffness while going through the fatigue protocol.

5.5 Discussion

It is often assumed that the small-scale structure of meta-biomaterials such as the porous structures studied in the current study dictate their macro-scale homogenized mechanical behavior. In this work, we studied the relationship between the small-scale morphological design of a specific class of meta-biomaterials, namely SLM porous titanium biomaterials, and their fatigue properties. The results of the study clearly show that the fatigue properties of porous biomaterials are strongly dependent on the type of unit cell as well as on the porosity of the porous structures. More importantly, the dependency of the fatigue properties on the morphological design of the structure is independent from their static mechanical properties. This point is based on the observation that even when the S-N curves of the porous structures based on the different types of unit cells are

normalized with respect to the static mechanical properties of the porous structures, that is, yield or plateau stress, the normalized S-N curves are still very much different from each other. In addition, the order of the static mechanical properties of the porous structures based on the different unit cells is not necessarily the same as the order of the fatigue properties of the same structures.

The most interesting case among all porous structures studied here and in a previous study of ours (Amin Yavari et al., 2013) is the case of porous structures based on the cube unit cell. Regardless of how porous they are; these porous structures basically do not fail under fatigue after 10⁶ loading cycles even when the maximum applied stress is 80% of their yield stress. Maximum loads higher than that are not really relevant, because they could easily induce (at the very least) local plastic deformations, meaning that the failure mechanisms is not fatigue anymore. It is important to realize that the porous structures based on the cube unit cell develop only compressive internal stresses (Campoli et al., 2013), while other types of unit cells are loaded in compression as well as in bending (Campoli et al., 2013), meaning that both tensile and compressive stresses are present in the other types of porous structures. Compressive stresses are known to play an important role in fatigue crack growth (Elbert, 1970 and Schijve, 2001). In general, compressive stresses could cause crack closure and retard fatigue crack growth. It is therefore extremely difficult for the fatigue crack to grow in a porous structure that is predominantly loaded in compression, while it could grow much faster in the porous structures based on the other types of unit cells where both compressive and tensile stresses are present due to bending effects.

It is also interesting to understand why the normalized S-N curves of the other types of porous structures are so much different from each other. In particular, why do the porous structures based on the truncated cuboctahedron unit cell show the longest fatigue lives? Detailed analysis of the porous structures under SEM revealed certain differences between the different types of unit cells (Fig. 5-6) that could explain some of the variations in the fatigue behavior of the porous structures. The porous structures based on the cube unit cell were different from the other types of porous structures in the sense that not many notches or manufacturing imperfections could be detected in their struts (Fig. 5-6a). There were also very minimal variations in the diameters of the struts. In comparison, the porous structures based on the diamond unit cell showed more notches and imperfections in the structure of the struts (Fig. 6b). The porous structures based on the truncated cuboctahedron unit cell showed certain level of imperfections as well as some notches in their

structure (Fig. 5-6c). However, the level of imperfections and notches was not as high as in the case of the diamond unit cell. In addition, there was good structural support in the truncated region of the unit cell, further improving the fatigue lives of those porous structures (Fig. 5-6c). Such imperfections and notches could cause stress concentrations and, thus, could have detrimental effects on the fatigue behavior of porous structures. These observations could therefore explain the differences observed in terms of the fatigue behavior of the porous structures based on the different types of unit cells to some extent. It should be, however, noted that comparing the fatigue performance of the porous structures based on the different types of unit cells requires comparative study of stress distribution and notch sensitivity of the different structures. Detailed computational models and/or full strain measurements (Gilat et al., 2009, Patterson et al., 2007, Schmidt et al., 2003 and Zadpoor et al., 2008), for example, using digital image correlation (DIC) (Helfrick et al., 2011 and Pan, 2011), during the mechanical testing of the porous structures are required to answer this type of questions. It is suggested that future studies try to answer this type of questions.

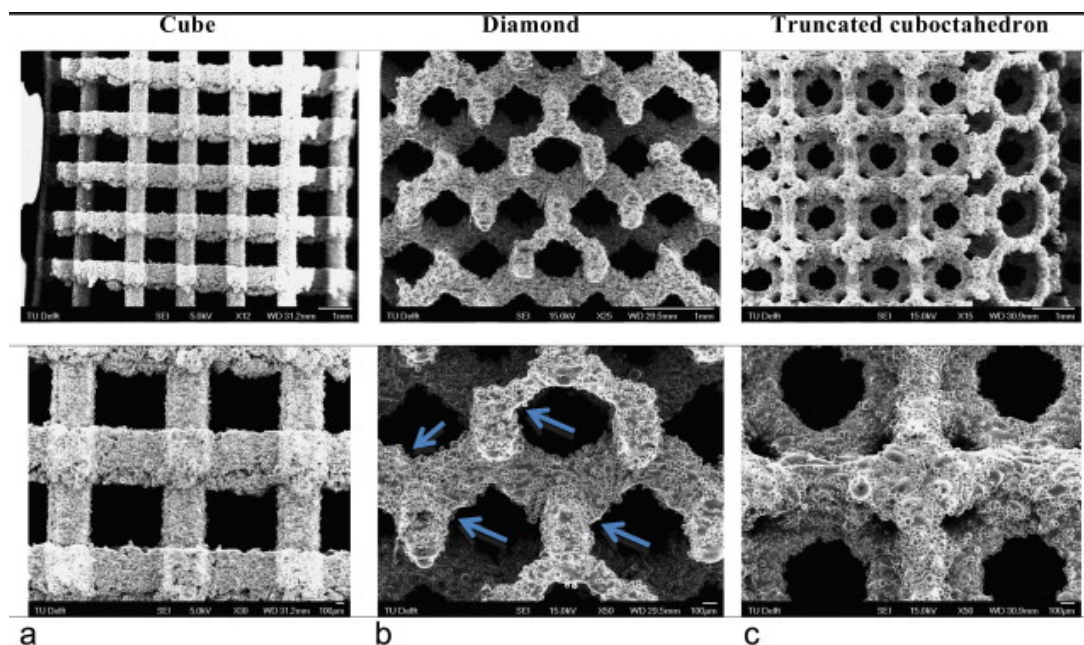


Figure 5-6. SEM pictures of the porous structures made from the cube (a), diamond (b), and truncated cuboctahedron (c) unit cells. Arrows show notches and imperfections in the struts.

One important aspect that needs to be taken into account when interpreting the results of the current study is the effect of loading direction on the fatigue behavior of the porous structures.

While some of the porous structures studied here are isotropic, for example, the ones based on the diamond unit cell, several other types are anisotropic. The mechanical and fatigue properties of the anisotropic porous structures are dependent on the angle between the loading direction and the vertical struts of the unit cell. These effects are probably the largest in the case of the porous structures based on the cubic unit cell. In this study, the porous structures based on the cubic unit cells were loaded in the direction of the vertical struts. As previously mentioned, this type of loading imposes chiefly compressive stresses in the porous structure, resulting in a very long fatigue life. The fatigue life of the cubic porous structures is expected to drastically decrease, if they are loaded in directions other than the direction of the struts of the cubic unit cell. The same anisotropic behavior is valid for several other types of unit cells (Campoli et al., 2013).

In addition to the anisotropic effects caused by the geometry of the unit cell, we have recently observed that the build orientation during the selective laser melting process could also introduce certain level of anisotropy to the porous structure (Wauthle et al., 2014). In general, vertical struts tend to have a much better quality as compared to horizontal struts, while the quality of diagonal struts is in between horizontal and vertical struts (Wauthle et al., 2014). In this context, good quality refers to a dense structure, minimal amount of pores, and good surface quality. These differences in the production quality of struts with different build orientations could also influence the comparative fatigue performance of the different types of porous structures. Porous structures that are primarily made of vertical struts may have better structural integrity as compared to the ones that are primarily made of diagonal and horizontal struts. This is consistent with our findings discussed above.

A three-stage development of strain vs. number of loading cycles was reported in our previous study (Amin Yavari et al., 2013) of the porous structures based on the rhombic dodecahedron unit cells as well as in other studies of the fatigue behavior of porous structures (Hrabe et al., 2011, Sugimura et al., 1999 and Venda et al., 2009). The last stage of the strain development had a much greater pace as compared to both preceding stages. The general trend of strain development during the fatigue tests and the appearance of the porous specimens tested here were consistent with that previously observed three-stage behavior.

As long as the type of unit cell is the same, the data points in the normalized S-N curves conform very well to one single power law. The coefficient of determination (R^2) is in all cases very high, that is, ≥ 0.8 and up to 0.94 (Amin Yavari et al., 2013). This is an important finding, because the power laws determined using the normalized S-N data points could be used as design tools for fatigue design of porous structures. If the power law is available for a specific type of unit cell, the absolute fatigue properties of any new porous structure based on that type of unit cell could be determined by performing some simple static mechanical tests. The static mechanical tests are needed to measure the yield or plateau stress of that particular porous structure and convert the normalized S-N curves estimated by the power laws to absolute S-N curves.

The fatigue behavior of porous biomaterials used for bone substitution is very important particularly when the biomaterials are used for grafting segmental load-bearing bone defects. In previous animal studies where similar porous biomaterials were used for grafting critical sized bone defects in rats, it was observed that a number of implants fractured after a number of weeks, presumably due to fatigue failure (Van der Stok et al., 2013). It is therefore important to consider the fatigue life of porous biomaterials when designing the porous structures aimed for grafting segmental bone defects. Accurate analysis of fatigue during the design process requires good understanding of the nature of the loads experienced by the porous biomaterials during their service life. This type of analysis requires connecting the biomechanical problem of human movement to the problem of designing porous biomaterials and could be performed using patient-specific finite element models of bones (Jaecques et al., 2004, Poelert et al., 2013 and Reggiani et al., 2007). On the other hand, one needs to have access to computational models that could predict the mechanical and failure properties of porous biomaterials given their morphological design. The latter type of computational models is currently only partially available. In particular, there is a lack of reliable computational models that could predict the failure and fatigue properties of meta-biomaterials such as the ones studied here. The data presented in the current study could be used for corroboration of any such computational models.

5.6 Conclusion

The fatigue properties of a particular class of meta-biomaterials, that is, porous titanium biomaterials manufactured using SLM, and the effects of the type of unit cell and porosity on the fatigue properties of the porous structures were studied in the current study. Porous structures based on three types of unit cells were considered, namely cube, diamond, and truncated cuboctahedron. It was observed that both unit cell type and porosity greatly influence the S-N curves of the porous structures. As for the porous structures based on the cube unit cell, none of the specimens failed even when they experienced loads amounting to 80% of their yield strength for 10^6 cycles. For both other types of unit cells, higher porosities resulted in shorter fatigue lives for the same level of applied stress. Moreover, the S-N curves normalized with respect to the yield stress of the porous structures conformed very well to one single power law for each type of unit cell. For the same level of normalized applied stress, the fatigue lives of the porous structures based on the truncated cuboctahedron unit cell were longer than those based on the diamond unit cell. Moreover, both types of unit cells resulted in longer fatigue lives for the same level of normalized applied stress as compared to the rhombic dodecahedron unit cell.

5.7 References

- S.M. Ahmadi, G. Campoli, S. Amin Yavari, B. Sajadi, R. Wauthlé, J. Schrooten, H. Weinans, A. Zadpoor. Mechanical behavior of regular open-cell porous biomaterials made of diamond lattice unit cells. *J. Mech. Behav. Biomed. Mater.*, 34 (2014), pp. 106–115
- S.M. Ahmadi, S. Amin Yavari, R. Wauthle, B. Pouran, J. Schrooten, H. Weinans, A. Zadpoor. Additively manufactured open-cell porous biomaterials made from six different space-filling unit cells: the mechanical and morphological properties (2014)
- S. Amin Yavari, R. Wauthlé, J. van der Stok, A. Riemsdag, M. Janssen, M. Mulier, J.-P. Kruth, J. Schrooten, H. Weinans, A.A. Zadpoor. Fatigue behavior of porous biomaterials manufactured using selective laser melting

-
- S. Amin Yavari, R. Wauthlé, A.J. Böttger, J. Schrooten, H. Weinans, A.A. Zadpoor. Crystal structure and nanotopographical features on the surface of heat-treated and anodized porous titanium biomaterials produced using selective laser melting. *Appl. Surf. Sci.*, 290 (2014), pp. 287–294
- S. Amin Yavari, S. Ahmadi, J. van der Stok, R. Wauthlé, A. Riemsdag, M. Janssen, J. Schrooten, H. Weinans, A. Zadpoor. Effects of bio-functionalizing surface treatments on the mechanical behavior of open porous titanium biomaterials. *J. Mech. Behav. Biomed. Mater.*, 36 (2014), pp. 109–119
- S. Amin Yavari, J. van der Stok, Y.C. Chai, R. Wauthle, Z. Tahmasebi Birgani, P. Habibovic, M. Mulier, J. Schrooten, H. Weinans, A.A. Zadpoor. Bone regeneration performance of surface-treated porous titanium. *Biomaterials*, 35 (24) (2014), pp. 6172–6181
- T. Aydoğmuş, Ş. Bor. Processing of porous TiNi alloys using magnesium as space holder. *J. Alloys Compd.*, 478 (1) (2009), pp. 705–710
- S. Babaei, B.H. Jahromi, A. Ajdari, H. Nayeb-Hashemi, A. Vaziri. Mechanical properties of open-cell rhombic dodecahedron cellular structures. *Acta Mater.*, 60 (6) (2012), pp. 2873–2885
- G. Campoli, M. Borleffs, S.A. Yavari, R. Wauthle, H. Weinans, A. Zadpoor. Mechanical properties of open-cell metallic biomaterials manufactured using additive manufacturing. *Mater. Des.*, 49 (Complete) (2013), pp. 957–965
- Y.C. Chai, S. Truscello, S.V. Bael, F.P. Luyten, J. Vleugels, J. Schrooten. Perfusion electrodeposition of calcium phosphate on additive manufactured titanium scaffolds for bone engineering. *Acta Biomater.*, 7 (5) (2011), pp. 2310–2319
- J. Christensen, F.J.G. de Abajo. Anisotropic metamaterials for full control of acoustic waves. *Phys. Rev. Lett.*, 108 (12) (2012), p. 124301
- A. Cohen, R. Chen, U. Frodis, M.-T. Wu, C. Folk. Microscale metal additive manufacturing of multi-component medical devices. *Rapid Prototyp. J.*, 16 (3) (2010), pp. 209–215
- P.D. Dalton, C. Vaquette, B.L. Farrugia, T.R. Dargaville, T.D. Brown, D.W. Huttmacher. Electrospinning and additive manufacturing: converging technologies. *Biomater. Sci.*, 1 (2) (2013), pp. 171–185

-
- M.R. Dias, J.M. Guedes, C.L. Flanagan, S.J. Hollister, P.R. Fernandes. Optimization of scaffold design for bone tissue engineering: a computational and experimental study. *Med. Eng. Phys.*, 36 (4) (2014), pp. 448–457
- M. Doube, M.M. Kłosowski, I. Arganda-Carreras, F.P. Cordelières, R.P. Dougherty, J.S. Jackson, B. Schmid, J.R. Hutchinson, S.J. Shefelbine. BoneJ: Free and extensible bone image analysis in ImageJ. *Bone*, 47 (6) (2010), pp. 1076–1079
- Elbert, W., The significance of fatigue crack closure. Proceedings of the Damage Tolerance in Aircraft Structures: A Symposium Presented at the Seventy-third Annual Meeting American Society for Testing and Materials, Toronto, Ontario, Canada, 21–26 June 1970, ASTM International, p. 230.
- N. Fang, D. Xi, J. Xu, M. Ambati, W. Srituravanich, C. Sun, X. Zhang. Ultrasonic metamaterials with negative modulus. *Nat. Mater.*, 5 (6) (2006), pp. 452–456
- C.R. Garcia, J. Correa, D. Espalin, J.H. Barton, R.C. Rumpf, R. Wicker, V. Gonzalez. 3D printing of anisotropic metamaterials. *Prog. Electromagn. Res. Lett.*, 34 (2012), pp. 75–82
- A. Gilat, T. Schmidt, A. Walker. Full field strain measurement in compression and tensile split Hopkinson bar experiments. *Experimental Mechanics*, 49 (2) (2009), pp. 291–302
- G.N. Greaves, A. Greer, R. Lakes, T. Rouxel. Poisson’s ratio and modern materials. *Nat. Mater.*, 10 (11) (2011), pp. 823–837
- L.D. Harris, B.-S. Kim, D.J. Mooney. Open pore biodegradable matrices formed with gas foaming. *J. Biomed. Mater. Res.*, 42 (3) (1998), pp. 396–402
- P. Heintz, L. Müller, C. Körner, R.F. Singer, F.A. Müller. Cellular Ti–6Al–4 V structures with interconnected macro porosity for bone implants fabricated by selective electron beam melting. *Acta Biomater.*, 4 (5) (2008), pp. 1536–1544
- M.N. Helfrick, C. Niezrecki, P. Avitabile, T. Schmidt. 3D digital image correlation methods for full-field vibration measurement. *Mechanical Syst. Signal Process.*, 25 (3) (2011), pp. 917–927

N.W. Hrabe, P. Heini, B. Flinn, C. Körner, R.K. Bordia. Compression-compression fatigue of selective electron beam melted cellular titanium (Ti-6Al-4V). *J. Biomed. Mater. Res. B: Appl. Biomater*, 99 (2) (2011), pp. 313–320

ISO, 2011. Mechanical testing of metals – Ductility testing – Compression test for porous and cellular metals, ISO 13314:2011.

S. Jaecques, H. Van Oosterwyck, L. Muraru, T. Van Cleynenbreugel, E. De Smet, M. Wevers, I. Naert, J. Vander Sloten. Individualised, micro CT-based finite element modelling as a tool for biomechanical analysis related to tissue engineering of bone. *Biomaterials*, 25 (9) (2004), pp. 1683–1696

Ju, J., Summers, J.D., Ziegert, J., Fadel, G., Design of honeycomb meta-materials for high shear flexure. Proceedings of the ASME 2009 International Design Engineering Technical Conferences and Computers and Information in Engineering Conference, American Society of Mechanical Engineers, pp. 805–813.

T.K. Kim, J.J. Yoon, D.S. Lee, T.G. Park. Gas foamed open porous biodegradable polymeric microspheres *Biomaterials*, 27 (2) (2006), pp. 152–159.

A. Kolk, J. Handschel, W. Drescher, D. Rothamel, F. Kloss, M. Blessmann, M. Heiland, K.-D. Wolff, R. Smeets. Current trends and future perspectives of bone substitute materials—from space holders to innovative biomaterials. *J. Cranio-Maxillofac. Surg*, 40 (8) (2012), pp. 706–718

U. Levy, M. Abashin, K. Ikeda, A. Krishnamoorthy, J. Cunningham, Y. Fainman. Inhomogenous dielectric metamaterials with space-variant polarizability. *Phys. Rev. Lett*, 98 (24) (2007), p. 243901

G. Lewis. Properties of open-cell porous metals and alloys for orthopaedic applications. *J. Mater. Sci.: Mater. Med*, 24 (10) (2013), pp. 2293–2325

S. Li, Q. Xu, Z. Wang, W. Hou, Y. Hao, R. Yang, L. Murr. Influence of cell shape on mechanical properties of Ti-6Al-4V meshes fabricated by electron beam melting method. *Acta Biomater.*, 10 (10) (2014), pp. 4537–4547

Y. Li, J. Xiong, C.S. Wong, P.D. Hodgson, C.E. Wen. Ti6Ta4Sn alloy and subsequent scaffolding for bone tissue engineering. *Tissue Eng. A*, 15 (10) (2009), pp. 3151–3159

-
- Z. Liang, J. Li. Extreme acoustic metamaterial by coiling up space. *Phys. Rev. Lett*, 108 (11) (2012), p. 114301. G.F. Méjica, A.D. Lantada
- Comparative study of potential pentamodal metamaterials inspired by Bravais lattices. *Smart Mater. Struct*, 22 (11) (2013), p. 115013
- F.P. Melchels, M.A. Domingos, T.J. Klein, J. Malda, P.J. Bartolo, D.W. Hutmacher. Additive manufacturing of tissues and organs. *Prog. Polym. Sci*, 37 (8) (2012), pp. 1079–1104
- L. Murr, K. Amato, S. Li, Y. Tian, X. Cheng, S. Gaytan, E. Martinez, P. Shindo, F. Medina, R. Wicker. Microstructure and mechanical properties of open-cellular biomaterials prototypes for total knee replacement implants fabricated by electron beam melting. *J. Mech. Behav. Biomed. Mater*, 4 (7) (2011), pp. 1396–1411
- W. Niu, C. Bai, G. Qiu, Q. Wang. Processing and properties of porous titanium using space holder technique. *Mater. Sci. Eng. A*, 506 (1) (2009), pp. 148–151
- B. Pan. Recent progress in digital image correlation. *Experimental Mechanics*, 51 (7) (2011), pp. 1223–1235
- C.M. Park, J.J. Park, S.H. Lee, Y.M. Seo, C.K. Kim, S.H. Lee. Amplification of acoustic evanescent waves using metamaterial slabs. *Phys. Rev. Lett*, 107 (19) (2011), p. 194301
- J. Parthasarathy, B. Starly, S. Raman. A design for the additive manufacture of functionally graded porous structures with tailored mechanical properties for biomedical applications. *J. Manufacturing Processes*, 13 (2) (2011), pp. 160–170
- E.A. Patterson, E. Hack, P. Brailly, R.L. Burguete, Q. Saleem, T. Siebert, R.A. Tomlinson, M.P. Whelan. Calibration and evaluation of optical systems for full-field strain measurement. *Optics Lasers Eng*, 45 (5) (2007), pp. 550–564
- L. Podshivalov, C.M. Gomes, A. Zocca, J. Guenster, P. Bar-Yoseph, A. Fischer. Design, analysis and additive manufacturing of porous structures for biocompatible micro-scale scaffolds. *Procedia CIRP*, 5 (2013), pp. 247–252

-
- S. Poelert, E. Valstar, H. Weinans, A.A. Zadpoor. Patient-specific finite element modeling of bones. *Proc. Inst. Mech. Eng. H: J. Eng. Med*, 227 (4) (2013), pp. 464–478
- B. Reggiani, L. Cristofolini, E. Varini, M. Viceconti. Predicting the subject-specific primary stability of cementless implants during pre-operative planning: preliminary validation of subject-specific finite-element models. *J. Biomech*, 40 (11) (2007), pp. 2552–2558
- A. Salerno, M. Oliviero, E. Di Maio, S. Iannace, P. Netti. Design of porous polymeric scaffolds by gas foaming of heterogeneous blends. *J. Mater. Sci. Mater. Med*, 20 (10) (2009), pp. 2043–2051
- J. Schijve. *Fatigue of Structures and Materials*. Springer, The Netherlands (2001)
- T. Schmidt, J. Tyson, K. Galanulis. Full-field dynamic displacement and strain measurement using advanced 3d image correlation photogrammetry: part 1. *Exp. Tech*, 27 (3) (2003), pp. 47–50
- J.A. Schuller, R. Zia, T. Taubner, M.L. Brongersma. Dielectric metamaterials based on electric and magnetic resonances of silicon carbide particles. *Physical Rev. Lett*, 99 (10) (2007), p. 107401
- Y. Sugimura, A. Rabieji, A. Evans, A. Harte, N. Fleck. Compression fatigue of a cellular Al alloy. *Mater. Sci. Eng. A*, 269 (1) (1999), pp. 38–48
- S. Truscello, G. Kerckhofs, S. Van Bael, G. Pyka, J. Schrooten, H. Van Oosterwyck. Prediction of permeability of regular scaffolds for skeletal tissue engineering: a combined computational and experimental study. *Acta Biomaterialia*, 8 (4) (2012), pp. 1648–1658
- S. Van Bael, Y.C. Chai, S. Truscello, M. Moesen, G. Kerckhofs, H. Van Oosterwyck, J.-P. Kruth, J. Schrooten. The effect of pore geometry on the in vitro biological behavior of human periosteum-derived cells seeded on selective laser-melted Ti6Al4V bone scaffolds. *Acta Biomaterialia*, 8 (7) (2012), pp. 2824–2834
- J. Van der Stok, O.P. Van der Jagt, S. Amin Yavari, M.F. De Haas, J.H. Waarsing, H. Jahr, E.M. Van Lieshout, P. Patka, J.A. Verhaar, A.A. Zadpoor. Selective laser melting-produced porous titanium scaffolds regenerate bone in critical size cortical bone defects. *J. Orthop. Res*, 31 (5) (2013), pp. 792–799

-
- L. Vendra, B. Neville, A. Rabiei. Fatigue in aluminum–steel and steel–steel composite foams. *Mater. Sci. Eng. A*, 517 (1) (2009), pp. 146–153
- K. Vynck, D. Felbacq, E. Centeno, A. Căbuz, D. Cassagne, B. Guizal. All-dielectric rod-type metamaterials at optical frequencies. *Phys. Rev. Lett*, 102 (13) (2009), p. 133901
- X. Wang, Y. Li, J. Xiong, P.D. Hodgson, C.E. Wen. Porous TiNbZr alloy scaffolds for biomedical applications. *Acta Biomaterialia*, 5 (9) (2009), pp. 3616–3624
- R. Wauthle, B. Vrancken, B. Beynaerts, K. Jorissen, J. Schrooten, J.-P. Kruth, J. Van Humbeeck. Effects of build orientation and heat treatments on the microstructure and mechanical properties of selective laser melted Ti6Al4V lattice structures. *Addit. Manuf* (2014) (submitted)
- C. Wen, J. Xiong, Y. Li, P. Hodgson. Porous shape memory alloy scaffolds for biomedical applications: a review. *Phys. Scr*, 2010 (T139) (2010), p. 014070
- J.J. Yoon, T.G. Park. Degradation behaviors of biodegradable macroporous scaffolds prepared by gas foaming of effervescent salts. *J. Biomed. Mater. Res*, 55 (3) (2001), pp. 401–408
- A.A. Zadpoor, J. Sinke, R. Benedictus. Experimental and numerical study of machined aluminum tailor-made blanks. *J. Mater. Process. Technol*, 200 (1) (2008), pp. 288–299
- Q. Zhao, J. Zhou, F. Zhang, D. Lippens. Mie resonance-based dielectric metamaterials. *Mater. Today*, 12 (12) (2009), pp. 60–69
- Zhou, F., 2013. Three Dimensional Micro and Nano Fabrication of Metamaterials, (Ph.D. thesis). Northwestern University, US.

Chapter 6 Effects of laser processing parameters on the mechanical properties, topology, and microstructure of additively manufactured porous metallic biomaterials: a vector-based approach

This chapter has been published as:

SM Ahmadi, R Hedayati, RK Ashok Kumar Jain, Y Li, S Leeflang, AA Zadpoor, *Effects of laser processing parameters on the mechanical properties, topology, and microstructure of additively manufactured porous metallic biomaterials: A vector-based approach*, Materials & Design, 2017. p.234-243.

6.1 Abstract

Additively manufactured (AM) porous structures are a new class of biomaterials with many advantages as compared to conventionally produced biomaterials. The goal of this study was to find out how the laser processing parameters including laser power and exposure time affect the mechanical properties, topology, and microstructure of porous biomaterials AM using a novel vector-based approach. Several cylindrical porous specimens were additively manufactured using a wide range of exposure time and laser power. The effects of those parameters on the surface roughness, strut diameter, relative density, hardness, elastic modulus, yield stress, first maximum stress, and plateau stress of the porous structures were studied. The results showed that the rate of change in mechanical and topological properties with respect to exposure time was non-linear while it was linear with respect to the laser power. The results also showed that the effects of laser power and exposure time on the mechanical properties and topology of AM porous structures could be decoupled from each other, enabling derivation of predictive empirical relationships. The empirical and experimental curves showed very good agreement, which further validates the validity of the separation method used for obtaining the empirical relationships. The analytical relationships for elastic modulus and yield stress that we had obtained in a previous study could predict the elastic modulus and yield stress of the porous structures when the energy input was high enough (i.e. exposure times $\geq 450 \mu\text{s}$), because the local mechanical properties of the matrix material decreased for the lower levels of energy input. The change in the mechanical properties of the bulk material due to change in laser processing parameters should thus be taken into account.

6.2 Introduction

Additively manufactured (AM) porous structures are a new class of biomaterials, which have shown many advantages [1-4] over conventional biomaterials. Moreover, it is possible to use AM techniques to fabricate patient-specific implants based on the computed tomography (CT) images of each patient. Titanium and its alloys exhibit properties that make them suitable for biomedical

applications including a high degree of biocompatibility, corrosion resistance, and durability [5-7]. Using AM techniques, it is also possible to manufacture interconnected open-cell porous biomaterials with controlled unit cell shape and size. Porous biomaterials have shown several advantages over traditional solid implants. For example, the high degree of porosity in the volume of such structures drastically decreases the stiffness of the metallic implant to the values close to the stiffness of natural bone. The low stiffness of the implant helps in better distributing the mechanical load between implant and natural bone and, thus, assists in avoiding future bone resorption. The hollow space inside porous structures also allows for easy body fluid transport inside the implant [8, 9] and consequently stimulates bone ingrowth, thereby improving implant fixation and longevity.

The most well-known AM techniques for making metallic porous biomaterials are selective laser melting (SLM) [10] and selective electron beam melting (SEBM) [11]. In both techniques, the usual workflow starts off with constructing a stereo lithography (STL) file describing the geometry of the to-be-manufactured part. The CAD file is then virtually cut into several slices with predefined thicknesses (usually in the range of 30-100 μm [12]). The laser or electron beam then follows the contours found in every slice and melts the specified areas within the powder bed, thereby fusing the powder together and creating a solid part in a layer-by-layer fashion. After the laser/electron beam has scanned the contours found in each layer, the powder bed moves down by the slice thickness and a fresh layer of powder is deposited on the build plate. As a rapid melting-solidification process, the microstructure, topology, and mechanical properties of the resulting part are strongly dependent on the laser/electron beam processing parameters [13-17].

In the past, a few groups [12, 18-23] have studied the effects of laser beam parameters on the microstructure and the mechanical properties of porous biomaterials. In the previous studies, the 3D constructed CAD files of the porous structure have been used to determine the scanning line of the laser beam. In the current study, we use a different, i.e. vector-based, approach to manufacture porous biomaterials. In this approach, no STL files are needed for creating the porous structure. The laser beam simply follows the vectors describing the geometry of the porous biomaterial. The scanning line of the laser beam is located in the central axis of the to-be-manufactured struts. Therefore, only one laser beam path goes through each strut. The laser processing parameters determine the density of the energy input and, thus, the size of the melt pool and the diameter of the struts constituting the porous structure. This approach has two major advantages. First, it

removes the intermediate steps required for creating the STL file and slicing the resulting geometry. Those intermediate steps could be computationally expensive and reduce the accuracy of the contours. Second, there is a direct relationship between the processing parameters and the microstructure, topology, and mechanical properties of the resulting porous structure. We studied how the laser processing parameters including laser power and exposure time affect the microstructure, topology, and mechanical properties of the resulting AM porous biomaterials. Porous structures were therefore additively manufactured with a wide range of exposure times and laser powers. The effect of those parameters on the surface roughness, strut diameter, hardness, relative density, elastic modulus, yield stress, first maximum stress, and plateau stress of the porous structures was studied.

6.3 Materials and methods

6.3.1 Materials and manufacturing

Cylindrical specimens ($\varnothing 15 \times L20\text{mm}$) with a diamond-type cubic lattice structure were built using a commercially available SLM125 machine (Realizer GmbH, Borchten, Germany). The SLM machine was equipped with a YLM-400-AC Ytterbium fiber laser (IPG Photonics Corporation, Oxford, USA) with the ability to emit 400 W of radiation in the wavelength range of 1070 ± 10 nm. As the feedstock, plasma atomized, spherical Ti-6Al-4V-ELI grade 23 powder, according to ASTM B348, with a particle size range of 10 to 40 μm was acquired from AP&C (AP&C Advanced Powders and Coatings Inc., Boisbriand, Canada). Prior to fabrication, the building chamber was flushed with argon gas until an oxygen level of 0.2% and the mild steel building substrate was pre-heated to 100 °C. Table 1 provides an overview of the process parameter settings that were varied during the experiments.

On the build plates, 24 coordinates were defined, 4 horizontally and 6 vertically, with an equal distance of 16 mm. On each coordinate, a specimen was printed. The specimens were divided in three groups (see Table 6-1) based on the scanning time, namely (i) 150, 250, 350 μs , (ii) 450, 550, 650 μs , and (iii) 750, 850, 950 μs . In total, three build plates of a group were manufactured, each containing two specimens of a selected process parameter setting (figure 6-1). Specimens with the same settings were not built on the same build plate coordinate twice. In addition, the printing

sequence was selected to keep a distance of at least three coordinates between subsequently built specimens. In this manner, we attempted to avoid significant deviations in the mechanical and dimensional properties within the specimens of each process parameter setting caused by location on the build plate, neighbouring specimens, or powder coating variations.

The specimens were designed with RDesigner software (Realizer GmbH, Borchten, Germany) based on a vector-driven approach. In this approach, a single diamond cubic unit cell with a cell edge length of 1 mm was prepared by defining its sixteen struts as vectors. Subsequently, this unit cell was translated in three dimensions up to a cylindrical boundary. This cylindrical lattice structure was then sliced in layers of 50 μm , generating a point cloud where each point is an intersection of a slice plane and a vector. Each intersection point represents a site for the laser to melt. In this manner, the strut thickness of the lattice structure is determined by the size of the melt pool during the building process, which is dependent on the laser power and scanning time. This approach therefore differs from the STL-driven approach where the strut thickness is dependent on predefined structural dimensions.

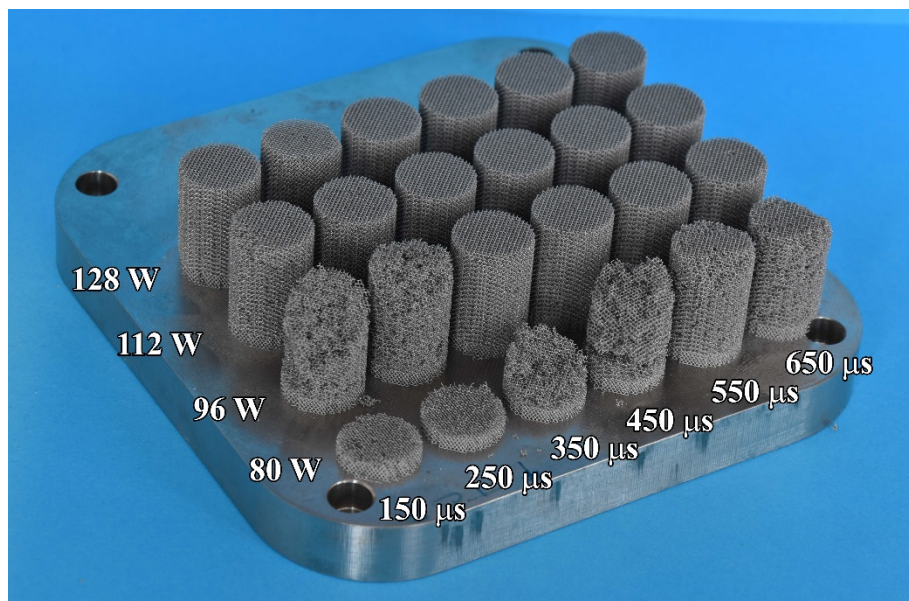


Figure 6-1. A view of all the specimens manufactured by laser powers in the range of 80 W-128 W and exposure times in the range of 150 μs -650 μs .

6.3.2 Static mechanical testing

The mechanical properties of the porous structures were obtained by static compression test using a static test machine (INSTRON 5985, 100 kN load cell) by applying a constant deformation rate of 1.8 mm/min. The compression test was carried out in accordance with ISO standard 13314:2011 [24], which specifies the standard procedure for the mechanical testing of porous and cellular metals. The tests were continued until 60% strain was applied to the specimens. Three specimens were tested for every variation of the porous structures. According to the above-mentioned standard, the elastic gradient ($E_{\sigma_{20-70}}$) was calculated as the gradient of the elastic straight line between two stress values, namely σ_{20} and σ_{70} . σ_{20} and σ_{70} respectively correspond to stress levels 20% and 70% of yield stress. The first maximum compressive strength (σ_{max}) that corresponds to the first local maximum in the stress-strain curve was also calculated. The plateau stress (σ_p) was defined according to the same standard as the arithmetical mean of the stresses between 20% and 40% compressive strain and was calculated for all specimens [24].

6.3.3 Characterization

To measure the density of each structure, the dry weighing method was used. The mass of each porous structure was divided by its volume to calculate its density. The density obtained for each specimen was divided by the density of Ti-6Al-4V bulk material (4430 kg/m^3) to obtain its relative density. MATLAB and Simulink R2014a (MathWorks Inc., Natick, MA, USA) and Microsoft Excel (Microsoft Corporation, Redmond, WA, USA) were used to determine the correlation between the compressive mechanical properties of the specimens and relevant density. Closeness of the data to the fitted regression line was measured by the coefficient of determination.

Optical microscopy (OM, model BX60M, Olympus) was used to measure the average strut diameter of each porous structure type as well as its surface roughness. For each series of porous structures, two specimens were chosen for micro-structural observation. In each porous structure, eight locations were chosen randomly and the strut thickness at that location was measured. By averaging the eight strut thicknesses, the average strut thickness d_{ave} was calculated for each structure type. To calculate the surface roughness R_a , the roughness average formula was used:

$$R_a = \frac{1}{n} \sum_{i=1}^n |y_i| \quad (1)$$

where n is the number of strut thickness measurements ($n = 8$) and y_i is the difference between the measured strut thickness and the calculated average strut thickness ($y_i = d_i - d_{ave}$). Analytical relationships obtained in our previous study [25] for the elastic modulus and yield stress of porous structures based on the diamond unit cell were used for comparing our experimental results with the currently available analytical predictions:

$$E = E_s \frac{(0.46 + 0.17\rho)\rho^2}{(0.46 + 1.17\rho)(3.85 + 1.41\rho)} \quad (2)$$

$$\sigma_y = \sigma_{y,s}(0.35\rho^{1.5}) \quad (3)$$

where E_s and $\sigma_{y,s}$ are respectively the elastic modulus and yield stress of bulk material and are equal to 113.8 GPa and 980 MPa for Ti-6Al-4V [26].

To measure the hardness of the struts, the cross-section of each specimen was grinded to 320 grit size and then polished to 9 μm . The HV 0.5 test protocol devised for measuring the Vickers hardness (DuraScan-70, Struers, Netherlands) was used. The hardness was measured in three random positions on the cross-section of the porous structure, and their average value was calculated.

Six specimens (Table 6-2) were chosen for micro-structural observation. Each of the noted specimens were embedded, grinded to 2000 grit size, and then respectively polished to 3 μm and 1 μm . Finally, the surfaces of the specimens were etched using a modified Kroll's solution (50 ml H₂O + 25 ml HNO₃ + 5 ml HF). Optical microscopy (OM, model BX60M, Olympus) was used to observe the microstructure of the specimens.

Table 6-2. The specimens chosen for micro-structural observation

	150 μ s	250 μ s	350 μ s	450 μ s	550 μ s	650 μ s	750 μ s	850 μ s	950 μ s
80 W			*			*			*
96 W									
112 W									
128 W			*			*			*

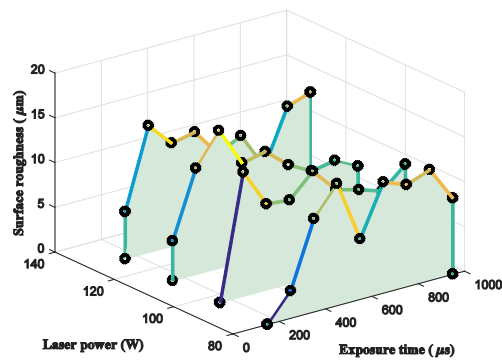
6.4 Results

By changing the laser power and exposure time parameters, porous structures with a wide range of strut diameter ($155 < d < 276$) and relative density ($0.06 < \mu < 0.46$) were manufactured (Figure 6-2b-c). The porous structures made by the lowest laser machine parameters (i.e. exposure time of 150 μ s and laser powers of 80 W and 96 W) were not completely manufactured and therefore were not suitable for mechanical testing. Therefore, the corresponding strut diameter, relative density, and mechanical property values of such porous structures are set to zero in Figure 6-2. The porous structures made by the parameters of $P = 112$ W and $t_s = 150$ μ s were very weak. Although the strut diameter and relative density of those structures were considerable (Figure 6-2b-c), their mechanical properties were negligible (Figure 6- 2d-g).

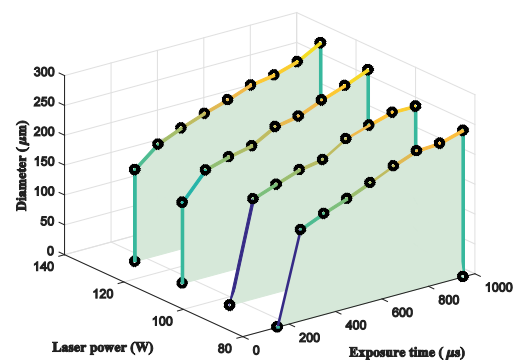
Surface roughness did not show a particular trend with increasing exposure time and/or laser power (Figure 6-2a). Hardness values significantly increased as the exposure time increased from 150 μ s to 250 μ s (Figure 6-2d). After 250 μ s exposure time, the increase in the hardness with increasing exposure time was very gentle. As for the other topological parameters and mechanical properties, increasing the exposure time from 150 μ s to 950 μ s increased all the topological parameters and mechanical properties, i.e. relative density, elastic modulus, yield stress, first maximum stress, and plateau stress, regardless of the laser power. The same was observed for the laser power, i.e. increasing the laser power from 80 W to 128 W always increased the the geometrical and mechanical properties of the porous structure, regardless of the selected exposure time. Therefore,

the specimens made by the largest exposure time and laser power values were the ones with the highest mechanical properties.

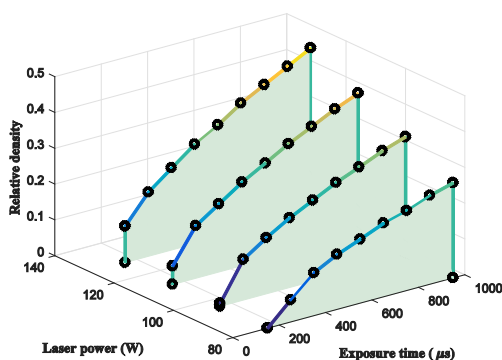
The rate of change in strut diameter, relative density, and the mechanical properties with respect to the laser power was linear, while the noted diagrams showed non-linear behaviour with respect to exposure time (Figure 6-2b-h). The change in the mechanical properties with laser processing parameters (Figure 6-2e-g) usually had two stages: in the first stage, the mechanical properties increased with an increasing slope as the exposure time increased from 150 μs to 350 μs . Most curves became linear at exposure time around 450 μs (as a turning point). From 550 μs to 950 μs , the mechanical properties continued increasing, but with a decreasing slope (Figure 6-2e-g).



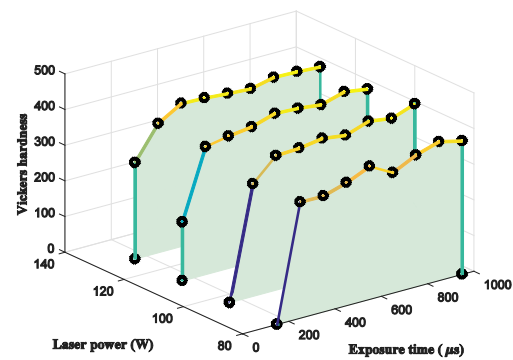
(a)



(b)



(c)



(d)

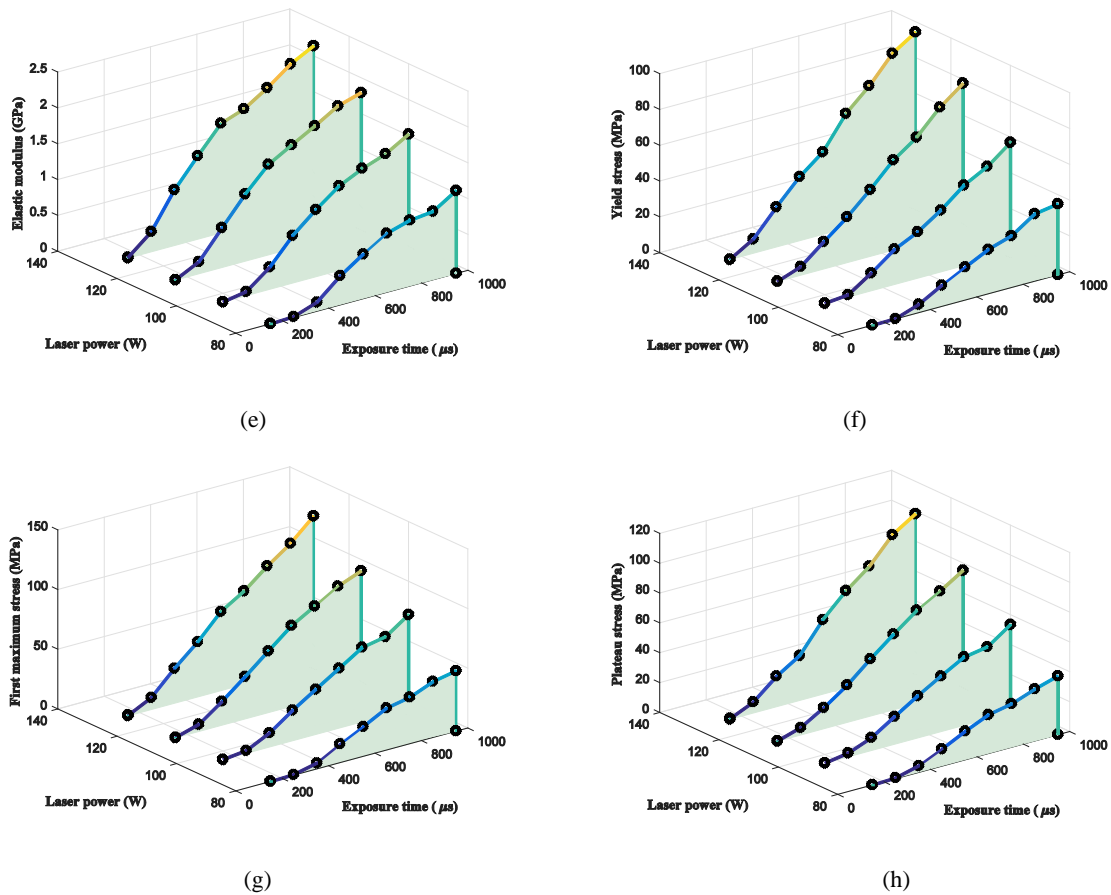


Figure 6-2. Effect of laser power and exposure time on different geometrical and mechanical properties of porous biomaterials: (a) surface roughness, (b) strut diameter, (c) relative density, (d) Vickers hardness, (e) elastic modulus, (f) yield stress, (g) first maximum stress, and (h) plateau stress

The topological and mechanical properties vs. exposure time diagrams of structures made by different laser powers showed similar trends (see Figure S.1b-h in the supplementary document). The topological and mechanical property vs. exposure time diagrams belonging to the structures made with laser powers of 96, 112, and 128 W were similar in shape and resembled the corresponding curves of structures made by laser power of 80 W, save for a scaling factor (Figure S.1b-h). Replotting the curves in a normalized way (by dividing each curve in Figure S.1 by the corresponding value of the structures made by exposure time of 950 μs) verified that observation, as the normalized curved in Figure S.2 almost coincide. On the other hand, the topological and mechanical property curves of structures made with an exposure time of 950 μs vs. laser power

demonstrated a linear trend (Figure S.4). The only exception was the strut diameter vs. laser power and Vickers hardness vs. laser power diagrams (Figure S.4a). By averaging the normalized topological and mechanical property curves (Figure S3), it was seen that it is possible to separate the effects of exposure time and laser power. By fitting curves to each geometrical/mechanical properties curves, the following empirical relationships were obtained:

$$d = (-1.21993 \times 10^{-7} T^2 + 0.000648 T + 0.49563)(0.8414 P + 174.7125) \quad (4)$$

$$\rho = (-5.073232 \times 10^{-7} t_s^2 + 0.00154 t_s - 0.01036)(0.004 P - 0.053893) \quad (5)$$

$$E = (-1.1307 \times 10^{-6} t_s^2 + 0.0026819 t_s - 0.5439)(-0.000128 P^2 + 0.049083 P - 1.9356) \quad (6)$$

$$\sigma_{max} = (-4.9066 \times 10^{-7} t_s^2 + 0.001986 t_s - 0.44125)(1.5161 P - 69.6257) \quad (7)$$

$$\sigma_y = (-6.9939 \times 10^{-8} t_s^2 + 0.0014823 t_s - 0.3326)(1.2418 P - 58.468) \quad (8)$$

$$\sigma_p = (-2.33879 \times 10^{-7} t_s^2 + 0.00168 t_s - 0.3824)(1.3498 P - 69.64) \quad (9)$$

Comparing the empirical and experimental curves showed the validity of the separation method used for obtaining the empirical relationships (compare the black and red curves in Figure 6-3). Plotting the analytical elastic modulus and yield stress curves over the empirical and experimental curves (Figure 6-3c-d) also demonstrated the good correlation of the three noted values.

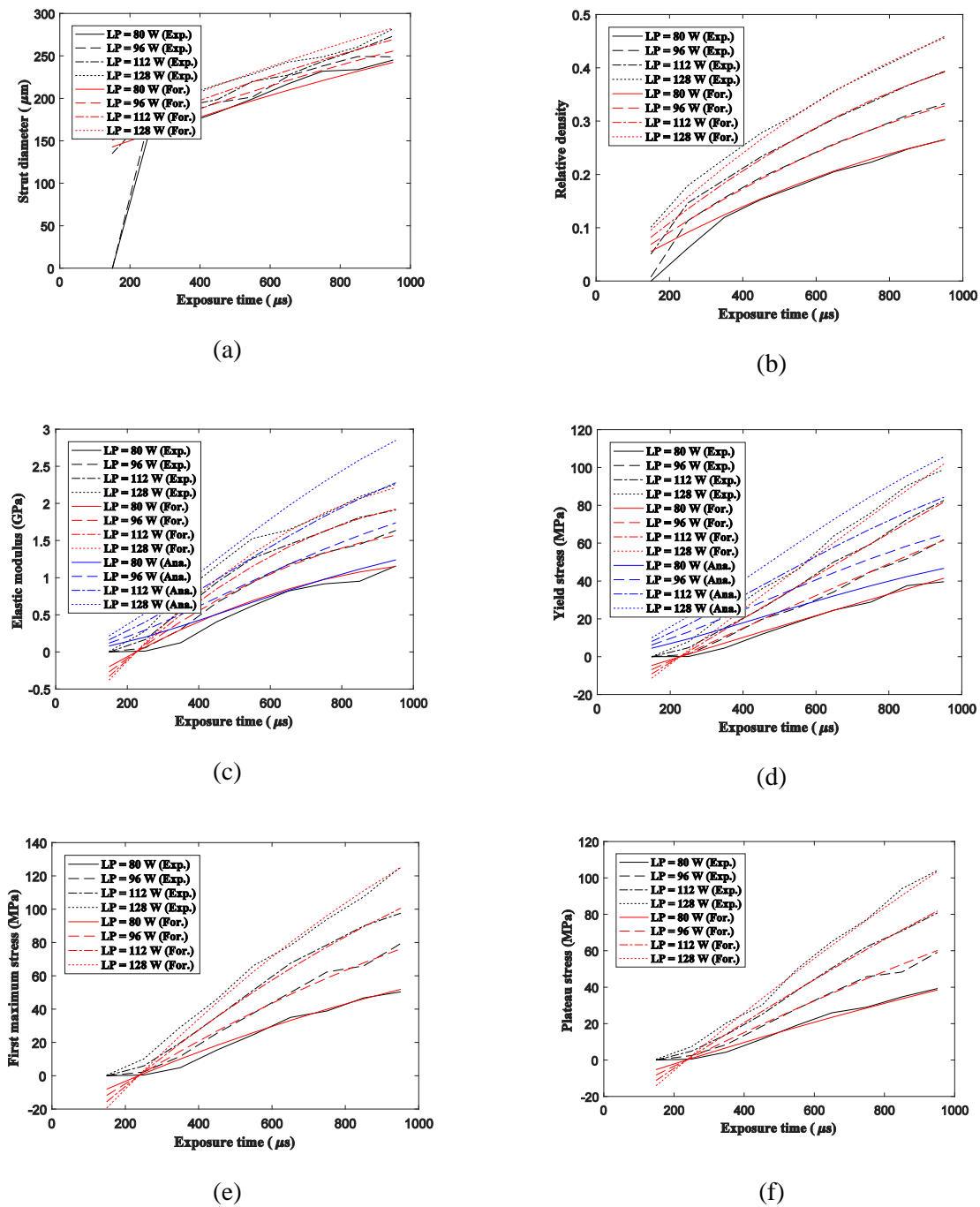


Figure 6-3 . Comparison of geometrical and mechanical properties curves of different processing parameters between the experimental results, empirical formulas, and analytical prediction: (a) strut diameter, (b) relative density, (c) elastic modulus, (d) yield stress, (e) first maximum stress, and (f) plateau stress.

Optical microscopy showed no significant difference between the microstructures of the selected specimens (Figure 6-4).

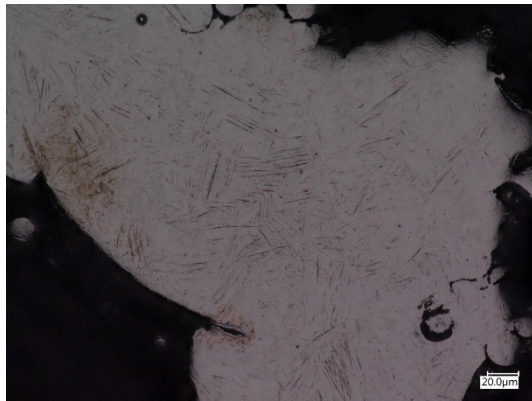
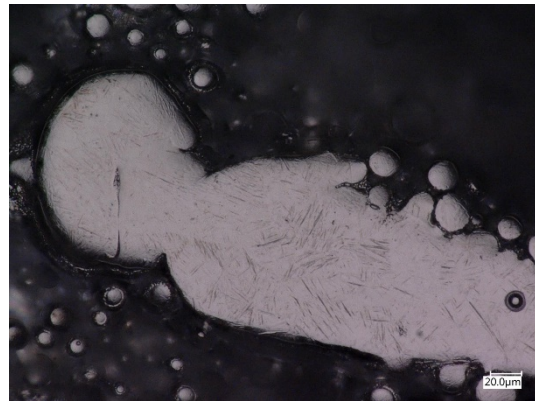
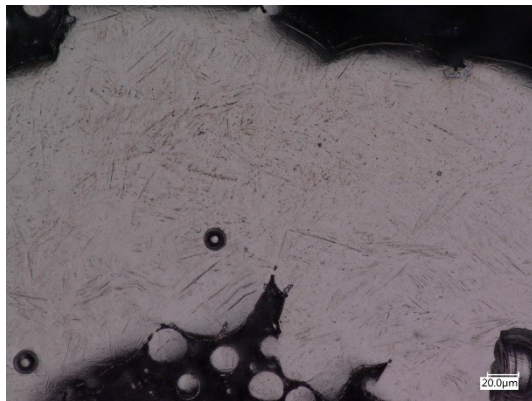
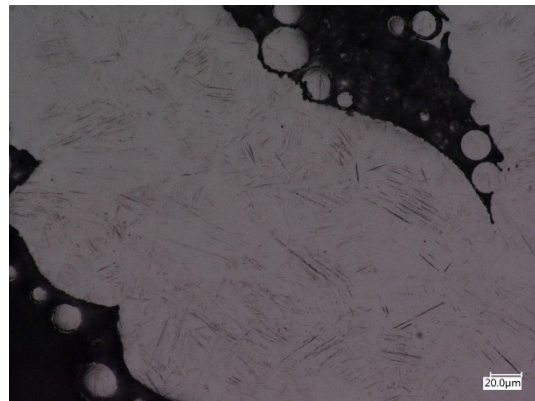
(a) 80 W - 350 μ s(b) 128 W - 350 μ s(c) 80 W - 650 μ s(d) 128 W - 650 μ s(e) 80 W - 950 μ s(f) 128 W - 950 μ s

Figure 6-4. Microscopic images of selected specimens.

6.5 Discussion

The results of this study demonstrated that the vector-based approach is a viable alternative for STL-based design of AM porous biomaterials. The microstructure and mechanical properties of the matrix material, as indicated by the hardness values within the struts, were similar as long as the laser energy input was high enough. It was therefore possible to achieve porous biomaterials with different porosities, strut diameters, and relative densities simply by modifying the laser processing parameters. By increasing both the exposure time and laser power, the global mechanical properties (elastic modulus, yield stress, first maximum stress, and plateau stress) of the porous structure increased. This increase could be due to two reasons: first, increasing the laser processing parameters increases the size of the melting pools. As shown by our previous analytical, numerical, and experimental studies [25, 27-29], this increase in melting pool (and as a result strut thickness and relative density) is very influential in increasing the mechanical properties of the porous structure. The other influence of increasing the laser processing parameters is the relatively modest increase in the local mechanical properties of the material. The results of the current study showed that both aspects of strut diameter and local mechanical properties (measured through Vickers hardness) have increased by increasing the laser processing parameters, although the effect of the former is of greater importance for most processing parameter ranges (compare Figure S1 b and d). For exposure times less than 350 μs , the Vickers hardness decreased significantly, which shows that the low mechanical properties in low processing parameters arises from both strut diameter and local mechanical properties of the material. The elastic modulus and yield stress of the porous structures made by medium and high laser processing parameters (i.e. exposure times $\geq 450 \mu\text{s}$) were in very good accordance with the mechanical properties predicted by analytical relationships presented in our previous study [25]. The experimentally measured elastic modulus and yield stress of porous structures manufactured by low processing parameters were, however, much lower than the analytical predictions. To have accurate analytical predictions, the change in mechanical properties of the matrix material due to change in the laser processing parameters should be also considered. Moreover, the irregularities caused by the AM process are known to decrease the mechanical properties of AM porous biomaterials [30]. Since the manufacturing irregularities are mostly related to the manufacturing technique and parameters such as powder size and laser spot

size, we could assume the absolute dimensions of the irregularities to be the same regardless of the relative density of the porous structures. The effects of manufacturing irregularities are therefore expected to be higher for porous structures with smaller strut dimensions and relative densities. That may be the reason why the measured mechanical properties do not match analytical predictions for the lower range of laser processing parameters that result in the lowest strut diameters and relative densities.

In addition to the laser power and scanning time, a few other parameters could influence the local and overall mechanical properties of porous biomaterials. The effects of changing the value of other parameters such as overlap rate, slice thickness, hatch angle, and slice thickness on the tensile properties of SLM 304 stainless steel solid structures have been studied before [18]. Investigation of the effect of changing such parameters in porous biomaterials is of greater significance. That is due to the fact that the ratio of external surface area to the occupied volume of porous structures is much greater than that of solid parts. That is due to the presence of the free surfaces inside the pores. Particularly, Guan et al [18] have found out that the slice thickness plays an important role in the surface roughness (rather than tensile properties) of SLM solid parts. The surface roughness plays an important role in determining the mechanical properties of porous biomaterials due to three main reasons. First, as mentioned above, the ratio of surface area to the occupied volume in porous biomaterials is very high, which gives rise to the importance of the surface roughness. Second, due to the cyclic nature of the movements of the human body, porous biomaterials may experience fatigue failure. The surface quality plays an important role in the size of micro-cracks, which is very important in crack initiation and propagation [31-34]. Third, since the strut thickness in porous structures is usually very small (mostly in the range of 100-300 μm), the thickness of rough external surface is usually comparable to the thickness of the inner well-molten parts of the struts. Therefore, decreasing the thickness of the rough surface in the external part will increase the thickness of the desired well-molten parts of the struts, which play the most important role in load-bearing of the implant. It is therefore suggested to carry out a similar study on the effects of other SLM processing parameters on the mechanical response of porous biomaterials.

The results of this study showed that by varying the exposure time and laser power processing parameters in the ranges of $150 \mu\text{s} < t_s < 950 \mu\text{s}$ and $80 \text{ W} < P < 128 \text{ W}$, it is possible to gain

relative densities in the range of $0 < \mu < 45.9\%$, relative elastic modulus in the range of $0 < \frac{E}{E_s} < 1.98\%$, and relative yield stress in the range of $0 < \frac{\sigma_y}{\sigma_{ys}} < 13.9\%$. The relatively low range of resulting elastic modulus and yield stress does not correspond to the chosen range of processing parameters but it mostly relates to the unit cell types. Using other unit cell types, it is possible to reach up to $\frac{E}{E_s} = 25\%$ and $\frac{\sigma_y}{\sigma_{ys}} < 17\%$ for relative densities around $\mu = 50\%$. By introducing the empirical relationship for the strut diameter (i.e. Eq. (4)) to the analytical relationships obtained for the relative density, elastic modulus, and yield stress of other unit cell types [27, 35-40], it is possible to generalize the empirical relationships to other unit cell types.

Since different topological and mechanical property empirical relationships presented in this study for vector-based porous structures (i.e. Eq. (4-9)) are different functions of processing parameters, one can reach a porous structure with the desired distribution of topological and mechanical properties using optimization algorithms. Therefore, one is able to manufacture any porous structure type by defining the unit cell type, unit cell shape, and laser processing parameters without any need to use CAD programs.

6.6 Conclusion

In this study, the effects of variation in two main laser processing parameters, namely laser power P and scanning time t_s , on the topological parameters and mechanical properties (relative density, surface hardness, elastic modulus, yield stress, plateau stress, and first maximum stress) were investigated. It was found that all the noted mechanical properties increase with increasing either laser power or scanning time. Therefore, among the 36 types of porous structure manufactured in this project (with $80\text{ W} < P < 128\text{ W}$ and $150\ \mu\text{s} < t_s < 950\ \mu\text{s}$), the structures with $P = 128\text{ W}$ and $t_s = 950\ \mu\text{s}$ had the highest mechanical properties. Manufacturing structures with the two lowest processing parameters (exposure time of $150\ \mu\text{s}$ and laser powers of 80 W and 96 W) was not possible since the lower layers of those porous structure were not able to support their higher layers. Among the successfully manufactured structures, the lowest mechanical properties belonged to the structure with the lowest processing parameters ($P = 112\text{ W}$ and $t_s = 150\ \mu\text{s}$). The rate of

change in the topological and mechanical properties with respect to the exposure time was non-linear while it was linear with respect to laser power. Most curves had two stages: in the first stage, the mechanical properties increased with an increasing slope as the exposure time increased from 150 μs to 350 μs . Most curves became linear at exposure times around 450 μs (as a turning point). From 550 μs to 950 μs , the mechanical properties continued increasing, but with a decreasing slope. The results also showed that the effects of laser power and exposure time on the topological and mechanical properties of AM porous structures could be decoupled. Empirical relationships for geometrical and mechanical properties as functions of processing parameters (exposure time and laser power) were therefore obtained. Comparing the empirical and experimental curves showed the validity of the separation method used for obtaining the empirical relationships. The *analytical* elastic modulus and yield stress relationships obtained in our previous study for the porous structures based on the diamond unit cell were also able to predict the noted mechanical properties provided that the laser processing parameters were sufficiently large (i.e. exposure times $\geq 450 \mu\text{s}$). To have accurate analytical predictions, the change in mechanical properties of the bulk material due to change in laser processing parameters as well as the effects of manufacturing irregularities on the mechanical properties of porous structures should also be taken into account.

6.7 References

- [1] Wang X, Xu S, Zhou S, Xu W, Leary M, Choong P, et al. Topological design and additive manufacturing of porous metals for bone scaffolds and orthopaedic implants: A review. *Biomaterials* 2016;83:127-41.
- [2] Zadpoor AA, Malda J. *Additive Manufacturing of Biomaterials, Tissues, and Organs*. Springer; 2017.
- [3] Horn TJ, Harrysson OL. Overview of current additive manufacturing technologies and selected applications. *Science progress* 2012;95:255-82.
- [4] Frazier WE. Metal additive manufacturing: a review. *Journal of Materials Engineering and Performance* 2014;23:1917-28.

-
- [5] Murr L, Quinones S, Gaytan S, Lopez M, Rodela A, Martinez E, et al. Microstructure and mechanical behavior of Ti–6Al–4V produced by rapid-layer manufacturing, for biomedical applications. *Journal of the mechanical behavior of biomedical materials* 2009;2:20-32.
- [6] Brunette DM, Tengvall P, Textor M, Thomsen P. *Titanium in medicine: material science, surface science, engineering, biological responses and medical applications*: Springer Science & Business Media; 2012.
- [7] Long M, Rack H. Titanium alloys in total joint replacement—a materials science perspective. *Biomaterials* 1998;19:1621-39.
- [8] Van Bael S, Chai YC, Truscello S, Moesen M, Kerckhofs G, Van Oosterwyck H, et al. The effect of pore geometry on the in vitro biological behavior of human periosteum-derived cells seeded on selective laser-melted Ti6Al4V bone scaffolds. *Acta biomaterialia* 2012;8:2824-34.
- [9] Bobbert F, Lietaert K, Eftekhari A, Pouran B, Ahmadi S, Weinans H, et al. Additively manufactured metallic porous biomaterials based on minimal surfaces: A unique combination of topological, mechanical, and mass transport properties. *Acta Biomaterialia* 2017.
- [10] Hedayati R, Sadighi M, Aghdam MM, Janbaz S, Zadpoor AA. How does tissue regeneration influence the mechanical behavior of additively manufactured porous biomaterials? *Journal of the mechanical behavior of biomedical materials* 2016;Submitted.
- [11] Li X, Wang C, Zhang W, Li Y. Properties of a porous Ti—6Al—4V implant with a low stiffness for biomedical application. *Proceedings of the Institution of Mechanical Engineers, Part H: Journal of Engineering in Medicine* 2009;223:173-8.
- [12] Song B, Dong S, Zhang B, Liao H, Coddet C. Effects of processing parameters on microstructure and mechanical property of selective laser melted Ti6Al4V. *Materials & Design* 2012;35:120-5.
- [13] Tsopanos S, Mines R, McKown S, Shen Y, Cantwell W, Brooks W, et al. The influence of processing parameters on the mechanical properties of selectively laser melted stainless steel microlattice structures. *Journal of Manufacturing Science and Engineering* 2010;132:041011.

-
- [14] Zhang B, Dembinski L, Coddet C. The study of the laser parameters and environment variables effect on mechanical properties of high compact parts elaborated by selective laser melting 316L powder. *Materials Science and Engineering: A* 2013;584:21-31.
- [15] Hrabec N, Quinn T. Effects of processing on microstructure and mechanical properties of a titanium alloy (Ti-6Al-4V) fabricated using electron beam melting (EBM), part 1: Distance from build plate and part size. *Materials Science and Engineering: A* 2013;573:264-70.
- [16] Safdar A, He H, Wei L-Y, Snis A, Chavez de Paz LE. Effect of process parameters settings and thickness on surface roughness of EBM produced Ti-6Al-4V. *Rapid Prototyping Journal* 2012;18:401-8.
- [17] Wauthle R, Vrancken B, Beynaerts B, Jorissen K, Schrooten J, Kruth J-P, et al. Effects of build orientation and heat treatment on the microstructure and mechanical properties of selective laser melted Ti6Al4V lattice structures. *Additive Manufacturing* 2015;5:77-84.
- [18] Guan K, Wang Z, Gao M, Li X, Zeng X. Effects of processing parameters on tensile properties of selective laser melted 304 stainless steel. *Materials & Design* 2013;50:581-6.
- [19] Zhang B, Liao H, Coddet C. Effects of processing parameters on properties of selective laser melting Mg-9% Al powder mixture. *Materials & Design* 2012;34:753-8.
- [20] Bormann T, Schumacher R, Müller B, Mertmann M, de Wild M. Tailoring selective laser melting process parameters for NiTi implants. *Journal of materials engineering and performance* 2012;21:2519-24.
- [21] Sallica-Leva E, Jardini A, Fogagnolo J. Microstructure and mechanical behavior of porous Ti-6Al-4V parts obtained by selective laser melting. *Journal of the mechanical behavior of biomedical materials* 2013;26:98-108.
- [22] Delgado J, Ciurana J, Rodríguez CA. Influence of process parameters on part quality and mechanical properties for DMLS and SLM with iron-based materials. *The International Journal of Advanced Manufacturing Technology* 2012;60:601-10.

-
- [23] Loh L-E, Chua C-K, Yeong W-Y, Song J, Mapar M, Sing S-L, et al. Numerical investigation and an effective modelling on the Selective Laser Melting (SLM) process with aluminium alloy 6061. *International Journal of Heat and Mass Transfer* 2015;80:288-300.
- [24] Standard I. ISO 13314: 2011 (E)(2011) Mechanical testing of metals—ductility testing—compression test for porous and cellular metals. Ref Number ISO;13314:1-7.
- [25] Ahmadi S, Campoli G, Yavari SA, Sajadi B, Wauthlé R, Schrooten J, et al. Mechanical behavior of regular open-cell porous biomaterials made of diamond lattice unit cells. *Journal of the mechanical behavior of biomedical materials* 2014;34:106-15.
- [26] Simonelli M, Tse YY, Tuck C. Effect of the build orientation on the Mechanical Properties and Fracture Modes of SLM Ti–6Al–4V. *Materials Science and Engineering: A* 2014;616:1-11.
- [27] Zadpoor AA, Hedayati R. Analytical relationships for prediction of the mechanical properties of additively manufactured porous biomaterials. *Journal of Biomedical Materials Research Part A* 2016.
- [28] Hedayati R, Sadighi M, Mohammadi-Aghdam M, Zadpoor A. Mechanical properties of regular porous biomaterials made from truncated cube repeating unit cells: Analytical solutions and computational models. *Materials Science and Engineering: C* 2016;60:163-83.
- [29] Ahmadi SM, Yavari SA, Wauthle R, Pouran B, Schrooten J, Weinans H, et al. Additively manufactured open-cell porous biomaterials made from six different space-filling unit cells: The mechanical and morphological properties. *Materials* 2015;8:1871-96.
- [30] Campoli G, Borleffs M, Yavari SA, Wauthle R, Weinans H, Zadpoor AA. Mechanical properties of open-cell metallic biomaterials manufactured using additive manufacturing. *Materials & Design* 2013;49:957-65.
- [31] Yavari SA, Ahmadi S, Wauthle R, Pouran B, Schrooten J, Weinans H, et al. Relationship between unit cell type and porosity and the fatigue behavior of selective laser melted meta-biomaterials. *Journal of the mechanical behavior of biomedical materials* 2015;43:91-100.

-
- [32] Hedayati R, Hosseini-Toudeshky H, Sadighi M, Mohammadi-Aghdam M, Zadpoor A. Computational prediction of the fatigue behavior of additively manufactured porous metallic biomaterials. *International Journal of Fatigue* 2016;84:67-79.
- [33] Chan KS, Koike M, Mason RL, Okabe T. Fatigue life of titanium alloys fabricated by additive layer manufacturing techniques for dental implants. *Metallurgical and Materials Transactions A* 2013;44:1010-22.
- [34] Wycisk E, Solbach A, Siddique S, Herzog D, Walther F, Emmelmann C. Effects of defects in laser additive manufactured Ti-6Al-4V on fatigue properties. *Physics Procedia* 2014;56:371-8.
- [35] Hedayati R, Sadighi M, Mohammadi-Aghdam M, Zadpoor A. Analytical relationships for the mechanical properties of additively manufactured porous biomaterials based on octahedral unit cells. *Applied Mathematical Modelling* 2017.
- [36] Hedayati R, Sadighi M, Mohammadi Aghdam M, Zadpoor AA. Mechanical properties of additively manufactured thick honeycombs. *Materials* 2016;9:613.
- [37] Gibson LJ, Ashby MF. *Cellular solids: structure and properties*: Cambridge university press; 1999.
- [38] Babae S, Jahromi BH, Ajdari A, Nayeb-Hashemi H, Vaziri A. Mechanical properties of open-cell rhombic dodecahedron cellular structures. *Acta Materialia* 2012;60:2873-85.
- [39] Ko W. Deformations of foamed elastomers. *Journal of Cellular Plastics* 1965;1:45-50.
- [40] Ptochos E, Labeas G. Elastic modulus and Poisson's ratio determination of micro-lattice cellular structures by analytical, numerical and homogenisation methods. *Journal of Sandwich Structures & Materials* 2012;14:597-626.

Chapter 7 Isolated and Modulated effects of topological design and material type on the mechanical properties of additively manufactured porous biomaterials

This chapter has been published as:

R Hedayati, **SM Ahmadi**, K Lietaert, B Pouran, Y Li, H Weinans, CD Rans, AA Zadpoor, *Isolated and modulated effects of topology and material type on the mechanical properties of additively manufactured porous biomaterials, Journal of the mechanical behavior of biomedical materials*, 2018

7.1 Abstract

Additive manufacturing (AM) techniques offer the possibility to produce open-cell porous implants with the desired topological design at the micro-scale. The vast majority of previous theoretical and numerical studies carried out on the mechanical properties of AM porous biomaterials had assumed their normalized elastic mechanical properties to be independent from the material type and only dependent on the topological design. In this study, we evaluated this assumption and tried to quantify the isolated and modulated effects of topological design and material type on the mechanical properties of AM porous biomaterials. Towards this aim, we assembled a large dataset comprising the mechanical properties of AM porous with different topological designs (i.e. different unit cell types and relative densities) and material types. Porous structures were additively manufactured from Co-Cr using selective laser melting (SLM) machine and tested under quasi-static compression. The normalized mechanical properties obtained from those structures were compared with mechanical properties available from our previous studies for porous structures made from Ti-6Al-4V, tantalum, and pure titanium as well as with analytical solutions. The normalized values of elastic modulus and yield stress were found to be relatively close to each other as well as in agreement with analytical solutions regardless of material type. However, the material type was found to systematically affect the mechanical properties of AM porous biomaterials in general and the plateau stress and energy absorption capacity in particular. To put this in perspective, topological design could cause up to 10-fold difference in the mechanical properties of AM porous biomaterials while up to 2-fold difference was observed as a consequence of changing the material type.

7.2 Introduction

Recent advances in additive manufacturing (AM) techniques have enabled fabrication of porous biomaterials with arbitrarily complex topology of the micro-architecture. Since the mechanical properties of such AM porous biomaterials are directly related to the topology of their

microarchitecture [1-5], it is possible to design porous biomaterials that satisfy certain design objectives. For example, AM porous biomaterials with mechanical properties similar to those of native bone tissue could be made from metallic alloys whose mechanical properties are a few orders of magnitude higher than bone [6-8]. This decreased stiffness prevents a common problem associated with solid implants known as stress shielding. The open-cell interconnected hollow space inside porous implants also allows for adjustment of scaffold permeability [9, 10] to facilitate mass transport and, thus, cell oxygenation and nutrition. Moreover, bone could grow into the open pore structure, which in turn results in improved implant fixation and osseointegration [11, 12]. Finally, the porous structure increases the surface area of such AM biomaterials, which could then be used for bio-functionalization purposes, for example, to attach molecules that improve bone tissue regeneration performance [13-15] or to induce antibacterial effects [16-18].

Most of the properties discussed above including the mechanical properties, mass transport properties (such as permeability), and surface area are directly related to the topology of the micro-architecture of additively manufactured porous biomaterials. That is why a major paradigm in the development of such biomaterials has been “topological design” [19]. Within the context of mechanical properties, topological design refers to the adjustment of the quasi-static [20-22] and fatigue [23, 24] properties of additively manufactured porous biomaterials through rational design of the geometry of their micro-architecture. This approach has been supported by a relatively large number of studies within the last few years that have found that the normalized (i.e. the ratio of a property in the porous structure to that of the bulk material) elastic mechanical properties including the elastic modulus, yield stress, and Poisson’s ratio of AM porous biomaterials are strongly dependent on the topology of the porous structure [25-29]. The relevant topological parameters include relative density or adjustable porosity, geometry of the strut cross-section, and shape of the unit cell [25-32].

Given the direct and strong influence of topology, the vast majority, if not all, of analytical and computational models used for predicting the mechanical properties of such biomaterials assume that the *normalized* mechanical properties of AM porous biomaterials are the same regardless of the material used for making the porous structure [27, 33, 34]. In other words, previous studies have assumed there is no modulation between the material type and topology in determining the mechanical properties of AM porous biomaterials. Therefore, the material properties of the bulk

material can be used as scale factors which convert the normalized mechanical properties of the porous structure to its absolute values.

In this study, we aim to determine whether such an assumption is valid and, thus, try to separate the effects of topology from those of material type. Investigating the effects of material type is important, because laser processing parameters and the resulting microstructure as well as bulk material properties could change from one material to the other. A large dataset of the mechanical properties of AM porous biomaterials based on various types of topological designs and different material types is needed to answer the above-mentioned research question. We therefore used selective laser melting to manufacture porous metallic biomaterials from Co-Cr with three different types of repeating unit cells and three to four porosities (for each unit cell type). The topological features and compressive mechanical properties of the obtained specimens were then determined respectively using micro-computed tomography (μ CT) and mechanical testing. In our previous studies, we had additively manufactured, topologically characterized, and mechanically tested similar (same unit cell designs) porous structures from other types of materials including the titanium alloy Ti-6Al-4V [35], pure titanium [36], and tantalum [37]. The entire dataset of four different types of materials, three types of repeating unit cells, and multiple porosities was then used to determine whether or not there is a modulation between the material type and topology in determining the *normalized* mechanical properties of AM porous biomaterials.

7.3 Materials and method

7.3.1 Materials and manufacturing

Co-Cr porous structures (Figure 7-1) were additively manufactured using a ProX DMP 320 (3D Systems). Co-Cr powder (Cr 28.5%, Mo 6%, other specifications according to ASTM F75) was processed on top of a solid substrate under an inert atmosphere with less than 50 ppm of O₂. Three different unit cell types (truncated cuboctahedron, diamond, and rhombic dodecahedron) were chosen for fabricating the porous structures. For each unit cell type, different strut thicknesses were used in order to achieve porous structures with different relative densities (Table 7-1).

Table 7-1. Topological design and morphological properties of the porous structures having different unit cell types and sizes

	Relative density		Strut size (μm)		Pore size (μm)	
	Dry weighting	μCT	Nominal (Design)	μCT	Nominal (Design)	μCT
Truncated cuboctahedron (TCO)						
TCO-1	0.236	0.27	324	343.2	876	917.76
TCO-2	0.269	0.28	356	339.84	844	895.2
TCO-3	0.336	0.334	410	396.96	790	821.472
TCO-4	0.386	0.424	460	433.584	740	669.312
Rhombic dodecahedron (RD)						
RD-1	0.299	0.292	310	349.44	590	506.256
RD-2	0.372	0.475	370	402.528	530	492.576
RD-3	0.415	0.532	430	446.4	470	431.76
Diamond (D)						
D-1	0.209	0.272	320	357.216	580	650.736
D-1	0.267	0.35	375	390.384	525	541.488
D-3	0.34	0.445	415	440.928	485	465.6
D-4	0.401	0.526	450	486.288	450	411.36

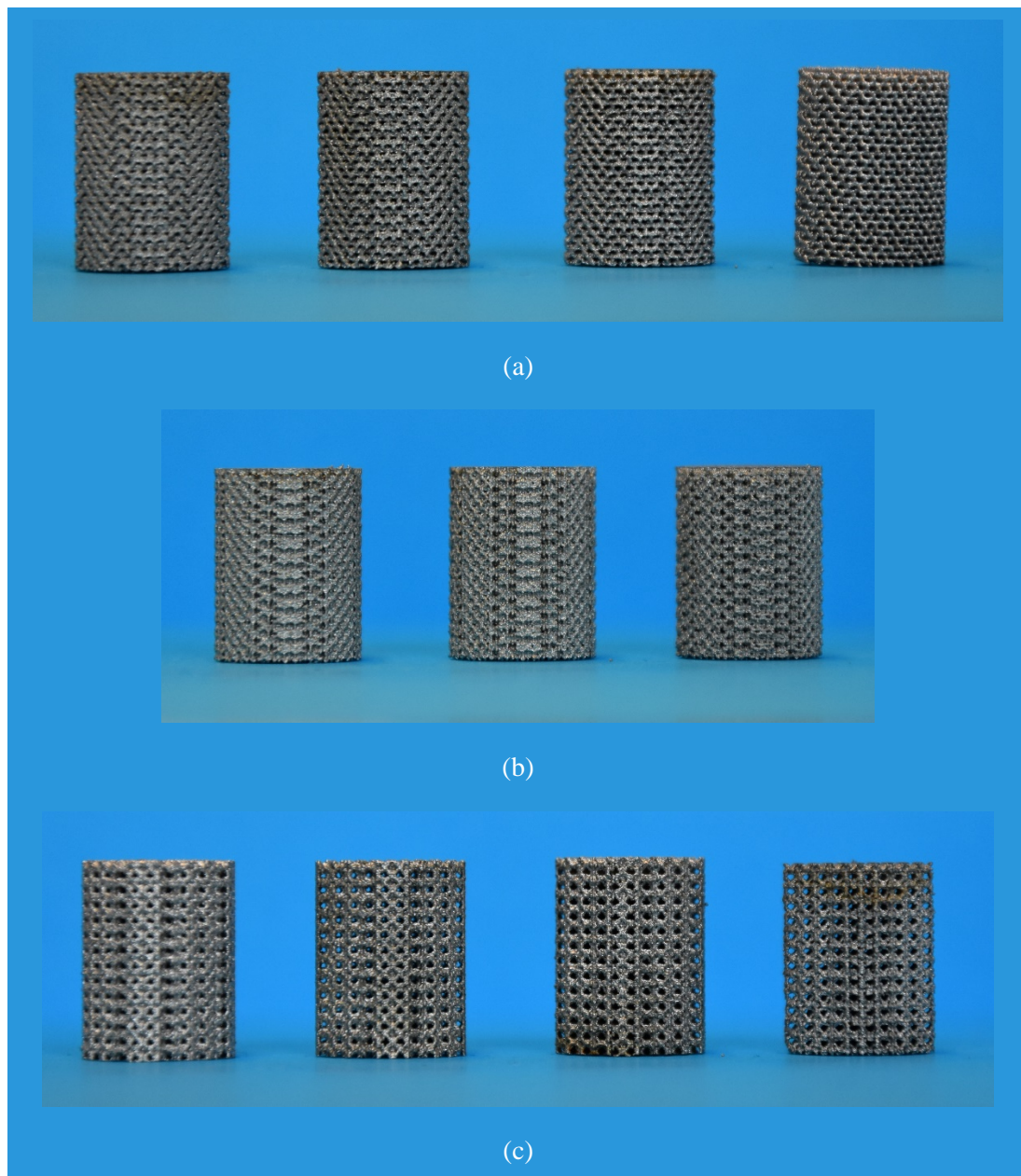


Figure 7-1. Side view of the additively manufactured Co-Cr porous structures based on (a) diamond (b) rhombic dodecahedron, and (c) truncated cuboctahedron unit cells

All specimens were cylindrical in shape with diameters of 15 mm and lengths of 20 mm. The unit cell size was 1.5 mm. In addition to porous biomaterials, several solid specimens were additively manufactured and tested to obtain the mechanical properties of the bulk material (Figure 7-2 and Table 7-2). For the bulk Co-Cr material, the elastic modulus was obtained using an MTS with 500 kN load cell (MTS Systems Corporation, Eden Prairie, MN, USA) mechanical testing machine and a setup

employing the impulse excitation technique (RFDA basic, IMCE, Genk, Belgium) that works on the basis of measuring natural frequencies in vibration [38]. Several solid cylindrical samples with diameters of 15 mm and lengths of 20 mm were AM manufactured and compressed with displacement rate of 1.8 mm/min. To leave out the non-sample displacement from the results read from the test machine, the load-displacement of the machine without installed sample was obtained and subtracted from the results [39]. As another displacement recording method, KFG-5-120-D16-11 (KYOWA, Japan) strain gauges (length of 5 mm, resistance of $119.8 \pm 0.3 \Omega$, adoptable thermal expansion of 11.7 PPM/°C) were installed on the solid cylindrical samples. The specimens used for impulse excitation technique were brick-shaped with the following dimensions: 6.9×34.9×89.5 mm. The stress-strain curves and mechanical properties of the porous structures with the same unit cell types but made from other materials including Ti-6Al-4V [35], pure titanium [36], tantalum [37] were adopted from our previous studies and were used for comparison purposes.

Table 7-2. Mechanical properties of the bulk materials

	σ_{ys} [MPa]	E_s [GPa]
Ti-6Al-4V [32]	980	122
Co-Cr		201.5 (Mechanical test)
	657	205 (Impulse Excitation)
Commercial pure titanium (CPT) [27]	300	100
Tantalum [28]	180	179

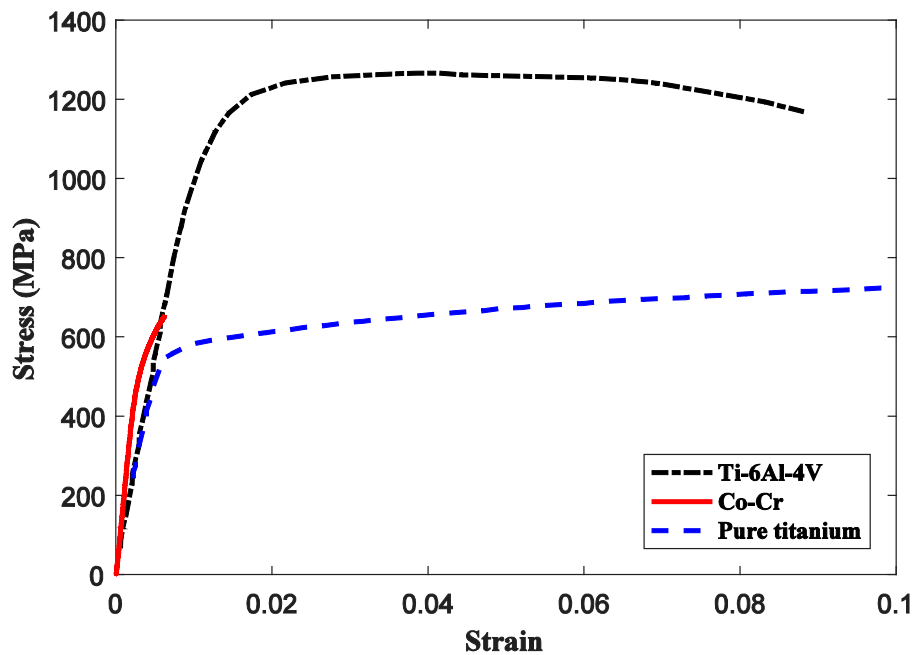


Figure 7-2. Stress-strain curves of different bulk materials used for additive manufacturing of porous biomaterials

7.3.2 Topological characterization

Dry weighing and μ CT scanning were both used to determine the relative density of the porous structures. In dry weighing, the weight of each specimen was measured in room temperature and in normal atmospheric conditions. The measured weight was then divided by the volume of the specimens to determine the density of the specimens. The obtained density of the specimens was then divided by the density of the bulk material they were made of (i.e. 8800 kg/m^3) to obtain the relative density of the porous structures.

In another approach, the Co-Cr porous structures were imaged using a μ CT scanner (Quantum FX, Perkin Elmer, USA) (Figure 7-3). Pure titanium [36] and Ti-6Al-4V [35] structures were also imaged using the same scanner. The tantalum specimens could not be scanned due to the fact that they were too dense for μ CT. The porous structures were scanned under a tube current of $180 \mu\text{A}$ and a tube voltage of 90 kV . The scan time was 3 min and the voxel size of the images was $42 \mu\text{m} \times 42 \mu\text{m} \times 42 \mu\text{m}$. The automatically reconstructed μ CT images were converted into a series of 2D images using Analyze 11.0 (Perkin Elmer, USA). The 2D images were exported to Fiji (NIH, Bethesda, MD,

USA) and regions of interest (ROIs) were defined. After local segmentation in Fiji, the prebuilt plugin of BoneJ (available in ImageJ) was used to calculate the ratio of void volume to the 3D ROI volume, the strut size as well as the pore size of the scaffolds.

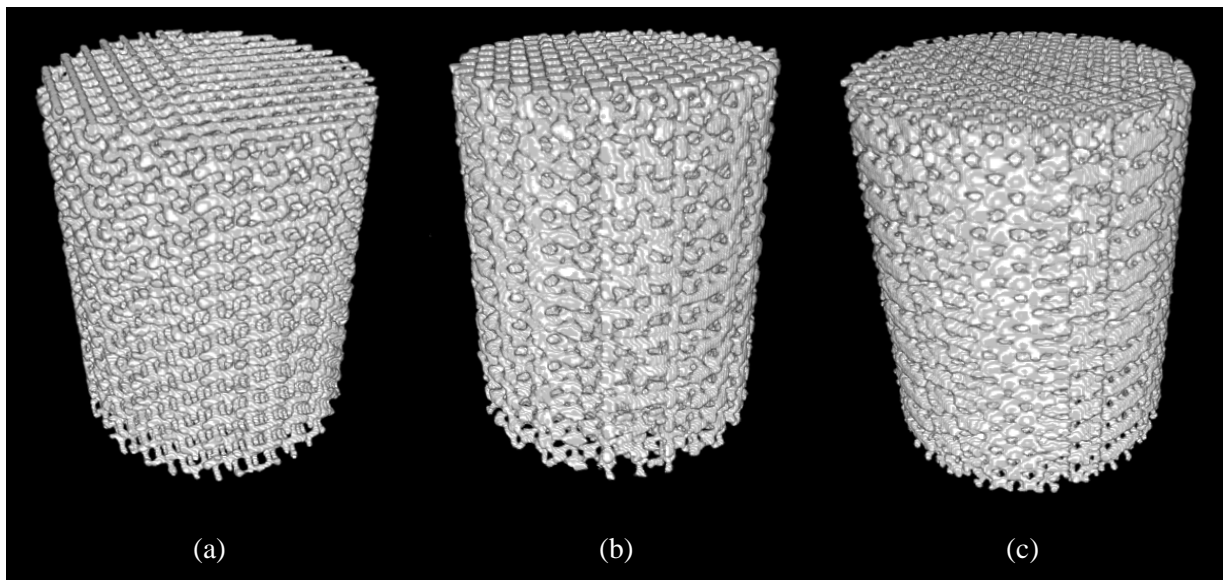


Figure 7-3. Reconstructed CT images of Co-Cr porous structures based on (a) diamond, (b) truncated cuboctahedron, and (c) rhombic dodecahedron unit cells

7.3.3 Microstructural analysis

For each series of porous structures, one sample was chosen for micro-structural observation. To do this, each specimen was first ground from 80 to 2000 grit size and then polished respectively with 3 μm and 1 μm polishing papers. Different etching solutions were used to reveal the grains of Co-Cr porous structures mechanically tested here as well as pure titanium and Ti-6Al-4V specimens used in our previous studies. Pure titanium and Ti-6Al-4V samples were immersed in Kellers etchant (190 ml water + 5 ml nitric acid + 3 ml Hydrochloric acid + 2 ml Hydrofluoric acid) for about 150s. Co-Cr samples were immersed in a solution of 37%HCl + 1g $\text{K}_2\text{S}_2\text{O}_5$ for about 5 min. The microstructure of the specimens was observed with an optical microscope (OM, model BX60M, Olympus) and a scanning electron microscope (SEM, JSM-IT100, JEOL).

7.3.4 Static mechanical testing

The mechanical tests were carried out using an Instron 5985 mechanical testing machine with a 100 kN load cell. The loading rate was set to 1.8 mm/min. The methodology used for carrying out the experimental tests was the same as the one described in the ISO standard 13314:2011 [40] which specifies the compression test methods for porous and cellular metals. The porous structures based on the diamond and truncated cuboctahedron unit cells were compressed up to 60% strain, while the porous structures based on the rhombic dodecahedron unit cell were compressed up to 80% strain. The mechanical tests were repeated three times for each type of porous structure. The mechanical properties obtained from three samples of each type were used to calculate the mean and standard deviations of the corresponding mechanical properties. The following mechanical properties were calculated: elastic modulus, yield stress, plateau stress, and energy absorption. Elastic modulus was determined by measuring the slope of the initial linear part of the stress-strain curve. Yield stress was obtained by offsetting a line to the right side of the initial linear part of the stress-strain curve for 0.2 % strain and obtaining its intersection with the stress-strain curve. Plateau stress refers to the second stage of the stress-strain curves in which the strain value increases significantly with minor change in stress value. As suggested by the ISO standard 13314:2011 [40], to calculate the plateau stress, the arithmetical mean of stresses values between 20% and 40% strains were determined. The energy absorption capacity of each structure was defined as the area below the load-displacement curve for up to 50% strain.

The noted parameters were plotted against the relative density of the porous structures as determined by μ CT. To be able to compare the mechanical properties of porous structures systematically, power law relationships, i.e. $P = a \mu^b$, where P stands for the property and μ represents the relative density of the porous structure, were fitted to all the mechanical property-relative density data points. The constants a and b are reported in the corresponding curves.

To measure the hardness of the struts, the cross-section of each specimen was grinded to 320 grit size and then polished to 9 μ m (diamond suspension). The HV 0.5 test protocol devised for measuring the Vickers hardness (DuraScan-70, Struers, Netherlands) was used. The loading time was set to 10 s. The hardness was measured in 20 random positions on the cross-section of the porous structures, and their average value as well as the standard deviation was calculated.

7.3.5 Analytical relationship

Experimental elastic modulus and yield stress curves will be compared to the corresponding analytical curves obtained for the three noted unit cell types in previous studies. The relative density and normalized elastic modulus of the porous structures based on the truncated cuboctahedron unit cell are given as [41]:

$$\mu = 24 \frac{2\pi \left(\frac{r}{l}\right)^2 - 5.1475 \left(\frac{r}{l}\right)^3}{(2\sqrt{2} + 1)^3} \quad (1)$$

$$\frac{E}{E_s} = \frac{18 A \beta}{l^2 (2\sqrt{2} + 1)} \left\{ \frac{(26\alpha + 5) + 4(296\alpha + 69)\beta + 864(5\alpha + 3)\beta^2}{(16\alpha + 3) + 72(19\alpha + 4)\beta + 72(275\alpha + 81)\beta^2 + 9504(5\alpha + 3)\beta^3} \right\} \quad (2)$$

where r , A , and l are respectively the radius, cross-section area, and length of the struts, E_s is the elastic modulus of the bulk material, and α and β are two parameters defined as $\alpha = \frac{E_s I}{G_s J}$ and $\beta = \frac{l}{Al^2}$ for analytical derivations based on the Euler-Bernoulli beam theory. For the Timoshenko beam theory, $\alpha = \frac{l^3}{G_s J \left(\frac{l^3}{E_s I} + \frac{12l}{2\kappa A G_s} \right)}$ and $\beta = \frac{l}{A E_s \left(\frac{l^3}{E_s I} + \frac{12l}{2\kappa A G_s} \right)}$. I and J are respectively the area moment of inertia and polar area moment of inertia of the struts. An analytical relationship presented in the supplementary material of [41] was used to determine the normalized yield stress of the truncated cuboctahedron porous structures.

The relative density, normalized elastic modulus, and normalized yield stress of porous structures based on the diamond unit cell are as follows [34]:

$$\mu = 2\pi \left(\frac{r}{l}\right)^2 - 2\sqrt{6} \left(\frac{r}{l}\right)^3 \quad (3)$$

$$\frac{E}{E_s} = \frac{\sqrt{6}\pi \left(\frac{3}{4}\right)^2 \left(\frac{r}{l}\right)^4}{1 + \frac{3}{2} \left(\frac{r}{l}\right)^2} \quad (4)$$

$$\frac{\sigma_y}{\sigma_{ys}} = \frac{9\pi}{4\sqrt{6}} \left(\frac{r}{l}\right)^3 \quad (5)$$

where σ_{ys} is the yield stress of the bulk material. Finally, the relative density, normalized elastic modulus, and normalized yield stress of the porous structures based on the rhombic dodecahedron unit cell are [27]

$$\mu = \frac{3\sqrt{3}}{2} \pi \left(\frac{r}{l}\right)^2 \quad (6)$$

$$\frac{E_1}{E_s} = \frac{E_2}{E_s} = \frac{27 \frac{\sin \theta}{\sin 2\theta}}{\frac{3l^4}{\pi r^4} + \frac{18 l^2}{\pi r^2}} \quad (7)$$

$$\frac{E_3}{E_s} = 9\pi r^4 \frac{\cos \theta}{2l^4 \sin^2 \theta}$$

$$\frac{\sigma_{y1}}{\sigma_{ys}} = \frac{\sigma_{y2}}{\sigma_{ys}} = \frac{3\sqrt{6}}{8} \left(\frac{b}{l}\right)^3 \quad (8)$$

with $\theta = 54.73^\circ$. Subscripts 1, 2 and 3 denote the main directions of the rhombic dodecahedron unit cell.

7.4 Results

The Vicker's micro-hardness measurements on porous structures gave the hardness values of 461 ± 30 , 433 ± 9 , and 220 ± 18 for the Co-Cr, Ti-6Al-4V, and pure titanium structures, respectively. The typical optical microscopy images of the cross-section of three sample specimens are presented in Figure 7-4. Pure titanium showed lath-shaped grains with a length range of sizes between 20 and 50 μm , which could be identified as a hexagonal close packing (hcp) α phase (Figure 7-4a). A fully acicular α' martensitic microstructure was developed in Ti-6Al-4V during the SLM process, which had lengths in the range of 10-20 μm (Figure 7-4b) and widths in the range of 1-2 μm (Figure 7-5a and

Figure 7-6a). The grains of Co-Cr material were of elongated cellular shape with diameters around 1 μm (Figure 7-4d, Figure 7-5b and Figure 7-6b). The welding line between different melting pools of Co-Cr porous structures were visible in the microstructural images (Figure 7-4c). The grain growth direction was different for different melt pools (Figure 7-4d).

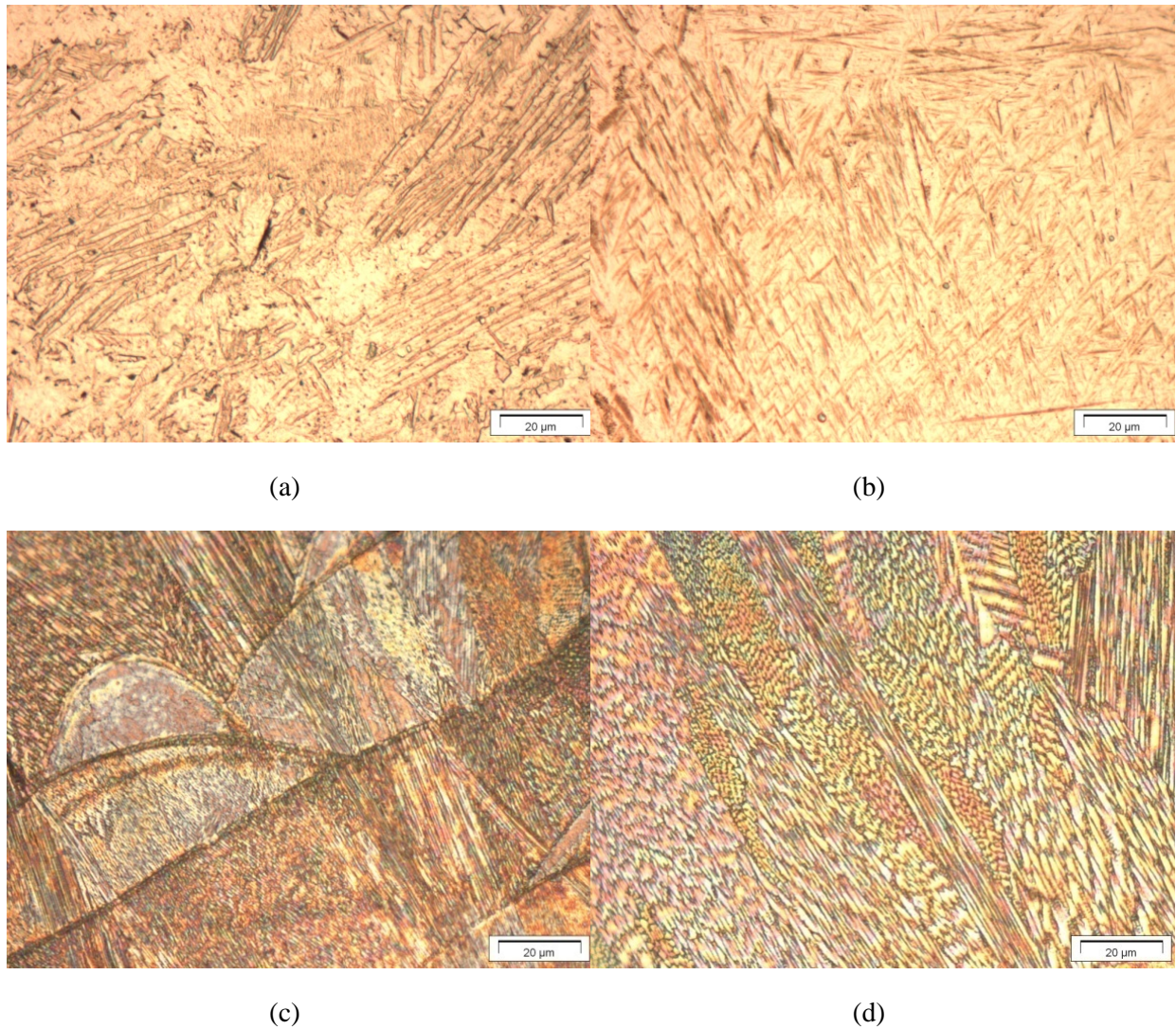
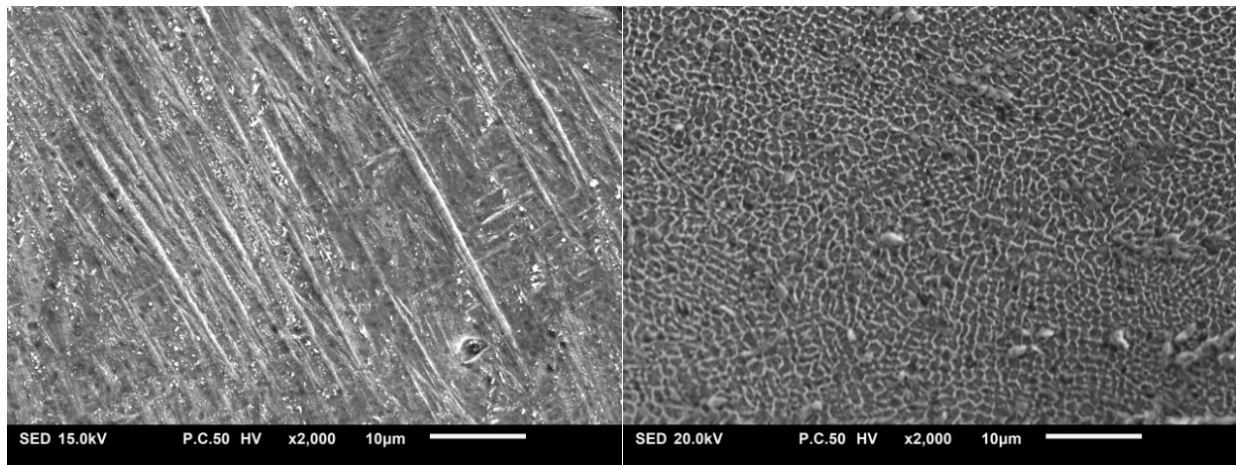


Figure 7-4. Microscopic views of the microstructure of additively manufactured (a) pure titanium, (b) Ti-6Al-4V, and (c-d) Co-Cr porous structures with etched cross-sections



(a)

(b)

Figure 7-5. SEM picture of the microstructure of additively manufactured (a) Ti-6Al-4V, (b) Co-Cr porous structures with etched cross-sections



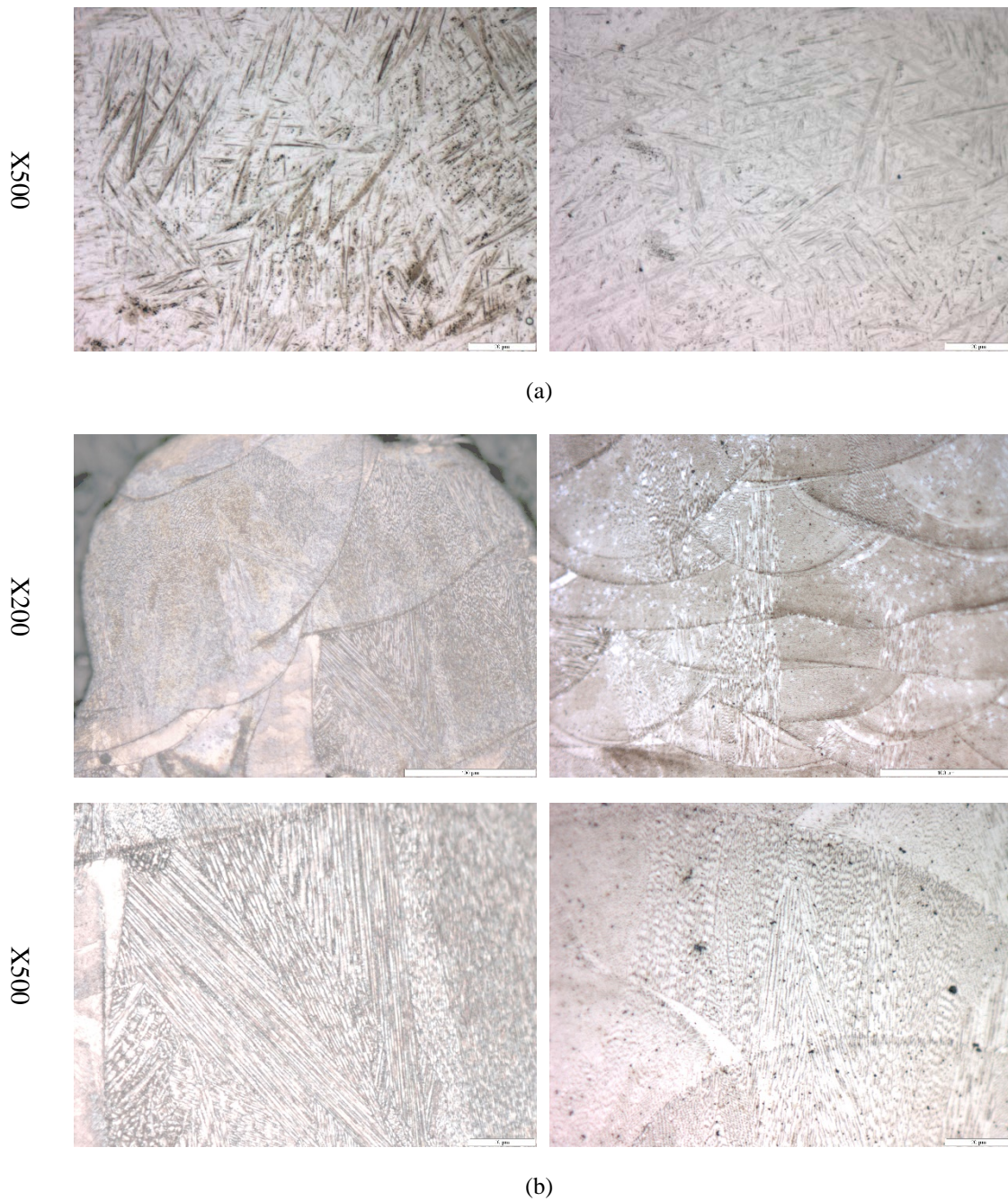


Figure 7-6. Comparison of microstructure of additive manufactured solid and porous specimens with different magnifications: (a) Ti-6Al-4V and (b) Co-Cr.

Under compression, all the structures demonstrated the three-stage stress-strain curves that are typical of porous structures including porous biomaterials (Figure 7-7 to Figure 7-9). The first part was linear elastic after which the slope of the diagram rapidly decreased. In the second stage (known

as the plateau stage), the strain increased significantly with small increases in the stress value. In the final stage known as the densification stage, the stress started to increase exponentially (Figure 7-7 to Figure 7-9). For all the relative densities of the porous structures based on the diamond unit cell, densification occurred in strains about 40% (Figure 7-7). In the porous structures based on the rhombic dodecahedron and truncated octahedron unit cells, densification occurred at strains around 60%. In high-density ($\mu = 0.415$) porous structures based on the rhombic dodecahedron unit cell, densification started earlier ($\varepsilon_d \approx 41.5\%$) (Figure 7-8c).

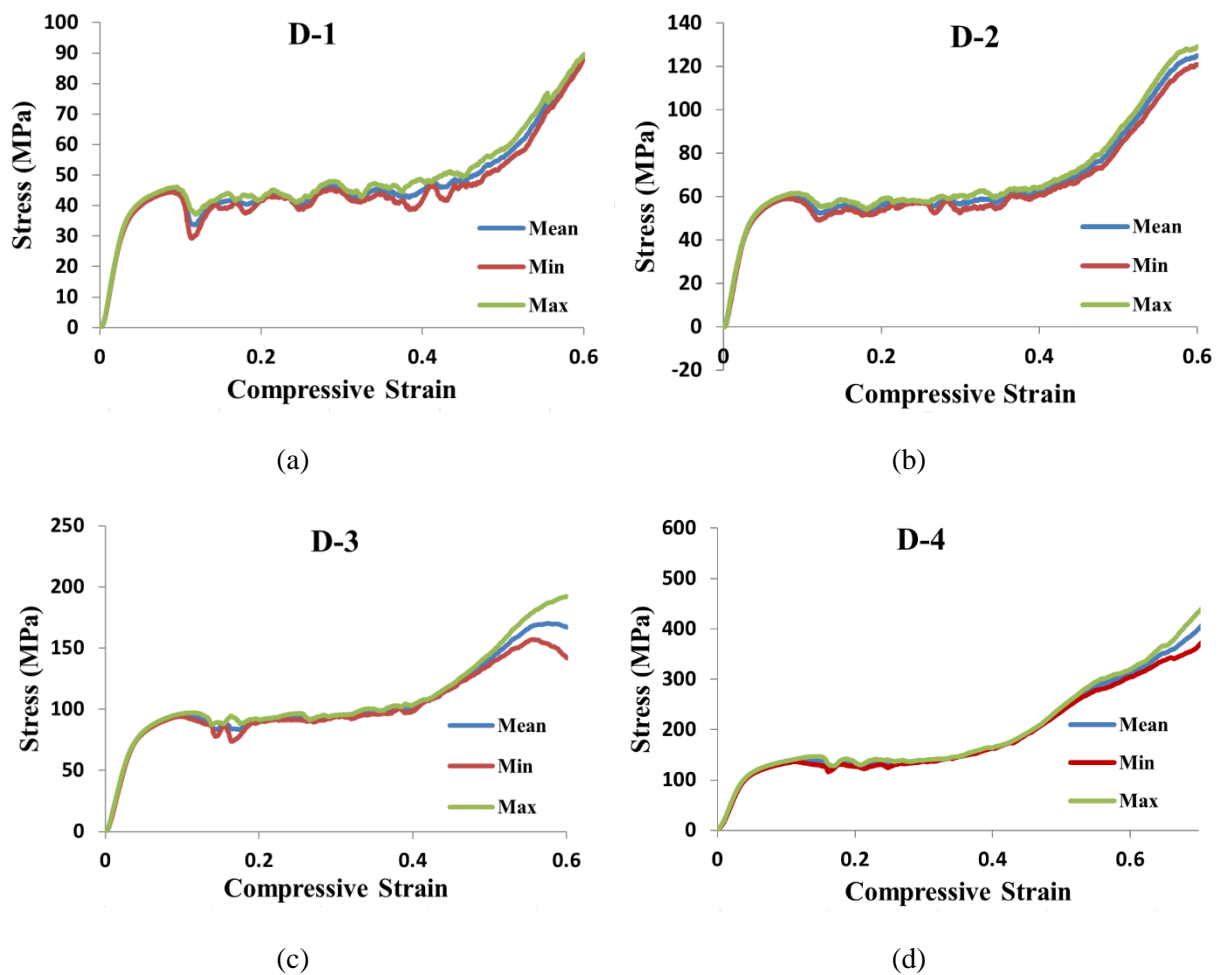


Figure 7-7. Stress-strain curves for Co-Cr porous structures based on diamond unit cell with different relative density values: (a) 0.209, (b) 0.267, (c) 0.34, and (d) 0.401.

Using the stress-strain curves obtained from different specimens, the normalized elastic modulus, yield stress, plateau stress, and energy absorption of all the specimens were determined and plotted against relative density (Figure 7-10 to Figure 7-13). In two of the graphs (i.e. normalized elastic modulus and normalized yield stress) for which analytical relationships were available from the literature [27, 34, 41], analytical curves are plotted as well (Figure 7-10 and 7-11).

Regardless of the unit cell type, the normalized values of the elastic moduli and yield stress for the porous structures made from both Ti-6Al-4V and Co-Cr were in general agreement with each other ((Figure 7-10 and 7-11). As for the normalized plateau stress diagrams, the results of both Co-Cr and Ti-6Al-4V structures were close to each other for the rhombic dodecahedron unit cell (Figure 7-12b). For the porous structures based on the diamond and truncated cuboctahedron unit cells, the normalized values of the plateau stress of the Co-Cr structures were higher than those of the Ti-6Al-4V structures (Figure 7-12a, c).

The energy absorption capacities of the Co-Cr structures were higher than those of the Ti-6Al-4V structures for the diamond unit cell type, while the opposite held for the rhombic dodecahedron and truncated cuboctahedron unit cells (Figure 7-13). The elastic modulus and yield stress vs. relative density curves of commercially pure Ti (CPT, grade 1) porous structures were generally close to those of Ti-6Al-4V structures (Figure 7-10 and 7-11). However, the normalized plateau stress curve of CPT was significantly higher than that of Ti-6Al-4V (Figure 7-12).

For all unit cell types, both the Ti-6Al-4V and Co-Cr porous structures showed normalized elastic modulus and normalized yield stress values that were relatively close to the corresponding analytical curves (Figure 7-10 and 7-11). In the diamond and truncated cuboctahedron unit cells, the normalized elastic modulus curves of both the Ti-6Al-4V and Co-Cr porous structures almost overlapped with the analytical curves (Figure 7-10). For the rhombic dodecahedron unit cell, however, the normalized elastic modulus and yield stress of the porous structures made of different materials showed more deviations from each other and from the analytical predictions (Figure 7-11).

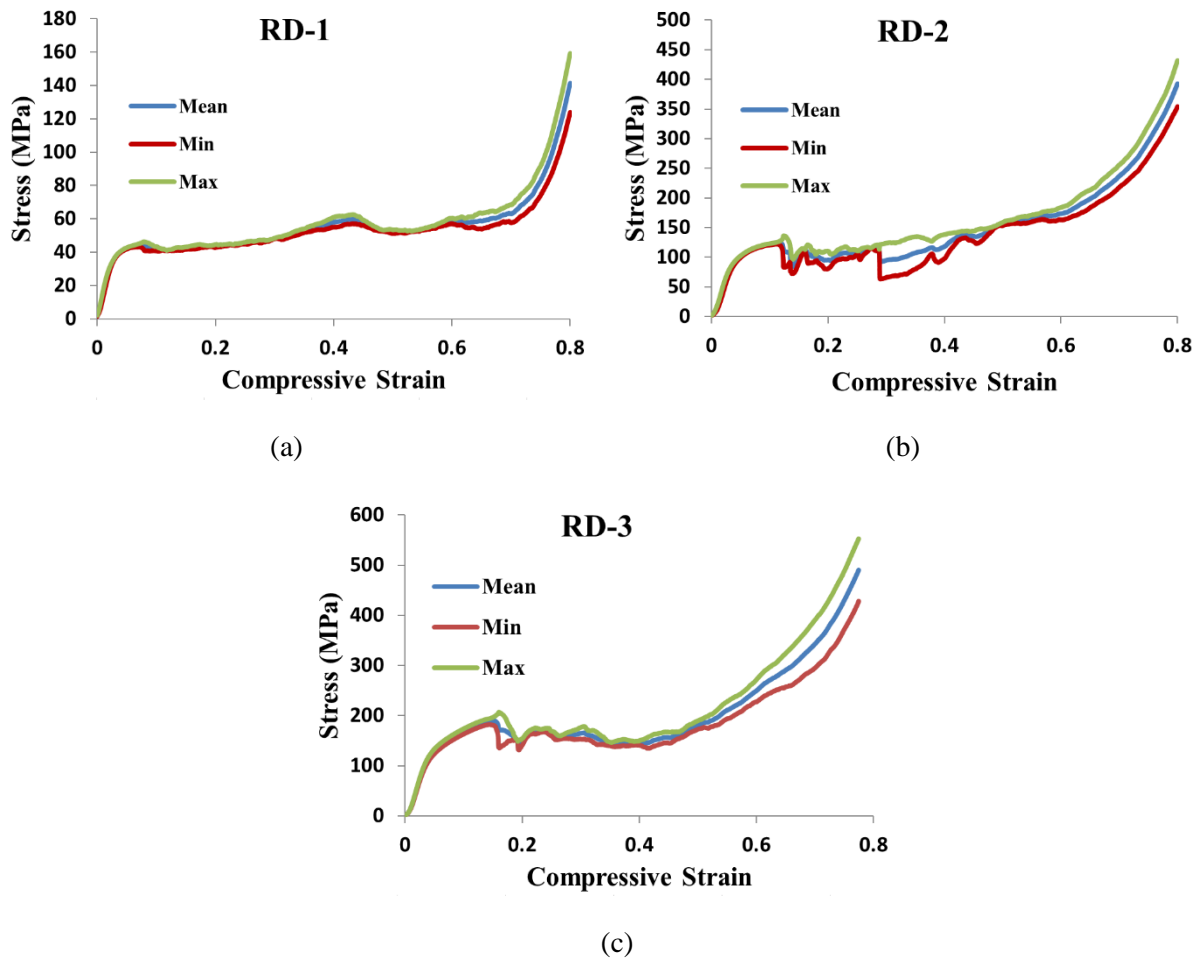


Figure 7-8. Stress-strain curves for Co-Cr porous structures based on rhombic dodecahedron unit cell with different relative density values: (a) 0.299, (b) 0.372, and (c) 0.415.

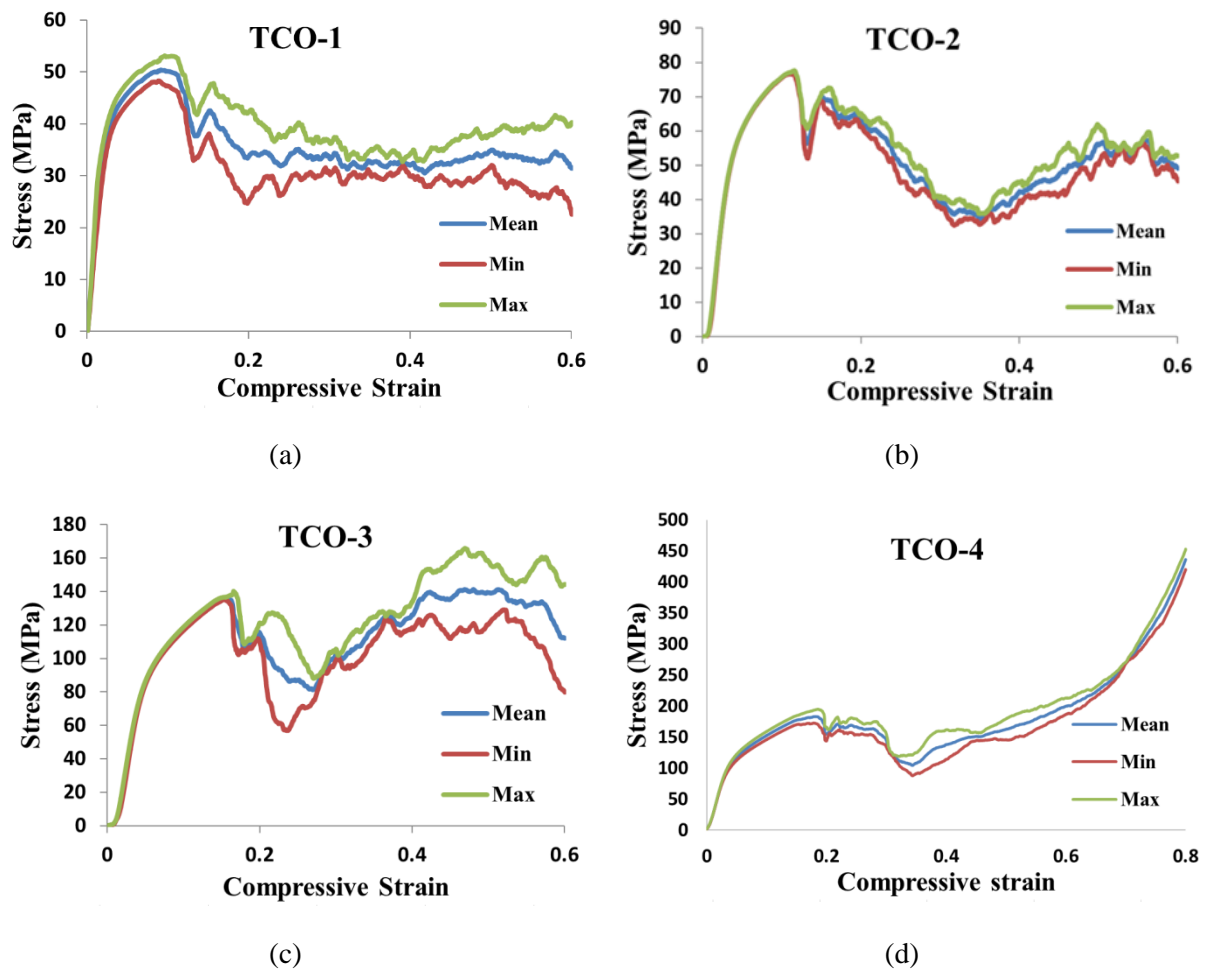
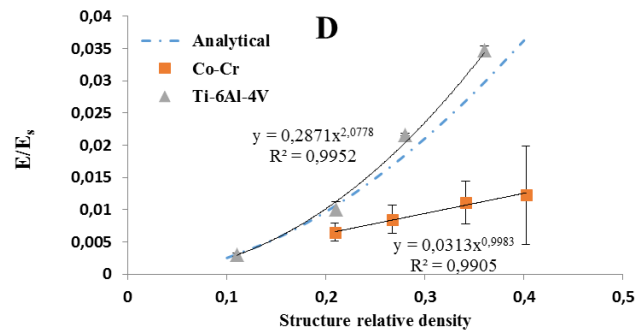
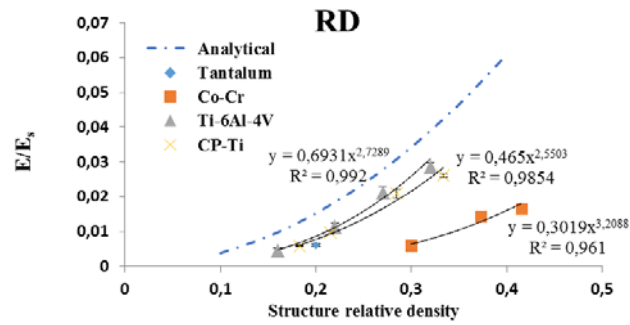


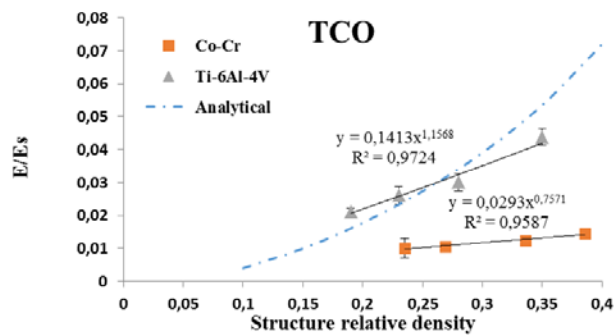
Figure 7-9. Stress-strain curves for Co-Cr porous structures based on truncated octahedron unit cell with different relative density values: (a) 0.236, (b) 0.269, (c) 0.336, and (d) 0.386.



(a)



(b)



(c)

Figure 7-10. Comparison of normalized elastic modulus of Ti-6Al-4V, Co-Cr, Tantalum, and CPT porous structures based on (a) diamond, (b) rhombic dodecahedron, and (c) truncated octahedron unit cells.

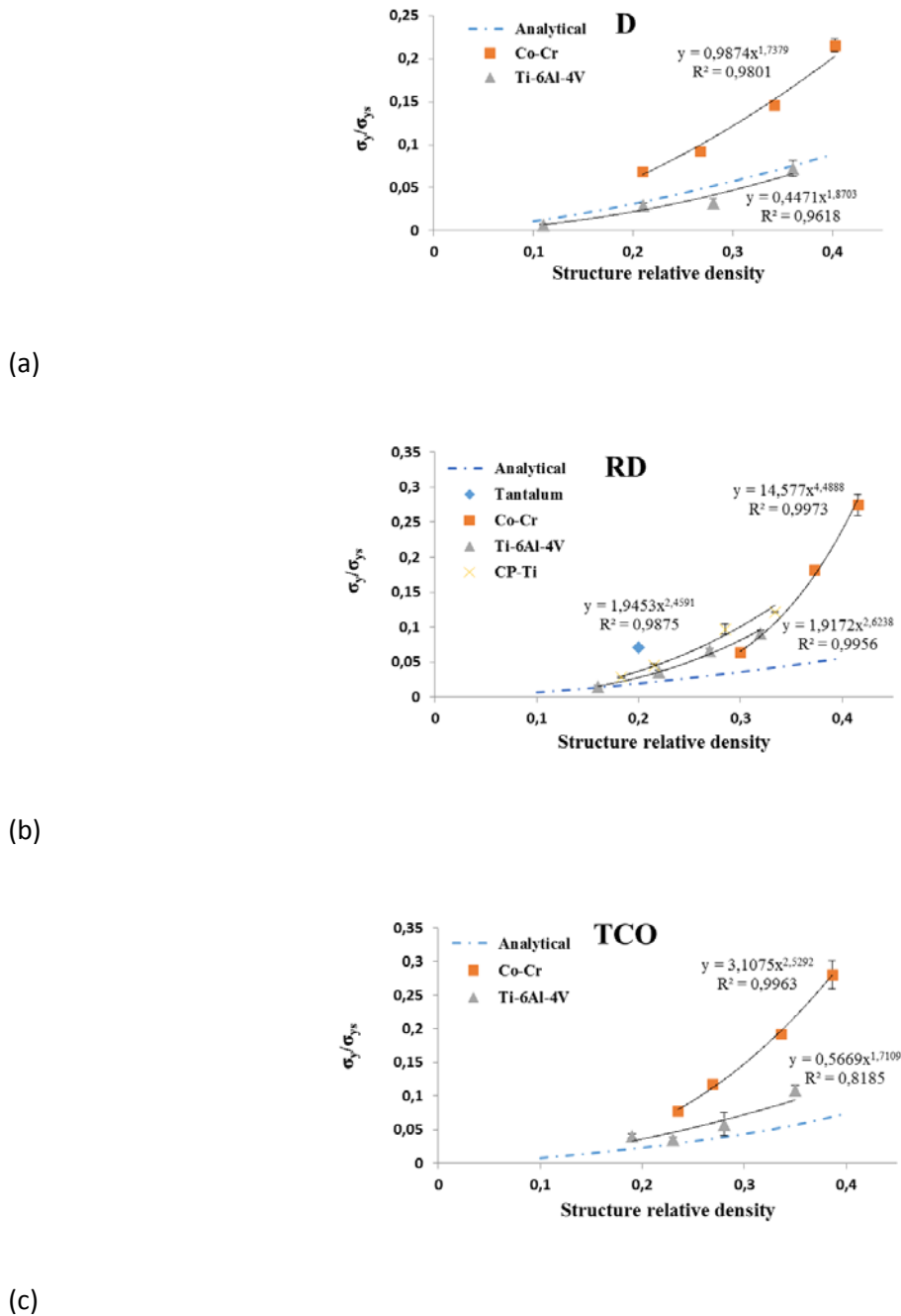


Figure 7-11. Comparison of normalized yield stress of Ti-6Al-4V, Co-Cr, Tantalum, and CPT porous structures based on (a) diamond, (b) rhombic dodecahedron, and (c) truncated octahedron unit cells.

7.5 Discussion

Previous theoretical and analytical studies on the mechanical properties of AM porous biomaterials [42] have generally assumed that the normalized mechanical properties of porous structures (normalized elastic modulus, normalized yield stress, and Poisson's ratio) are not dependent on the material type and that the only influencing factor is the topological design of the micro-architecture. The main goal of this study was to find whether the material type in isolation or in modulation with topology influences the mechanical properties of AM porous biomaterials. Comparison of experimental results with analytical solutions demonstrated that, save for few exceptions, the elastic modulus and yield stress values of the porous structures made from all the studied materials (Co-Cr, Ti-6Al-4V, pure titanium, and tantalum) are relatively close to each other and in general agreement with the analytical predictions. The normalized plateau stress and energy absorption capacity of the porous structures made of different materials, however, showed significant differences with respect to each other (Figure 7-12 and Figure 7-13).

The results of this study clearly show that both topological design and material type are important factors determining the response of AM porous structures although topological design is the dominating factor. It is therefore important to quantify the effects of both factors on the mechanical properties of AM porous biomaterials. Quantitatively speaking, choosing different materials (and their associated manufacturing parameters) could result in up to 200% difference in the normalized mechanical properties. To put this in perspective, the results of our previous studies have shown that topological design could cause differences in the elastic properties that could go as high as 1000% [42]. At a relative density of 50%, for example, analytically estimated normalized elastic modulus of porous structures based on the diamond unit cell is about 0.025 while the corresponding value for the porous structures based on isocubes is about 0.25 [42]. Increasing the relative density of porous structures based on different unit cell types from 10% to 50% could increase the normalized elastic modulus up to 2400% (see the normalized elastic modulus curve of isocube in Figure 3a of [42]). Changing the cross-section type (square, circular, triangular) in constant relative density of porous structure does not have a significant influence on the normalized elastic modulus but it could cause up to 200% change in the normalized yield stress (see Figure 12 in [43]). Comparison of the percentages mentioned above shows that the topological design of porous

structure is the dominant factor determining the normalized elastic properties of the porous structures. It is, nevertheless, important to take the effects of the manufacturing parameters as well as the mechanical properties of the bulk material into account to obtain more accurate estimations of the mechanical properties that are needed in the rational design process.

7.5.1 Mechanistic aspects

There could be several reasons behind the relatively minor differences between the normalized elastic modulus and yield stress curves of the porous structures made from different materials. One of the first reasons is the difference between the materials in terms of the AM process including the quality of the powder and suitability of the chosen laser beam parameters such as the laser power and scanning speed. Two types of irregularities are usually created in AM porous biomaterials [44]. In the first type, the cross-section areas of the struts are not constant and show deviations with respect to the nominal (i.e. design) values (see Figure 7-14a,c). The second type of irregularities corresponds to the fusion process of the particles during which some micro-porosities may be created in the fused solid material (see Figure 7-14b, d). Depending on the suitability of the chosen manufacturing parameters and powder characteristics, the irregularities created in the porous structure could be quite different. Such irregularities may decrease both the elastic modulus and yield stress values. It is also important to note that we studied the mechanical properties of the AM porous biomaterials in their as-manufactured conditions. Surface modifications [45] and heat treatments [46-48] could both alter the internal pores, manufacturing irregularities, and residual stresses, thereby influencing mechanical properties. The other manufacturing aspects such as additive manufacturing technique (electron beam melting (EBM), SLM, fused deposition modeling (FDM), etc.), printing speed, layer thickness, etc. can all affect the resulted mechanical properties. For example the measured elastic modulus of Ti-6Al-4V presented in this work and those presented by Li et al [30] which are made by EBM technique show up to 40% difference. It must be noted that in a paper published by Han et al [22], the mechanical properties of Co-Cr SLM porous structures were studied for structures based on cubic closed packed (CCP), face-centered cubic (FCC), spherical hollow cubic (SHC), and body-centered cubic (BCC) unit cells. None of these unit cell types have been studied in this paper. Therefore no comparison between our results and the data provided in [22] was possible to make. In another study [49] which compared the mechanical properties of Co-Cr and

Ti-6Al-4V dode-thin porous structures manufactured by EBM technique, the relative elastic modulus-relative density diagram of porous structures made from both the materials could be fitted into a single line in a log-log plot. This is in line with our elastic modulus diagram (Figure 7-10) which showed that elastic modulus of porous structures made from different materials are all close to each other as well as to the analytical curve.

Moreover, compositions and microstructures are important factors influencing the mechanical behavior of AM porous structures. In pure metals, the elastic modulus mainly depends on the inter-atomic forces: metals with smaller inter-atomic distances have higher elastic moduli. As for the metallic alloys, the alloying elements could also change the elastic modulus by introducing lattice distortion or forming second phase particles. Taking Ti-6Al-4V as an example, the α phase has a higher elastic modulus than the β phase [50, 51]. The elastic modulus of this alloy could therefore vary for different manufacturing processes and different laser processing parameters in AM [34], because the compositions of α and β phases could vary. The same holds for Co-Cr. Although there is no extensive literature describing the effects of different phases on the elastic modulus of AM Co-Cr, the basic phase of Co-Cr is expected to have lower elastic modulus than the second phase in the boundary. In addition to the microstructural compositions, strong crystallographic anisotropy could also cause variations in the elastic modulus, as the elastic modulus is usually dependent on the crystal orientations. These are why the elastic modulus of Ti-6Al-4V could change from 95 GPa to 145 GPa [46, 47, 52] while that of Co-Cr varies between 178 GPa and 230 GPa [53-55], according to different studies.

There are also studies dedicated to the build orientation effect on the mechanical properties of Co-Cr and Ti-6Al-4V AM structures by keeping the other manufacturing parameters constant. In a study by Kajima et al [56] it was shown that the mechanical properties of Co-Cr SLM materials in the directions parallel and perpendicular to the building direction can be to 7% different. In a similar study on Ti-6Al-4V SLM materials [57], it was shown that build orientation can cause up to 10% difference in the resulting mechanical properties. While in the analytical derivations (i.e. equations (2), (4-5), (7-8)), it is assumed that the mechanical properties of the bulk material is constant in all the directions, the experimental data shows difference. The build orientation effect is different in different AM materials (as already noted, we can see 7% difference in Co-Cr and 10% in Ti-6Al-4V). The build orientation also affects the porous structures based on different unit cells in different

extents, due to the fact that strut orientations are different in different unit cell types. The latter is in particular of no importance in the bulk material (since it does not have any unit cell). No need to say that the normalized values of elastic modulus and yield stress depends on the mechanical properties of both the bulk material and the porous structure. This explains deviations of experimental curves from the analytical curves in different direction (increase or decrease) and with different extents in the normalized elastic modulus (Figure 7-10) and yield stress (Figure 7-11) diagrams of porous structure made from different materials and based on different unit cells.

As for the yield strength, microstructure has a larger contribution. Yield strength is affected by many microstructural characteristics such as grain size, second phase distribution, anisotropy, and cooling rate. Smaller grains lead to more grain boundaries. According to the Hall-Petch relationship, the yield strength of materials increase as the grain size decrease. Smaller grains could decrease the dislocation amount in each dislocation cluster, which decreases the stress concentration. Selective laser melted Co-Cr alloy has a very small columnar grain size, which results in higher yield strengths than conventionally manufactured alloys [58]. Moreover, the fine and uniform second phase distributions could improve the yield strength by effectively inhibiting the dislocation movement. SEM pictures of Co-Cr show that the second phases (aligned carbide precipitates [59]) are all uniformly distributed in the grain boundary (Figure 7-5b). The pin effect of the second phases in the grain boundary could keep the boundary from sliding. Microstructural anisotropy, textures as well as a number of other parameters could give rise to different yield strengths in different directions. Previous studies have found that yield strength is higher when the (tensile) test direction is perpendicular to the build direction for both selective laser melted Ti-6Al-4V and Co-Cr solid materials [60, 61]. In our Co-Cr samples, the texture resembling a common weaved fabric [62] could have also been effective in improving of the yield strength of the material.

In addition to the defects introduced by the AM process, the deviations from the analytical solution may have been also caused by the microstructural differences between AM bulk material and porous material. This difference between the fully solid material and porous structures is due to the different laser processing parameters as well as different heat transfer conditions in the powder bed (given their difference in terms of topology). Struts in the porous structures are mostly overhang structures, while solid parts are always supported by the former layers. The fully solid parts could therefore generate textures in parallel with the build direction, but the same may not happen in

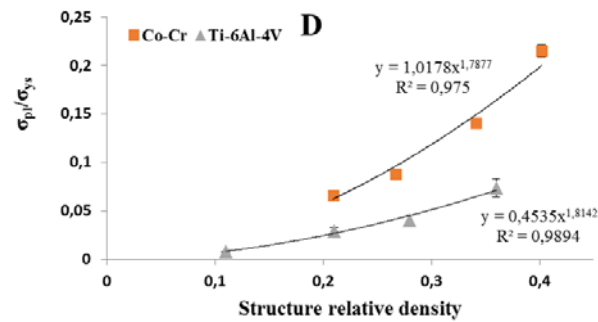
porous materials, as laser has limited influence on the former layer in the tilted struts. Second, the normalization of mechanical properties was performed based on the assumption that the porous samples all have homogeneous microstructures, while the microstructural observations showed that there are some variations (Figure 7-4 to Figure 7-6). Rapid cooling of the Ti-6Al-4V during the SLM process creates needle shaped α' phases in Ti-6Al-4V which increase the strength of the alloy [63]. In a similar way, rapid cooling of Co-Cr structures during the SLM process creates finer [64] more irregular [65] columnar dendritic microstructure which increases the yield strength [66]. It has been shown that the rapid cooling effect is of greater importance in Ti-6Al-4V as compared to Co-Cr [49].

7.5.2 Difference between various mechanical properties

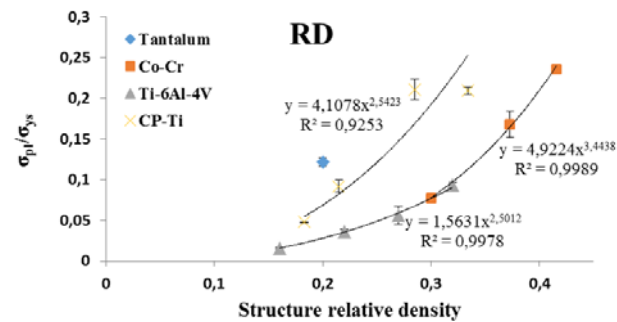
Not all mechanical properties were similar in terms of the effects of topological design and material type. The normalized plateau stress values of pure titanium and Co-Cr were significantly higher than that of Ti-6Al-4V (Figure 7-12). This difference in the plateau stress diagram could be attributed to the different post-elastic behaviors of the noted materials. Pure titanium and Co-Cr materials are more ductile than Ti-6Al-4V. That is why the porous structures made from pure titanium and Co-Cr keep their integrity and (distorted) cell walls up to very large strains, while in the Ti-6Al-4V porous structures, collapsing and crushing of the cells start from the very beginning of deformations (compare the deformed porous structures made of pure titanium and Ti-6Al-4V in Figure 2a and Figure 2b of [36]). This difference in the post-elastic behavior of the noted materials substantially affects their stress-strain curves. In the Ti-6Al-4V porous structures, the stress-strain curves show an initial peak point after yielding followed by considerable fluctuations in the plateau part (see Figures 4,6,7 in [35]). After this point, the stress decreases sharply, continuing up to the densification point with stress values much lower than the initial maximum stress. Therefore, in AM porous structures made of Ti-6Al-4V structures, the plateau stress is usually around the yield stress (and much lower than the initial maximum stress) (compare e.g. Figure 7-11 and Figure 7-12). On the other hand, the stress-strain curves of pure titanium do not show any initial peak and stresses keep slowly and constantly accumulate up until the very end of deformations. In the AM porous structures made from pure titanium, the plateau stress could therefore be much higher than the yield stress (see Figure 2a in [36]). In the stress-strain curves of Co-Cr porous structures, the initial peak point and the fluctuations in the plateau regime are less significant than those in the stress-strain curves of Ti-6Al-

4V. The higher ductility levels in the AM Co-Cr and pure titanium structures as compared to AM Ti-6Al-4V structures explains the higher plateau stress levels in the AM Co-Cr and pure titanium porous structures.

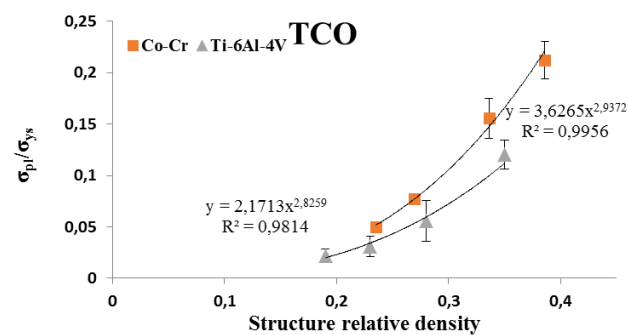
The energy absorption capacity diagrams did not show any particular trend regarding which of the two Co-Cr and Ti-6Al-4V structures could absorb more energy (Figure 7-13). In fact, the order of normalized energy absorption capacity with respect of the material type was different in structures having different unit cell types. The main reason is that the total energy absorption capacity, which was measured up to 60% strain, is a sum of the elastic and plastic energy absorption capacities. The elastic modulus is a major factor in determining the elastic energy absorption capacity of the AM porous structures, while the plateau stress is more influential in the case of the plastic energy absorption capacity (for which the Co-Cr structures showed higher values than the Ti-6Al-4V structures). The order of the total energy absorption magnitude with respect to the material type is determined by the contribution of both elastic and plastic parts. What is stated above also implies that if the energy absorption capacity is measured up to lower strains (than 50%), the order of energy absorption values may have become more similar to the one observed for the normalized elastic moduli (Figure 7-10), and that if the energy absorption capacity was measured up to higher strains (than 50%), the order of energy absorption magnitude may have been more similar to the normalized plateau stress diagrams (Figure 7-12).



(a)

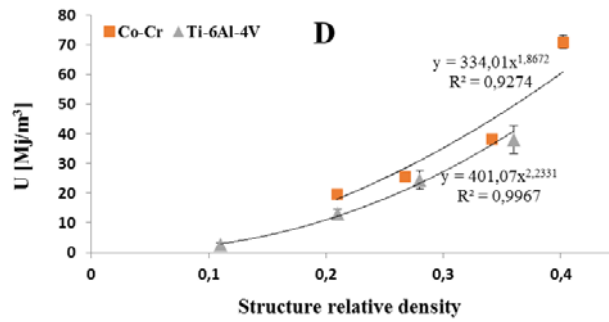


(b)

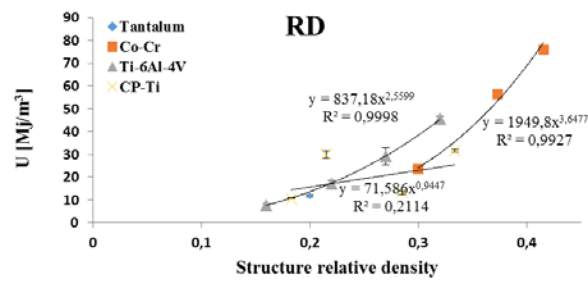


(c)

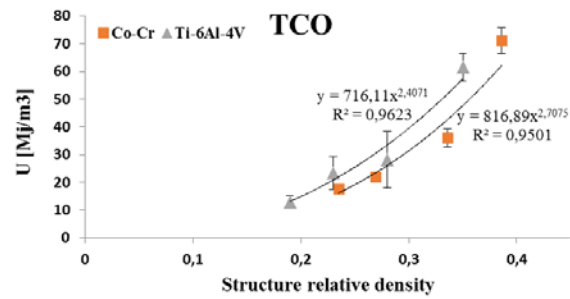
Figure 7-12. Comparison of normalized plateau stress of Ti-6Al-4V, Co-Cr, Tantalum, and CPT porous structures based on (a) diamond, (b) rhombic dodecahedron, and (c) truncated octahedron unit cells.



(a)



(b)



(c)

Figure 7-13. Comparison of energy absorption of Ti-6Al-4V, Co-Cr, Tantalum, and CPT porous structures based on (a) diamond, (b) rhombic dodecahedron, and (c) truncated octahedron unit cells.

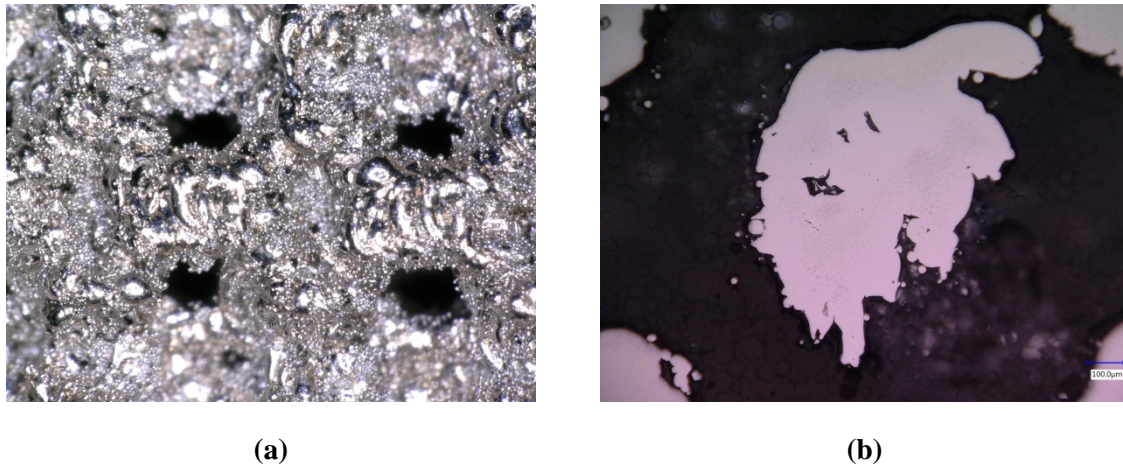


Figure 7-14. Different types of irregularities in additively manufactured porous biomaterials: (a) diameter (cross-section area) irregularity and (b) internal pore irregularity in Co-Cr porous structure. It must be noted that the internal pores shown in (b) were very rare in our structures (the percentage of internal pores was less than 0.5%) and this picture was chosen to better demonstrate the internal porosity irregularity.

7.6 Conclusion

This systematic study on the effects of topological design and material type on the mechanical response of AM porous biomaterials showed that topological design has the dominant effect on the normalized elastic modulus and yield stress values. However, the material properties of the bulk material (such as ductility) could have considerable effects on the plateau stress and energy absorption capacity of the porous structure. Although the effect of material type on the post-elastic response of porous structure is much more significant than its effect on the elastic properties, its effect is still lower as compared to topological design. Quantitatively speaking, topological design could cause up to 10-fold difference in the mechanical properties of AM porous biomaterials while up to 2-fold difference was observed as a consequence of changing the material type.

7.7 References

1. Lin, C.Y., N. Kikuchi, and S.J. Hollister, *A novel method for biomaterial scaffold internal architecture design to match bone elastic properties with desired porosity*. Journal of biomechanics, 2004. **37**(5): p. 623-636.
2. Hollister, S.J., R. Maddox, and J.M. Taboas, *Optimal design and fabrication of scaffolds to mimic tissue properties and satisfy biological constraints*. Biomaterials, 2002. **23**(20): p. 4095-4103.
3. Hollister, S.J., *Porous scaffold design for tissue engineering*. Nature materials, 2005. **4**(7): p. 518-524.
4. Bandyopadhyay, A. and S. Bose, *Bone replacement materials*. 2016, Google Patents.
5. Bandyopadhyay, A., et al., *Influence of porosity on mechanical properties and in vivo response of Ti6Al4V implants*. Acta biomaterialia, 2010. **6**(4): p. 1640-1648.
6. Staiger, M.P., et al., *Magnesium and its alloys as orthopedic biomaterials: a review*. Biomaterials, 2006. **27**(9): p. 1728-1734.
7. Krishna, B.V., S. Bose, and A. Bandyopadhyay, *Low stiffness porous Ti structures for load-bearing implants*. Acta biomaterialia, 2007. **3**(6): p. 997-1006.
8. Bandyopadhyay, A., et al., *Application of laser engineered net shaping (LENS) to manufacture porous and functionally graded structures for load bearing implants*. Journal of Materials Science: Materials in Medicine, 2009. **20**(1): p. 29.
9. Van Bael, S., et al., *The effect of pore geometry on the in vitro biological behavior of human periosteum-derived cells seeded on selective laser-melted Ti6Al4V bone scaffolds*. Acta biomaterialia, 2012. **8**(7): p. 2824-2834.
10. Zadpoor, A.A., *Bone tissue regeneration: the role of scaffold geometry*. Biomaterials Science, 2015. **3**(2): p. 231-245.
11. Hutmacher, D.W., *Scaffolds in tissue engineering bone and cartilage*. Biomaterials, 2000. **21**(24): p. 2529-2543.
12. Liu, X., et al., *Relationship between osseointegration and superelastic biomechanics in porous NiTi scaffolds*. Biomaterials, 2011. **32**(2): p. 330-338.
13. Pattanayak, D.K., et al., *Bioactive Ti metal analogous to human cancellous bone: fabrication by selective laser melting and chemical treatments*. Acta Biomaterialia, 2011. **7**(3): p. 1398-1406.
14. Pyka, G., et al., *Surface modification of Ti6Al4V open porous structures produced by additive manufacturing*. Advanced Engineering Materials, 2012. **14**(6): p. 363-370.
15. Yavari, S.A., et al., *Crystal structure and nanotopographical features on the surface of heat-treated and anodized porous titanium biomaterials produced using selective laser melting*. Applied Surface Science, 2014. **290**: p. 287-294.
16. Vaithilingam, J., et al., *Immobilisation of an antibacterial drug to Ti6Al4V components fabricated using selective laser melting*. Applied Surface Science, 2014. **314**: p. 642-654.
17. Jia, Z., et al., *Additively Manufactured Macroporous Titanium with Silver-Releasing Micro/nanoporous Surface for Multipurpose Infection Control and Bone Repair— A Proof of Concept*. ACS Applied Materials & Interfaces, 2016.

18. Amin Yavari, S., et al., *Antibacterial behavior of additively manufactured porous titanium with nanotubular surfaces releasing silver ions*. ACS applied materials & interfaces, 2016. **8**(27): p. 17080-17089.
19. Wang, X., et al., *Topological design and additive manufacturing of porous metals for bone scaffolds and orthopaedic implants: A review*. Biomaterials, 2016. **83**: p. 127-141.
20. Amin Yavari, S., et al., *Relationship between unit cell type and porosity and the fatigue behavior of selective laser melted meta-biomaterials*. Journal of the mechanical behavior of biomedical materials, 2015. **43**: p. 91-100.
21. Ptochos, E. and G. Labeas, *Elastic modulus and Poisson's ratio determination of micro-lattice cellular structures by analytical, numerical and homogenisation methods*. Journal of Sandwich Structures and Materials, 2012: p. 1099636212444285.
22. Han, C., et al., *Effects of the unit cell topology on the compression properties of porous Co-Cr scaffolds fabricated via selective laser melting*. Rapid Prototyping Journal, 2017. **23**(1): p. 16-27.
23. Van Hooreweder, B., et al., *Improving the fatigue performance of porous metallic biomaterials produced by Selective Laser Melting*. Acta Biomaterialia, 2017. **47**: p. 193-202.
24. Hedayati, R., et al., *Computational prediction of the fatigue behavior of additively manufactured porous metallic biomaterials*. International Journal of Fatigue, 2016. **84**: p. 67-79.
25. Hedayati, R., et al., *Mechanical properties of regular porous biomaterials made from truncated cube repeating unit cells: analytical solutions and computational models*. Materials Science and Engineering: C, 2016. **60**: p. 163-183.
26. Hedayati, R., et al., *Mechanics of additively manufactured porous biomaterials based on the rhombicuboctahedron unit cell*. Journal of the Mechanical Behavior of Biomedical Materials, 2016. **53**: p. 272-294.
27. Babaei, S., et al., *Mechanical properties of open-cell rhombic dodecahedron cellular structures*. Acta Materialia, 2012. **60**(6): p. 2873-2885.
28. Zheng, X., et al., *Ultralight, ultrastiff mechanical metamaterials*. Science, 2014. **344**(6190): p. 1373-1377.
29. Warren, W. and A. Kraynik, *Linear elastic behavior of a low-density Kelvin foam with open cells*. Journal of Applied Mechanics, 1997. **64**(4): p. 787-794.
30. Li, S., et al., *Influence of cell shape on mechanical properties of Ti-6Al-4V meshes fabricated by electron beam melting method*. Acta biomaterialia, 2014. **10**(10): p. 4537-4547.
31. Ko, W., *Deformations of foamed elastomers*. Journal of Cellular Plastics, 1965. **1**(1): p. 45-50.
32. Zhu, H., J. Knott, and N. Mills, *Analysis of the elastic properties of open-cell foams with tetrakaidecahedral cells*. Journal of the Mechanics and Physics of Solids, 1997. **45**(3): p. 319327-325343.
33. Gibson, L.J. and M.F. Ashby, *Cellular solids: structure and properties*. 1999: Cambridge university press.
34. Ahmadi, S., et al., *Mechanical behavior of regular open-cell porous biomaterials made of diamond lattice unit cells*. Journal of the mechanical behavior of biomedical materials, 2014. **34**: p. 106-115.
35. Ahmadi, S., et al., *Additively manufactured open-cell porous biomaterials made from six different space-filling unit cells: the mechanical and morphological properties*. Materials, 2015. **8**(4): p. 1871-1896.

36. Wauthle, R., et al., *Revival of pure titanium for dynamically loaded porous implants using additive manufacturing*. Materials Science and Engineering: C, 2015. **54**: p. 94-100.
37. Wauthle, R., et al., *Additively manufactured porous tantalum implants*. Acta biomaterialia, 2015. **14**: p. 217-225.
38. Heritage, K., C. Frisby, and A. Wolfenden, *Impulse excitation technique for dynamic flexural measurements at moderate temperature*. Review of scientific instruments, 1988. **59**(6): p. 973-974.
39. Kalidindi, S., A. Abusafieh, and E. El-Danaf, *Accurate characterization of machine compliance for simple compression testing*. Experimental mechanics, 1997. **37**(2): p. 210-215.
40. Standard, I., *ISO 13314: 2011 (E)(2011) Mechanical testing of metals—ductility testing—compression test for porous and cellular metals*. Ref Number ISO. **13314**(13314): p. 1-7.
41. Hedayati, R., et al., *Mechanical behavior of additively manufactured porous biomaterials made from truncated cuboctahedron unit cells*. International Journal of Mechanical Sciences, 2016. **106**: p. 19-38.
42. Zadpoor, A.A. and R. Hedayati, *Analytical relationships for prediction of the mechanical properties of additively manufactured porous biomaterials*. Journal of Biomedical Materials Research Part A, 2016. **104**(12): p. 3164–3174.
43. Hedayati, R., et al., *Comparison of elastic properties of open-cell metallic biomaterials with different unit cell types*. Journal of Biomedical Materials Research Part B: Applied Biomaterials, 2017.
44. Campoli, G., et al., *Mechanical properties of open-cell metallic biomaterials manufactured using additive manufacturing*. Materials & Design, 2013. **49**: p. 957-965.
45. Han, C., et al., *Surface modification on a porous Co-Cr scaffold fabricated by selective laser melting for bone implant applications*.
46. Vilaro, T., C. Colin, and J.D. Bartout, *As-Fabricated and Heat-Treated Microstructures of the Ti-6Al-4V Alloy Processed by Selective Laser Melting*. Metallurgical and Materials Transactions A, 2011. **42**(10): p. 3190-3199.
47. Vrancken, B., et al., *Heat treatment of Ti6Al4V produced by selective laser melting: microstructure and mechanical properties*. Journal of Alloys and Compounds, 2012. **541**: p. 177-185.
48. Wauthle, R., et al., *Effects of build orientation and heat treatment on the microstructure and mechanical properties of selective laser melted Ti6Al4V lattice structures*. Additive Manufacturing, 2015. **5**: p. 77-84.
49. Murr, L., et al., *Microstructure and mechanical properties of open-cellular biomaterials prototypes for total knee replacement implants fabricated by electron beam melting*. Journal of the mechanical behavior of biomedical materials, 2011. **4**(7): p. 1396-1411.
50. Fan, Z., *On the young's moduli of Ti-6Al-4V alloys*. Scripta Metallurgica et Materialia, 1993. **29**(11): p. 1427-1432.
51. Lee, Y.T. and G. Welsch, *Young's modulus and damping of Ti ~~6Al4V~~ alloy as a function of heat treatment and oxygen concentration*. Materials Science and Engineering: A, 1990. **128**(1): p. 77-89.
52. Facchini, L., et al., *Ductility of a Ti-6Al-4V alloy produced by selective laser melting of prealloyed powders*. Rapid Prototyping Journal, 2010. **16**(6): p. 450-459.
53. Murr, L.E., et al., *Next Generation Orthopaedic Implants by Additive Manufacturing Using Electron Beam Melting*. International Journal of Biomaterials, 2012. **2012**: p. 14.

54. Koutsoukis, T., et al., *Selective Laser Melting Technique of Co-Cr Dental Alloys: A Review of Structure and Properties and Comparative Analysis with Other Available Techniques*. Journal of Prosthodontics, 2015. **24**(4): p. 303-312.
55. España, F.A., et al., *Design and fabrication of CoCrMo alloy based novel structures for load bearing implants using laser engineered net shaping*. Materials Science and Engineering: C, 2010. **30**(1): p. 50-57.
56. Kajima, Y., et al., *Fatigue strength of Co–Cr–Mo alloy clasps prepared by selective laser melting*. Journal of the mechanical behavior of biomedical materials, 2016. **59**: p. 446-458.
57. Simonelli, M., Y.Y. Tse, and C. Tuck, *Effect of the build orientation on the Mechanical Properties and Fracture Modes of SLM Ti–6Al–4V*. Materials Science and Engineering: A, 2014. **616**: p. 1-11.
58. Georgette, F. and J. Davidson, *The effect of HIPing on the fatigue and tensile strength of a cast, porous-coated Co-Cr-Mo alloy*. Journal of Biomedical Materials Research Part A, 1986. **20**(8): p. 1229-1248.
59. Gaytan, S.M., et al., *A TEM study of cobalt-base alloy prototypes fabricated by EBM*. Materials Sciences and Applications, 2011. **2**(05): p. 355.
60. Song, C., et al., *Research on rapid manufacturing of CoCrMo alloy femoral component based on selective laser melting*. The International Journal of Advanced Manufacturing Technology, 2014. **75**(1): p. 445-453.
61. Rafi, H.K., T.L. Starr, and B.E. Stucker, *A comparison of the tensile, fatigue, and fracture behavior of Ti–6Al–4V and 15-5 PH stainless steel parts made by selective laser melting*. The International Journal of Advanced Manufacturing Technology, 2013. **69**(5): p. 1299-1309.
62. Qian, B., et al., *Defects-tolerant Co-Cr-Mo dental alloys prepared by selective laser melting*. Dental Materials, 2015. **31**(12): p. 1435-1444.
63. Ahmed, T. and H. Rack, *Phase transformations during cooling in $\alpha + \beta$ titanium alloys*. Materials Science and Engineering: A, 1998. **243**(1): p. 206-211.
64. Kaiser, R., D. Browne, and K. Williamson. *Investigation of the effects of cooling rate on the microstructure of investment cast biomedical grade Co alloys*. in *IOP Conference Series: Materials Science and Engineering*. 2012. IOP Publishing.
65. Murr, L., et al., *Open-cellular Co-base and Ni-base superalloys fabricated by electron beam melting*. Materials, 2011. **4**(4): p. 782-790.
66. Zhuang, L. and E. Langer, *Effects of cooling rate control during the solidification process on the microstructure and mechanical properties of cast Co-Cr-Mo alloy used for surgical implants*. Journal of materials science, 1989. **24**(2): p. 381-388.

Chapter 8 Fatigue performance of additively manufactured meta-biomaterials: the effects of topology and material type

This chapter has been published as:

SM Ahmadi, R Hedayati, Y Li, K Lietaert, N Tümer, A Fatemi, CD Rans, B Pouran, H Weinans, AA Zadpoor, *Fatigue performance of additively manufactured meta-biomaterials: The effects of topology and material type*, Acta biomaterialia, 2018. p. 292-304.

8.1 Abstract

Additive manufacturing (AM) techniques enable fabrication of bone-mimicking meta-biomaterials with unprecedented combinations of topological, mechanical, and mass transport properties. The mechanical performance of AM meta-biomaterials is a direct function of their topological design. It is, however, not clear to what extent the material type is important in determining the fatigue behavior of such biomaterials. We therefore aimed to determine the isolated and modulated effects of topological design and material type on the fatigue response of metallic meta-biomaterials fabricated with selective laser melting. Towards that end, we designed and additively manufactured Co-Cr meta-biomaterials with three types of repeating unit cells and three to four porosities per type of repeating unit cell. The AM meta-biomaterials were then mechanically tested to obtain their normalized S-N curves. The obtained S-N curves of Co-Cr meta-biomaterials were compared to those of meta-biomaterials with same topological designs but made from other materials, i.e. Ti-6Al-4V, tantalum, and pure titanium, available from our previous studies. We found the material type to be far more important than the topological design in determining the normalized fatigue strength of our AM metallic meta-biomaterials. This is the opposite of what we have found for the quasi-static mechanical properties of the same meta-biomaterials. The effects of material type, manufacturing imperfections, and topological design were different in the high and low cycle fatigue regions. That is likely because the cyclic response of meta-biomaterials depends not only on the static and fatigue strengths of the bulk material but also on other factors that may include strut roughness, distribution of the micro-pores created inside the struts during the AM process, and plasticity.

8.2 Introduction

Metamaterials are materials with (unusual) mechanical, physical, or biological properties that result from the topological design of their micro-architecture as well as the type of the material from which they are made. In essence, metamaterials are repetitive structures that are convenient to treat as materials for many applications given the length scale of their micro-architectures.

Depending on the physical property of interest, metamaterials are called optical metamaterials [1-4], mechanical metamaterials [5-8], or acoustic metamaterials [9-11]. Meta-biomaterials [12] are a specific class of metamaterials with biomedical applications. As opposed to the other types of metamaterials where only one specific property of the material is of interest, meta-biomaterials are simultaneously designed for several types of properties including mechanical, mass transport, and biological properties [13-17]. Given the importance of topological design in determining the properties of metamaterials, the form-freedom offered by additive manufacturing (AM) techniques is instrumental in realizing meta-biomaterials with arbitrarily complex topologies of the micro-architecture and, thus, unique properties.

Bone-mimicking meta-biomaterials are a special type of such materials that are used either as bone substitutes to expedite bone tissue regeneration or as parts of orthopedic implants to facilitate osseointegration and improve implant longevity. Various properties of bone-mimicking meta-biomaterials need to be simultaneously adjusted for optimal bone tissue regeneration and implants fixation. In this study, however, we are primarily concerned with the mechanical properties in general and the fatigue behavior in particular while focusing on the metallic meta-biomaterials that show high mechanical properties and long fatigue lives. Those biomaterials are often subjected to many cycles of musculoskeletal loads specially when used in load-bearing parts of the skeleton, highlighting the importance of studying their fatigue response. Significant research has been conducted during the last few years into the fatigue behavior of metallic meta-biomaterials. The major modes of loading in bone-mimicking meta-biomaterials is compression and bending. Given the relative simplicity of compression test setups, the fatigue behavior of meta-biomaterials is usually studied under compression-compression loading when establishing S-N curves [12, 18-22].

Previous studies have shown that the topological design of meta-biomaterials including the geometry of the repeating unit cell and the relative density of the porous structure (i.e. the ratio of the density of the porous structure to the density of the bulk material it is made of: $\mu = \rho/\rho_s$) could influence their static [23-27] and fatigue [12, 28] properties. In our previous studies, it was demonstrated that the normalized S-N curves of meta-biomaterials with different relative densities but with the same unit cell and material type are close to each other [22]. The normalized S-N curves are obtained by dividing the levels of stress applied to the meta-biomaterial by its yield stress [12].

The main concerns of the previous studies have been to investigate the effects of the topological characteristics of the porous structure on their fatigue response, and as a result the performance comparisons have been made between porous structures with different topological designs but made from the same bulk materials (e.g. steel [29, 30], magnesium [31, 32], titanium [33-35], Co-Cr [36, 37]). Therefore, it is currently not clear what the effects of material type on the normalized S-N curve are. Moreover, possible modulations between the topological design and material type in determining the fatigue life have not been studied before.

The aim of the current study was to investigate the isolated and modulated effects of topological design and material type on the compressive-compressive fatigue behavior of bone-mimicking metallic meta-biomaterials. Fatigue responses (S-N curves) of meta-biomaterials with different topological designs made from different materials were needed to systematically address that research question. We therefore determined the compression-compression S-N curves for a large set of different topological designs of bone-mimicking meta-biomaterials made from a Co-Cr alloy. The topological designs included three different types of repeating unit cells and three or four porosities for each type of the repeating unit cell. The generated data was used in combination with the S-N curves available from our previous studies on the fatigue behavior of meta-biomaterials made from Ti-6Al-4V [12, 22], pure titanium [38], and tantalum [39].

8.3 Materials and methods

8.3.1 Materials and manufacturing

Meta-biomaterials (Figure 8-1) with a wide range of relative densities ($0.27 < \mu < 0.42$ for truncated cuboctahedron, $0.29 < \mu < 0.42$ for rhombic dodecahedron, and $0.21 < \mu < 0.41$ for diamond) (Table 8-1) were AM using a selective laser melting (SLM) machine. The strut sizes of all meta-biomaterials were in the range of 339.8 μm to 486.3 μm (Table 8-1). To manufacture the structures, Co-Cr powder conforming to ASTM F75 (Cr 28.5%, Mo 6%) was processed on top of a solid substrate under inert atmosphere. After the manufacturing process, the specimens were removed from the solid substrate using electro discharging machine (EDM). Ultrasonic cleaning was used to remove the powder residues before microstructural, morphological, and mechanical

characterizations. All specimens were cylindrical with diameters of 15 mm and lengths of 20 mm. For the meta-biomaterials based on the diamond and truncated cuboctahedron unit cells, four different densities were considered, while for the those based on rhombic dodecahedron, three different densities were designed and AM (Table 8-1). For each unit cell size and porosity, more than 15 specimens were manufactured. Three of the specimens were used for compressive static tests (to obtain the yield stress of each structure type) [40] and the rest of the specimens were used for fatigue tests under different stress levels to obtain the S-N curve.

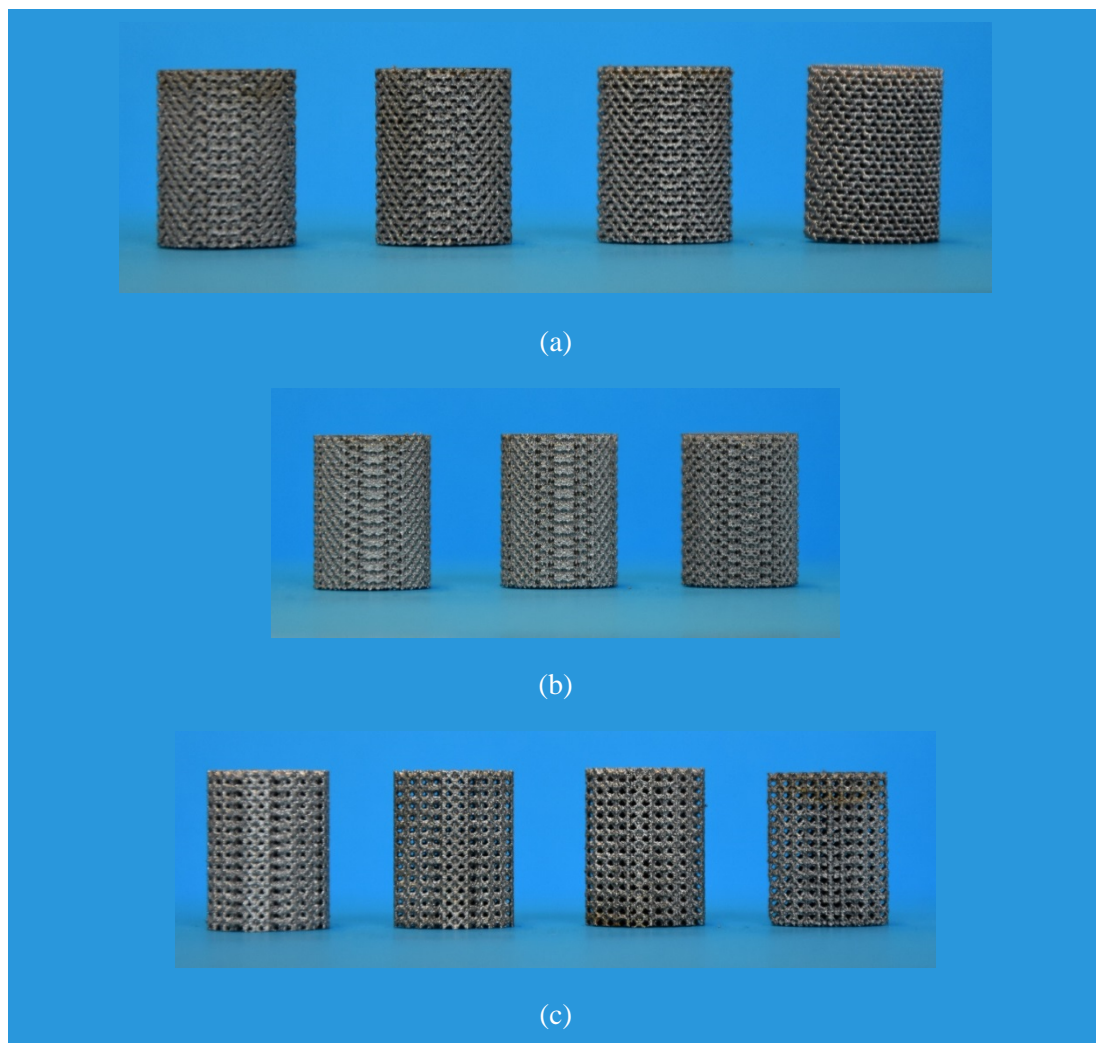


Figure 8-1. Side view of the additively manufactured Co-Cr porous structures based on (a) diamond (b) rhombic dodecahedron, and (c) truncated cuboctahedron unit cells [22]

Table 8-1. Topological design and morphological properties of the porous structures having different unit cell types and sizes [22]

	Relative density		Strut size (μm)		Pore size (μm)	
	Dry weighting	μCT	Nominal (Design)	μCT	Nominal (Design)	μCT
Truncated cuboctahedron (TCO)						
TCO-1	0.236	0.27	324	343.2	876	917.76
TCO-2	0.269	0.28	356	339.84	844	895.2
TCO-3	0.336	0.334	410	396.96	790	821.472
TCO-4	0.386	0.424	460	433.584	740	669.312
Rhombic dodecahedron (RD)						
RD-1	0.299	0.292	310	349.44	590	506.256
RD-2	0.372	0.475	370	402.528	530	492.576
RD-3	0.415	0.532	430	446.4	470	431.76
Diamond (D)						
D-1	0.209	0.272	320	357.216	580	650.736
D-1	0.267	0.35	375	390.384	525	541.488
D-3	0.34	0.445	415	440.928	485	465.6
D-4	0.401	0.526	450	486.288	450	411.36

8.3.2 Topological characterization

Two different techniques, namely micro-computed tomography (μCT) and dry weighing, were used to measure the topological parameters of Co-Cr porous structures including density, strut size, and pore size [40]. In the dry weighing method, the weight of each specimen was measured in

atmospheric conditions, and was then divided by the volume of the specimen to obtain the average density. Subsequently, the obtained average density value was divided by the density of the bulk Co-Cr material (i.e. $\rho_s = 8800 \text{ kg/m}^3$) to calculate the relative density of each specimen. Archimedes technique was used in combination with dry weighing to measure the volume occupied by the internal pores in the struts.

As for μ CT scanning, specimens were scanned using Quantum FX (Perkin Elmer, Waltham, MA, USA). The following parameters were used as a part of the scanning protocol: tube current = 180 μ A, tube voltage = 90 kV, scanning time = 3 min, and resolution = 42 μ m. Based on the scanned 2D images, 3D geometries were constructed using the algorithms built in the scanner software. The constructed 3D geometries were then exported to Caliper Analyze 11.0 (Perkin Elmer, USA) to regain the 2D images of the specimens. Using ImageJ software, the regions of interest (ROIs) of the 2D images were created and the porosity was calculated. The inverse of porosity was used to calculate the volume occupied by the metallic parts of the porous structure, thus, giving the relative density.

8.3.3 Microstructural characterization

To observe the microstructural features of the specimens, optical microscopy and scanning electron microscope (SEM) were used. From each set of specimens, two specimens were selected for metallography. The specimens were first ground using sand papers from coarse (i.e. 180 grit size) to fine (i.e. 2000 grit size). The ground surfaces were then polished respectively by 3 μ m and 1 μ m polishing papers. Two etching solutions were used to reveal the grain boundaries of the polished surfaces from the current study as well as specimens from the previous studies [12, 38] whose S-N curves are adopted in the current study for a more comprehensive analysis. The pure titanium and Ti-6Al-4V specimens were etched using the Kellers etchant (190 ml water + 5 ml nitric acid + 3 ml Hydrochloric acid + 2 ml Hydrofluoric acid) for about 150 s, while another etching solution, i.e. 37%HCl + 1g K₂S₂O₅, was used to etch Co-Cr specimens for 5 min.

The surface morphology, microstructure, and fatigue fracture surfaces were observed with a scanning electron microscope (SEM, JSM-IT100, JEOL). To evaluate the difference between the roughness of Co-Cr and Ti-6Al-4V structures, their roughness values were measured for the same unit cell type (i.e. diamond). Several SEM images were taken from both structure types made from

Co-Cr and Ti-6Al-4V structures and the surface roughness was calculated by measuring the diameters at the central part of randomly chosen struts. The surface roughness for both structures were obtained using the arithmetical mean deviation technique:

$$R_a = \frac{1}{n} \sum_{i=1}^n |y_i| \quad (1)$$

where $n = 10$ is the number of the struts chosen and y_i is the difference between the diameter of the i th strut and the average diameter.

8.3.4 Mechanical testing

To have a better understanding of the local mechanical properties of both the bulk and porous structures made of Co-Cr and Ti-6Al-4V structures, Vicker's micro-hardness tests were performed. The polished surfaces of the bulk and porous specimens (with roughness values up to $1 \mu\text{m}$) were indented using a Vickers hardness test machine (DuraScan-70, Struers, Netherlands) while applying the HV 0.5 test protocol. The hardness was measured in 20 random positions and the average and standard deviation values were calculated.

The quasi-static mechanical properties of the porous structures were obtained [40] using Instron 5985 in accordance with ISO 13314:2011 [41]. The displacement rate was set to 1.8 mm/min and a 100 kN load cell was used to measure the load. The yield and plateau stresses of the porous structures were used for normalizing their S-N curves. To calculate the yield stress, a line was offset to the right side of the initial linear part of the stress-strain curve for 0.2% and its intersection with the stress-strain curve was obtained. The plateau stress was calculated by obtaining the arithmetical mean of the stress values between 20% and 30% strains [41]. The static mechanical test results for Co-Cr were adopted from our other study [40].

The fatigue tests were performed following the protocols established in our previous studies on the bone-mimicking meta-biomaterials made from Ti-6Al-4V [12, 22], pure titanium [38], and tantalum [39]. All the fatigue tests were compressive-compressive with a minimum to maximum compressive loading ratio of 0.1 and a frequency of 15 Hz . The fatigue tests were stopped after the stiffness of

the specimens had reached 10% of their initial value (i.e. when the displacement magnitude was 10 times higher than its initial value). If the specimen did not fail after 10^6 cycles of loading, the test was stopped. For each type of porous structure, the fatigue tests were repeated for several levels of stress and the corresponding fatigue lives were obtained. The stress levels chosen for each porous structure type was chosen in such a way that the meta-biomaterial gave fatigue lives in the range of $10^3 - 10^6$. Using the applied stress level and the resulted fatigue life values, the S-N curve of each specimen was obtained. By dividing the stress in the S-N curve of each structure by its yield, σ_y , or plateau stress, σ_{pl} , value, the normalized S-N curves of all meta-biomaterials were obtained.

8.3.5 Statistical analysis

A two-term power series model ($ax^b + c$) was fit to each normalized S-N curve of Co-Cr structures. Lower and upper confidence limits for each fitting was obtained using the Statistics and Machine Learning Toolbox of MATLAB (2013b, MathWorks, USA). The confidence level was chosen as 95%.

8.4 Results

Microscopic images (Figure 8-2) demonstrated that the surface of the struts of the meta-biomaterials made from Ti-6Al-4V are coarser than those of the Co-Cr porous structures. Moreover, there was more powder adhered to the struts of Ti-6Al-4V structures as compared to the Co-Cr specimens. The roughness values measured for the Co-Cr porous structure were about half of that of the Ti-6Al-4V porous structure ($25.85 \mu\text{m}$ as compared to $48.46 \mu\text{m}$). The percentages of the volume occupied by the internal pores in the struts of Ti-6Al-4V and Co-Cr porous structures were found to be close ($97.86 \pm 1.49\%$ for Ti-6Al-4V as compared to $98.23 \pm 0.55\%$ for Co-Cr). The microstructure was also different in both materials. The Co-Cr microstructure was composed of columnar grains in different directions. Metastable, high-temperature cubic γ phase was observed in the microstructure of Co-Cr specimens, which is likely due to high cooling rates experienced during the SLM process (Figure 8-3a-b). The Ti-6Al-4V specimens exhibited needle-shaped α' martensite grains (Figure 8-3c-d). The α phase normally possesses a lamellar morphology while α' is needle-shaped. Since the SLM

process has cooling rates in the order of 106 K/s [42], this results in the transformation of α to α' . The fatigue fracture images showed that there were no uniform crack growth directions in the Co-Cr specimens and the fracture path was tortuous (Figure 8-4a). However, the fracture surface of Ti-6Al-4V specimens were relatively flat and the crack propagation was in a uniform direction. Visual examination clearly showed that manufacturing defects like unwelded and unmelted powders are more visible on the strut surface of the Ti-6Al-4V specimens as compared to the Co-Cr specimens (compare Figure 8-2b with Figure 8-2d).

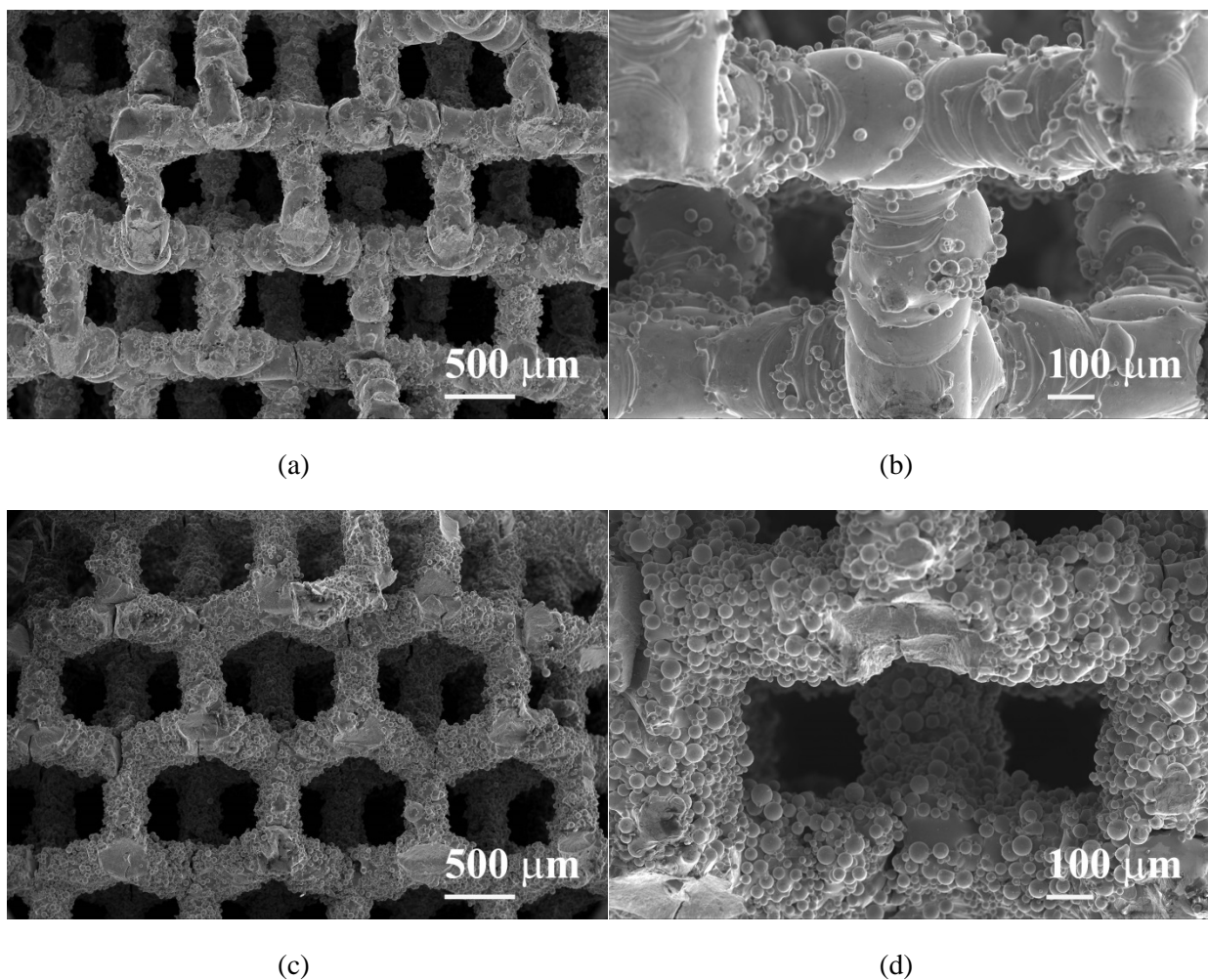


Figure 8-2. Strut surface morphology of selective laser melted (a) Co-Cr (magnification: X30), (b) Co-Cr (magnification: X100), (c) Ti-6Al-4V (magnification: X30), and (d) Ti-6Al-4V (magnification: X100) porous structures based on diamond unit cell

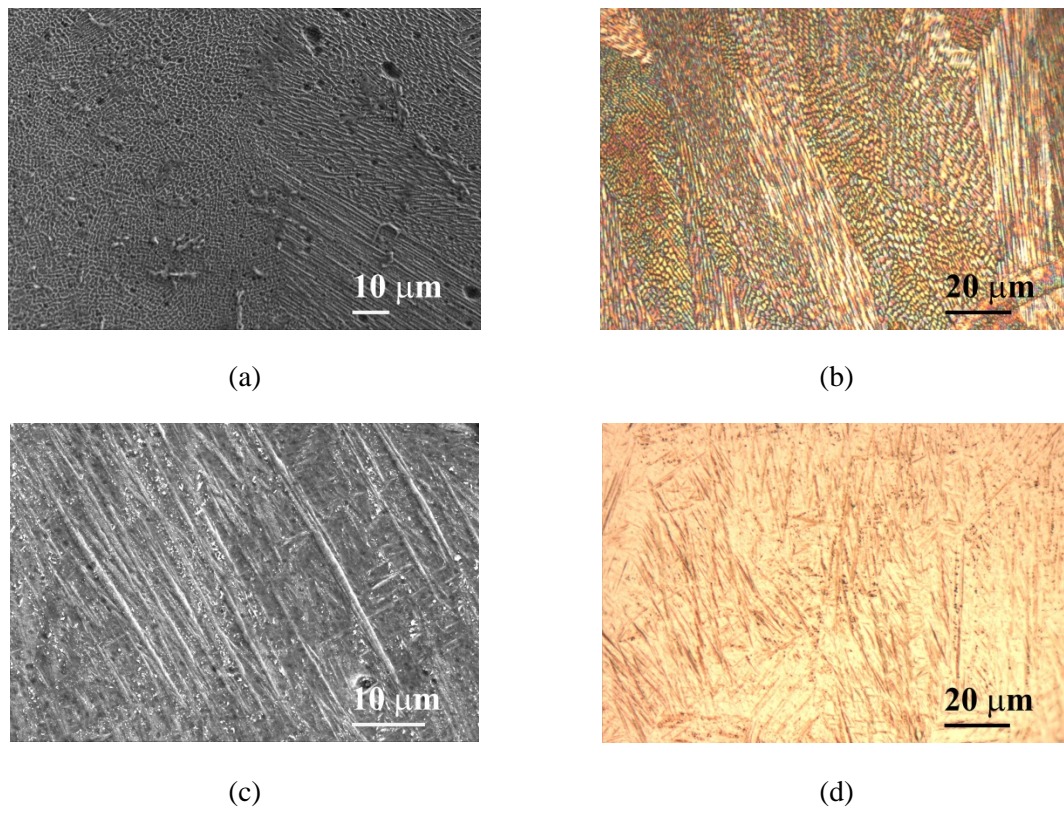


Figure 8-3. SEM and optical microscopy images of the microstructure of the struts in selective laser melted (a-b) Co-Cr and (c-d) Ti-6Al-4V porous structure.

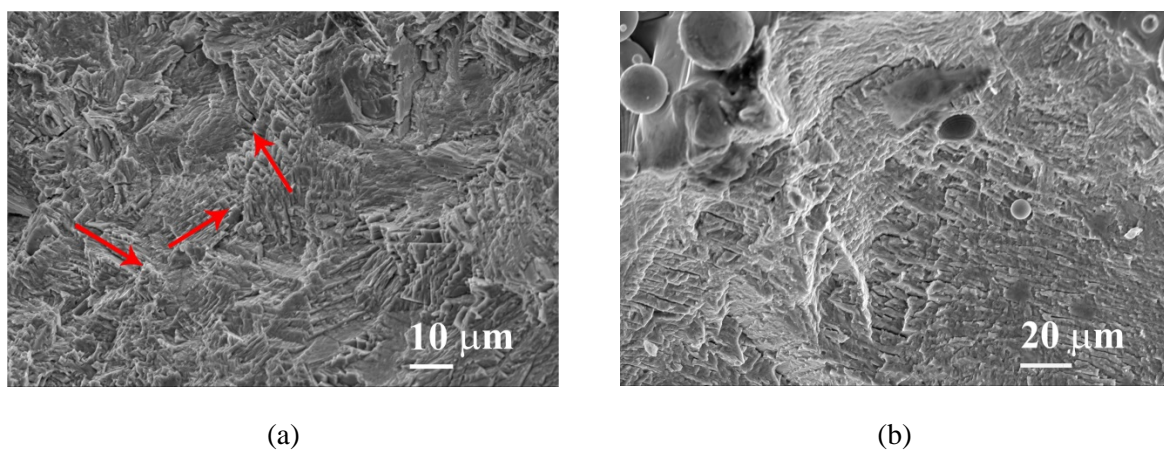
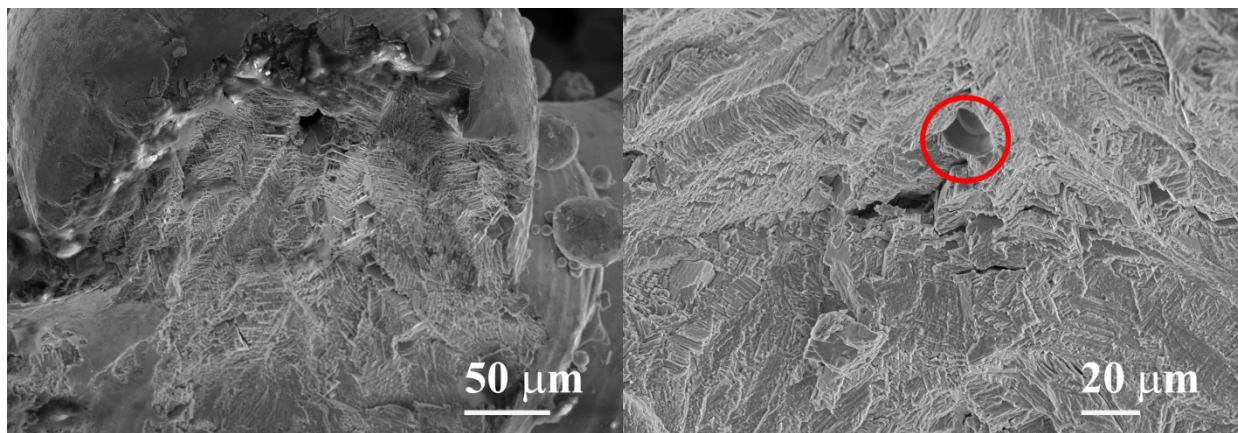
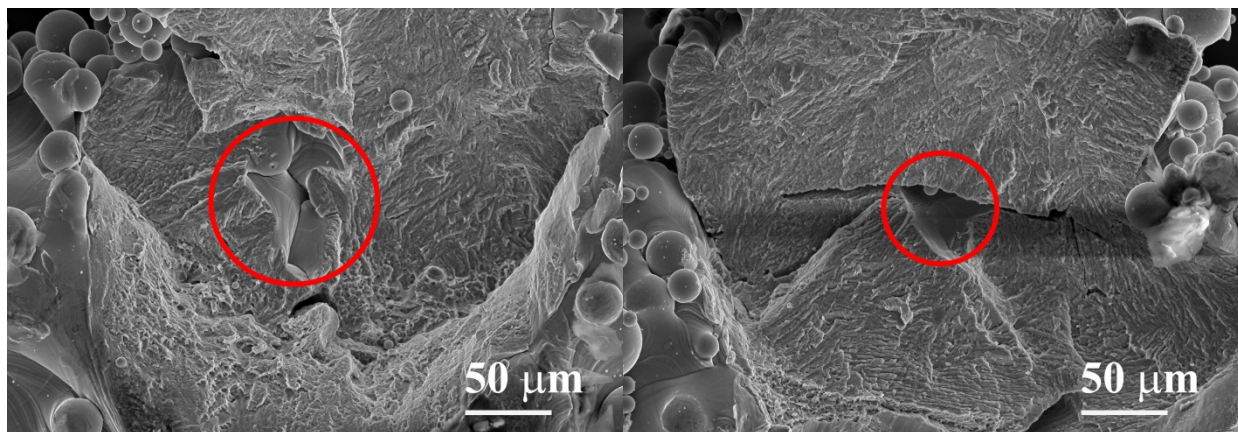


Figure 8-4. Fatigue fracture morphology of the struts in selective laser melted (a) Co-Cr and (b) Ti-6Al-4V porous structure. Fatigue fracture surfaces are indicated by red arrows.



(a)



(b)

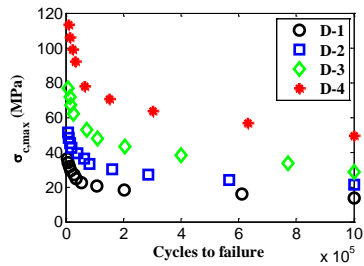
Figure 8-5. Manufacturing defects in the struts of selective laser melted (a) Co-Cr and (b) Ti-6Al-4V porous structures

The Vickers hardness values for the bulk and porous structures of Co-Cr were close (both around 460), while the Vickers hardness value of Ti-6Al-4V porous structure was 17% lower than that of bulk Ti-6Al-4V material (Table 8-2). As expected, by increasing the relative density of each type of meta-biomaterials, the absolute compressive stress, $\sigma_{c,max}$, corresponding to the same fatigue life increased (Figure 8-6). The normalized S-N data points of diamond structure normalized with respect to both yield stress and plateau stress as well as for truncated cuboctahedron structure normalized with respect to plateau stress had small spreads (Figure 8-7a,b,f). The spread of data points was larger for the other cases (i.e. rhombic dodecahedron structure normalized with respect to both

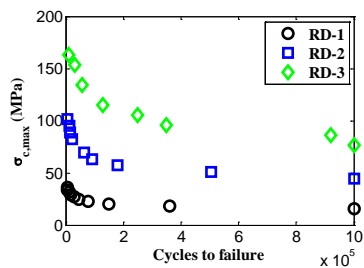
yield stress and plateau stress as well as the truncated cuboctahedron structure normalized with respect to yield stress) (Figure 8-7c,d,e). The S-N data points of all the structures normalized by yield stress was in the range of 0.48-1.64 (Figure 8-7, left), while the range for the S-N data points normalized with respect to plateau stress was in the range of 0.31-1.2 (Figure 8-7, right).

Table 8-2. Vickers hardness values obtained from the hardness tests

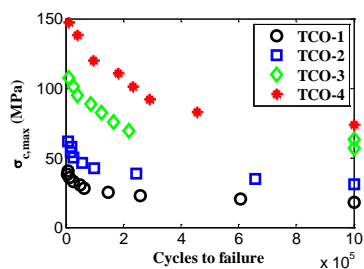
	<i>Bulk</i>	<i>Porous</i>
<i>Co-Cr</i>	460 ± 28.897	460.75 ± 29.994
<i>Ti-6Al-4V</i>	523.25 ± 47.4983	433.142 ± 8.952



(a)



(b)



(c)

Figure 8-6. S-N curves of Co-Cr porous structures based on (a) diamond, (b) rhombic dodecahedron, and (c) truncated cuboctahedron unit cells ($\sigma_{c,max}$ stands for maximum compressive stress, i.e. minimum stress, in each loading cycle)

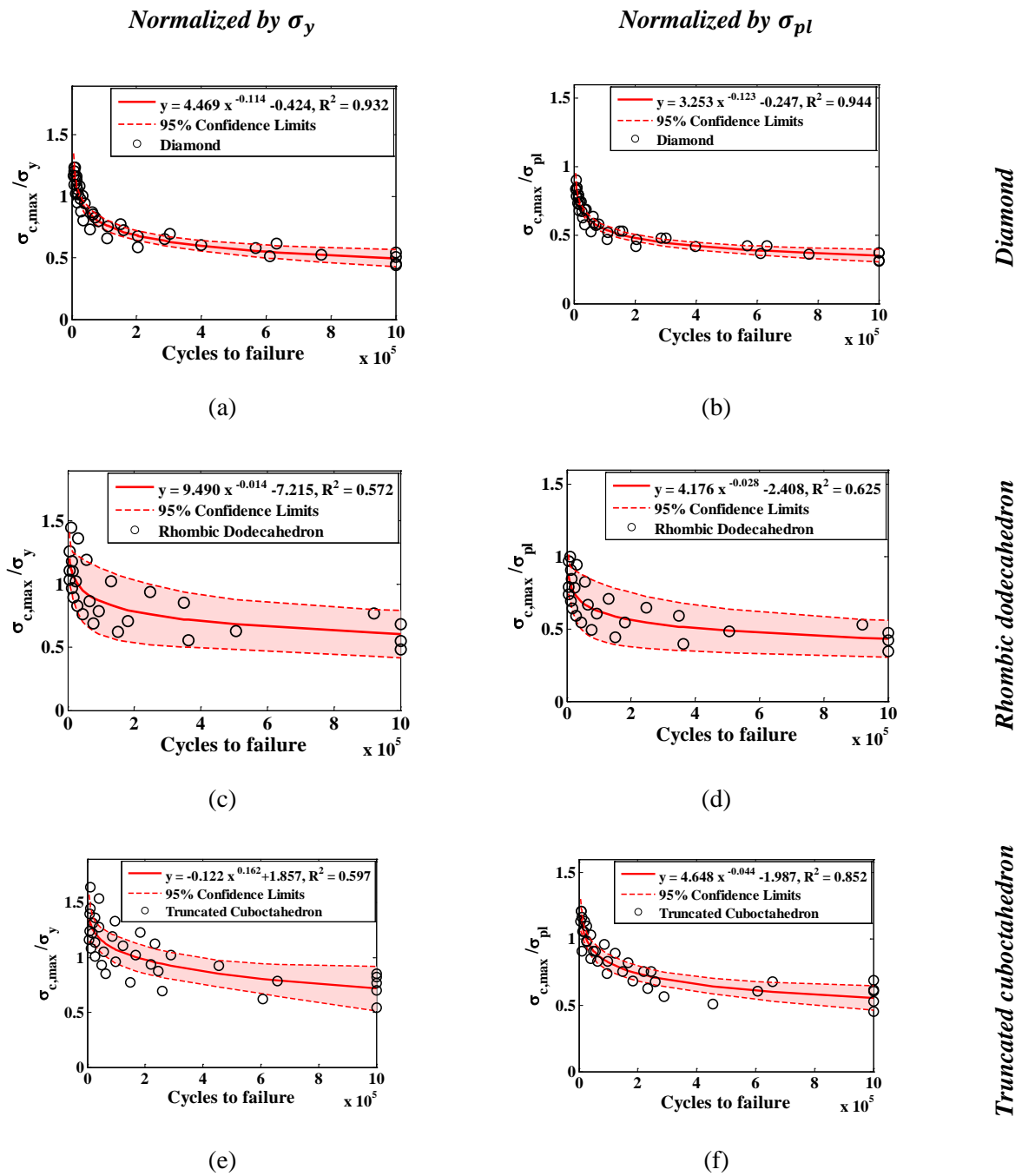


Figure 8-7. Normalized S-N curves of Co-Cr porous structures based on diamond, rhombic dodecahedron, and truncated cuboctahedron unit cells. In equations presented in each graph, y represents the vertical axis parameter (i.e. $\sigma_{c,max}/\sigma_x$) and x represents the horizontal parameter (i.e. number of cycles to failure). R^2 represents the coefficient of determination for the simple linear regression method used for fitting the curves to the data.

The differences between the normalized S-N curves of meta-biomaterials with the same unit cell type but made of different materials were significant (Figure 8-8). For all unit cell types, the stress values in the normalized S-N curve of the structures based on Co-Cr were significantly higher than those of the structures made from other materials (Figure 8-8). Among the meta-biomaterials based on the rhombic dodecahedron unit cell, the highest stress values in the normalized S-N curve respectively belonged to Co-Cr, pure titanium, tantalum, and Ti-6Al-4V (Figure 8-8). None of the normalized S-N curves intersected each other in the considered range of cycle numbers (i.e. in the high cycle region). The 95% CIs of the Co-Cr and Ti-6Al-4V structures based on the same unit cell type did not also show any overlapping (Figure 8-8).

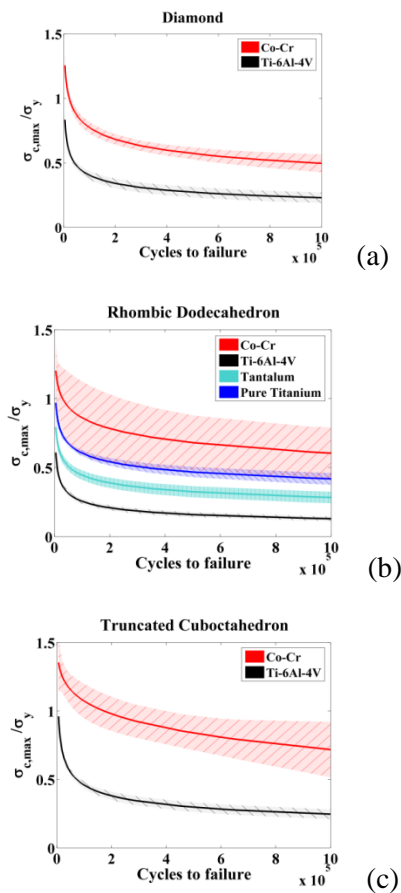


Figure 8-8. Comparison of normalized S-N curves of porous structures made from Co-Cr, Ti-6Al-4V, tantalum, and commercially pure titanium based on (a) diamond, (b) rhombic dodecahedron, and (c) truncated cuboctahedron unit cells

8.5 Discussion

8.5.1 Topological/material modulation

The results of this study clearly showed that the normalized S-N curves of AM meta-biomaterials are determined by both their topological design and material type (Figure 8-8 and Figure 8-9). Comparing the effects of topological design with those of the material type show that material type influenced the normalized S-N curves to a much greater extent (Figure 8-9). The S-N curves and 95% confidence limits of meta-biomaterials made from Co-Cr and Ti-6Al-4V constitute two separate clusters, which do not overlap with each other. However, structures made from the same material but based on different unit cells showed considerable overlapping (Figure 8-9).

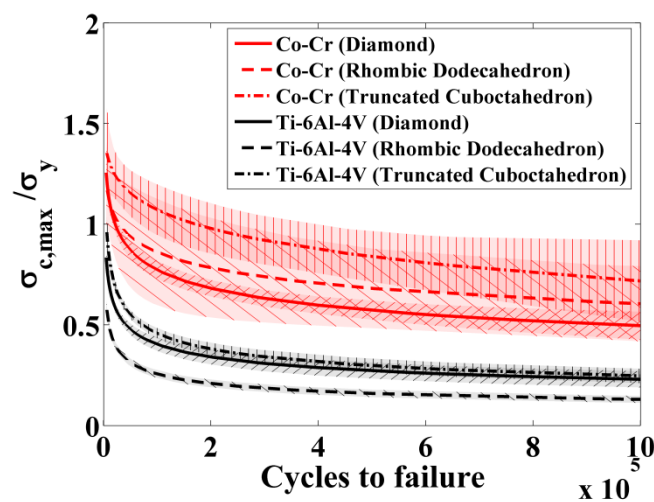


Figure 8-9. Comparison of normalized S-N curves of Co-Cr porous structures based on different unit cell types

The modulated effects of topological design and bulk material properties on the fatigue response of meta-biomaterials is the opposite of what we have found for the *quasi-static* properties of the same meta-biomaterials [40]. In our other study [40], we found that the topological design could result in up to 10-fold difference in the quasi-static mechanical properties of meta-biomaterials, while the effects of material type did not go beyond 2-fold. It would be interesting to extend the current study to other prevalent biocompatible materials as well as other promising unit cell types (see for

examples [43]) to see which of the two factors of material type or topological design is more influential in determining the fatigue response of AM meta-biomaterials.

The other interesting difference observed between the fatigue performance of meta-biomaterials made of Co-Cr and that of Ti-6Al-4V was the maximum strength recorded in their S-N curves normalized with respect to yield stress (Figure 8-7 left and Figure 8-8, see also [12]). The maximum fatigue strength of meta-biomaterials made of Ti-6Al-4V did not exceed 80-90% of the yield stress (in cycles around $10^3 - 10^4$) [12, 22]. By setting the applied stress in the fatigue test of meta-biomaterials made of Ti-6Al-4V to values around 90% of yield stress, the structure experienced immediate fatigue failure before reaching 100 cycles. The maximum fatigue strength of meta-biomaterials made of Co-Cr, however, could go up to values around 170% of their yield strengths (in cycles around $10^3 - 10^4$) (Figure 8-7 left). A similar trend has been observed in the literature regarding the high fatigue strength of Co-Cr *solid* materials which showed fatigue strengths around 130% of yield stress [44], 99% of yield stress [45], and 127% of yield stress [46] at 10^5 cycles. In the same studies, fatigue strengths around 124% of yield stress [45] and 150% of yield stress [46] at cycle numbers around 10^4 was reported. This is another observation that signifies the importance of material type in determining the fatigue response of meta-biomaterials.

Ideally, one would like to use scaffolds that have exactly same morphological parameters. In this study, however, we also used the data available from several studies that were previously performed and whose designs changed during the current study. There were therefore some differences in the absolute values of morphological parameters between the different material types. In particular, the strut size of the Co-Cr porous structures used in this study was almost twice that of the reported Ti-6Al-4V and Ta scaffolds. This may have also contributed to the improved fatigue behavior of Co-Cr-Mo scaffolds as compared to other materials.

8.5.2 The effects of surface roughness and grain morphology

Surface roughness affects the fatigue crack initiation because stress concentration is drastically raised in sharp-angled particles. One of the reasons behind the higher fatigue lives of Co-Cr structures as compared to Ti-6Al-4V specimens could be the much smoother surface of the Co-Cr porous structures (Figure 8-2). Moreover, the columnar grains of Co-Cr grow in different orientations

and could therefore interlock each other [47]. The texture resembling a common weaved fabric could improve the fatigue resistance of the material, as the crack path will be more tortuous than and the fatigue crack growth rate will likely slow down. Figure 8-4(a) shows the crack propagation tortured in different orientations. The crack propagation energy could be absorbed at multiple scales, respectively, by the microscopically weaved elongated grains and by the grain boundaries, resulting in longer fatigue lives of Co-Cr structures.

As for the SLM Ti-6Al-4V, the microstructure is of needle α' martensite type due to the rapid cooling rate. As is clear from Figure 8-4(b), the cracks grew along the needle-shaped grains. The crack growth resistance seems to be lower and the crack surface is fairly smooth. The low ductility of the martensite phase in Ti-6Al-4V implies sensitivity to notches. This could be another explanation for the shorter fatigue lives observed. We also found more manufacturing defects in Ti-6Al-4V struts. The internal pores and unmelted powders on the surface could both serve as stress concentration sites for fatigue crack initiation. Although the internal pore volume percentage was similar and negligible in both the materials, the much higher external surface roughness in the Ti-6Al-4V structures (Figure 8-2) could lead to more significant decrease in the fatigue life of Ti-6Al-4V meta-biomaterials as compared to Co-Cr structures. The hardness tests also demonstrated the detrimental effects of rapid cooling on porous Ti-6Al-4V specimens (i.e. 17% reduction in the local hardness as compared to bulk Ti-6Al-4V), while the rapid cooling effect was almost negligible in Co-Cr porous structures (Table 8-2).

In surface-finished parts, the design geometry of the part plays an important role in determining the stress concentration factor. In AM porous structures with pore sizes smaller than 1 mm, however, the irregularities created by the manufacturing processes play the dominant role in determining the stress concentration factor. These irregularities in the external surface are created by first large melt pools the size of which is comparable to the strut size and second by unmelted powders on the surface. While the stress concentration effect of the powder particles adhered to the final product is similar in the porous structures with different relative density, the effect of melt pool size on the stress concentration factor becomes larger as the nominal strut diameter decreases. This is due to the fact that as the nominal strut diameter decreases the ratio of the melt pool size to the nominal strut diameter increases (compare Figure 8-10a and 8-10b). This can also explain the lower lives of structures with lower relative densities. Moreover, the stress concentration factors are expected to

be higher for scaffolds with higher roughness values. For example, the stress concentration factors of Ti-6Al-4V specimens are expected to be higher than those of Co-Cr specimens.

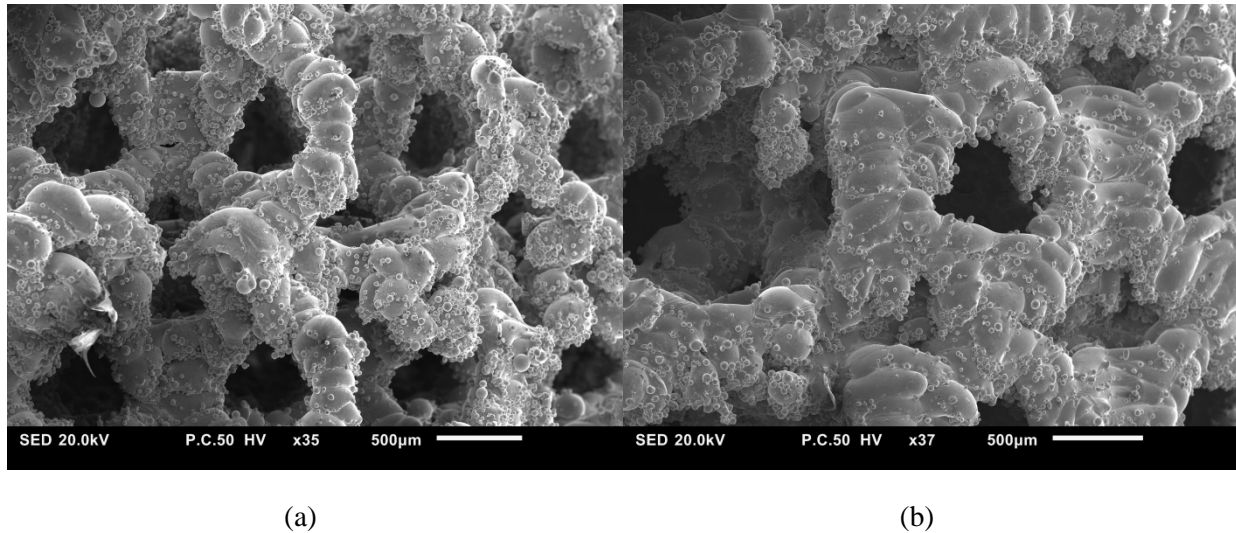


Figure 8-10. Morphology of Co-Cr porous structures based on truncated cuboctahedron unit cell with relative densities of 0.236 (TCO-1) and (b) 0.386 (TCO-4).

8.5.3 The effects of the mechanical behavior of the bulk material

Our results demonstrated that the normalized fatigue strengths of meta-biomaterials made of Co-Cr are much higher than those of other meta-biomaterials (Figure 8-8 and Figure 8-9). This could be attributed to the intrinsic properties of stress concentration factor and its different effects on fatigue and static loadings as well as to the difference in the mechanical behavior of the bulk material. Co-Cr specimens demonstrate higher levels of strain-hardening while the degree of strain hardening in pure titanium and Ti-6Al-4V is much less. In other words, the difference between ultimate stress and yield stress in bulk Co-Cr is significant (our tests [40] demonstrated that ultimate stress is about 3-4 times larger than the yield stress) while in pure titanium and Ti-6Al-4V they are relatively close. In Co-Cr porous structures, due to high strain-hardening capacity, the effects of stress concentration are offset by local plasticity particularly in the vicinity of crack front. In Ti-6Al-4V structures, due to much less strain-hardening capacity, the stress-concentration effects lead to quicker crack initiation and therefore quicker failure in the struts of the porous structures. This could explain why the

normalized S-N curves of Ti-6Al-4V meta-biomaterials are generally much lower than those of Co-Cr meta-biomaterials.

The results also demonstrated that in the normalized S-N curves of porous structures, the spread of the data points is greater in Co-Cr specimens as compared to Ti-6Al-4V, pure titanium, and tantalum specimens. In particular, the spread of the data points was relatively large in Co-Cr rhombic dodecahedron and truncated cuboctahedron cases. In the normalized S-N curves of Co-Cr meta-biomaterials based on the same unit cell type, as the relative density of the porous structure increased, the data points of the meta-biomaterials with higher relative densities lie higher. This could be once more attributed to the post-elastic behavior of the bulk Co-Cr material. It has been reported [40] that by increasing the relative density, the porous Co-Cr material shows more strain-hardening behavior in its stress-strain curve before reaching the first maximum stress. This is expected, as the similarity between the fatigue response of porous structures and that of the bulk Co-Cr material should increase with relative density. It is worth noting that bulk Co-Cr exhibits S-N data points that are as large as 150% of its yield stress [44-46]). That is why the normalized S-N curves of structures with higher relative densities tend to be higher than those with lower relative densities, and therefore a spread in normalized S-N curve is observed.

8.5.4 HCF/LCF differences

The fatigue response of meta-biomaterials depends not only on the static and fatigue behavior of the bulk material and topological design but also on the roughness of the outer surface of the struts (which greatly affects crack initiation), distribution of the micro-pores created inside the struts during the AM process (which affects the crack propagation mechanism), and plasticity (which affects both crack initiation and crack propagation mechanisms). Effects such as surface finish and material imperfections are more dominant in high cycle fatigue (HCF) range as compared to low cycle fatigue (LCF), because their influence increases as the stress level decreases. This is due to the fact that in HCF, the crack nucleation occurs due to intrusion and extrusion in the material. However, in LCF, the main cause of crack nucleation is bulk plastic deformations. The effects of surface irregularities and the material internal imperfections are therefore much less apparent in LCF as compared to HCF. As is clear from Figure 8-9, the material and imperfection effects are most

prominent in the HCF region. For example, for the rhombic dodecahedron unit cell, for fatigue lives around 10^4 cycles (i.e. LCF), the ratio of the stress level of Co-Cr porous structure to that of the Ti-6Al-4V porous structure is about 2.58:1. For fatigue lives around 10^6 cycles (i.e. HCF), the noted ratio becomes about 5.5:1. As another example, for the diamond unit cell type, for fatigue lives around 10^4 cycles (i.e. LCF), the ratio of the stress level of Co-Cr porous structure to that of the Ti-6Al-4V porous structure is about 1.68:1, while for fatigue lives around 10^6 cycles (i.e. HCF) the noted ratio is about 2.6:1. Empirical approaches are typically used to account for imperfection effects particularly when using the S-N approach. Another type of effect comes from cyclic plasticity, which typically is more prominent in the LCF as compared to HCF. Those include effects such as strain hardening, cyclic softening or hardening, stress gradient, etc. Such effects are more prominent in the LCF due to the higher plastic deformation in this regime. It is difficult to account for those effects using empirical approaches and, therefore, more analytical methods such as strain-life method are more suited. As it can be seen in Figure 8-9, the S-N curves of the Co-Cr and Ti-6Al-4V structures become closer to each other in the LCF. It is not easy to say which of the two parameters of manufacturing imperfection and post-elastic material behavior of Co-Cr or Ti-6Al-4V stand for this significant decrease in the difference between the S-N curves of the two structures in LCF as compared to HCF in Figure 8-9. Due to intrinsic differences in the AM parameters such as powder size, laser power, layer thickness, and working temperature used to manufacture meta-biomaterials made of different materials, it is difficult to answer the above-mentioned question using only empirical methods. To better distinguish between the material and manufacturing imperfection effects, computational methods [48] could be implemented to investigate the effects of each parameter exclusively by keeping other parameters unchanged. Using computational methods such as the finite element method, it is also possible to study the changes in the local stresses and strains in the most vulnerable locations of each unit cell type, which itself can be obtained using microscopic imaging as well as finite element modeling. Effects such as multiaxial stresses could also become important in AM meta-biomaterials due to the complex loading conditions in the struts and vertices of the porous structures.

In the LCF regime, it might be better to use methods not just based on stress or strain, but both. For example, when material response changes based on the applied stress, such as in strain hardening or cyclic hardening/softening, such approaches (for example SWT [49, 50], Fatemi-Socie [51], energy

methods [52, 53], etc.) are more quantitative and could better account for those effects. It should be kept in mind that discussing the fatigue response in terms of LCF and HCF is only useful for distinguishing the main trends, as such a classification typically only applies to constant applied loading. The realistic loading conditions of most components and structures, including biomedical implants is variable amplitude. In such loading cases, there are many low amplitude cycles belonging to HCF and some overload cycles belonging to LCF. Therefore, such problems cannot be classified as either LCF or HCF. The approaches incorporating both stress and strain typically work better for this class of problems.

4.5. Loading condition

Although after implantation, the porous structures are usually loaded in both compression and bending loads, in this study, similar to previous studies in the literature [12, 18-22], only the compression-compression tests were carried out for comparing the performance of porous structures with different topological designs and made from different materials. Testing the fatigue behavior of meta-biomaterials under bending load is more challenging, as the loading conditions will be dependent on the anatomical site, the type of implant, and anatomical features of the patient. In comparison, the number of factors in axial compression-compression testing is more limited. However, to validate an implant (with or without porous body), it is always recommended to carry out experimental fatigue tests with loading conditions which are chosen to be as close as possible to the actual loading conditions experienced in the human body.

4.6. Applications in biomedical implants

As previously mentioned, AM meta-biomaterials need to satisfy several requirements regarding their mechanical, mass transport (e.g. permeability, diffusivity), and topological (e.g. curvature) properties in order to qualify as suitable bone substitutes. It is often assumed that the various properties of AM meta-biomaterials should mimic those of the native bone tissue. Since there are significant variations in the properties of the native bone tissue, it is generally more appropriate to present a range of acceptable properties. All AM porous meta-biomaterials considered here show elastic moduli in the range of those reported for bone [40, 54-56]. As for the fatigue behavior, the S-N curves determined here and in the previous studies are often used to determine the stress level for which the implants could undergo at least one million of loading cycles without failure. Regarding

the bio-compatibility requirements, all included materials are considered to be sufficiently bio-compatible [57, 58]. In certain applications of AM meta-biomaterials including treatment of critical sized bony defects, it is often ideal to use biodegradable metallic biomaterials that break down after fully regenerating functional bone tissue. None of the materials considered here are biodegradable. Indeed, the progress in development of AM biodegradable metallic meta-biomaterials has been very limited so far. Ultimately, all the developed meta-biomaterials need to be tested in animal models and clinical studies before routine clinical application. Our previous animal studies have shown the potential of both AM porous Ti-6Al-4V [59, 60] and AM porous tantalum [39] for treatment of critical size bony defects. The *in vivo* response to Co-Cr alloys may not be as favorable as the response to titanium alloys [61]. However, it has been recently shown that adding small amounts of Zr could significantly improve the osseointegration of Co-Cr implants [62].

8.6 Conclusion

We studied the isolated and modulated effects of topological design and material type on the fatigue behavior of AM meta-biomaterials. The relative density of the Co-Cr meta-biomaterials based on diamond unit cell did not have a significant effect on their normalized S-N curves similar to what was previously observed for Ti-6Al-4V structures based on all the unit cell types. However, unlike what had been previously observed for Ti-6Al-4V structures, the relative density had a considerable effect on the normalized S-N curves of Co-Cr porous structures based on truncated cuboctahedron and particularly rhombic dodecahedron unit cells. These differences could be attributed to the large difference between the post-elastic behavior of Co-Cr as compared to the other considered materials. Bulk Co-Cr material showed a substantial strain-hardening behavior which also leads to its very high fatigue strength (previous studies have shown that it can have S-N data points as large as 150% of its yield stress [44-46]). As the relative density increases, the fatigue response of porous structure becomes more similar to the bulk Co-Cr material and topology contributes less to the fatigue response. It was observed that, in general, as compared to the topological design (unit cell type and porosity), the material type and manufacturing imperfections are more important in determining the normalized S-N curves of AM meta-biomaterials particularly in the HCF region. This is the opposite of what we found for the quasi-static mechanical properties of the same materials and topologies. The effects of material type, manufacturing imperfections, and topological design were different in the LCF and HCF regions. That is due to the fact that the fatigue response of AM meta-biomaterials is dependent not only on the static and fatigue strengths of the bulk material but also on other factors such as the roughness of the outer surface of the struts (affecting crack initiation), distribution of the micro-pores created inside the struts during the AM process (affecting crack propagation procedure), and plasticity (affecting both crack initiation and crack propagation procedures). The contribution of each of the noted parameters is different in the HCF and LCF regions.

8.7 References

1. Valentine, J., S. Zhang, T. Zentgraf, E. Ulin-Avila, D.A. Genov, G. Bartal, and X. Zhang, *Three-dimensional optical metamaterial with a negative refractive index*. *nature*, 2008. **455**(7211): p. 376-379.
2. Zhao, Y., M. Belkin, and A. Alù, *Twisted optical metamaterials for planarized ultrathin broadband circular polarizers*. *Nature communications*, 2012. **3**: p. 870.
3. Menzel, C., C. Helgert, C. Rockstuhl, E.-B. Kley, A. Tünnermann, T. Pertsch, and F. Lederer, *Asymmetric transmission of linearly polarized light at optical metamaterials*. *Physical review letters*, 2010. **104**(25): p. 253902.
4. Shalaev, V.M., W. Cai, U.K. Chettiar, H.-K. Yuan, A.K. Sarychev, V.P. Drachev, and A.V. Kildishev, *Negative index of refraction in optical metamaterials*. *Optics letters*, 2005. **30**(24): p. 3356-3358.
5. Lee, J.H., J.P. Singer, and E.L. Thomas, *Micro-/Nanostructured Mechanical Metamaterials*. *Advanced materials*, 2012. **24**(36): p. 4782-4810.
6. Akagawa, Y., Y. Ichikawa, H. Nikai, and H. Tsuru, *Interface histology of unloaded and early loaded partially stabilized zirconia endosseous implant in initial bone healing*. *The Journal of prosthetic dentistry*, 1993. **69**(6): p. 599-604.
7. Hedayati, R., A. Leeflang, and A. Zadpoor, *Additively manufactured metallic pentamode meta-materials*. *Applied Physics Letters*, 2017. **110**(9): p. 091905.
8. Zadpoor, A.A., *Mechanical meta-materials*. *Materials Horizons*, 2016. **3**(5): p. 371-381.
9. Torrent, D. and J. Sánchez-Dehesa, *Acoustic metamaterials for new two-dimensional sonic devices*. *New journal of physics*, 2007. **9**(9): p. 323.
10. Chen, H. and C. Chan, *Acoustic cloaking in three dimensions using acoustic metamaterials*. *Applied physics letters*, 2007. **91**(18): p. 183518.
11. Zhang, S., L. Yin, and N. Fang, *Focusing ultrasound with an acoustic metamaterial network*. *Physical review letters*, 2009. **102**(19): p. 194301.
12. Amin Yavari, S., S. Ahmadi, R. Wauthle, B. Pouran, J. Schrooten, H. Weinans, and A. Zadpoor, *Relationship between unit cell type and porosity and the fatigue behavior of selective laser melted meta-biomaterials*. *Journal of the mechanical behavior of biomedical materials*, 2015. **43**: p. 91-100.
13. Fielding, G.A., A. Bandyopadhyay, and S. Bose, *Effects of silica and zinc oxide doping on mechanical and biological properties of 3D printed tricalcium phosphate tissue engineering scaffolds*. *Dental Materials*, 2012. **28**(2): p. 113-122.
14. Wu, C., Y. Ramaswamy, P. Boughton, and H. Zreiqat, *Improvement of mechanical and biological properties of porous CaSiO₃ scaffolds by poly (d, l-lactic acid) modification*. *Acta Biomaterialia*, 2008. **4**(2): p. 343-353.
15. Hollister, S.J., *Porous scaffold design for tissue engineering*. *Nature materials*, 2005. **4**(7): p. 518-524.
16. Drury, J.L. and D.J. Mooney, *Hydrogels for tissue engineering: scaffold design variables and applications*. *Biomaterials*, 2003. **24**(24): p. 4337-4351.
17. Meinel, L., V. Karageorgiou, R. Fajardo, B. Snyder, V. Shinde-Patil, L. Zichner, D. Kaplan, R. Langer, and G. Vunjak-Novakovic, *Bone tissue engineering using human mesenchymal stem*

- cells: effects of scaffold material and medium flow*. Annals of biomedical engineering, 2004. **32**(1): p. 112-122.
18. Hrabe, N.W., P. Heintz, B. Flinn, C. Körner, and R.K. Bordia, *Compression-compression fatigue of selective electron beam melted cellular titanium (Ti-6Al-4V)*. Journal of Biomedical Materials Research Part B: Applied Biomaterials, 2011. **99**(2): p. 313-320.
 19. Zhao, S., S. Li, W. Hou, Y. Hao, R. Yang, and R. Misra, *The influence of cell morphology on the compressive fatigue behavior of Ti-6Al-4V meshes fabricated by electron beam melting*. Journal of the mechanical behavior of biomedical materials, 2016. **59**: p. 251-264.
 20. Yan, C., L. Hao, A. Hussein, and P. Young, *Ti-6Al-4V triply periodic minimal surface structures for bone implants fabricated via selective laser melting*. Journal of the mechanical behavior of biomedical materials, 2015. **51**: p. 61-73.
 21. Yavari, S.A., S. Ahmadi, R. Wauthle, B. Pouran, J. Schrooten, H. Weinans, and A. Zadpoor, *Relationship between unit cell type and porosity and the fatigue behavior of selective laser melted meta-biomaterials*. Journal of the mechanical behavior of biomedical materials, 2015. **43**: p. 91-100.
 22. Yavari, S.A., R. Wauthlé, J. van der Stok, A. Riemslag, M. Janssen, M. Mulier, J.-P. Kruth, J. Schrooten, H. Weinans, and A.A. Zadpoor, *Fatigue behavior of porous biomaterials manufactured using selective laser melting*. Materials Science and Engineering: C, 2013. **33**(8): p. 4849-4858.
 23. Babaei, S., B.H. Jahromi, A. Ajdari, H. Nayeb-Hashemi, and A. Vaziri, *Mechanical properties of open-cell rhombic dodecahedron cellular structures*. Acta Materialia, 2012. **60**(6): p. 2873-2885.
 24. Ahmadi, S., S. Yavari, R. Wauthle, B. Pouran, J. Schrooten, H. Weinans, and A. Zadpoor, *Additively manufactured open-cell porous biomaterials made from six different space-filling unit cells: the mechanical and morphological properties*. Materials, 2015. **8**(4): p. 1871-1896.
 25. Hedayati, R., M. Sadighi, M. Mohammadi-Aghdam, and A. Zadpoor, *Analytical relationships for the mechanical properties of additively manufactured porous biomaterials based on octahedral unit cells*. Applied Mathematical Modelling, 2017. **46**: p. 408-422.
 26. Zheng, X., H. Lee, T.H. Weisgraber, M. Shusteff, J. DeOtte, E.B. Duoss, J.D. Kuntz, M.M. Biener, Q. Ge, and J.A. Jackson, *Ultralight, ultrastiff mechanical metamaterials*. Science, 2014. **344**(6190): p. 1373-1377.
 27. Hedayati, R., M. Sadighi, M. Mohammadi Aghdam, and A.A. Zadpoor, *Mechanical properties of additively manufactured thick honeycombs*. Materials, 2016. **9**(8): p. 613.
 28. Balla, V.K., S. Bodhak, S. Bose, and A. Bandyopadhyay, *Porous tantalum structures for bone implants: fabrication, mechanical and in vitro biological properties*. Acta biomaterialia, 2010. **6**(8): p. 3349-3359.
 29. Yan, C., L. Hao, A. Hussein, P. Young, and D. Raymont, *Advanced lightweight 316L stainless steel cellular lattice structures fabricated via selective laser melting*. Materials & Design, 2014. **55**: p. 533-541.
 30. Tsoupanos, S., R. Mines, S. McKown, Y. Shen, W. Cantwell, W. Brooks, and C. Sutcliffe, *The influence of processing parameters on the mechanical properties of selectively laser melted stainless steel microlattice structures*. Journal of Manufacturing Science and Engineering, 2010. **132**(4): p. 041011.
 31. Kirkland, N., I. Kolbeinsson, T. Woodfield, G. Dias, and M. Staiger, *Synthesis and properties of topologically ordered porous magnesium*. Materials Science and Engineering: B, 2011. **176**(20): p. 1666-1672.

32. Nguyen, T.L., M.P. Staiger, G.J. Dias, and T.B. Woodfield, *A Novel Manufacturing Route for Fabrication of Topologically-Ordered Porous Magnesium Scaffolds*. *Advanced Engineering Materials*, 2011. **13**(9): p. 872-881.
33. Sun, J., Y. Yang, and D. Wang, *Mechanical properties of a Ti6Al4V porous structure produced by selective laser melting*. *Materials & Design*, 2013. **49**: p. 545-552.
34. Lipinski, P., A. Barbas, and A.-S. Bonnet, *Fatigue behavior of thin-walled grade 2 titanium samples processed by selective laser melting. Application to life prediction of porous titanium implants*. *Journal of the mechanical behavior of biomedical materials*, 2013. **28**: p. 274-290.
35. Parthasarathy, J., B. Starly, S. Raman, and A. Christensen, *Mechanical evaluation of porous titanium (Ti6Al4V) structures with electron beam melting (EBM)*. *Journal of the mechanical behavior of biomedical materials*, 2010. **3**(3): p. 249-259.
36. Han, C., X. Chen, J. Tan, Y. Yao, Q. Wei, Z. Zhang, and Y. Shi, *Surface modification on a porous Co-Cr scaffold fabricated by selective laser melting for bone implant applications*.
37. Han, C., C. Han, C. Yan, C. Yan, S. Wen, S. Wen, T. Xu, T. Xu, S. Li, and S. Li, *Effects of the unit cell topology on the compression properties of porous Co-Cr scaffolds fabricated via selective laser melting*. *Rapid Prototyping Journal*, 2017. **23**(1): p. 16-27.
38. Wauthle, R., S.M. Ahmadi, S.A. Yavari, M. Mulier, A.A. Zadpoor, H. Weinans, J. Van Humbeeck, J.-P. Kruth, and J. Schrooten, *Revival of pure titanium for dynamically loaded porous implants using additive manufacturing*. *Materials Science and Engineering: C*, 2015. **54**: p. 94-100.
39. Wauthle, R., J. Van der Stok, S.A. Yavari, J. Van Humbeeck, J.-P. Kruth, A.A. Zadpoor, H. Weinans, M. Mulier, and J. Schrooten, *Additively manufactured porous tantalum implants*. *Acta biomaterialia*, 2015. **14**: p. 217-225.
40. Hedayati, R., S.M. Ahmadi, K. Lietaert, B. Pouran, Y. Li, H. Weinans, C.D. Rans, and A.A. Zadpoor, *Isolated and modulated effects of topology and material type on the mechanical properties of additively manufactured porous biomaterials*. Submitted.
41. Standard, I., *ISO 13314: 2011 (E)(2011) Mechanical testing of metals—ductility testing—compression test for porous and cellular metals*. Ref Number ISO. **13314**(13314): p. 1-7.
42. Zheng, Y., X. Xu, Z. Xu, H. Cai, and J.-Q. Wang, *Metallic Biomaterials: New Directions and Technologies*. 2017: John Wiley & Sons.
43. Zadpoor, A.A. and R. Hedayati, *Analytical relationships for prediction of the mechanical properties of additively manufactured porous biomaterials*. *Journal of Biomedical Materials Research Part A*, 2016. **104**(12): p. 3164–3174.
44. *ASTM F75 CoCr Alloy*, A.E. system, Editor.: Mölndal, Sweden.
45. Marrey, R.V., R. Burgermeister, R.B. Grishaber, and R. Ritchie, *Fatigue and life prediction for cobalt-chromium stents: A fracture mechanics analysis*. *Biomaterials*, 2006. **27**(9): p. 1988-2000.
46. Okazaki, Y., *Comparison of fatigue properties and fatigue crack growth rates of various implantable metals*. *Materials*, 2012. **5**(12): p. 2981-3005.
47. Qian, B., K. Saeidi, L. Kvetková, F. Lofaj, C. Xiao, and Z. Shen, *Defects-tolerant Co-Cr-Mo dental alloys prepared by selective laser melting*. *Dental Materials*, 2015. **31**(12): p. 1435-1444.
48. Hedayati, R., M. Sadighi, M. Mohammadi-Aghdam, and A.A. Zadpoor, *Computational prediction of the fatigue behavior of additively manufactured porous metallic biomaterials*. *International journal of fatigue*, 2016. **84**: p. 67–79.

49. Stephens, R., P. Dindinger, and J. Gunger, *Fatigue damage editing for accelerated durability testing using strain range and SWT parameter criteria*. International Journal of fatigue, 1997. **19**(8): p. 599-606.
50. Wu, Z.-R., X.-T. Hu, and Y.-D. Song, *Multiaxial fatigue life prediction for titanium alloy TC4 under proportional and nonproportional loading*. International Journal of Fatigue, 2014. **59**: p. 170-175.
51. Fatemi, A. and D.F. Socie, *A Critical Plane Approach to Multiaxial Fatigue Damage Including out-of-Phase Loading*. Fatigue & Fracture of Engineering Materials & Structures, 1988. **11**(3): p. 149-165.
52. Morrow, J., *Cyclic plastic strain energy and fatigue of metals*, in *Internal friction, damping, and cyclic plasticity*. 1965, ASTM International.
53. Moumni, Z., A. Van Herpen, and P. Riberty, *Fatigue analysis of shape memory alloys: energy approach*. Smart Materials and Structures, 2005. **14**(5): p. S287.
54. Zysset, P.K., X.E. Guo, C.E. Hoffler, K.E. Moore, and S.A. Goldstein, *Elastic modulus and hardness of cortical and trabecular bone lamellae measured by nanoindentation in the human femur*. Journal of biomechanics, 1999. **32**(10): p. 1005-1012.
55. Bayraktar, H.H., E.F. Morgan, G.L. Niebur, G.E. Morris, E.K. Wong, and T.M. Keaveny, *Comparison of the elastic and yield properties of human femoral trabecular and cortical bone tissue*. Journal of biomechanics, 2004. **37**(1): p. 27-35.
56. Rho, J.-Y., L. Kuhn-Spearing, and P. Zioupos, *Mechanical properties and the hierarchical structure of bone*. Medical engineering & physics, 1998. **20**(2): p. 92-102.
57. Krishna, B.V., W. Xue, S. Bose, and A. Bandyopadhyay, *Functionally graded Co–Cr–Mo coating on Ti–6Al–4V alloy structures*. Acta biomaterialia, 2008. **4**(3): p. 697-706.
58. Matsuno, H., A. Yokoyama, F. Watari, M. Uo, and T. Kawasaki, *Biocompatibility and osteogenesis of refractory metal implants, titanium, hafnium, niobium, tantalum and rhenium*. Biomaterials, 2001. **22**(11): p. 1253-1262.
59. Van Der Stok, J., D. Lozano, Y.C. Chai, S. Amin Yavari, A.P. Bastidas Coral, J.A. Verhaar, E. Gómez-Barrena, J. Schrooten, H. Jahr, and A.A. Zadpoor, *Osteostatin-coated porous titanium can improve early bone regeneration of cortical bone defects in rats*. Tissue Engineering Part A, 2015. **21**(9-10): p. 1495-1506.
60. Van der Stok, J., O.P. Van der Jagt, S. Amin Yavari, M.F. De Haas, J.H. Waarsing, H. Jahr, E.M. Van Lieshout, P. Patka, J.A. Verhaar, and A.A. Zadpoor, *Selective laser melting-produced porous titanium scaffolds regenerate bone in critical size cortical bone defects*. Journal of Orthopaedic Research, 2013. **31**(5): p. 792-799.
61. Jakobsen, S.S., J. Baas, T. Jakobsen, and K. Soballe, *Biomechanical implant fixation of CoCrMo coating inferior to titanium coating in a canine implant model*. Journal of Biomedical Materials Research Part A, 2010. **94**(1): p. 180-186.
62. Stenlund, P., S. Kurosu, Y. Koizumi, F. Suska, H. Matsumoto, A. Chiba, and A. Palmquist, *Osseointegration enhancement by Zr doping of Co-Cr-Mo implants fabricated by electron beam melting*. Additive Manufacturing, 2015. **6**: p. 6-15.
63. Ahmadi, S., G. Campoli, S. Amin Yavari, B. Sajadi, R. Wauthlé, J. Schrooten, H. Weinans, and A.A. Zadpoor, *Mechanical behavior of regular open-cell porous biomaterials made of diamond lattice unit cells*. Journal of the mechanical behavior of biomedical materials, 2014. **34**: p. 106-115.

Chapter 9 Conclusions

9.1 Overview and conclusions

In this thesis, a series of analytical analysis, numerical modelling and experiments were carried out to predict the mechanical properties of volume-porous metallic biomaterials fabricated using an additive manufacturing technique, namely selective laser melting. In general terms, it is clear that the mechanical properties of such biomaterials are highly dependent on their topological design at the micro-scale, i.e. the shape and dimensions of the repeating unit cell. Moreover, the material type plays some role in determining even the normalized mechanical properties of AM porous biomaterials. The effects of material type on normalized quasi-static mechanical properties were largely neglected in the past but this thesis shows that, while being less important than the topological design, material type plays a detectable role in determining the quasi-static mechanical properties of AM porous biomaterials. As for the fatigue behaviour, both topological design and material type play important role the fatigue life of the studied biomaterials. Indeed, for a certain range of unit cell designs, the effects of material type on normalized S-N curves are even stronger than those of the topological design. These observations together with the presented data, analysis, and models should provide the basis for understudying how AM porous biomaterials respond to repeated loading after implantation and how the designer could design the topology of such biomaterials and choose the right material type for achieving the desired mechanical behaviour.

For example, the analytical and numerical solutions that were presented in Chapter 2 could be used to predict the elastic modulus, Poisson's ratio, elastic buckling limit, and yield stress of cellular structures with diamond unit cell type. From the results obtained in Chapter 2, it can be concluded that the analytical and numerical solutions are in good agreements with experimental observations for small apparent density values. For large apparent density values, the results of the analytical solution based on the Euler-Bernoulli beam theory deviate from the experimental results while the

mechanical properties predicted with FE models and the analytical solution based on the Timoshenko beam theory, though less accurate than for small apparent density values, are still relatively close to experimental observations. This type of analytical solutions are beneficial for medical implant designers, because they could help in avoiding costly numerical calculations for their initial designs. However, for the final design, more comprehensive studies are likely required.

Based on the findings from a series of experiments in Chapter 3, it can be concluded that AM pure titanium is a proper candidate for dynamically loaded porous implants. It has similar mechanical behaviour and properties as compared to porous Tantalums. Moreover, in high cycle fatigue, CP Ti shows better results than Ti6Al4V ELI, but for statically loaded or low cycle fatigue applications, Ti6Al4V ELI remains the preferred material. These conclusions could have a potentially large impact on the medical device industry, because it brings CP Ti back in the scope of implant designers. CP Ti is less costly as compared to Tantalum and has the advantage of no potential hazardous or toxic alloying components like the presently applied titanium alloys. However, two important points must be taken into consideration. First of all, additive manufacturing is a near net-shape manufacturing technique and for a final product, some additional post processing treatments are needed which are not taken into account in this study. And second of all, to launch a medical device, pre-trial and clinical studies are necessary which can take 5-10 years, meaning that substantial investment may be needed to switch from one material to another.

The relationship between morphological and mechanical properties of selective laser melted porous titanium alloy biomaterials based on six different types of space-filling unit cells were studied in Chapter 4. It was observed that the mechanical behavior and failure mechanisms of the porous structures are highly dependent on the type and dimensions of the unit cells out of which the porous structures are made. When comparing the mechanical properties of the porous structures based on the different types of unit cells, it was observed that in many cases the comparative performance of the structures is different for low and high values of apparent density with a separating apparent density of 0.15-0.2. Among all unit cells, the diamond unit cell consistently showed lower mechanical properties. Regarding the stiffness values, the unit cells were divided into a high stiffness group including truncated cube, truncated cuboctahedron, rhombicuboctahedron, and cube and a low stiffness group including diamond and rhombic dodecahedron. However, truncated cube showed remarkably higher stiffness than other members of its group for apparent densities exceeding 0.2.

These results could be used as a library for design of porous medical devices. However, it must be noted that the purpose of this chapter is not to choose one unit cell, as the preferred unit cell may be dependent on other criteria such as permeability, fatigue behavior, surface area, etc.

The fatigue properties of a particular class of AM porous biomaterials, and the effects of the type of unit cell and porosity on the fatigue properties of the porous structures were studied in Chapter 5. Porous structures based on three types of unit cells, namely cube, diamond, and truncated cuboctahedron, were considered. It was observed that both unit cell type and porosity greatly influence the S-N curves of the porous structures. As for the porous structures based on the cube unit cell, none of the specimens failed even when they experienced loads amounting to 80% of their yield strength for 10⁶ cycles. For both other types of unit cells, higher porosities resulted in shorter fatigue lives for the same level of applied stress. Moreover, the S-N curves normalized with respect to the yield stress of the porous structures conformed very well to one single power law for each type of unit cell. Similar to data of Chapter 4, these data could be used by medical device designers for fatigue design of medical devices based on such porous structures.

The effects of variation in two main laser processing parameters, namely laser power P and scanning time t_s , on the topological parameters and mechanical properties of the resulting biomaterials (e.g. relative density, surface hardness, elastic modulus, yield stress, plateau stress, and first maximum stress) were investigated in Chapter 6. It was found that all the noted mechanical properties increase with increasing either laser power or scanning time. The rate of change in the topological and mechanical properties with respect to the exposure time was found to be non-linear, while it is linear with respect to laser power. Most curves exhibited two stages: in the first stage, the mechanical properties increase with an increasing slope as the exposure time increased from 150 μs to 350 μs . The majority of the curves become linear at exposure times around 450 μs (as a turning point). From 550 μs to 950 μs , the mechanical properties continue to increase but with a decreasing slope. Empirical relationships between geometrical features and mechanical properties of the resulting porous structures and the processing parameters (exposure time and laser power) have been obtained. Comparing the empirical and experimental curves shows the validity of the separation method used for obtaining the empirical relationships. It must be noted that, there are other factors which are important to gain a better understanding of the mechanical properties of these structures such as microstructure or/and internal pores which were out of the scope of this

study. Also, in general more than 100 parameters could affect the final product quality but in this study the two most important ones are taken into considerations.

In Chapter 7, a systematic study was performed to understand the isolated and modulated effects of topological design and material type on the quasi-static mechanical properties of AM porous metallic biomaterials. Even though the effects of topological design on quasi-static mechanical properties were dominant, we could still detect notable effects of material type on the same properties. Moreover, the material type affect the absolute and normalized properties of porous structures in different ways. For example, porous structures made of Co-Cr had normalized elastic moduli and yield stresses respectively lower and higher than porous structures having same topological design but made of Ti-6Al-4V.

The effects of material type and topological design on the fatigue behavior of AM porous biomaterials were studied in Chapter 8. It was confirmed that the porosity of the porous structure does not have a significant effect on the normalized S-N curve of the porous structure. However, the shape of the unit cell, manufacturing imperfections, and the mechanical properties of the bulk material were found to affect the normalized S-N curve. For the three unit cell types considered here, the bulk material properties and manufacturing imperfections are far more important in determining the normalized fatigue strength of porous biomaterials, particularly in the high-cycle fatigue region. The effects of bulk material properties, manufacturing imperfections, and topological design were found to be different in the high- and low cycle fatigue regions. This is due to the fact that the fatigue response of a porous structure not only depends on the static and fatigue strengths of the bulk material, but is also dependent on other factors such as the roughness of the outer surface of the struts (effective on crack initiation), the distribution of the micro-pores created inside the struts during additive manufacturing process (effective on crack propagation procedure), and plasticity (effective on both crack initiation and crack propagation procedures). The contribution of each of the noted parameters is different in high- and low-cycle fatigue regions.

The methodology and results which are presented in this study provide in-depth insight into design and manufacture of porous bone-mimicking implants. Since each patient has a unique anatomy and bone mechanical properties, the results which are presented in this thesis could be beneficial and cost effective for medical device designers. This thesis assist the designer in the essential steps that

are required for the design of customized implants, namely selecting the right material, optimizing the topological design, and understanding the role of additive manufacturing technique in determining the properties of the final product.

9.2 Recommendations for future research

There are many factors that lead to a successful orthopaedic implant. In this thesis, mainly the effects of different topologies, porosities and materials on the mechanical properties of additively manufacture structures have been covered. However, design optimization considering all relevant factors and the limitation of additive manufacturing was out of the scope of this thesis. The next steps may therefore involve application of computational design approaches such as topology optimization to improve the mechanical properties of the final product.

All the specimens in this thesis were manufactured by additive manufacturing technique. As discussed earlier in this thesis, this technique delivers a near net-shape products and in order to have the final product ready, post processing of specimens is requested which are not covered in this thesis. An interesting step after this study could be the investigation of the effects of different heat treatments on the microstructure and, thus, the mechanical properties of such structures. For instance, the microstructure of titanium and its alloys usually contains two different phases, namely α and β . Additively manufactured specimens often only have α' phase which is very brittle in nature. To have proper mechanical properties, a combination of α and β is required which has superior strength as well as ductility. To reach the desired microstructure, a series of heat treatment regimens (below and above β transus) must be applied followed by quasi-static and fatigue mechanical testing.

To enhance the bond between implants and bone, the surface of the implants needs to be engineered. There are a different methods to achieve this goal including chemical treatments such as chemical etching or physical treatments such sand blasting. This aspect is missing in this thesis since none of the mentioned methods are applied to the specimens in this thesis. An interesting approach to continue this work would be investigating the effects of different surface treatments on

the mechanical behaviour of AM porous biomaterials. To picture a broader view, the final step could be bio-functionalization of the surface, which means surface modification of the surface by adding some biological functions for different purposes such as drug delivery or for inducing antimicrobial properties.

Additive manufacturing techniques, as compared to other manufacturing techniques, are still immature. There are a relatively large number of known and unknown aspects which have not been investigated and may affect the final product. In this thesis, a few of them such as a few main processing parameters (laser power, exposure time) were explored but the effects of many other parameters remain unknown. More in-depth study considering a wider range of processing and design parameters is suggested as a next step to enhance the quality of the final product.

9.3 Summary

One of the main functions of bone is to support the human body mechanically. To fulfil its complex role, bone possesses unique mechanical properties: it is stiff enough to resist deformation while being able to absorb energy.

Looking at bone at the macroscopic scale, two distinct types of tissues are detectable, namely trabecular and cortical. Cortical (compact) bone has a high density and low porosity with a great compressive strength while trabecular (cancellous) bone is highly porous and provides internal support of bone. Cortical bone which constitutes up to 80% of bone mass endures the mechanical loads while trabecular bone which has 50-90% of total bone volume, make mechanical loads distribute evenly by acting as energy absorbent. Additively manufactured porous metallic biomaterials are promising candidates for application as bone-mimicking implants since they are capable of delivering both above-mentioned functions.

In this thesis, a comprehensive study has been carried out using analytical methods, numerical methods and experiments to gain a better understanding of these structures. A wide range of porous structures with several topological designs and material types were considered. The quasi-static and fatigue behaviour of those AM porous biomaterials were determined experimentally and were compared with analytical solutions and computational (i.e. finite element modelling) results. The quasi-static mechanical properties and fatigue S-N curves were analysed both in absolute and in normalized terms. In the case of quasi-static mechanical properties, normalization was performed with respect to the mechanical properties of the bulk (i.e. matrix) material from which the porous biomaterials were made while stress levels in the S-N curves were normalized with respect to the yield or plateau stress of the porous biomaterial.

In general terms, both topological design and material type were found to influence the quasi-static mechanical properties and fatigue behaviour of AM porous metallic biomaterials. In the case of quasi-static mechanical properties, the effects of the topological design were dominant but the material type had considerable effects too. The analytical solutions and computational results were generally in agreement with experimental observations particularly for the lower values of the relative density. As for the fatigue behaviour, the absolute S-N curves were found to be highly

dependent on the porosity of the biomaterials. Once normalized with respect to the yield or plateau stress, the effects of porosity largely disappeared. The normalized S-N curves were, however, highly dependent on topological design as defined by the type of the repeating unit cell. The material type was also found to play an important role in defining the S-N curves. Indeed, for a group of unit cells considered in this thesis, the material type had a larger effect than the type of the unit cell on the normalized S-N curves of AM porous metallic biomaterials.

Due to the uniqueness of each patient's bone structure and differences in various types of orthopaedic procedures, there is no specific porous structure or material type with best properties. However, the methods and results presented in this thesis provide some useful information that could be applied when designing a dedicated implant. In particular, they could be used for selecting the right topological design (i.e. the type of repeating unit cell), the appropriate porosity, and strut size, and for deciding about the material type. The ultimate goal often is to mimic the properties of the bone that is being replaced. The results of this thesis show AM porous metallic biomaterials could mimic several aspects of bone tissue properties and are therefore promising candidates.

9.4 Samenvatting

Één van de belangrijkste functies van bot is het mechanisch ondersteunen van het menselijk lichaam. Bot bezit unieke mechanische eigenschappen om deze complexe rol te vervullen: het is stijf genoeg om vervormingen te weerstaan terwijl het ook in staat is om energie te absorberen.

Op de macroscopische schaal kunnen twee verschillende soorten botweefsel worden onderscheiden, namelijk trabeculair en corticaal bot. Corticaal (compact) bot heeft een hoge dichtheid en een lage porositeit met een hoge compressiesterkte terwijl trabeculair (spongieus) bot een hoge porositeit bezit en interne ondersteuning verleent aan het bot. Corticaal bot, dat tot 80% van de botmassa inneemt, weerstaat de mechanische belasting terwijl trabeculair bot, dat 50-90% van het totale botvolume beslaat, ervoor zorgt dat de mechanische belasting gelijk verdeeld wordt door op te treden als energie absorberend materiaal. Additief vervaardigde poreuze metalen biomaterialen zijn veelbelovende kandidaten voor bot-imiterende implantaten omdat ze beide van de bovengenoemde functies kunnen vervullen.

In dit proefschrift wordt een diepgaande studie uitgevoerd aan de hand van analytische en numerieke methodes en experimenten om een beter inzicht te krijgen in deze structuren. Een breed scala aan poreuze structuren met verschillende topologische ontwerpen en materiaaltypes worden onderzocht. Het quasi-statische en vermoeiingsgedrag van deze additief vervaardigde poreuze biomaterialen wordt experimenteel bepaald en wordt vergeleken met analytische oplossingen en computerresultaten (i.e. eindige elementen modellering). De quasi-statische mechanische eigenschappen en S-N vermoeiingscurven worden zowel in absolute als genormaliseerde termen geanalyseerd. In geval van de quasi-statische mechanische eigenschappen wordt de normalisering uitgevoerd met betrekking tot de mechanische eigenschappen van het bulkmateriaal (i.e. matrix) waarvan de poreuze biomaterialen worden vervaardigd terwijl de spanningsniveaus van de S-N curven genormaliseerd worden met betrekking tot de vloeigrens of plateauspanning van het poreuze biomateriaal.

Algemeen gesproken wordt vastgesteld dat zowel het topologische ontwerp als het materiaaltipe de quasi-statische en vermoeiingseigenschappen van de additief vervaardigde poreuze metalen biomaterialen beïnvloeden. De invloeden van het topologische ontwerp zijn dominant in het geval

van de quasi-statische mechanische eigenschappen, maar het materiaaltype speelde ook een aanzienlijke rol. De analytische oplossingen en computerresultaten stemmen in het algemeen goed overeen met de experimentele observaties, vooral voor de lagere waarden van de relatieve dichtheid. Wat betreft het vermoeiingsgedrag is vastgesteld dat de absolute S-N curven sterk afhankelijk zijn van de porositeit van de biomaterialen. De effecten van de porositeit van de biomaterialen verdwijnen grotendeels na de normalisering met betrekking tot de vloeigrens of plateauspanning. Echter, de genormaliseerde S-N curven zijn sterk afhankelijk van het topologisch ontwerp dat wordt gedefinieerd door het type van de herhalende eenheidscel. Er is vastgesteld dat ook het materiaaltype een belangrijke rol speelt in het bepalen van de S-N curven. Voor een bepaalde groep eenheidscellen onderzocht in dit proefschrift heeft het materiaaltype een groter effect dan het type eenheidscel op de genormaliseerde S-N curven van de additief vervaardigde poreuze metalen biomaterialen.

Als gevolg van de uniciteit van de botstructuur van elke patiënt en de verschillende soorten orthopedische procedures is er geen specifieke poreuze structuur of materiaaltype met de beste eigenschappen. De methodes en resultaten gepresenteerd in dit proefschrift verschaffen echter wel nuttige informatie die kan toegepast worden bij het ontwerpen van een specifiek implantaat. Ze kunnen met name gebruikt worden voor het selecteren van het geschikte topologische ontwerp (i.e. het type van herhalende eenheidscel), de passende porositeit en de strutgrootte, en voor het kiezen van het materiaaltype. Het ultieme doel is vaak om de eigenschappen van het te vervangen bot na te bootsen. De resultaten van dit proefschrift tonen aan dat additief vervaardigde poreuze metalen biomaterialen veelbelovende kandidaten zijn, aangezien ze verschillende aspecten van de eigenschappen van botweefsel kunnen nabootsen.

9.5 Author Curriculum Vitae

Seyed Mohammad Ahmadi

18-09-1985 Tehran, Iran

9.5.1 Education

- Doctor of Philosophy (2013-2018), Biomechanical department, Delft University of Technology, Delft, the Netherlands
- Master of Science (2008-2011), Biomedical department, Amirkabir University of Technology, Tehran, Iran
- Bachelor of Science (2003-2008), Sharif University of Technology, Iran

9.5.2 Professional experience

- Postdoctoral researcher (2017-present), Delft University of Technology, Delft, the Netherlands
Topic: Functional Grading and Microstructural Design of Porous Titanium Produced by Additive Manufacturing
- Co-founder Amber Implants B.V. (2016-now), Delft, the Netherlands
Topic: Design and manufacture medical devices
- Mechanical design engineer (2014-2015), E2M Technologies, Amsterdam, the Netherlands
- Mechanical design engineer (2011-2013), IPDC, Tehran, Iran

9.6 List of publications

1. **SM Ahmadi**, R Hedayati, Y Li, K Lietaert, N Tümer, A Fatemi, CD Rans, B Pouran, H Weinans, AA Zadpoor, *Fatigue performance of additively manufactured meta-biomaterials: The effects of topology and material type*, Acta biomaterialia, 2018 (from this thesis).
2. R Hedayati, **SM Ahmadi**, K Lietaert, B Pouran, Y Li, H Weinans, CD Rans, AA Zadpoor, *Isolated and modulated effects of topology and material type on the mechanical properties of additively manufactured porous biomaterials*, Journal of the mechanical behavior of biomedical materials, 2018(from this thesis).
3. **S M Ahmadi**, R K Ashok Kumar Jain, A A Zadpoor, C Ayas, V A Popovich, *Effects of heat treatment on microstructure and mechanical behaviour of additive manufactured porous Ti6Al4V*, ICSMR, 2018.
4. **SM Ahmadi**, R Hedayati, RK Ashok Kumar Jain, Y Li, S Leeflang, AA Zadpoor, *Effects of laser processing parameters on the mechanical properties, topology, and microstructure of additively manufactured porous metallic biomaterials: A vector-based approach*, Materials & Design, 2017(from this thesis).
5. FSL Bobbert, K Lietaert, AA Eftekhari, B Pouran, **SM Ahmadi**, H Weinans, AA Zadpoor, *Additively manufactured metallic porous biomaterials based on minimal surfaces: A unique combination of topological, mechanical, and mass transport properties*, Acta Biomaterialia, 2017.
6. J Kadkhodapour, H Montazerian, A Ch Darabi, AP Anaraki, **SM Ahmadi**, AA Zadpoor, S Schmauder, *Failure mechanisms of additively manufactured porous biomaterials: Effects of porosity and type of unit cell*, Journal of the mechanical behavior of biomedical materials, 2015.
7. R Wauthle, **SM Ahmadi**, S Amin Yavari, M Mulier, AA Zadpoor, H Weinans, J Van Humbeeck, JP Kruth, J Schrooten, *Revival of pure titanium for dynamically loaded porous implants using additive manufacturing*, Materials Science and Engineering: C, 2015 (from this thesis).
8. **SM Ahmadi**, S Amin Yavari, R Wauthle, B Pouran, J Schrooten, H Weinans, AA Zadpoor, *Additively manufactured open-cell porous biomaterials made from six different space-filling unit cells: The mechanical and morphological properties*, Materials, 2015 (from this thesis).
9. S Amin Yavari, **SM Ahmadi**, R Wauthle, B Pouran, J Schrooten, H Weinans, AA Zadpoor, *Relationship between unit cell type and porosity and the fatigue behavior of selective laser melted meta-biomaterials*, Journal of the mechanical behavior of biomedical materials, 2015 (from this thesis).
10. S Amin Yavari, **SM Ahmadi**, Johan van der Stok, Ruben Wauthlé, AC Riemsdag, Michael Janssen, Jan Schrooten, Harrie Weinans, Amir Abbas Zadpoor, *Effects of bio-functionalizing surface treatments on the mechanical behavior of open porous titanium biomaterials*, Journal of the mechanical behavior of biomedical materials, 2014.

-
11. S Amin Yavari, J van der Stok, **SM Ahmadi**, R Wauthlé, J Schrooten, H Weinans, AA Zadpoor, *Mechanical analysis of a rodent segmental bone defect model: The effects of internal fixation and implant stiffness on load transfer*, Journal of biomechanics, 2014.
 12. **SM Ahmadi**, G Campoli, S Amin Yavari, B Sajadi, Ruben Wauthlé, Jan Schrooten, H Weinans, AA Zadpoor, *Mechanical behavior of regular open-cell porous biomaterials made of diamond lattice unit cells*, Journal of the mechanical behavior of biomedical materials, 2015 (from this thesis).
 13. **SM Ahmadi**, E Shirzad, Sajadi, M Cheraghi, K Haghighi, *An Experimental Study on the Kinematics of a Skilled Service in Playing Tennis*, American Society of Mechanical Engineers, 2010.

9.7 Acknowledgment

First and foremost, I would like to express my sincere gratitude to my supervisors, Prof. Amir Zadpoor and Prof. Harrie Weinans for giving me this opportunity to work on such a novel project at one of the best technical universities in the world. I clearly remember how enthusiastic Amir was about this topic when we met for the first time in his previous office. Amir's eagerness for knowledge always steered me in the right direction and indeed without his passion for success, this project would have ended differently. Harrie's role in my academic and career life is of great value. His comments (in our infrequent meetings) guided me step by step through my Ph.D. process. Also, at the most crucial moments in my career life, I always knew he was the one that I could rely on.

Beside my supervisors, I would also like to thank Dr. Saber Amin Yavari and Dr. Reza Hedayati for their endless support during my Ph.D. project. Saber is not only a great colleague but also a supportive friend and I was lucky that first two years of my Ph.D. time overlapped with his presence at TU Delft.

I would also like to thank Gianni, Shahram, Nazli, Axel, Paolo, Behnam, Sina, Martina, Vahid, Budi, Nima, Francoise, Mahya, Ingmar, Yageng, Eline, Sander and all my dear colleagues and friends at 3ME. Thank you for all of the enjoyable time we shared together in the last 5 years. And special thanks to Sebastien for translating the summary to Dutch.

Finally, I must express my very profound gratitude to my family and dear wife for everything. I really don't know how to show my appreciation for the endless love and support which I received from my family throughout my years of study. And, Banafsheh; I could not even imagine myself in this position without you and your unlimited support in the last decade of my life. It is a blessing that my best friend and my best colleague is my loving wife, and I am thankful for each second I spend beside you.

Thank you.

Mohammad

